

TECHNISCHE UNIVERSITÄT KAISERSLAUTERN

**London dispersion investigated on
molecular balances in multiple electronic
states**

Autor:

Patrick Horst STREBERT

Betreuer:

Prof. Dr. Markus GERHARDS[†]

PD Dr. Christoph RIEHN

*Vom Fachbereich Chemie der Technischen Universität Kaiserslautern zur Verleihung
des akademischen Grades "Doktor der Naturwissenschaften" genehmigte
Dissertation*

D 386

Die vorliegende Arbeit wurde im Zeitraum von November 2018 bis Dezember 2022 im Fachbereich Chemie der Technischen Universität Kaiserslautern angefertigt. Die Betreuung der Arbeit wurde von Prof. Dr. Markus Gerhards (bis Dezember 2020) und PD Dr. Christoph Riehn übernommen (ab Dezember 2020).

Datum des Antrags auf Eröffnung des Promotionsverfahrens: 22.11.2022

Datum der wissenschaftlichen Aussprache: 16.12.2022

Promotionskommission:

Vorsitzende: Jun.-Prof. Dr. Sabine Becker

1. Berichterstatter: PD Dr. Christoph Riehn

2. Berichterstatter: Prof. Dr. Dr. Gereon Niedner-Schatteburg

Declaration of Authorship

Hiermit bestätige ich, Patrick Horst STREBERT, dass die vorliegende Arbeit mit dem Titel "London dispersion investigated on molecular balances in multiple electronic states" gemäß der Promotionsordnung des Fachbereiches Chemie der Technischen Universität Kaiserslautern selbstständig und ausschließlich mit den angegebenen Hilfsmitteln und Quellen erstellt wurde.

Unterschrift:

Ort, Datum: Kaiserslautern, 03.01.2023

“Door meten tot weten.”
(Durch Messen zum Wissen)

Heike Kamerlingh Onnes

Contents

1	Introduction	1
2	Experimental setup and methods	7
2.1	Spectroscopic techniques	7
2.1.1	R2PI spectroscopy	7
2.1.2	IR/R2PI spectroscopy	9
2.1.3	UV/IR/UV spectroscopy	9
2.1.4	Stimulated Raman spectroscopy	10
2.2	Laser systems	12
2.2.1	UV laser system	12
2.2.2	IR laser system	13
2.2.3	Raman laser system	14
2.3	Molecular beam technique	15
2.3.1	Theoretical background	15
2.3.2	Molecular beam apparatus	16
3	Quantum chemical methods	21
3.1	Density functional theory	21
3.1.1	Range-separated functionals	24
3.1.2	Dispersion correction	24
3.2	Time-dependent density functional theory	25
3.2.1	Natural transition orbitals	27
3.3	Coupled-Cluster methods	29
3.3.1	CC2	30
3.3.2	ADC(2)	31
3.3.3	Spin-component scaling	33
3.3.4	Domain-based local pair natural orbital method (DLPNO)	33
3.4	Conformer search	34
3.5	Energy decomposition analysis	35
3.5.1	Symmetry-adapted perturbation theory	35
3.5.2	Local energy decomposition	37
3.6	Calculation of anharmonic frequencies	39
3.7	Auxiliary programs	41

4 Results	43
4.1 Dispersion in the ground state: Triphenylmethane and ^t BuTPM	44
4.2 Dispersion in the ground state: ⁱ PrTPM	46
4.2.1 DFT calculations	47
4.2.2 SAPT calculations	53
4.3 Benchmark of anharmonic frequencies	58
4.4 Dispersion in excited states: Chromone-methanol cluster	68
4.5 Dispersion in excited states: Cluster of chromone derivatives with methanol	70
4.5.1 Identification of suitable candidates	70
4.5.2 Analysis of suitable candidates	76
5 Summary and Outlook	101
6 Zusammenfassung und Ausblick	105
Bibliography	111
A Publications	127
A.1 Publication I	127
A.2 Supporting Information of Publication I	133
A.3 Publication II	165
A.4 Supporting Information of Publication II	175
B Dispersion in ground state and benchmark of anharmonic frequencies	197
B.1 ⁱ PrTPM	197
B.2 Benchmarking tests	201
B.3 Source code	229
C Chromone derivatives	253
C.1 Ground state	253
C.2 Excited state	265
D Reprint Permissions	277
E Contributions to conferences	285
E.1 Oral presentations	285
E.2 Poster presentations	285

List of Figures

1.1	Foot of a gecko. ^[15]	3
2.1	Scheme for R2PI methods including a) one-color R2PI b) one-color R2PI, when $\Delta E(S_N, D_0)$ is larger than $\Delta E(S_0, S_N)$ c) two-color R2PI. Two-color R2PI is required for successful ionization when the S_N state is too low in energy.	8
2.2	Scheme for the IR/R2PI and UV/IR/UV method, illustrating the depopulation of the electronic ground state and excited state, respectively.	9
2.3	Scheme for the stimulated Raman methods IGSRS and ILSRS, illustrating the depopulation of the electronic ground state by stimulated Raman emission respectively.	11
2.4	Scheme of the UV laser system, for a pump laser wavelength of 532 nm.	12
2.5	Scheme of the IR laser system, using both 532 nm (green) and 1064 nm (grey) of the pump laser.	13
2.6	Scheme of the Raman laser, including the optical pathway with the delay line. The dichroic mirror is essential to ensure good overlap between Stokes and Pump beam.	15
2.7	Model of adiabatic cooling during the supersonic expansion with sketches of the velocity distribution. Adapted by permission from Springer Nature Customer Service Centre GmbH: Springer Laserspektroskopie 2 by Wolfgang Demtröder, 2013. ^[120]	16
2.8	Schematic depiction of the molecular beam apparatus, with dotted lines indicating the three vacuum chambers. Laser beam paths are indicated in blue(UV) and red(IR), the vacuum pumps are omitted for clarity.	17
2.9	Photo of the thermal source showing the sample storage wrapped in THERMOCOAX heating elements. The sample storage is connected to the carrier gas supply and the pulse valve. Additional heating resistors are mounted to the valve head and the sample storage.	18
3.1	“Schematic plots of the contributions to exchange from r_{12}^{-1} , apportioned into DFT and HF, for: B3LYP (left) and CAM-B3LYP (right).” Adapted from ref. [141].	24
3.2	$S_0 \rightarrow S_3$ transition of chromone, expressed with canonical molecular orbitals.	28

3.3	$S_0 \rightarrow S_3$ transition of chromone, expressed with natural transition orbitals.	28
4.1	Different dimer motifs of triphenylmethane derivatives (R=H, ^t Bu). Reprinted with permission from Wiley-VCH. ^[107]	44
4.2	Structures of TPM, ⁱ PrTPM and ^t BuTPM, with increasing size of dispersion energy donors.	47
4.3	Different structures of the ⁱ PrTPM dimer calculated at B97D/def2-TZVP level. For clarity, most hydrogen atoms are omitted.	47
4.4	Head-to-tail motif of the ⁱ PrTPM dimer calculated at B3LYP-D3(BJ)/def2-TZVP level. For clarity, most hydrogen atoms are omitted. $\Delta E = 0$ kJ/mol, $\Delta E_0 = 0$ kJ/mol	48
4.5	Head-to-head motif of the ⁱ PrTPM dimer calculated at B3LYP-D3(BJ)/def2-TZVP level. For clarity, most hydrogen atoms are omitted. $\Delta E = 27.6$ kJ/mol, $\Delta E_0 = 21.6$ kJ/mol	49
4.6	Tail-to-tail motif of the ⁱ PrTPM dimer calculated at B3LYP-D3(BJ)/def2-TZVP level. For clarity, most hydrogen atoms are omitted. $\Delta E = 52.6$ kJ/mol, $\Delta E_0 = 47.1$ kJ/mol	49
4.7	Crystal structure of ⁱ PrTPM. For clarity, most hydrogen atoms and all disordered atoms are omitted.	50
4.8	Calculated harmonic C-H stretching frequencies for the head-to-head motif of the ⁱ PrTPM dimer (gaussian envelope, FWHM=5 cm ⁻¹ , scaled by 0.96). The orange arrows indicate the stretching vibration of the central aliphatic C-H groups.	51
4.9	Calculated harmonic C-H stretching frequencies for the head-to-tail motif of the ⁱ PrTPM dimer (gaussian envelope, FWHM=5 cm ⁻¹ , scaled by 0.96). The orange arrows indicate the stretching vibration of the central aliphatic C-H groups.	51
4.10	Calculated harmonic C-H stretching frequencies for the tail-to-tail motif of the ⁱ PrTPM dimer (gaussian envelope, FWHM=5 cm ⁻¹ , scaled by 0.96). The orange arrows indicate the stretching vibration of the central aliphatic C-H groups.	51
4.11	Calculated harmonic C-D stretching frequencies for all three motifs of the ⁱ PrTPM dimer (gaussian envelope, FWHM=5 cm ⁻¹). The tail-to-tail motif exhibits two close-lying transitions which overlap. The monomer frequency is indicated with a dashed line.	52
4.12	Calculated anharmonic C-D stretching frequencies for all three motifs of the ⁱ PrTPM dimer (gaussian envelope, FWHM=5 cm ⁻¹). The anharmonic frequencies are the result of one-dimensional variational calculation. The tail-to-tail motif exhibits two close-lying transitions which overlap. The monomer frequency is indicated with a dashed line.	53

4.13	Visualization of the methyl and phenyl distances for the TPM dimer. The phenyl groups are represented by the orange (A1-A3) and red points (B1-B3). The methyl groups are represented by the dark blue (C1-C6) and light blue points (D1-D6).	55
4.14	Box plot of the phenyl-phenyl distances for the different dimer motifs of TPM derivatives. The individual data points are represented by black points and the mean by a red line. The box describes an interval containing the middle third of the distribution.	57
4.15	Box plot of the methyl-methyl distances for the head-to-head and head-to-tail motif of TPM derivatives. The individual data points are represented by black points, the mean by a red line and the median by an orange line. The box describes an interval containing the middle third of the distribution.	57
4.16	Box plot of the phenyl-methyl distances for the head-to-head and head-to-tail motif of TPM derivatives. The individual data points are represented by black points, the mean by a red line and the median by an orange line. The box describes an interval containing the middle third of the distribution.	58
4.17	Comparison of anharmonic frequencies (B3LYP) with literature values. The ideal correspondence is achieved if all values lie on the bisecting straight. The amount of atoms with an amplitude of over 0.2 is indicated with different colors.	63
4.18	Deviation of anharmonic frequencies (B3LYP) from literature values.	64
4.19	Deviation of anharmonic frequencies (B3LYP) from literature values in dependence of the locality of the normal mode. The amount of atoms with an amplitude of over 0.2 is indicated with different colors.	64
4.20	Comparison of anharmonic frequencies (M06-2X) with literature values. The ideal correspondence is achieved if all values lie on the bisecting straight. The amount of atoms with an amplitude of over 0.2 is indicated with different colors.	65
4.21	Deviation of anharmonic frequencies (M06-2X) from literature values.	67
4.22	Deviation of anharmonic frequencies (M06-2X) from literature values in dependence of the locality of the normal mode. The amount of atoms with an amplitude of over 0.2 is indicated with different colors.	67
4.23	Schematic depiction of the chromone-solvent cluster with the “inside” and “outside” pocket, stabilized by secondary C-H . . . O contacts. Reproduced from Ref. [266] with permission from the PCCP Owner Societies.	69
4.24	Structure of the unsubstituted chromone molecule with possible substitution positions.	72

4.25	Change of ΔE between inside and outside pocket for different mono-substituted chromone derivatives with respect to unsubstituted chromone. Positive values indicate an increased preference for the outside pocket and <i>vice versa</i> . For better visualization of the data, the y-axis is interrupted between -2 and -5 kJ/mol.	74
4.26	Jablonski term scheme for the clusters of methanol with different chromone derivatives showing the first two singlet and triplet excited states. The excited states were calculated with (TDA)-TD-DFT/CAM-B3LYP/def2-TZVP.	85
4.27	Geometry of the chromone-methanol cluster showing the puckering effect in the excited triplet state. The loss of planarity of the 4-pyrone ring is clearly visible in the images taken from above (left), the front (middle) and the right of (right) the cluster.	86
4.28	Planar structure of the chromone-methanol cluster calculated with SCS-ADC(2)/def2-TZVP, shown from a) above, b) the front and c) the right.	88
4.29	An exemplary cartoon explaining how for a certain starting geometry the wrong triplet state (dashed line) can be chosen as T_1 state. It is also possible that the T_n state is the T_2 state, a case which is not depicted here.	88
4.30	Structures of the 6-methylchromone-methanol cluster in the triplet state calculated with UDFT/CAM-B3LYP. The spin densities (cutoff=95 %) are shown in orange. The two structures on the left have most of the spin density distributed on the puckered carbon atoms. In contrast, the carbonyl oxygen carries most of the spin density for the outside planar structures. The relative energies and the respective OH stretching frequencies are given below the structure.	90
4.31	Planar structure of the 6-methylchromone-methanol cluster calculated with (a) SCS-CC2 and (b) SCS-ADC(2) using the basis set def2-TZVP, shown from above.	90
4.32	Structures of the 2-CF ₃ chromone-methanol cluster in the triplet state calculated with UDFT/CAM-B3LYP. The spin densities (cutoff=95 %) are shown in orange. The relative energies and the respective OH stretching frequencies are given below the structure.	92
4.33	Structures of the 2-CF ₃ ,6-methylchromone-methanol cluster in the lowest triplet state calculated with UDFT/CAM-B3LYP. The spin densities (cutoff=95 %) are shown in orange. The relative energies and the respective OH stretching frequencies are given below the structure.	93
4.34	Structures of 6-methylchromone-methanol cluster in the T_2 state calculated with TD-DFT/CAM-B3LYP. The relative energies and the respective OH stretching frequencies are given below the structure.	97

4.35	Structures of 2-CF ₃ chromone-methanol cluster in the T ₂ state calculated with TD-DFT/CAM-B3LYP. Concerning the outside motif, the calculation does not converge and oscillates. Thus, the shown structure represents the best approximation for comparison. The relative energies and the respective OH stretching frequencies are given below the structure.	97
4.36	Structures of 2-CF ₃ ,6-methylchromone-methanol cluster in the T ₂ state calculated with TD-DFT/CAM-B3LYP. Concerning the outside motif, the calculation does not converge and oscillates. Thus, the shown structure represents the best approximation for comparison. The relative energies and the respective OH stretching frequencies are given below the structure.	98
B.1	Potential energy curves for the ⁱ PrTPM monomer.	197
B.2	Potential energy curves for the head-to-tail motif of the ⁱ PrTPM dimer with the corresponding normal modes.	198
B.3	Potential energy curves for the head-to-head motif of the ⁱ PrTPM dimer with the corresponding normal modes.	199
B.4	Potential energy curves for the tail-to-tail motif of the ⁱ PrTPM dimer with the corresponding normal modes.	200
B.5	Potential energy curves and corresponding normal mode for methane.	202
B.6	Potential energy curves for acetylene.	203
B.7	Potential energy curves and corresponding normal mode for ethylene.	204
B.8	Potential energy curves and corresponding normal mode for ammonia.	205
B.9	Potential energy curves and corresponding normal mode for methylamine.	206
B.10	Potential energy curves and corresponding normal mode for methylamine.	207
B.11	Potential energy curves and corresponding normal mode for pyrrol.	208
B.12	Potential energy curve and corresponding normal mode for pyrrol.	209
B.13	Potential energy curves for water.	210
B.14	Potential energy curves for the OH stretching vibration of methanol.	210
B.15	Potential energy curves for the OH stretching vibration of phenol.	211
B.16	Potential energy curves for dihydrogen.	211
B.17	Potential energy curves for carbon monoxide.	211
B.18	Potential energy curves and corresponding normal mode for furan.	212
B.19	Potential energy curves for the CH stretching vibration of methyl fluoride.	213
B.20	Potential energy curves for the CH stretching vibration of methyl chloride.	213
B.21	Potential energy curves for the CH stretching vibration of methyl bromide.	213

B.22	Potential energy curves for the CH stretching vibration of fluoroethyne.	214
B.23	Potential energy curves for the CH stretching vibration of chloroethyne.	214
B.24	Potential energy curves for the CH stretching vibration of bromoethyne.	214
B.25	Potential energy curves and corresponding normal mode for methane.	216
B.26	Potential energy curves for acetylene.	217
B.27	Potential energy curves and corresponding normal mode for ethylene.	218
B.28	Potential energy curves and corresponding normal mode for ammonia.	219
B.29	Potential energy curves and corresponding normal mode for methylamine.	220
B.30	Potential energy curves and corresponding normal mode for methylamine.	221
B.31	Potential energy curves and corresponding normal mode for pyrrol.	222
B.32	Potential energy curve and corresponding normal mode for pyrrol.	223
B.33	Potential energy curves for water.	224
B.34	Potential energy curves for the OH stretching vibration of methanol.	224
B.35	Potential energy curves for the OH stretching vibration of phenol.	225
B.36	Potential energy curves for dihydrogen.	225
B.37	Potential energy curves for carbon monoxide.	225
B.38	Potential energy curves and corresponding normal mode for furan.	226
B.39	Potential energy curves for the CH stretching vibration of methyl fluoride.	227
B.40	Potential energy curves for the CH stretching vibration of methyl chloride.	227
B.41	Potential energy curves for the CH stretching vibration of methyl bromide.	227
B.42	Potential energy curves for the CH stretching vibration of fluoroethyne.	228
B.43	Potential energy curves for the CH stretching vibration of chloroethyne.	228
B.44	Potential energy curves for the CH stretching vibration of bromoethyne.	228
C.1	Structures of 6-SiMe ₃ , 2-nitrochromone with methanol for both inside and outside motif	255
C.2	Structures of 6- ^t Bu, 2-Nitrochromone with methanol for both inside and outside motif	255
C.3	Structures of 6-SiMe ₃ chromone with methanol for both inside and outside motif	255
C.4	Structures of 6-methoxychromone with methanol for both inside and outside motif	256
C.5	Structures of 6- ^t Bu-chromone with methanol for both inside and outside motif	256
C.6	Structures of 6-ethyl, 2-nitrochromone with methanol for both inside and outside motif	256

C.7	Structures of 6-methyl, 2-nitrochromone with methanol for both inside and outside motif	257
C.8	Structures of 6,7,8-methyl, 2-nitrochromone with methanol for both inside and outside motif	257
C.9	Structures of 6-SiH ₃ chromone with methanol for both inside and outside motif	257
C.10	Structures of 6-ethylchromone with methanol for both inside and outside motif	258
C.11	Structures of 6-methyl, 2-CF ₃ chromone with methanol for both inside and outside motif	258
C.12	Structures of 2-nitrochromone with methanol for both inside and outside motif	258
C.13	Structures of 6-methylchromone with methanol for both inside and outside motif	259
C.14	Structures of 6,7,8-methylchromone with methanol for both inside and outside motif	259
C.15	Structures of 6-SiH ₃ -chromone with methanol for both inside and outside motif	259
C.16	Structures of 2-chlorochromone with methanol for both inside and outside motif	260
C.17	Structures of 7-methylchromone with methanol for both inside and outside motif	260
C.18	Structures of 2-fluorochromone with methanol for both inside and outside motif	260
C.19	Structures of 2-CF ₃ -chromone with methanol for both inside and outside motif	261
C.20	Structures of 7-methoxychromone with methanol for both inside and outside motif	261
C.21	Structures of 2-isocyanidechromone with methanol for both inside and outside motif	261
C.22	Structures of 2-cyanidechromone with methanol for both inside and outside motif	262
C.23	Structures of 8-methoxychromone with methanol for both inside and outside motif	262
C.24	Structures of 8-methylchromone with methanol for both inside and outside motif	263
C.25	Structures of 2-cyanatechromone with methanol for both inside and outside motif	263
C.26	Structures of 2-isocyanatechromone with methanol for both inside and outside motif	264

C.27	NTOs of 6-methylchromone-methanol cluster for both inside and outside motif, $S_0 \rightarrow S_1$ with the occupied NTO at the bottom. The NTO pair accounts for 99% (out) and 99% (in) of the calculated transition.	265
C.28	NTOs of 6-methylchromone-methanol cluster for both inside and outside motif, $S_0 \rightarrow S_2$ with the occupied NTO at the bottom. The NTO pair accounts for 83% (out) and 84% (in) of the calculated transition.	266
C.29	NTOs of 6-methylchromone-methanol cluster for both inside and outside motif, $S_0 \rightarrow T_1$ with the occupied NTO at the bottom. The NTO pair accounts for 91% (out) and 91% (in) of the calculated transition.	267
C.30	NTOs of 6-methylchromone-methanol cluster for both inside and outside motif, $S_0 \rightarrow T_2$ with the occupied NTO at the bottom. The NTO pair accounts for 98% (out) and 99% (in) of the calculated transition.	268
C.31	NTOs of 2-CF ₃ chromone-methanol cluster for both inside and outside motif, $S_0 \rightarrow S_1$ with the occupied NTO at the bottom. The NTO pair accounts for 99% (out) and 99% (in) of the calculated transition.	269
C.32	NTOs of 2-CF ₃ chromone-methanol cluster for both inside and outside motif, $S_0 \rightarrow S_2$ with the occupied NTO at the bottom. The NTO pair accounts for 82% (out) and 83% (in) of the calculated transition.	270
C.33	NTOs of 2-CF ₃ chromone-methanol cluster for both inside and outside motif, $S_0 \rightarrow T_1$ with the occupied NTO at the bottom. The NTO pair accounts for 93% (out) and 93% (in) of the calculated transition.	271
C.34	NTOs of 2-CF ₃ chromone-methanol cluster for both inside and outside motif, $S_0 \rightarrow T_2$ with the occupied NTO at the bottom. The NTO pair accounts for 99% (out) and 99% (in) of the calculated transition.	272
C.35	NTOs of 2-CF ₃ ,6-methylchromone-methanol cluster for both inside and outside motif, $S_0 \rightarrow S_1$ with the occupied NTO at the bottom. The NTO pair accounts for 99% (out) and 99% (in) of the calculated transition.	273
C.36	NTOs of 2-CF ₃ ,6-methylchromone-methanol cluster for both inside and outside motif, $S_0 \rightarrow S_2$ with the occupied NTO at the bottom. The NTO pair accounts for 85% (out) and 86% (in) of the calculated transition.	274
C.37	NTOs of 2-CF ₃ ,6-methylchromone-methanol cluster for both inside and outside motif, $S_0 \rightarrow T_1$ with the occupied NTO at the bottom. The NTO pair accounts for 92% (out) and 92% (in) of the calculated transition.	275
C.38	NTOs of 2-CF ₃ ,6-methylchromone-methanol cluster for both inside and outside motif, $S_0 \rightarrow T_2$ with the occupied NTO at the bottom. The NTO pair accounts for 99% (out) and 99% (in) of the calculated transition.	275
D.1	Reuse permissions requests from https://www.rsc.org/journals-books-databases/author-and-reviewer-hub/authors-information/licences-copyright-permissions/	284

List of Tables

3.1	Physical interpretation of the different terms occurring in the SAPT0 energy formula.	37
4.1	Vibrational data for the three different motifs of ⁱ PrTPM with and without deuteration of the central C-H bond. The low IR intensities make IR/UV experiments unfeasible, thus stimulated Raman methods are more promising. The C-H and C-D frequencies are scaled by 0.96.	52
4.2	Results of energy decomposition analysis by SAPT0/jun-cc-pVDZ based on geometries obtained with DFT. The values for each interaction for the respective motif are given, as well as the energy difference Δ between the motifs. All values are given in kJ/mol.	53
4.3	Correlation of energy, dispersion and geometry for TPM, ⁱ PrTPM and ^t BuTPM dimer calculated at B3LYP-D3(BJ)/def2-TZVP level. The average r^{-6} -weighted distances d between p(henyl) and m(ethyl) are given together with the regular average in brackets. All values are given in Å. The total SAPT0 energy and the dispersion contribution are given in kJ/mol.	54
4.4	Anharmonic frequencies calculated with a one-dimensional variational method. The calculations were carried out at B3LYP-D3(BJ)/def2-TZVP level.	61
4.5	Anharmonic frequencies calculated with a one-dimensional variational method. The calculations were carried out at the M06-2X-abD3/def2-TZVP level.	66
4.6	Energy difference with and without zero-point vibrational energy between inside and outside motif for multiple derivatives of chromone calculated at CAM-B3LYP-D3(BJ)/def2-TZVP level. A positive ΔE indicates preference for the outside pocket (bottom of the table) and <i>vice versa</i> . The molecules marked in bold are chosen for further investigation. 73	73
4.7	Energy difference ΔE between inside and outside motif for multiple derivatives of chromone in the S_0 state calculated with different quantum chemical methods using a def2-TZVP basis set. The SAPT0 calculations are based on the final DFT geometries. A positive ΔE indicates preference for the outside pocket and <i>vice versa</i> . All values are given in kJ/mol.	77

- 4.8 OH stretching frequencies of chromone (derivative)-methanol clusters calculated with different methods. The values are given in the format X/Y, with X denoting the value for the inside motif and Y for the outside motif. All values are unscaled and are given in cm^{-1} . $\Delta(\text{method})$ describes the difference between the wavenumber of the OH stretching band for the inside and the outside motif. 79
- 4.9 Results of energy decomposition analysis by SAPT0/jun-cc-pVDZ based on geometries obtained with DFT. The values for each interaction for the respective motif are given, as well as the energy difference Δ between both motifs. All values are given in kJ/mol. A positive Δ refers to stabilization of the outside structure relative to the inside isomer. 80
- 4.10 Results of energy decomposition analysis by SAPT0/jun-cc-pVDZ based on geometries obtained with DFT. The values the combined 2-CF₃,6-methylchromone for each interaction for the respective motif are given, as well as the energy difference Δ between both motifs. All values are given in kJ/mol. Positive values refer to stabilization of the outside structure relative to the inside isomer. 81
- 4.11 Results of energy decomposition analysis by LED/DLPNO-CCSD(T) based on geometries obtained with DFT. The values for each interaction for the respective motif are given, as well as the energy difference Δ between both motifs. All values are given in kJ/mol. Positive values refer to stabilization of the outside structure relative to the inside isomer. C stands for chromone (derivative), M for methanol. 82
- 4.12 Results of energy decomposition analysis by LED/DLPNO-CCSD(T) based on geometries obtained with DFT. The values for each interaction for the respective motif are given, as well as the energy difference Δ between both motifs. All values are given in kJ/mol. Positive values refer to stabilization of the outside structure relative to the inside isomer. C stands for chromone (derivative), M for methanol. 83
- 4.13 Energy difference between inside and outside motif for multiple derivatives of chromone in the T₁ state calculated with different quantum chemical methods with a def2-TZVP basis set. The SAPT0 calculations are based on the final UDFT geometries. A positive ΔE indicates preference for the outside pocket and *vice versa*. All values in kJ/mol. 86
- 4.14 Relative electronic energies ΔE for different structures of 6-methylchromone-methanol. All values are given in kJ/mol. 90
- 4.15 OH stretching frequencies of the investigated chromone derivatives calculated with different methods. The values are given in the format X/Y, with X denoting the value for the inside motif and Y for the outside motif. All values are unscaled and are given in cm^{-1} . $\Delta(\text{method})$ describes the difference between the wavenumber of the OH stretching band for the inside and the outside motif. 94

- 4.16 Results of energy decomposition analysis by SAPT0/jun-cc-pVDZ based on geometries obtained with UDFT. The values for each interaction for the respective motif are given, as well as the energy difference Δ between both motifs. All values are given in kJ/mol. Positive values refer to stabilization of the outside structure relative to the inside isomer. 94
- 4.17 Results of energy decomposition analysis by SAPT0/jun-cc-pVDZ based on geometries obtained with UDFT. The values for each interaction for the respective motif are given, calculated as percentage of the S_0 value. A value close to 1 indicates that the interaction has the same strength in the T_1 state as in the electronic ground state. 96
- 4.18 Results of energy decomposition analysis by SAPT0/jun-cc-pVDZ based on geometries obtained with UDFT. The values for each interaction for the respective motif are given, as well as the energy difference Δ between both motifs. All values are given in kJ/mol. Positive values refer to stabilization of the outside structure relative to the inside isomer. 96
- C.1 Selected distances d for clusters of methanol and chromone derivatives calculated at CAM-B3LYP-D3(BJ)/def2-TZVP level. All distances are given in Å, ΔE is given in kJ/mol. 253
- C.2 Selected distances d and angles a for clusters of methanol and chromone derivatives calculated at CAM-B3LYP-D3(BJ)/def2-TZVP level. All distances are given in Å, ΔE is given in kJ/mol. 254

List of Abbreviations

ADC	Algebraic Diagrammatic Construction
BSSE	Basis Set Superposition Error
CI	Configuration Interaction
CIS	Configuration Interaction Singles
CC	Coupled Cluster
CREST	Conformer-Rotamer Ensemble Sampling Tool
DED	Dispersion Energy Donor
DFT	Density Functional Theory
DLPNO	Domain-based Local Pair Natural Orbital
EDA	Energy Decomposition Analysis
FWHM	Full Width at Half Maximum
HF	Hartree Fock
IR	Infrared
ISC	Intersystem Crossing
L(S)DA	Local (Spin) Density Approximation
LED	Local Energy Decomposition
MeOH	Methanol
MPn	Moller-Plesset Perturbation Theory of nth Order
NTO	Natural Transition Orbitals
PES	Potential Energy Surface
RI	Resolution of the Identity
RMSD	Root-mean-square deviation
R2PI	Resonant 2 Photon Ionization
SAPT	Symmetry-Adapted Perturbation Theory
SCF	Self Consistent Field
SCS	Spin Component Scaled
^tBuOH	<i>tert</i> -Butanol
TDA	Tamm-Dancoff Approximation
TD-DFT	Time-dependent Density Functional Theory
TPM	Triphenylmethane
ⁱPrTPM	<i>all-meta iso</i> -propyl Triphenylmethane
^tBuTPM	<i>all-meta tert</i> -butyl Triphenylmethane
UDFT	Unrestricted Density Functional Theory
UV	Ultraviolet
VCC	Vibrational Coupled-Cluster
VCI	Vibrational Configuration-Interaction
VSCF	Vibrational Self-consistent Field
Vis	Visible
XTB	Extended Tight Binding
ZPVE	Zero Point Vibrational Energy

Chapter 1

Introduction

Non-covalent interactions play a central role in science and are especially important in the context of chemistry, physics, biology and all disciplines in between. Although they are significantly weaker than the covalent bonds due to their r^{-6} -dependence, non-covalent interactions are of utmost importance. The binding energy of ≈ 5 kJ/mol in the argon dimer is certainly smaller than a C-H bond with ≈ 440 kJ/mol, but is central for this dimer, which would not exist without non-covalent interactions.^[1] The argon dimer would not be stable without non-covalent interactions. The name "van der Waals forces" is also used in literature dating back to the introduction of the van der Waals equation to account for the intermolecular interactions of real gases.^[2] They describe the interaction between atoms and molecules can be classified into multiple categories. The van der Waals forces typically include electrostatic interactions between permanent multipoles, also called Keesom forces and inductive interactions between permanent and induced multipoles, the Debye forces.^[3] A well-known example for electrostatic interactions is the ubiquitous H-bond. Furthermore, London dispersion between spontaneous and induced multipoles can occur. Additionally, charge-transfer, ionic and metallic interactions can also be considered part of the non-covalent interactions.^[4] The importance of these interactions can be seen especially in the existence of condensed matter, *e.g.*, resulting in the formation of liquid water from separate water molecules under suitable conditions. Nearly every chemical or biological process is governed by non-covalent interactions such as molecular recognition, solvation, catalysis and many more.^[5] In the vast field of non-covalent interaction, the focus in this work lies on London dispersion, which will be introduced in more detail in the following.

Although the importance of London dispersion was long underestimated after its description by Robert Eisenschitz and Fritz London in 1930,^[6,7] this has been changing slowly since the millennium with the inclusion of dispersion corrections to the nowadays routinely used density functional methods.^[8] In an unphysical but easy to understand picture, London dispersion can be understood as the attractive force between two atoms caused by spontaneous changes in the electron density of one atom. This leads to the formation of a spontaneous dipole in one atom and induces a dipole in the second atom resulting in an attraction of two nonpolar atoms. The London dispersion energy E_{disp}^{AB} between two atoms A and B can be expressed in dependence of their distance R , polarizabilities α_A and α_B and ionization energies I_A and I_B , as derived by Eisenschitz and London:^[7]

$$E_{disp}^{AB} \approx -\frac{3}{2} \frac{I_A I_B}{I_A + I_B} \alpha_A \alpha_B r^{-6} \quad (1.1)$$

Nevertheless, the correct description is a quantum mechanical one. Fluctuations in the electron density in one atom lead to correlated changes in the electron density in a second atom resulting in an attractive force between both atoms. London dispersion is always attractive and grows approximately with the number of pairwise interactions and can already be structure-defining for medium-sized molecules.^[8] Although it is not directional, it pushes molecular structures towards more compact, folded arrangements in order to increase the intramolecular interacting region. London dispersion plays a central role in the interaction of nonpolar molecular and, *e.g.*, enables the liquefaction of noble or homodiatomic gases. Other examples are the structure and physical properties (boiling point) of nonpolar alkanes influenced by the increasing dispersion attraction of the larger homologues.^[9] The gecko also showcases London dispersion in its ability to walk on vertical surfaces due to the strong interaction of millions of microscopic hairs (setae) on his feet with the wall,^[10-12] although the importance of dispersion is sometimes disputed.^[13,14] This thesis is embedded into the larger context of the priority program SPP 1807 ("Control of London Dispersion Interactions in Molecular Chemistry") by the DFG (German Research Foundation). The focus of the thesis lies in the subject of molecular dispersion interaction in different electronic states. Thus, the following presented research is for the most part

connected with this thesis as part of a cooperation or related/joint research inside the SPP.



FIGURE 1.1: Foot of a gecko.^[15]

As said, the influence of dispersion leads to more compact structures in order to maximize the interaction due to the r^{-6} dependence with respect to the interatomic distances.^[8] More folded structures exhibit a higher degree of Pauli repulsion (“steric effects”) acting against the dispersion effect. In the liquid phase, dispersion directly competes with solvation effects favoring an open structure which could compensate the dispersion effect. The group of Chen investigated the attenuation of London dispersion on multiple model systems including symmetric proton-bound dimers of organic mono-nitrogen bases.^[16–18] They concluded that although solvation compensates or cancels a significant amount of London dispersion in the liquid phase, the influence of dispersion on the molecular structure cannot be neglected and has to be taken into account. This is supported by work of the Ludwig group on ionic liquids whose viscosity represents a central parameter for the use in electrochemical applications.^[19–21] London dispersion can explain the different vaporization energies of protic and aprotic ionic liquids which are closely linked to viscosity by the theory of Eyring.^[22–24] The groups of Schreiner and Wegner studied molecular balances to probe and quantify the effects of dispersion in multiple solvents.^[25–29] Molecular balances are systems in which a molecule or molecular cluster is able to assume two or more isomeric structures which are close in energy exhibiting distinct stabilization by a non-covalent interaction.^[30,31] This can be realized in intramolecular fashion as, *e.g.*, in torsion balances^[32] and cyclooctatetraene (COT) balances.^[33,34] Another possibility

are intermolecular systems, *e.g.*, the aforementioned proton-bound nitrogen base dimers.^[17,35]

Furthermore, due to the strong connection between structure and reactivity, dispersion is important for catalytic reactions including transition metal catalysts and has led to a better understanding of the underlying mechanism (see refs. [36–44]). An accurate understanding of dispersion allows to describe catalytic cycles and identify the reaction-defining transition states. This enhances the chemist's ability to develop strategies and use London dispersion in a deliberate manner to tune molecular systems. Consequently, so-called dispersion energy donors (DEDs) were introduced to describe the stabilization of unusual geometries by London dispersion. The definition by Grimme states that "inherently unstable bonding situations might be stabilized thermodynamically by introducing spatially close-lying (densely packed) substituents (bulky groups)."^[45]

In order to study London dispersion, gas phase spectroscopy is an ideal tool enabling the probing of isolated molecules and molecular clusters, *i.e.*, the study of intermolecular interactions under restricted conditions (no solvent, small number of interaction partners etc.) in particular for benchmarking theoretical methods. Application of the molecular beam technique enables to probe single molecules or molecular clusters at very low temperatures reducing the chemical space. Consequently, meaningful spectra can be obtained which allow to determine the structure of the system. In a bottom-up approach, the knowledge gained from well-controlled model systems can be transferred and applied to larger, more complicated problems. In the context of this work, the model system represents a molecular balance allowing systematic investigation of weak interactions like London dispersion isolating its effect among the other inter- and intramolecular interactions. Intermolecular interactions are generally absent due to solvent-free environment in the gas phase but can be re-introduced by deliberate clustering. Intramolecular interactions can certainly not be excluded but the importance of certain interactions can be tuned by an appropriate choice of system, *e.g.*, a nonpolar dimer to obtain a mostly dispersion-bound system. Consequently, the strength of London dispersion can be studied in a controlled and isolated manner. In the Gerhards group, this approach was used to study ether-solvent complexes in a collaborative effort. Multiple systems including diphenyl

ether and dibenzofuran,^[46-51] phenyl vinyl ether,^[52] anisole^[53] and furan^[54,55] were characterized. As laid out in a comprehensive review,^[56] these balances can be studied by a multitude of spectroscopic methods including microwave, FT-IR, Raman and combined IR/UV methods. Recently, combined stimulated Raman/UV were introduced to compliment the routinely used IR/UV methods to investigate nonpolar dimers which are relevant for this work.^[57] Probing the delicate balance between multiple motifs with a small energetic difference between them allows to benchmark the used quantum chemical methods. Especially the application of energy decomposition methods as symmetry-adapted perturbation theory (SAPT) developed by the Sherill group and the local energy decomposition (LED) of the DLPNO-CCSD(T) method by the Neese group provide critical insight into the deciding factors. The DLPNO method is also connected to Kaiserslautern with the pioneering work of Wilfried Meyer.^[58,59] These methods were, *e.g.*, applied to the C₆₀ dimer^[60] and the activation of alkanes in transition metal complexes.^[61] Benchmarking with experimental results was carried out for dissociation energies of aromatic molecular complexes^[62] and hydrogen-bonded dimers (water and HF)^[63] showing favorable performance. A quantitative study on a realistic DNA model shows that the specific base pairing *by* hydrogen bonds accounts for most of its binding energy, but London dispersion provides a fundamental contribution.

The vast amount of work discussed and cited prior concentrates on London dispersion in the electronic ground state. The few studies of dispersion in the excited states are focused on the application of SAPT^[64-66] and LED^[67] for small open-shell model systems. Other theoretical work was carried out on clusters of anisole-water^[68] and formaldehyde-methane,^[69] stilbene,^[70] general photophysics^[71] and aromatic excimers.^[72] This motivated the investigation of chromone-solvent clusters as an extension of the previously described ether-alcohol complexes. The chromone molecule undergoes, similar to related xanthone, an intersystem crossing into the triplet manifold upon electronic excitation.^[73,74] This molecule serves as an ideal molecular balance with the two free electron pairs of the carbonyl oxygen offering two binding sites with the same binding motif. This enables an efficient error compensation and could reduce the error of quantum chemical predictions significantly.^[56]

An improved description of London dispersion in the excited state is certainly

a desirable goal due to the increased polarizability of electronically excited states increasing the influence of London dispersion. The development of robust dispersion-corrected TD-DFT methods^[75] would improve the current ground-state based dispersion corrections. A deeper understanding of dispersion leading to an improved quantum chemical description allows better cooperation between the experiment and theory and allows mutual improvement of both. Powerful theoretical methods not only benefit from spectroscopic work as applied in this thesis but also extend to other applications. Especially with regards to catalysis and material science, an improved model enables a powerful pre-screening of candidates *in silico*, which is paramount for successful and sustainable research. Instead of tedious and often wasteful optimization of a chemical reaction in the lab, quantum chemical methods can often predict how a chemical challenge can be overcome. As shown above, the elucidation of dispersion is still an ongoing task of high relevance to physical chemistry but also to other chemical fields and sciences. In this work, the effect of dispersion is studied in the electronic ground state on nearly completely dispersion-bound system in the form of dimers of triphenylmethane dimers. The strength of dispersion is controlled by introduction of different dispersion energy donors (H, *iso*-propyl, *tert*-butyl). Furthermore, aromatic ketone-solvent clusters acting as molecular balances are investigated both in the electronic ground and excited state. For the first time, a neutral, non-covalently bound molecular cluster is investigated in the triplet state by gas phase spectroscopy and analyzed by several quantum-chemical methods. Additionally, the binding energy of a molecular balance is analyzed by energy decomposition analysis in multiple electronic states. Lastly, chromone derivatives are scrutinized and studied by quantum chemical calculations and energy decomposition methods in order to identify suitable candidate molecules for further experiments are identified.

Chapter 2

Experimental setup and methods

2.1 Spectroscopic techniques

All used spectroscopic methods are based on the TOF (time-of-flight) mass spectrometric detection of molecular ions produced by resonant (multiphoton) laser ionization. Thus, the used methods can be characterized as action or consequence spectroscopy in contrast to the linear absorption technique used in FT-IR or condensed phase UV and IR spectroscopy. The difference between both types is that the latter is performed by direct measurement of the light intensity while action spectroscopy considers the consequences of light absorption. In this case, changes of the ion signal are monitored in dependence of the incident laser beam. Further references concerning this topic can be found in a recent review article^[76] and references therein.^[77–80]

2.1.1 R2PI spectroscopy

Resonant two-photon ionization (R2PI) is the basis for all other combined IR/UV and stimulated Raman/UV techniques applied for the conducted experiments and is based on the general resonance-enhanced multiphoton ionization (REMPI) using tunable laser radiation.^[81–84] The ionization typically occurs by successive absorption of two photons, with the first photon facilitating the resonant transition to an electronically excited state and subsequent ionization by absorption of the second photon. The resonant character of this process enhances the ion signal significantly with respect to the non-resonant case and allows to determine vertical excitation energies. These transitions and especially their intensities can be described using the Franck-Condon principle.^[85–87] Combining the R2PI technique with a time-of-flight

(TOF) mass spectrometer allows mass-selective measurements, making simultaneous measurements of multiple mass traces possible. Isomers of a molecule or molecular cluster usually differ in their respective vertical excitation energy which can enable an isomer-selective measurement and in combination with the aforementioned TOF-MS resulting in mass- and isomer-selective experiments.

The R2PI process can be facilitated in a one- or two-color way differing in the number of employed laser pulses and accordingly absorbed UV photons. In the most simple one-color case, a (1+1) process is used with two UV photons of equal energy for excitation and subsequent ionization (see fig. 2.1). Although this approach is not always feasible since it depends on a favorable energy difference between the electronically excited state (often S_N) and the electronic ground state (S_0) and ionic ground state (D_0) respectively. If the energy difference between the S_N state and the D_0 state is larger than the energy difference between the S_0 state and the S_N state, a one-color (1+1) process is not possible because the ionization potential cannot be reached with two photons. In these cases two-color R2PI is required, utilizing two UV photons of different energy in a (1+1') process. This method provides multiple advantages: It is possible to minimize the excess energy in the ion to prevent fragmentation by tuning the energy of the excitation photon. Additionally, the temporal delay between both photons can be varied, which is critical for spectroscopic investigations in the excited state, *e.g.*, as applied in the UV/IR/UV technique (see in the following).

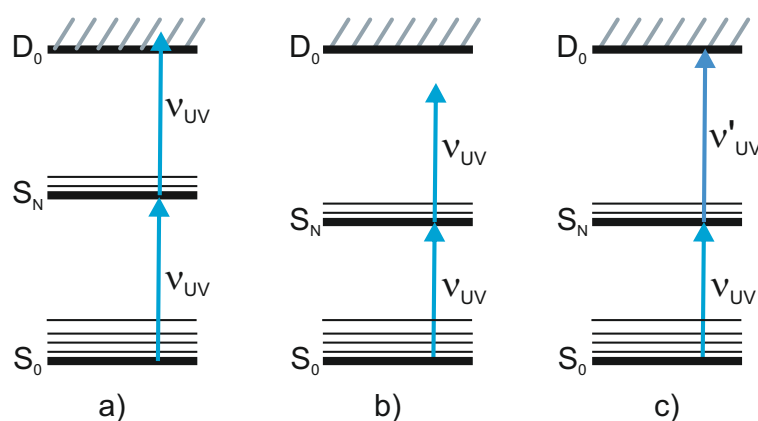


FIGURE 2.1: Scheme for R2PI methods including a) one-color R2PI b) one-color R2PI, when $\Delta E(S_N, D_0)$ is larger than $\Delta E(S_0, S_N)$ c) two-color R2PI. Two-color R2PI is required for successful ionization when the S_N state is too low in energy.

2.1.2 IR/R2PI spectroscopy

IR/R2PI spectroscopy represents a combination of R2PI spectroscopy with IR spectroscopy and provides a powerful tool for measuring vibrational spectra of neutral molecules or molecular clusters in the electronic ground state (S_0) (see refs. [88–94]). To achieve this, a tunable IR laser is fired prior (usually ≈ 40 ns) to an UV laser induced R2PI process, which generates a constant ion signal with one (1+1) or two (1+1') frequency-fixed UV lasers (see fig. 2.2). If the energy of the IR laser is in resonance with a vibrational transition of the molecule, the vibrational ground state (S_0) is depopulated, while the corresponding vibrational excited state is populated. Due to the resulting decrease of the ground state population, the R2PI signal is depleted because a smaller number of molecules is available for resonant electronic excitation and subsequent ionization. The IR/R2PI method is mass-selective and can also be isomer-selective if the underlying R2PI process is likewise.

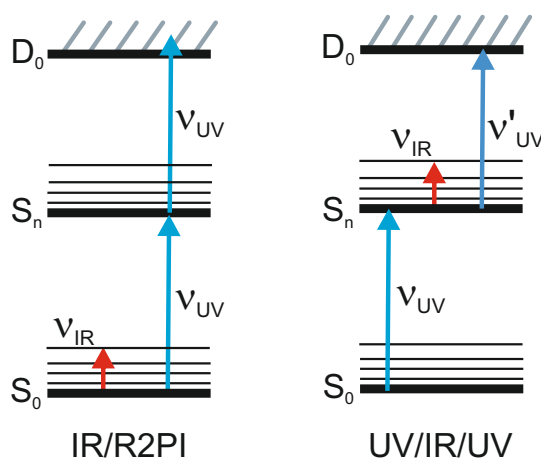


FIGURE 2.2: Scheme for the IR/R2PI and UV/IR/UV method, illustrating the depopulation of the electronic ground state and excited state, respectively.

2.1.3 UV/IR/UV spectroscopy

As mentioned before, R2PI spectroscopy can be used to elucidate low-frequency vibrations in the electronically excited state. For analysis of higher-frequency vibrations, *e.g.*, CH, NH and OH stretching modes, the UV/IR/UV technique can be applied (see refs. [89, 95–98]). Analogous to the IR/R2PI method, a constant ion signal produced by R2PI is required. Similarly, depletion of the ion signal occurs when the IR laser is in

resonance with an excited state vibrational mode (see fig. 2.2). The use of a two-color R2PI process is mandatory since the IR photon needs to be positioned in time between the excitation and ionization laser pulses in order to probe the excited state structure. Thus, the excited state lifetime is a central parameter for this method. If the lifetime of the excited state is very short, the three laser pulses (typical pulse width ≈ 5 ns) exhibit significant temporal overlap. Consequently, vibrational transitions from the S_0 and D_0 state as well the excited state are observed. Nevertheless, comparison of the UV/IR/UV spectrum with the respective spectra of the S_0 and D_0 state can still allow the identification and interpretation of the excited state vibrational signature.

2.1.4 Stimulated Raman spectroscopy

Based on the IR/R2PI method, a related method named Ionization Loss Stimulated Raman Spectroscopy (ILSRS) is used to measure Raman-active instead of IR-active vibrational modes (see refs. [99–107]). Again, a constant ion signal is produced by an R2PI process. In contrast to the IR/R2PI method, two laser beams are required for the depopulation process by Stimulated Raman Scattering (SRS).^[108] A frequency-fixed pump laser pulse (532 nm) is followed by a red-shifted, tunable Stokes laser pulse, which are spatially overlapped on the molecular beam. If the energy difference between the pump laser and the Stokes laser corresponds to a Raman-active vibrational mode, the Stokes laser leads to a stimulated scattering process, populating the corresponding vibrationally excited state (see fig. 2.3). Thus, temporal and spatial overlap of the pump and Stokes laser require cautious and thorough adjustment to observe the weak stimulated Raman effect and the resulting depletion of the ion signal. ILSRS in comparison to IR/R2PI provides a complementary approach to probe the vibrational signature of a system.

Similarly, Ionization Gain Stimulated Raman Spectroscopy^[101,102,107] can be understood as the Stimulated Raman equivalent to the IR+UV technique described in refs. [109–112]. The UV laser wavelength is set so that absorption of two photons does not exceed the ionization potential and no ion signal is observed. If the energy difference of the Stokes and pump photon matches a Raman-active transition, the vibrationally excited state is populated by the stimulated Raman process. By choosing an appropriate UV wavelength, the energy sum of vibrational excitation and

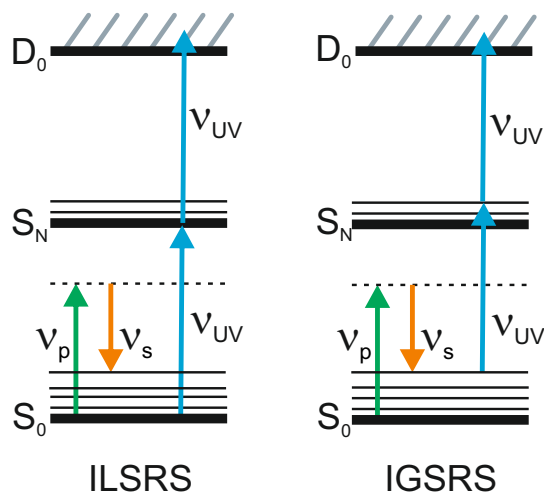


FIGURE 2.3: Scheme for the stimulated Raman methods IGSRs and ILSRS, illustrating the depopulation of the electronic ground state by stimulated Raman emission respectively.

UV excitation can overcome the ionization energy resulting in detection of an ion signal. The advantage of IGSRs is the measurement against a zero background which enhances the signal-to-noise ratio significantly. On the other hand, IGSRs loses the isomer-specificity since the UV excitation occurs from a vibrationally excited state. Additionally, the lifetime of the vibrationally excited state is a critical parameter for the IGSRs method in comparison to the ILSRS method, so that fast IVR processes can be problematic for observing the gain effect. Nevertheless, stimulated Raman spectroscopy provides an additional tool for structural analysis of molecules and molecular clusters. This is especially true for systems with an inversion center since then the rule of mutual exclusion applies stating that a vibrational transition cannot be IR- and Raman-active at the same time resulting in “orthogonal” spectra. Furthermore, for large unpolar systems without strong NH or OH oscillators, the IR spectrum can be difficult to interpret because the change in dipole moment can be too small to observe significant IR bands. Here, the stimulated Raman Spectroscopy provides a powerful alternative to characterize these systems with vibrations of high symmetry, low change in dipole moment, but high polarizability.

2.2 Laser systems

All described experiments were carried out using pulsed nanosecond laser systems with a repetition rate of 10 Hz. The three UV and two IR laser systems used are described in the following.

2.2.1 UV laser system

All three UV laser systems operate on the same optical layout with variations in the model of the pump or dye laser. Every system consists of a Nd:YAG laser pumping a dye laser (A: Spitlight 600, CobraStretch, B: Spitlight 1000, PrecisionScan, C: Spitlight 1000.2, PrecisionScan). The Nd:YAG lasers (Innolas) exhibit a pulse width of 7 ns and can be operated at 532 nm (all lasers) and 355 nm (A and C). The dye laser system (Sirah) is depicted in figure 2.4.

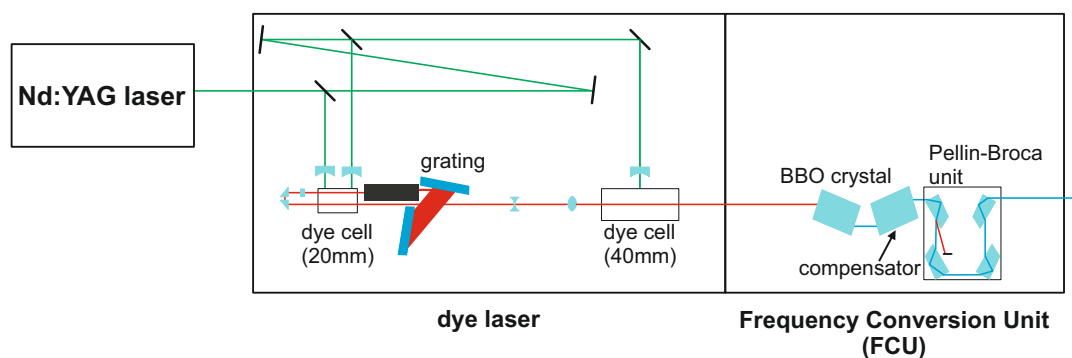


FIGURE 2.4: Scheme of the UV laser system, for a pump laser wavelength of 532 nm.

The Nd:YAG laser operates on a fundamental wavelength of 1064 nm, which is converted to 532 nm or 355 nm by second harmonic (SHG) or third harmonic generation (THG) depending on the used laser dye. The pump laser radiation is then transferred into the dye laser, generating tunable dye laser radiation in the range of 360 nm to 880 nm.

The generated dye radiation in the Vis/NIR regime can be used as such, but typically enters the attached frequency conversion unit (FCU). Inside the FCU, the dye radiation is frequency-doubled using a nonlinear optical process in a BBO (β -BaB₂O₄) crystal, resulting in UV laser radiation in the region of 205-450 nm, depending on the type of laser dye. Furthermore, a compensator crystal is used to correct the geometric

shift of the beam path by the first crystal. Finally, the generated UV radiation is separated from the remaining fundamental dye radiation by Pellin-Broca prisms.

2.2.2 IR laser system

The IR radiation required for the aforementioned IR-spectroscopic techniques is generated by two independent IR laser systems which are closely related in their technical layout. Both systems use a Nd:YAG laser (Quanta-Ray Pro-230, Newport-Spectra Physics) pumping a dye laser (PrecisionScan, Sirah). In contrast to the UV laser system, not only the second harmonic (532 nm) but also the residual fundamental (1064 nm) is used to generate the IR radiation. The Vis radiation is generated in a similar manner to the UV laser system with an oscillator/amplifier system and is introduced into the FCU. In a first step, the dye radiation is mixed with 30% of the fundamental Nd:YAG radiation to generate IR radiation in a nonlinear optical process called difference frequency mixing (DFM). The remaining dye and fundamental radiation are separated from the IR beam, which is mixed with the remaining 70% of the 1064 nm beam in a second non-linear optical process, optical parametric amplification (OPA). This process generates an “idler” and “signal” beam, the latter is split off as well as the remaining fundamental, so that only the “idler” radiation, the amplified IR radiation, remains. This “idler” radiation can be tuned in a range from 2200 cm^{-1} to 4700 cm^{-1} .

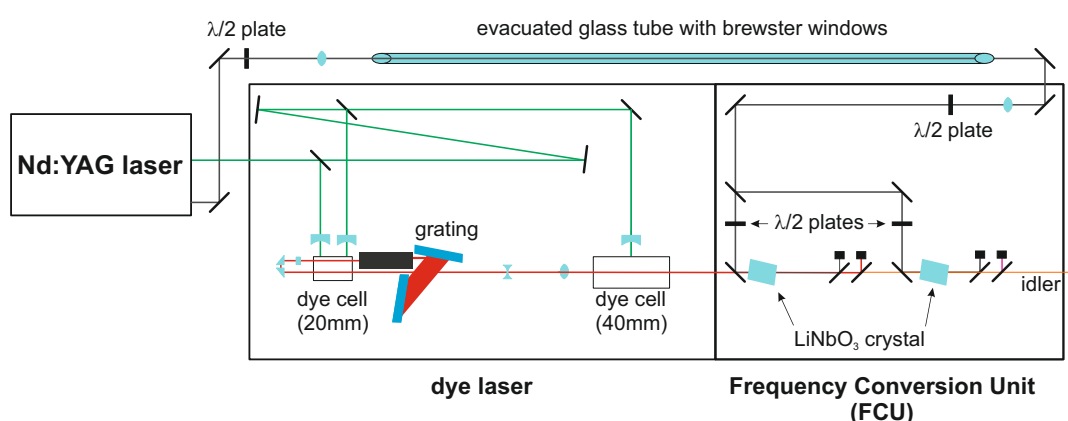


FIGURE 2.5: Scheme of the IR laser system, using both 532 nm (green) and 1064 nm (grey) of the pump laser.

To improve the beam profile quality for the DFM and OPA process, the “relay

imaging” technique is used to project the near-field beam profile over multiple meters. This is realized by a focusing telescope with two convex lenses ($f=1000$ mm). The resulting focus of the high-power beam requires the use of an evacuated glass tube with windows oriented in the Brewster angle. This ensures a high beam quality for the nonlinear optical processes, prevents damage to the used crystals leading to stable operation of the IR laser system.

The used LiNbO_3 crystals exhibit a gap between 3460 cm^{-1} and 3520 cm^{-1} where self-absorption occurs resulting in an incomplete spectrum. To circumvent this problem, a special LiNbO_3 crystal is used which is doped with MgO , shifting the spectral gap to the range between 3520 cm^{-1} and 3580 cm^{-1} . Since only a DFM crystal and no corresponding OPA crystal is available, the resulting pulse energy in this range is restricted to 3.5 mJ compared to up to 20 mJ outside the gap.

2.2.3 Raman laser system

The pump and Stokes beam required for the Stimulated Raman Spectroscopy are generated by a combination of a Nd:YAG laser (Spitlight 1000, Innolas) and a dye laser (Precision Scan, Sirah). The fundamental of the Nd:YAG laser is frequency-doubled, and the resulting radiation with a wavelength of 532 nm is split in a ratio of 4:1. The larger portion of the beam is used as pump radiation for the dye laser, generating the Stokes beam. The remaining 20 % which are used as pump beam, pass through a delay line compensating for the different optical path lengths to ensure temporal overlap. Finally, the spatial overlap is ensured by a dichroic mirror (LPD02-532RU-25, Semrock), which reflects the Pump beam and is transparent for the Stokes beam in a range of 539 nm to 824 nm. Both beams are then focused onto the molecular beam with a focal lens ($f=30$ cm) to maximize the Stimulated Raman Effect (see fig. 2.6). The dichroic mirror limits the measuring range of Raman vibrations to 244 cm^{-1} - 6661 cm^{-1} . Measurements down to 90 cm^{-1} could be possible, if the remaining transmission of 50 % is considered acceptable. A detailed description and explanation of the Raman laser system can be found in the PhD thesis of D. Maué.^[57]

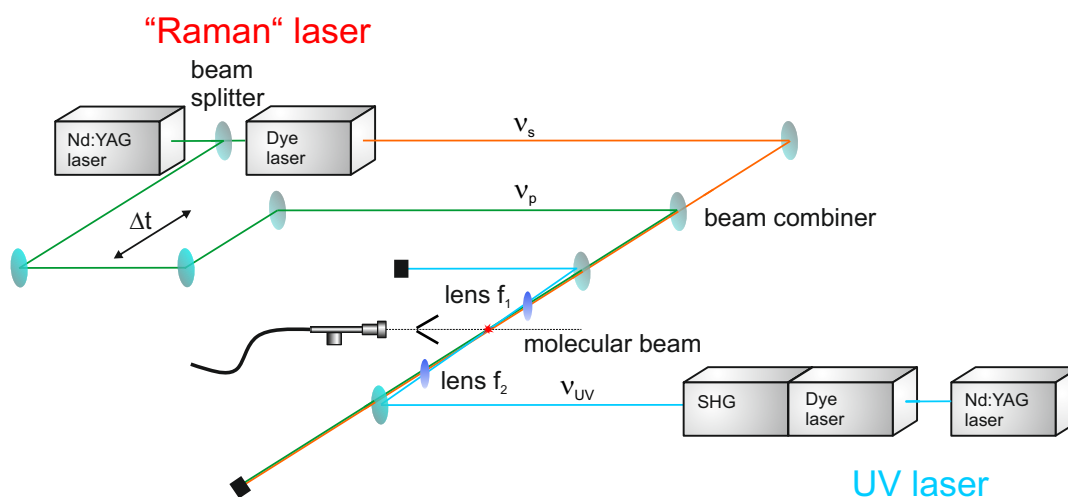


FIGURE 2.6: Scheme of the Raman laser, including the optical pathway with the delay line. The dichroic mirror is essential to ensure good overlap between Stokes and Pump beam.

2.3 Molecular beam technique

All aforementioned spectroscopic methods were employed in experiments utilizing a molecular beam apparatus which was built in the Gerhards group.^[113] In the following, the molecular beam technique itself as well as the experimental setup is presented.

2.3.1 Theoretical background

The molecular beam technique^[114–116] was developed in the early 20th century by Louis Dunoyer de Segonzac and Otto Stern, with Stern receiving the noble prize partly for the development of this technique. A molecular beam can be formed by expansion of a gas or gas mixture into the vacuum through a pin hole. To obtain the desired jet-beam, the backing pressure must be high (multiple atmospheres) and the hole diameter small, so that the mean free path is much smaller than the hole diameter. If this is not the case, an effusive beam is generated, characterized by the lack of collisions during the expansion. These collisions, which occur in the used jet-beam, lead to conversion of internal energy U into kinetic energy. Since this process occurs on a short time scale, this energy transfer is adiabatic preventing heat exchange with the environment. This results in a supersonic beam with a low relative velocities between the atoms or molecules, as depicted in figure 2.7. The

translational temperature T_{trans} is effectively reduced and may approach 0 K, while the rotational and vibrational energies are still significantly reduced, a major advantage of this technique for spectroscopic applications.^[117–119] Low temperatures for T_{rot} and T_{vib} lead to an increased population of the lowest rotational and vibrational levels, reducing the effect of hot bands.

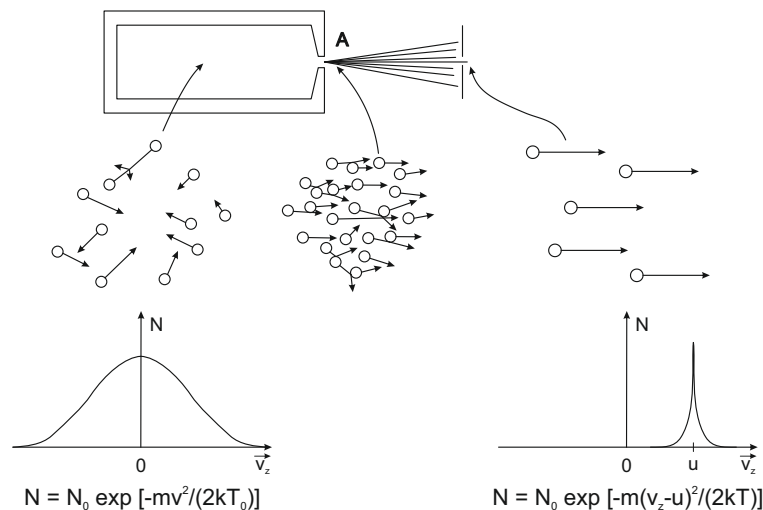


FIGURE 2.7: Model of adiabatic cooling during the supersonic expansion with sketches of the velocity distribution. Adapted by permission from Springer Nature Customer Service Centre GmbH: Springer Laser-spektroskopie 2 by Wolfgang Demtröder, 2013.^[120]

The significant cooling by the supersonic expansion also facilitates condensation processes of multiple atoms or molecules, resulting in the formation of clusters. The condensation occurs in the first section of the supersonic expansion, where the collision rate is high. The condensation can be modulated by a “seeded beam” using noble gases as a carrier gas and seeding the molecules of interest into the resulting gas mixture. This leads to more efficient cooling, since the collisional energy transfer is more efficient, especially for the larger noble gases. The “seeded beam” cooling technique was employed for all experimental work presented and can be achieved in multiple ways, *e.g.*, the used thermal sublimation as well as other experimental implementations like laser desorption, laser ablation *etc.*

2.3.2 Molecular beam apparatus

The aforementioned molecular beam apparatus is depicted in fig. 2.8 and consists of three differentially pumped chambers: the source chamber (I) with the thermal source

(see below), the ionization chamber (II), where the lasers intersect the molecular beam and the flight tube (length: 800 mm), serving as time-of-flight mass spectrometer.

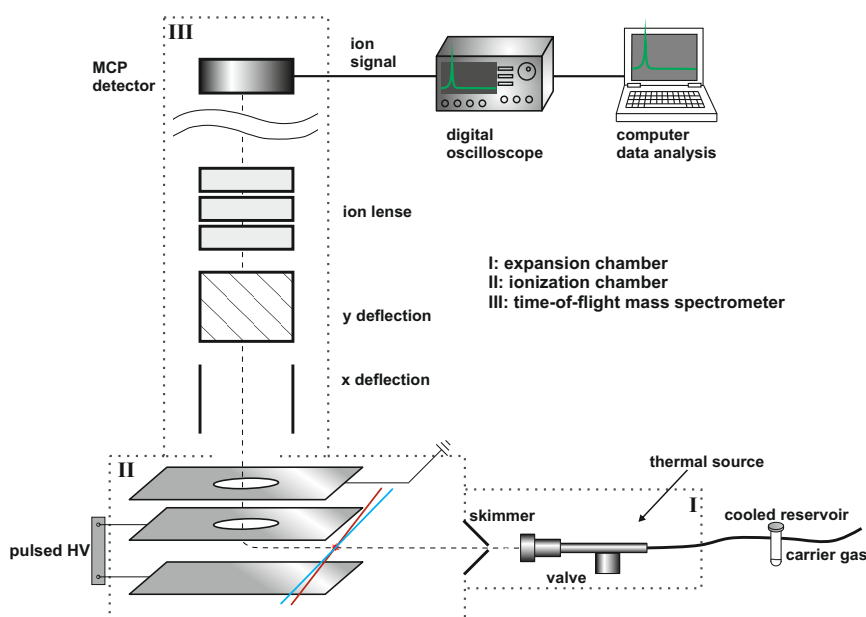


FIGURE 2.8: Schematic depiction of the molecular beam apparatus, with dotted lines indicating the three vacuum chambers. Laser beam paths are indicated in blue (UV) and red (IR), the vacuum pumps are omitted for clarity.

The first chamber is evacuated by an oil diffusion pump (DI 3000, Leybold, pumping speed: $3 \text{ m}^3/\text{s}$), with a roots pump (Alcatel, $250 \text{ m}^3/\text{h}$) and a rotary vane pump (Trivac D65B, Leybold, $65 \text{ m}^3/\text{h}$) providing the necessary fore vacuum. The pressure in the source chamber is typically around 10^{-6} mbar with the thermal source not operating and increases to about 5×10^{-5} to 2×10^{-4} mbar during operation. The second chamber, the ionization chamber, is connected to the source chamber by a skimmer (orifice diameter: 1 mm). The chamber is equipped with windows for the laser beams and contains the high-voltage plates accelerating the formed ions. A turbomolecular pump (Turbovac 1000, Leybold, $4140 \text{ m}^3/\text{h}$) is evacuating this chamber, with the previously mentioned roots and rotary vane pump serving as fore vacuum pumps, resulting in a pressure of around 10^{-7} mbar. The third chamber, the flight tube, is attached perpendicular to the second chamber and is used as time-of-flight mass spectrometer (TOFMS). A second turbomolecular pump (Turbovac 361, Leybold, $1242 \text{ m}^3/\text{h}$) in combination with a rotary vane pump (D8B, Leybold, $8 \text{ m}^3/\text{h}$) provides the necessary high vacuum in the range of 10^{-8} mbar.

After this general introduction, the thermal source is described in the following (see fig. 2.9). The thermal source mainly consists of two sample holders in which glass pots with solid samples can be introduced. The sample storage is on one side connected to the pulsed valve, on the other side with the carrier gas supply. Substances with an insufficient vapor pressure at room temperature can be thermalized by the heating resistors and the THERMOCOAX cable wrapped around the sample storage. Thermocouples at the sample storage and pulse valve are used to monitor the temperature and prevent resublimation inside the thermal source. In the context of this work, only the left chamber was used, since mainly solvent aggregates were studied, which are introduced by a cooled reservoir. The carrier gas passes through a glass reservoir, which is cooled by a surrounding liquid (ethylene glycol) in a brass pot. A thermoelectrical cooling plate (UEPT-240-185-065C200, uwe electronic) allows to cool the sample down to -20°C . The amount of the volatile compound introduced into the gas mixture can be regulated by needle valves to change the ratio of gas flow through the reservoir respective to the bypass line and the temperature of the reservoir itself.

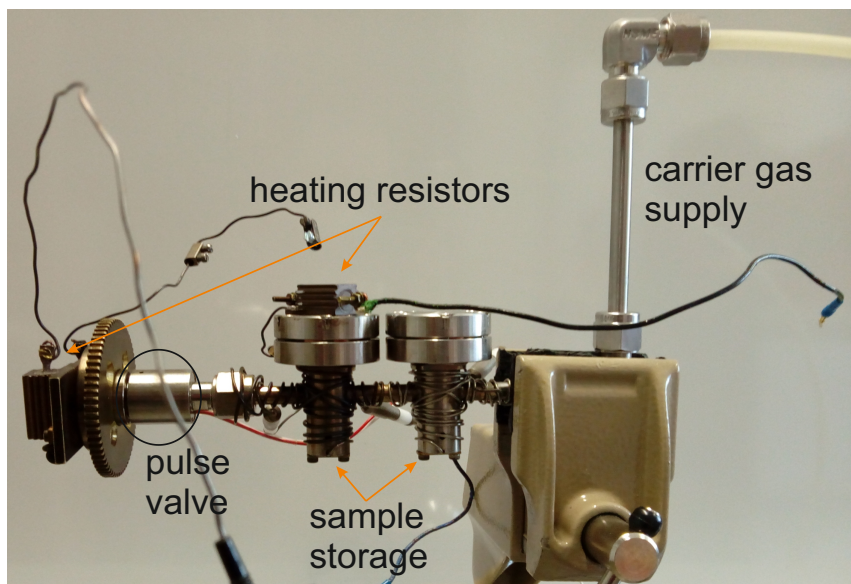


FIGURE 2.9: Photo of the thermal source showing the sample storage wrapped in THERMOCOAX heating elements. The sample storage is connected to the carrier gas supply and the pulse valve. Additional heating resistors are mounted to the valve head and the sample storage.

After describing the molecular beam apparatus and thermal source, the experimental procedure including the ion generation is described in the following. The pulse valve (IotaOne, General Valve, orifice diameter: 500 μm) is opened for a short time (typically 220 to 290 μs), with the gas mixture expanding into the vacuum generating the described supersonic beam. The inner laminar part of the supersonic beam passes through the skimmer into the ionization chamber, while the outer turbulent part is skimmed off. In the ionization chamber the molecular beam can interact with multiple laser beams, which enter perpendicularly through CaF_2 or quartz windows, depending on the used wavelength. To achieve optimal overlap, all laser beams have to be aligned close to collinear and intersect the molecular beam at a point of high molecular density, so that electronic excitation and ionization with the R2PI process can occur in a satisfying manner. After a field-free drift region of around 30 mm, the formed cations enter the ion acceleration stage, three acceleration plates in a Wiley-McLaren arrangement.^[121] The two lowest plates are connected to a high voltage switch (HTS 50, Behlke), while the third plate is grounded, with a voltage of +4130 V being applied to first plate, +3520 V to the second plate. The high voltage is provided by a separate power supply (D-603 TOF power supply, Jordan). The cations are consequently accelerated perpendicularly to their previous flight path into the flight tube of the time-of-flight mass spectrometer, reducing the background signal. The remaining velocity vector along the initial drift axis is compensated by a deflection plate to which a voltage of +230 V is applied. This, together with the acceleration plates in a Wiley-McLaren arrangement, focuses ions of equal mass but different spatial origin, leading to a mass resolution $\frac{m}{\Delta m}$ of around 1800 for a mass of 110 a.u. A second deflection plate combined with a high voltage push-pull switch (HTS 31-03 GSM, Behlke) can be used as a mass gate to deflect ions in a certain mass range reducing the observed ion signal thus preventing damage to the micro channel plate (MCP) detector. The ion signal detected by the MCP detector is intensified by a broadband voltage amplifier (HVA-200M-40B, 40dB, Femto) before being displayed on a digital oscilloscope (TDS 520A, Tektronix). The oscilloscope stores and averages the data, which can be analyzed by a computer using a GPIB interface.

The experiment is conducted in a pulsed manner with a repetition rate of 10 Hz. The exact timing of all involved components including the flash lamps and Pockels

cells of the Nd:YAG lasers, the pulse valve, the high-voltage switches and the oscilloscope is of key importance. The control unit for the pulse valve acts as the main trigger for three digital delay generators (DG535, Stanford Research Systems), which are responsible for triggering the aforementioned components.

Chapter 3

Quantum chemical methods

Quantum chemical calculations are of high importance to aid the interpretation of experimental results gained by the conducted experiments. The calculations provide minimum energy geometries of molecules and clusters, their relative energies, vibrational frequencies and intensities and many other properties. Comparison of theory and experimental data can not only support interpretation but also serve as benchmark studies improving the theoretical approaches.^[54,122–126] In the context of this work, a variety of methods is used including dispersion-corrected density functional theory (DFT), time-dependent DFT (TD-DFT) and wavefunction methods like coupled-cluster (CC2). Furthermore, energy decomposition analysis is performed utilizing symmetry-adapted perturbation theory (SAPT) and the local energy decomposition (LED) of the domain-based local pair orbital coupled-cluster framework [DLPNO-CCSD(T)]. Additionally, one-dimensional anharmonic calculations of vibrational frequencies were carried out. In order to not exceed the scope of this thesis, most of the methods are introduced in a brief manner, a more detailed description and derivation can be found in typical quantum chemistry textbooks^[127–129] and the respective references cited in this chapter.

3.1 Density functional theory

The Schrödinger equation is the central equation of quantum mechanics and describes a system by its wavefunction Ψ . The stationary or time-independent form of the Schrödinger equation is as follows, with the Hamiltonian \hat{H} acting as an operator describing the total energy of the system:

$$\hat{H}|\Psi\rangle = E|\Psi\rangle \quad (3.1)$$

The wavefunction itself contains all information of the system. Solving the Schrödinger equation in an exact manner gives the exact solution for the wavefunction for a non-relativistic system. An exact solution of the Schrödinger equation is only possible for small model systems (particle in a box, hydrogen atom). More complicated systems can typically not be solved analytically and thus only approximated solutions can be obtained. This can be done by, *e.g.*, density functional theory or coupled-cluster methods (see section 3.3). Density functional theory is based on the Hohenberg-Kohn-Theorem which states that the ground state of an electronic system is fully described by its electronic density $\rho(\vec{r})$.^[130] Furthermore, there must exist a functional $E[\rho(\vec{r})]$ which evaluates the corresponding electronic energy. Kohn and Sham derived the following approach for this functional:^[131]

$$E[\rho] = T_S[\rho] + V_{e-e} + V_{Ne} + E_{XC}[\rho] + V_{NN} \quad (3.2)$$

$$E[\rho] = T_S[\rho] + \frac{1}{2} \iint \frac{\rho(\vec{r}_1)\rho(\vec{r}_2)}{r_{12}} d\vec{r}_1 d\vec{r}_2 + \int v_{ext}\rho(\vec{r})d\vec{r} + E_{XC}[\rho] + V_{NN} \quad (3.3)$$

In contrast to Hartree-Fock (HF) theory, where solutions to the exact system are approximated, a contrary approach is followed in Kohn-Sham DFT, where exact solutions to an approximated system are determined. A detailed description of the Hartree-Fock method can be found in literature.^[127-129] $T_S[\rho]$ is the Kohn-Sham kinetic energy for the system with the electron density ρ which depends on the three spatial coordinates \vec{r} . V_{e-e} represents the coulomb repulsion of the electron density. V_{Ne} describes the interaction between the nuclei and electrons facilitated by the external potential $v_{ext}(\vec{r})$. E_{XC} is the exchange-correlation functional also containing the correction of T_S to the true kinetic energy T . V_{NN} contains the nuclei-nuclei interaction which does not depend on the electronic structure. The wavefunction Ψ of N electrons can be expressed as a Slater determinant of molecular orbitals ϕ_i . The electron density ρ can then be expressed as the square value of the molecular orbitals.

$$\Psi(\vec{r}_1, \vec{r}_2, \dots, \vec{r}_N) = \frac{1}{\sqrt{N!}} \begin{vmatrix} \phi_1(\vec{r}_1) & \phi_2(\vec{r}_1) & \dots & \phi_N(\vec{r}_1) \\ \phi_1(\vec{r}_2) & \phi_2(\vec{r}_2) & \dots & \phi_N(\vec{r}_2) \\ \vdots & \vdots & \ddots & \vdots \\ \phi_1(\vec{r}_N) & \phi_2(\vec{r}_N) & \dots & \phi_N(\vec{r}_N) \end{vmatrix} \quad (3.4)$$

$$\rho(\vec{r}) = \sum_i^N |\phi_i(\vec{r})|^2 \quad (3.5)$$

The functional can also be written as a function of the molecular orbitals ϕ_i , resulting in:

$$E[\rho] = -\frac{1}{2} \sum_i^N \langle \phi_i | \nabla^2 | \phi_i \rangle + \sum_{i,j}^{N,N} \iint \frac{|\phi_i(\vec{r}_1)|^2 |\phi_j(\vec{r}_2)|^2}{r_{12}} d\vec{r}_1 d\vec{r}_2 + E_{XC}[\rho(\vec{r})] + \int v_{\text{ext}} \rho(\vec{r}) d\vec{r} + V_{NN} \quad (3.6)$$

Most of the terms in the equation above are known except for the exchange-correlation functional E_{XC} . The challenge of DFT is to describe this exchange-correlation functional in a satisfactory manner using sensible approximations. One approach is local spin density approximation (LSDA), with exchange and correlation energy derived from the free electron gas, only depending on the local density. This was extended by including the gradient of the electron density resulting in the generalized gradient approximation (GGA).^[132] B3LYP (Becke, 3-parameter, Lee-Yang-Parr), one of the most popular functionals uses a hybrid of multiple functionals to describe the exchange and correlation contribution. LSDA, the GGA functional B88^[133] and exact HF exchange are used to describe the exchange contribution, while LSDA and the GGA functional LYP^[134] describe the correlation,^[135,136] weighted by three empirical parameters $a = 0.2$, $b = 0.72$ and $c = 0.81$.

$$E_{XC}(\text{B3LYP}) = (1 - a)E_X^{\text{LSDA}} + aE_X^{\text{HF}} + b\Delta E_X^{\text{B88}} + cE_C^{\text{LYP}} + (1 - c)E_C^{\text{LSDA}} \quad (3.7)$$

3.1.1 Range-separated functionals

The hybrid approach of B3LYP makes it a versatile tool to obtain meaningful molecular geometries, vibrational frequencies and other properties for a variety of molecular systems and is one of the most popular density functionals used today. Good error compensation plays an important role for its success but B3LYP is not able to describe every system in a satisfactory manner. In the context of this work, especially the description of charge-transfer excitations and dispersion interactions must be corrected. The charge-transfer excitations are faulty due to the wrong long-range behavior of the exchange potential caused by the DFT exchange functionals.^[137–139] This can be improved by introducing a range dependence to the description of the exchange.^[140] In the case of CAM-B3LYP,^[141] the “Coulomb-attenuating method” is used. The composition of the total exchange is depicted in fig. 3.1.

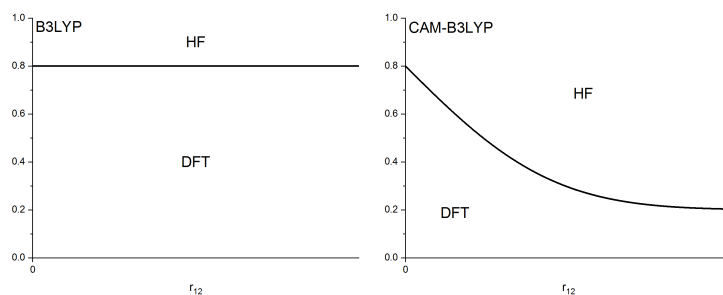


FIGURE 3.1: “Schematic plots of the contributions to exchange from r_{12}^{-1} , apportioned into DFT and HF, for: B3LYP (left) and CAM-B3LYP (right).” Adapted from ref. [141].

3.1.2 Dispersion correction

The lacking description of dispersion interactions can be overcome by introducing correction terms developed by Grimme^[142] and other groups. The attractive dispersion is typically introduced as a negative correction term to the Kohn-Sham energy. In the context of this work, the D3-correction is used which can be expressed as a sum of two- and three-body terms.

$$E_{D3} = E^{(2)} + E^{(3)} \quad (3.8)$$

The dominating two-body term can be expressed as a sum over all atom pairs AB , with the n -th order dispersion coefficient C_n^{AB} for atom pair AB with a interatomic distance of r_{AB} . This series is truncated after $n = 8$ and a global density-functional dependent scaling factors s_n are introduced, especially for density functionals which already partly account for dispersion. A damping function $f_{d,n}$ is introduced to avoid singularities for small values of r_{AB} . The smaller three-body term $E^{(3)}$ is neglected in the context of this work but can be calculated.

$$E^{(2)} = \sum_{AB} \sum_{n=6,8} s_n \frac{C_n^{AB}}{r_{AB}^n} f_{d,n}(r_{AB}) \quad (3.9)$$

In the context of this work, Becke-Johnson damping^[143] is used, modifying the equation above with the damping function $f_{d,n} = a_1 R_{AB}^0 + a_2$:

$$E^{(2)} = \sum_{AB} \sum_{n=6,8} s_n \frac{C_n^{AB}}{r_{AB}^n + f_{d,n}(R_{AB}^0)^n} \quad (3.10)$$

For the calculations conducted in this work, the functionals B97D,^[144] B3LYP^[135,136] and CAM-B3LYP^[141] were used with the def2-TZVP basis set.^[145] For B3LYP and CAM-B3LYP the D3-correction with Becke-Johnson damping was included.^[142,143] Revised damping variants with refitted coefficients are available^[146] but have not yet been implemented into the used quantum chemistry program packages Gaussian and TURBOMOLE.

3.2 Time-dependent density functional theory

For the description of electronic excitation and excited states, the time-independent density functional theory is not sufficient. Thus, time-dependent density functional theory (TD-DFT) is required, which is based on the time-dependent Schrödinger equation:

$$i \frac{\partial}{\partial t} \Psi(t) = \hat{H}(t) \Psi(t) \quad (3.11)$$

Analogous to the derivation of the time-independent method and the Hohenberg-Kohn theorem, a 1-1 mapping of a potential $v(\vec{r}, t)$ and density $\rho(\vec{r}, t)$ has been

proven by Runge and Gross in their famous theorem.^[147] Furthermore, a time-dependent Hamiltonian can be formulated including a time-dependent external potential $v_{\text{ext}}(\vec{r}, t)$. The Kohn-Sham equation 3.12 for the time-dependent case can be derived accordingly.^[148]

$$\begin{aligned} i \frac{\partial}{\partial t} \Psi(t) &= [T_S[\rho] + V_{e-e} + v_{\text{ext}}(\vec{r}, t)] \Psi(t) \\ i \frac{\partial}{\partial t} \Psi(t) &= \partial t \left[-\frac{\nabla^2}{2} + V_{\text{KS}}[n, \Psi_0](\vec{r}, t) \right] \Psi(\vec{r}, t) \end{aligned} \quad (3.12)$$

Similar to the ground state case, the exact description of the Kohn-Sham potential V_{KS} is unknown. In the context of this work, the adiabatic approximation is used defining V_{KS} as time-independent. V_{KS} is approximated by the previously introduced exchange-correlation functionals V_{XC} used for ground state DFT, together with the known V_{Ne} and V_{e-e} .

$$V_{\text{KS}} = V_{\text{Ne}} + V_{e-e} + V_{\text{XC}} \quad (3.13)$$

To calculate excited state energies, the response of the ground state density to an applied electric field is considered. Usually, the linear response approximation is used, under the assumption that the applied electric field induces a weak perturbation to the system. Finally, the Casida equation^[149] is obtained, an eigenvalue equation to obtain the the excitation energies ω .

$$\begin{pmatrix} A & B \\ B^* & A^* \end{pmatrix} \begin{pmatrix} X \\ Y \end{pmatrix} = \omega \begin{pmatrix} -1 & 0 \\ 0 & 1 \end{pmatrix} \begin{pmatrix} X \\ Y \end{pmatrix} \quad (3.14)$$

A, B, B^* and A^* are orbital-rotation matrices, whose exact definition can be found in literature.^[150] The off-diagonal matrices B and B^* describe the coupling between excitations and deexcitations and often contain only small values which is the base of the Tamm-Dancoff approximation (TDA)^[151,152] which neglects these contributions reducing equation 3.14 to 3.15.

$$AX = \omega X \quad (3.15)$$

TDA can improve the results obtained by TD-DFT and is more stable with regards

to triplet instabilities^[152-154] and is used for the calculation of the excited states of the chromone clusters discussed in chapter 4.4 and 4.5.

A more rigorous derivation of the TD-DFT linear response formalism can be found in most quantum chemistry textbooks and the literature cited, although the review of Dreuw and Head-Gordon^[155] provides an excellent overview and unfolds the relations of Hartree-Fock, time-dependent HF, DFT, time-dependent DFT and the Tamm-Dancoff approximation.

3.2.1 Natural transition orbitals

A useful tool to analyze the electronic excitations of a molecule or molecular cluster is the use of natural transition orbitals (NTO).^[156,157] Usually multiple pairs of occupied and virtual orbitals contribute to a single transition with varying degree, making interpretation difficult. This can be circumvented by unitary transformations of the occupied and virtual orbitals to achieve a more localized occupied-virtual orbital pair^[158] because most electronic excitations can be described by one or two NTOs instead of multiple pairs of canonical molecular orbitals. As an example the $S_0 \rightarrow S_3$ transition of chromone is shown below, expressed in canonical molecular orbitals and in natural transition orbitals. The first two electron-hole pairs include 86 % in the canonical picture and 98 % using NTOs, a considerable increase. Inclusion of a third pair still only results in a total sum of 94 % showing that NTOs simplify the interpretation of electronic transitions.

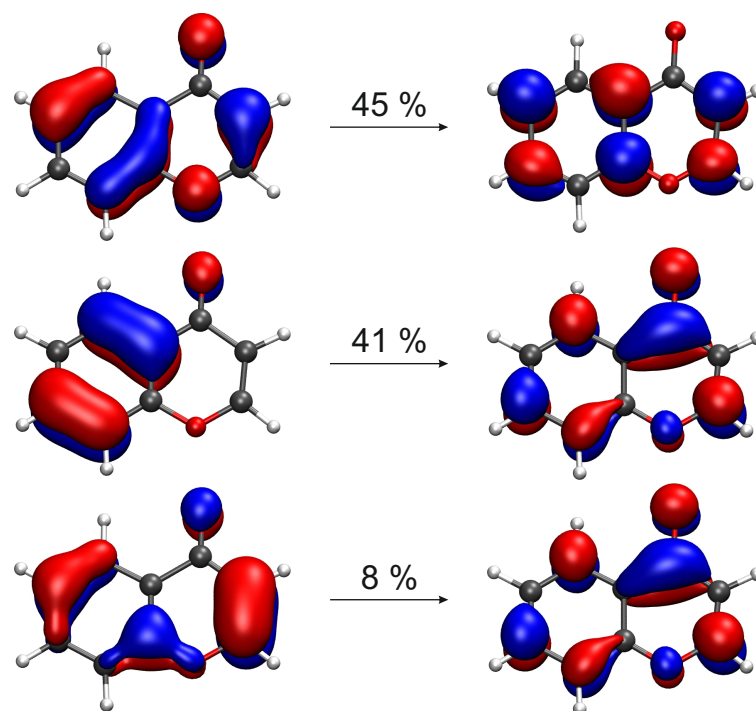


FIGURE 3.2: $S_0 \rightarrow S_3$ transition of chromone, expressed with canonical molecular orbitals.

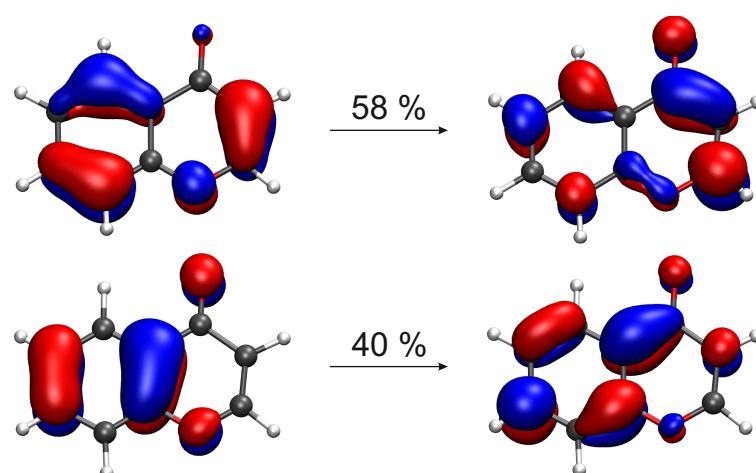


FIGURE 3.3: $S_0 \rightarrow S_3$ transition of chromone, expressed with natural transition orbitals.

3.3 Coupled-Cluster methods

The Coupled-Cluster (CC) method represents one of many post-HF methods to recover the missing explicit electron-electron interaction, also called Coulomb correlation. A detailed description of the HF method can be found in literature.^[127–129] HF is not able to describe the Coulomb correlation interaction adequately because a mean-field approximation is used. Consequently, HF is unable to describe London dispersion, a fault cured by the CC methods. The Coupled-Cluster method is based on the configuration interaction (CI) method which describes the wavefunction Ψ_{CI} based on an expansion of a reference wavefunction Φ_0 (see equation 3.16). Φ_0 consists of a Slater determinant of Hartree-Fock orbitals. Excited Slater determinants are formulated by exchanging occupied orbitals $\phi_{i,j,k}$ with virtual orbitals $\phi_{a,b,c}$ by application of the excitation operator \hat{T} .

$$\Psi_{\text{CI}} = \underbrace{\Phi_0 + \underbrace{\sum_{i,a} t_{ia} \Phi_i^a}_{1+\hat{T}_1:\text{CIS}} + \sum_{i<j,a<b} t_{ia,jb} \Phi_{ij}^{ab}}_{1+\hat{T}_1+\hat{T}_2:\text{CISD}} + \dots \quad (3.16)$$

This equation describes the full CI description for a wavefunction in a finite basis set and is computationally very demanding due to the fast growth of required Slater determinants. Thus, the full CI equation is often truncated resulting in the CI Singles (CIS) and CI Singles and Doubles (CISD) method. However, due to their lack of size consistency an improved method in form of the coupled-cluster theory was developed:

$$\Psi_{\text{CC}} = \exp(\hat{T})\Phi_0 \quad (3.17)$$

$$\exp(\hat{T}) = 1 + \hat{T} + \frac{1}{2}\hat{T}^2 + \frac{1}{6}\hat{T}^3 + \dots \quad (3.18)$$

The use of an exponential ansatz for the wavefunction ensures size consistency and improves upon the CI formalism.^[159] The excitation operator \hat{T}_n can be truncated in a similar manner, resulting in the commonly used CC Singles and Doubles (CCSD) method. Due to the already high scaling of $\approx N^6$ with system size regarding

CCSD, additional inclusion of the triple excitations (CCSDT) is unfeasible due to the resulting $\approx N^8$ scaling. Nevertheless, the CCSD(T) method^[160] was developed with a perturbative description of the triple excitations which is considered the “gold standard” of quantum chemistry with $\approx N^7$ scaling.

3.3.1 CC2

The CC2 method^[161] is a lower-cost coupled cluster method with a reduced $\approx N^5$ scaling, including single and double excitations. The single excitations are described by the coupled-cluster formalism, while the double excitations are treated in a perturbative manner. The energies are of similar quality as the related MP2 method, the advantage of CC2 is the possibility to derive response functions to define excitation energies and transition moments.

A short derivation of the CC2 model based on the original publication^[161] of Christiansen et al. is given in the following: The Hamiltonian \hat{H} is split into the Fock operator \hat{F} and a fluctuation operator \hat{U} . The equations for the CC2 cluster amplitudes can be derived from the CCSD cluster equations, with μ_1 and μ_2 denoting the singly and doubly excited determinants:

$$\langle \mu_1 | \hat{H} + [\hat{H}, T_2] | \text{HF} \rangle = 0 \quad (3.19)$$

$$\langle \mu_2 | \hat{H} + [\hat{H}, T_2] + \frac{1}{2} [[\hat{H}, T_2], T_2] | \text{HF} \rangle = 0 \quad (3.20)$$

In CC2, the doubles expression simplifies to:

$$\langle \mu_2 | \hat{H} + [\hat{F}, T_2] | \text{HF} \rangle = 0 \quad (3.21)$$

with:

$$\hat{O} = \exp(-T_1) O \exp(T_1) \quad (3.22)$$

The CCSD energy is correct through the third order, while CC2 was developed to be correct through the second order. The singles appear only in second order due

to the use of (optimized) Hartree-Fock orbitals, so that the first order contribution vanishes (Brillouin theorem). The singles respond to external perturbations to zeroth order in U which is also used in the CC2 method. Thus, the singles equations are retained in their CCSD form. The doubles need only to be included to first order, with the singles treated as zeroth-order parameters, resulting in the simplified equation 3.21.

Successful application of the CC2 approach and the coupled-cluster approach in general requires that the reference wavefunction is a good description for the investigated system. The size-intensive D_1 diagnostic by Janssen and Nielsen^[162] is an ideal tool to indicate a multireference character of the ground-state reference. Calculations with a high D_1 value should be carefully checked, with the cutoff point varying between 0.03 and 0.10.^[162,163] A high D_1 value indicates strong orbital relaxation effects, detected by large cluster amplitudes for the single excitations t_{ai} .

$$D_1 = \sqrt{\max \left(\lambda_{\max} \left[\sum_i t_{ai} t_{bi} \right], \lambda_{\max} \left[\sum_a t_{ai} t_{aj} \right] \right)} \quad (3.23)$$

$$\text{with: } \lambda_{\max} [M] - \text{largest eigenvalue of the matrix } M \quad (3.24)$$

In this thesis, RI-SCS-CC2^[164–168] calculations were performed to optimize ground state^[169,170] and excited state^[171] structures, calculate singlet and triplet excitation energies and transition moments^[172] utilizing the def2-TZVP basis set.^[145,173]

3.3.2 ADC(2)

The ADC(n) methods are based on the algebraic diagrammatic construction of the polarization propagator^[174,175] and were later reformulated using the intermediate state representation (ISR).^[176–178] A detailed explanation of the ADC(n) scheme can be found in a review by Dreuw and Wormit,^[179] only a brief introduction to the used ADC(2) method is given here.

First, an excited-state wavefunction Ψ_n on the basis of so-called intermediate states $\tilde{\Psi}_j$ is constructed. The intermediate states are generated by applying the excitation operator \hat{T} introduced before on a ground-state wavefunction Ψ_0 , generating excited

state wavefunctions Ψ_J . These are typically not orthogonal but can be orthogonalized, resulting in the intermediate state basis $\tilde{\Psi}_J$. The Hamiltonian and other operators can then be represented in the hermitian ADC matrix, shifted by the ground state energy E_0 :

$$\langle \mathbf{M}_{IJ} \rangle = \langle \tilde{\Psi}_I | \hat{H} - E_0 | \tilde{\Psi}_J \rangle \quad (3.25)$$

$$\langle \mathbf{O}_{IJ} \rangle = \langle \tilde{\Psi}_I | \hat{O} | \tilde{\Psi}_J \rangle \quad (3.26)$$

By solving the Hermitian eigenvalue problem, we obtain the eigenvectors x to construct the excited-state wavefunction Ψ_n .

$$\mathbf{M}\mathbf{X} = \mathbf{X}\mathbf{\Omega}, \text{ with } \mathbf{X}\mathbf{X}^T = \mathbf{I} \quad (3.27)$$

The corresponding reference wavefunction Ψ_0 can only be approximated, since the exact solution is usually not known. For the ADC(2) method Ψ_0 is approximated by the MP2 ground state. ADC(2) can also be interpreted as “MP2 for excited states” and should only be applied if the ground state of the investigated system is well described by MP2.^[179]

ADC(2) is closely related to CC2 — both are size-consistent second-order methods. The quality of excitation energies and excited states obtained with ADC(2) is similar to CC2. Due to the hermitian character of the Hamiltonian, the ADC equations need only to be solved once in contrast to the non-hermitian CC2 method, where double calculation of right and left eigenvectors is necessary, saving computational effort. Another advantage of ADC(2) is the correct description of conical intersections between states of the same symmetry. CC2 on the other hand provides a better description of the ground state which is only at MP2 level for the ADC(2) method. Similarly to CC2, spin-component scaling can improve the accuracy of ADC(2) (see section 3.3.3).

In this thesis, RI-SCS-ADC(2) calculations were performed to optimize ground state and excited state structures, calculate singlet and triplet excitation energies and transition moments^[180] utilizing the def2-TZVP basis set.^[145,173]

3.3.3 Spin-component scaling

Spin-component scaling (SCS) seeks to improve upon the correlation energy by introducing scaling factors for the same-spin and opposite-spin contributions to the correlation energy. Originally developed for MP2,^[181] the approach has been generalized for CC2 and ADC(2),^[167] using the same scaling factors as the original SCS-MP2 method: $c_{SS} = \frac{1}{3}$ for same-spin contributions, $c_{OS} = 1.2$ for opposite-spin contributions.^[181,182] The use of SCS improves the description of ground state and excited state potential surfaces of CC2 and ADC(2)^[167,183–185] and excitation energies.^[123]

3.3.4 Domain-based local pair natural orbital method (DLPNO)

The domain-based local pair natural orbital method (DLPNO) is a powerful local correlation method with nearly linear scaling.^[186] Local correlation methods utilize the short-range nature of dynamic correlation to reduce the computational cost of sophisticated Coupled-Cluster calculations.^[187] In the context of this thesis, DLPNO-CCSD(T) calculations were performed utilizing the program package ORCA5.^[188–190] The DLPNO method is described in detail in literature^[191,192] and will only be introduced in a brief manner since a complete derivation would exceed the scope of this chapter.

As introduced previously, CCSD(T) is considered the “gold standard” of quantum chemistry but suffers from its high formal scaling of $\approx N^7$. Thus, usage of CCSD(T) for larger systems with a substantial amount of atoms and basis functions incurs a large computational effort. Consequently, low-order scaling methods were developed exploiting the short-range nature of dynamic electronic correlation, while recovering the vast majority of the correlation energy (up to 99.9%). One of these low-order approaches are the first local correlation methods developed by Sæbø and Pulay.^[193–195] Their concept of utilizing localized molecular orbitals and projected atomic orbitals (PAO) was further developed by Schütz and Werner.^[196–199] Another important concept is the idea of pair natural orbitals (PNOs) to describe the virtual orbital space. Here, the pioneering contributions of Meyer resulting in his

coupled-electron pair approximation (CEPA) is important.^[58,200] One of the latest developments is the DLPNO method by the Neese group, utilizing the concept of sparse maps^[192] combined with the approaches mentioned before. This method allows to calculate energies of CCSD(T) quality with low computational effort, especially when compared to a canonical CCSD(T) calculation.

To achieve this, the occupied Hartree-Fock orbitals are localized using algorithms as Pipek-Mizy^[201] or Forster-Boys^[202] and generating local pair natural orbitals (LPNO) to describe the occupied space. The virtual space is expressed by an incomplete set of pair natural orbitals (PNO) which are constructed from localized projected atomic orbitals (PAO), resulting in a large reduction of the complexity of the virtual space. The correlation energy is then expressed as a sum of electron-pair correlation energies with additional perturbative triples correction. These contributions are separated into strong pairs and weak pairs according to a pre-screening with local MP2 (LMP2). The weak pairs are kept at second-order level, while the strong pairs are treated at coupled-cluster level.

3.4 Conformer search

An exhaustive manual search of the chemical space for a cluster of two or more molecules can be challenging and tedious. A possible solution to solve this problem is the use of an algorithm to systematically generate a selection of different isomers. For this purpose, CREST (Conformer-Rotamer Ensemble Sampling Tool) was developed by the Grimme group.^[203] It is based on the low-cost GFNn-xTB method^[204,205] for fast geometry optimizations and molecular dynamics. An iterative algorithm with an RMSD bias potential is used to explore the chemical space in a multi-step procedure resulting in a useful conformer ensemble. This ensemble can serve as the basis for subsequent optimizations with higher-cost methods. This algorithm is of course no substitute for a careful analysis of the molecular cluster but can aid in finding the global minimum structure. The subsequent geometry optimization is usually carried out using the Gaussian^[206] or TURBOMOLE^[207] program package. Geometry optimizations using DFT, TD-DFT and UDFT can be carried out using Gaussian or the Gaussian External interface. Latter uses a script written by Prof. Christoph van

Wüllen combining the two program packages: The geometry optimization is carried out using the Berny algorithm^[208] (see ref. [209] for more details) of Gaussian while energies, gradients and IR frequencies are calculated by TURBOMOLE. For SCS-CC2 and SCS-ADC(2), the optimization is performed using TURBOMOLE because the wavefunction methods are currently not correctly implemented into the used script.

3.5 Energy decomposition analysis

A central objective of this thesis is the analysis and quantification of intermolecular interactions, especially London dispersion in molecular clusters.

In principle, there exist two different approaches to describe the non-covalent interaction between two molecules in a molecular cluster. The perturbative approach is, *e.g.*, used in the symmetry-adapted perturbation theory (SAPT), where the interaction energy is calculated directly as a perturbation to a model Hamiltonian of individual monomers. In the context of this thesis, the focus will be on the HF-based implementation of SAPT by Hohenstein and Sherrill in the Psi4 package.^[66,210–212] In the alternative supermolecular approach, the binding energy and the eventual decomposition is based on a comparison of the energy of the complex with the sum of the energies of the isolated monomers. This kind of concept is used for the Local Energy Decomposition (LED) based on the DLPNO-CCSD(T) method which is described in section 3.3.4.

3.5.1 Symmetry-adapted perturbation theory

Symmetry-adapted perturbation theory (SAPT) is based on a perturbative approach to describe the interaction between two molecules. The interaction energies are usually multiple orders of magnitude smaller than the absolute electronic energies of the investigated molecules, motivating the treatment of the interaction as a small perturbation. Already in the 1930s, Fritz London and Robert Eisenschitz formulated an early version of SAPT.^[7] A detailed description of the SAPT theory can be found in literature,^[213–217] especially the excellent review by Jeziroski, Moszynski and Szalewicz^[218] should be mentioned here.

As mentioned above, SAPT expresses the interaction between two molecules A and B in double-perturbative manner, leading to the following Hamiltonian:

$$H = F_A + F_B + W_A + W_B + V \quad (3.28)$$

F_A and F_B are the Fock operators of the monomers A and B, and represent the zeroth-order Hamiltonian with the perturbation operators W_A , W_B and V . W_A and W_B represent the intramolecular fluctuation potential of the monomers A and B, while V is the intermolecular interaction potential between both monomers. The interaction energy is then expressed as a row of perturbative corrections E^{ij} in different orders i, j . i describes the order in V , j the order in $W_A + W_B$. These corrections can be decomposed into four interactions: electrostatics, exchange, induction and dispersion. The simplest truncation is named SAPT0 with $(i, j) = (2, 0)$ which is used in the context of this thesis. It is able to describe closed- and open-shell systems, an important advantage over the more advanced related SAPT methods. In SAPT0, the monomers and the dimer are essentially treated at HF-level to obtain the electrostatic and exchange contribution in first order of V . In second-order of V induction and dispersion terms appear, the subscript *resp* indicates that orbital-relaxation effects are included.

$$E_{\text{SAPT0}} = E_{\text{elst}}^{10} + E_{\text{exch}}^{10} + E_{\text{ind,resp}}^{20} + E_{\text{exch-ind,resp}}^{20} + E_{\text{disp}}^{20} + E_{\text{exch-disp}}^{20} + \delta HF^{(2)} \quad (3.29)$$

A physical interpretation of each term, reproduced according to the review of Jeziroski, Moszynski and Szalewicz^[218] is given in the following:

The term $\delta HF^{(2)}$ is necessary to account for all interaction energy included in the dimer at HF level. The classic supermolecular interaction energy at HF level $E_{\text{IE}}^{\text{HF}}$ is corrected by the electrostatic, induction and exchange terms:

$$\delta HF^{(2)} = E_{\text{IE}}^{\text{HF}} - \left(E_{\text{elst}}^{10} + E_{\text{exch}}^{10} + E_{\text{ind,resp}}^{20} + E_{\text{exch-ind,resp}}^{20} \right) \quad (3.30)$$

SAPT and especially SAPT0 rely on favorable error cancellation in small basis sets and will not be accurate approaching the complete basis set (CBS) limit. For SAPT0,

TABLE 3.1: Physical interpretation of the different terms occurring in the SAPT0 energy formula.

symbol	name	physical interpretation
E_{elst}^{10}	electrostatic energy	damped electrostatic interaction of HF permanent multipoles between unperturbed monomers
E_{exch}^{10}	exchange energy	exchange of electrons between unperturbed monomers at HF level
$E_{\text{ind,resp}}^{20}$	induction energy	damped interaction between permanent and induced multipoles at HF level
$E_{\text{exch-ind,resp}}^{20}$	exchange-induction energy	additional exchange repulsion due to coupling between induction and exchange
E_{disp}^{20}	dispersion energy	damped interaction between instantaneous multipoles at HF level
$E_{\text{exch-disp}}^{20}$	exchange-dispersion energy	additional exchange repulsion due to coupling between dispersion and exchange
$\delta HF^{(2)}$	HF correction	higher order effects, mainly including induction beyond the second-order

the jun-cc-pVDZ basis set is recommended, with ideal error cancellation^[219] for a large test set (S22,^[220] NBC10,^[221] HBC6^[222] and HSG^[223]) describing nonbonded interactions). jun-cc-pVDZ represents a “calendar” basis set which were introduced by Papajak and Truhlar.^[224] In these basis sets, a truncated augmentation of the basis starting from aug-cc-pVXZ. In jul-cc-pVXZ, the diffuse functions are omitted for hydrogen and helium and in jun-cc-pVXZ, the diffuse function with the highest angular momentum on each non-hydrogen atom is removed. For the calculations, the SAPT0 implementation in Psi4 was used with the jun-cc-pVDZ basis set.^[212]

3.5.2 Local energy decomposition

As described in section 3.3.4, DLPNO-CCSD(T) is a powerful method to approximate CCSD(T) at a much lower computational cost. However, it cannot only be used to determine accurate electronic energies of a system of interest but can also give insight into the intermolecular interaction of molecular clusters. Application of the “Local

Energy Decomposition" (LED) analysis allows to determine and partition the binding energy of molecular clusters into physically meaningful terms which is shown in equation 3.31.^[225-229] In comparison to the aforementioned SAPT method, DLPNO-CCSD(T)/LED constitutes a supermolecular approach to describe the binding energy of two monomers A and B forming the dimer AB.

$$\Delta E = \Delta E_{\text{geo-prep}} + \Delta E_{\text{el-prep}}^{\text{ref}} + E_{\text{elstat}}^{\text{ref}} + E_{\text{exch}}^{\text{ref}} + \Delta E_{\text{non-disp}}^{\text{CC}} + E_{\text{disp}}^{\text{CC}} + \Delta E^{\text{CC-(T)}} \quad (3.31)$$

The terms are divided into contributions from the HF reference denoted with a superscript ^{ref} and from the DLPNO Coupled-Cluster energy denoted with ^{CC} and (T).

The first term $\Delta E_{\text{geo-prep}}$ describes the energetic penalty (distortion energy) to distort the monomers A and B into the geometry adopted in the dimer by calculating the difference of the total DLPNO-CCSD(T) energies.

$$\Delta E_{\text{geo-prep}} = E(A, B)_{\text{relaxed-geo}} - E(A, B)_{\text{dimer-geo}} \quad (3.32)$$

The second term $\Delta E_{\text{el-prep}}^{\text{ref}}$ accounts for the electronic preparation in the HF reference, calculated by taking the difference of the HF energy of monomer A(B) in its dimer geometry interacting with B(A) and the lone monomer. All following terms are calculated with the monomers and dimer in the dimer geometry.

$$\Delta E_{\text{el-prep}}^{\text{ref}} = E(A, B)_{\text{mono-in-dimer}}^{\text{ref}} - E(A, B)_{\text{mono-alone}}^{\text{ref}} \quad (3.33)$$

The third and fourth term, $E_{\text{elstat}}^{\text{ref}}$ and $E_{\text{exch}}^{\text{ref}}$, describe intermolecular electrostatic attraction and exchange which stem from the decomposition of the intermolecular HF contribution. The electrostatic term includes both permanent and induced electrostatics, so that no specific value for the induction interaction is obtained. Importantly, the exchange component is stabilizing by lowering the repulsion between same-spin electrons.

$\Delta E_{\text{non-disp}}^{\text{CC}}$ accounts for all non-dispersive correlation energy, mainly including charge transfer, intrafragment double excitations and single contributions as well as

some electronic preparation. This term is calculated by taking the difference between the non-dispersive correlation energy of the dimer (strong and weak pairs) and the correlation energy of both monomers.

$$\Delta E_{\text{non-disp}}^{\text{CC}} = E(AB)_{\text{non-disp, strong}}^{\text{CC}} + E(AB)_{\text{non-disp, weak}}^{\text{CC}} - E(A)_{\text{corr}}^{\text{CC}} - E(B)_{\text{corr}}^{\text{CC}} \quad (3.34)$$

$E_{\text{disp}}^{\text{CC}}$ represents the dispersive contribution to the correlation energy and is calculated by summing the strong and weak pair terms.

$$E_{\text{disp}}^{\text{CC}} = E_{\text{disp, strong}}^{\text{CC}} + E_{\text{disp, weak}}^{\text{CC}} \quad (3.35)$$

Partitioning of the correlation energy occurs according to the localization of the corresponding contribution. A strong or weak pair is assigned to the dispersion energy, if one hole and one particle are present on different fragments and to the non-dispersive part if multiple holes or particles are present at a fragment.

Comparing results obtained with SAPT and DLPNO-CCSD(T) is possible, although a 1:1-mapping of each interaction is not possible due to the different approaches used in both methods. Nevertheless, multiple comparing studies have been published in literature and show good agreement.^[63,230] The calculations in this work were carried out using the program package ORCA.^[188–190]

3.6 Calculation of anharmonic frequencies

The calculation of vibrational frequencies is a central component of modern quantum chemistry. They provide useful information aiding the identification of the structure of a molecule or molecular clusters, especially in conjunction with experimental studies. In most applications, vibrational frequencies are calculated using a model of uncoupled harmonic oscillators by an analytic Hessian^[231] or by numeric differentiation, if the analytic expression is unknown. The neglect of higher-order terms in the harmonic approximation is usually treated by scaling factors.^[232] This procedure provides meaningful vibrational frequencies in most cases but can fail for systems,

where the harmonic approximation is an insufficient description of the potential (multiple minima, long-range effects, coupled vibrations). To achieve a better description of these systems anharmonic vibrational frequencies, going beyond the harmonic model, can be considered.

In the context of this work, a variational method based on the Ritz principle^[233–235] is applied for this purpose. This program was developed by Andreas Funk and Tobias Martin in the Gerhards group (source code in appendix B).^[236,237] A one-dimensional potential energy curve is calculated along a localized normal coordinate Q and interpolated between those known points with a cubic spline, since explicit calculation of all points would result in an unfeasible computational effort. The corresponding nuclear Schrödinger equation is:

$$\hat{H}\Psi_{\text{vib}} = \left(-\frac{\hbar^2}{2\mu} \frac{d}{dQ^2} + V(Q) \right) \Psi_{\text{vib}} = E_{\text{vib}} \Psi_{\text{vib}} \quad (3.36)$$

The wavefunction Ψ_{vib} can be expressed as a linear combination of harmonic oscillator base functions Φ_v up to a chosen quantum number v to obtain an approximate solution.

$$\Psi_{\text{vib}} = \sum_v^n c_v \Phi_v(Q) \quad (3.37)$$

More sophisticated approaches which improve upon the harmonic approximation include VSCF (vibrational self-consistent field), where all vibrational modes interact in a mean-field approximation similar to the Hartree-Fock method for the electronic structure.^[238–241] Similar to HF, improvements upon the mean-field approximation are possible by perturbative approaches, analogous to Møller-Plesset perturbation theory resulting in VPTn^[242–244] or VCI^[245–248] and VCC^[249,250] as the analogs of Configuration Interaction and Coupled-Cluster methods presented in chapter 3.3. These methods require an increasing amount of computational effort and are difficult to apply for large molecules.

3.7 Auxiliary programs

Apart from the extensive program packages used to perform geometry optimization, calculation of electronic energies, electronic transitions and harmonic frequencies, a multitude of auxiliary programs was used to aid the analysis and interpretation of the obtained results. Furthermore, some self-written python and bash-scripts are presented.

Concerning geometry optimization, Molden^[251] was used to visualize the final geometry which should be checked after every finished optimization. Molden also provides every intermediate geometry and plots of the energy and remaining force over the course of the optimization process. This can be especially useful in diagnosing oscillations in the optimization algorithm which are usually solved by a restart of the calculation at a point prior of the oscillating behavior. Significant changes in energy and geometry are also diagnosed quickly which can help understanding the cause for a failed calculation. Molden is also able to plot electronic densities, molecular orbitals and the normal modes of a molecule.

With regard to visualization of the normal modes, this task was usually performed by the program Avogadro^[252] which offers more functionality in this regard and is easier to use. Avogadro can also serve as a molecular editor providing a plethora of predefined fragments and implemented force fields. This allows fast generation of molecular structures including a rough pre-optimization or manual isomer search by combining chemical intuition with the force field as an alternative to the aforementioned CREST algorithm.

Generating high-quality images for publications or presentations is also an important task, carried out by the VMD program.^[253] A large pool of render methods and options are available to obtain excellent illustrations. In the scope of this thesis, VMD was mainly used to generate visualizations of molecular structures, (natural) transition orbitals and spin densities. It should be noted, that VMD offers a large variety of plug-ins, *e.g.*, for superimposing structures.

Chapter 4

Results

In this chapter, the results of the doctoral thesis are presented separated into two main parts. In the first part, the focus lies on dispersion effects in the ground state. Strongly dispersion-bound alkyl dimers including the triphenylmethane (TPM), the triphenylmethane dimer (TPM)₂ and the dimer of a substituted triphenylmethane (^tBuTPM)₂ are studied. A short introduction to the corresponding publication is given. Based on this work, the quantum chemical analysis of the dimer of a second substituted triphenylmethane (ⁱPrTPM)₂ is presented. A comparison of all three systems (TPM, ⁱPrTPM and ^tBuTPM) is carried out to explain the binding preferences. Additionally, the anharmonic frequencies which are central for the interpretation of the ^tBuTPM dimer are investigated. A benchmark study on a data set of multiple molecules is carried out. In the second part, the focus is extended to dispersion in ground and excited states with a study on aromatic ketone-solvent complexes. The binding behavior of the investigated chromone-methanol cluster is predominantly influenced by the hydrogen bond but the influence of London dispersion is not neglectable. Similarly, an introduction to the chromone-methanol topic is given together referring to the corresponding publication. Finally, an unpublished study of chromone derivatives-solvent clusters is discussed in a second section.

4.1 Dispersion in the ground state: Triphenylmethane and ^tBuTPM

Schreiner and coworkers synthesized and crystallized all-*meta tert*-butyl triphenylmethane (^tBuTPM), a sterically crowded molecule with six *tert*-butyl groups. Analysis of the solid state structure with neutron diffraction at 20 K revealed a head-to-head arrangement of two monomers with a central C-H...H-C distance of only 1.566(5) Å.^[254] This unusual arrangement exhibits strong Pauli repulsion between the central C-H bonds, but nevertheless results in the shortest intermolecular C-H...H-C distance measured to date. The central question is now, whether this peculiar arrangement is caused by packing effects in the solid state. To answer this question, ^tBuTPM was investigated in molecular beam experiments to exclude any external effects and only probe the intrinsic interaction of the respective dimer. Due to the large number of C-H stretching modes in ^tBuTPM, a deuterated derivative was used. The central aliphatic C-H bond was chosen as the deuteration target, acting as a discriminator between the head-to-head, head-to-tail and tail-to-tail arrangements (see fig. 4.1).

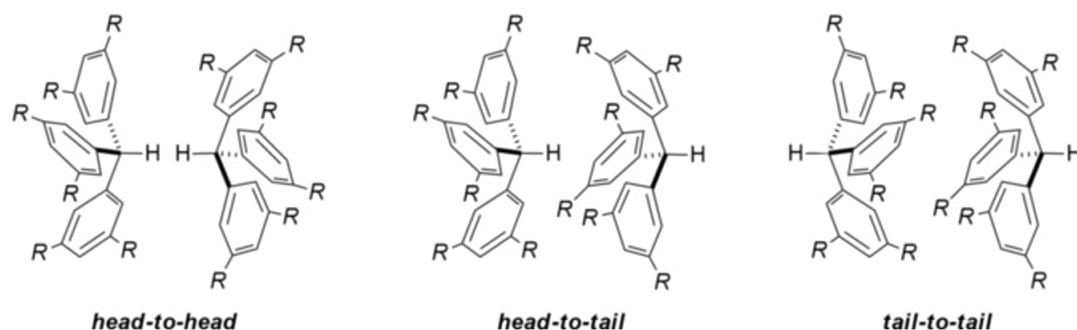


FIGURE 4.1: Different dimer motifs of triphenylmethane derivatives (R=H, ^tBu). Reprinted with permission from Wiley-VCH.^[107]

Combined IR/UV and stimulated Raman/UV experiments were carried out to determine the preferred arrangement in the gas phase, confirming the head-to-head arrangement. The use of stimulated Raman spectroscopy is necessary due to the unpolar nature of the hydrocarbons in symmetric arrangements leading to vanishing IR intensities for the diagnostic C-H(D) stretching bond. The close proximity of the C-H(D) bonds in the head-to-head structure leads to a strong blueshift of the corresponding stretching mode, which is not sufficiently described in the harmonic

approximation. A variational approach was used to improve the description by calculating anharmonic frequencies. A one-dimensional potential energy curve along the normal coordinate was used to calculate the vibrational eigenvalues. Finally, the head-to-head structure was confirmed to also be present in the gas phase. Energy decomposition calculations using SAPT0 reveal that the head-to-head structure is stabilized by enormous London dispersion interactions. This is caused by the ideal spatial interlocking of the twelve *tert*-butyl groups and the six benzene rings, enabling the strong binding between both monomers.

For the unsubstituted triphenylmethane (TPM), the lack of dispersion energy donors (DED) leads to a different binding preference. The TPM dimer prefers a tail-to-tail arrangement with both C-H bonds showing in opposite direction, avoiding the short C-H...H-C contact. This is also confirmed by quantum-chemical calculations, with the TPM dimer exhibiting a much weaker stabilization by London dispersion, resulting in the observed structure.

These results have been published in *Angewandte Chemie International Edition*, the manuscript (publication I) can be found in appendix A, page 127.

4.2 Dispersion in the ground state: ⁱPrTPM

Based on the results concerning the dimers of triphenylmethane and the all-*meta tert*-butyl substituted triphenylmethane presented in section 4.1, further research was conducted. Considering the large energy gap (68 kJ/mol) between the head-to-head and tail-to-tail motif for the *tert*-butyl-substituted derivative, the question arises whether a smaller dispersion energy donor (DED) like an *iso*-propyl group would still be sufficient to stabilize the head-to-head motif.

Additionally, the behavior of the head-to-tail motif is not easily predictable: For the triphenylmethane dimer, the head-to-tail motif is strongly disfavored due to the lack of dispersion energy donors (DEDs) and is of similar energy as the head-to-head motif. Considering the ^tBuTPM dimer, the head-to-tail motif is energetically favored over the tail-to-tail motif, although the assigned head-to-head motif is even more stable. It should be interesting whether the head-to-tail motif always stays in middle as a sort of "hybrid" structure or exhibits a particular stabilization relative to the head-to-head motif.

In the following, results of DFT calculations are presented for the all-*meta iso*-propyl substituted triphenylmethane (ⁱPrTPM) representing an intermediate point between TPM and ^tBuTPM as depicted in figure 4.2. Similarly to the investigations on those dimers, several structures in head-to-head, head-to-tail and tail-to-tail arrangements were created manually and optimized at B97D/def2-TZVP level with subsequent optimization at B3LYP-D3(BJ)/def2-TZVP level using the Gaussian program package. Afterwards, the obtained geometries were manually adapted and optimized again at B3LYP level in an attempt to find the most stable structure for a given structural motif. Furthermore, additional geometries based on the obtained ones were generated by hand and optimized as well. Finally, one-dimensional anharmonic frequency calculations for the central aliphatic C-H(D) bond were carried out to investigate the occurrence of a spectral shift similar to the ^tBuTPM dimer. Energy decomposition calculations using SAPT0 were used to investigate the binding energy and quantify the amount of dispersion interaction.

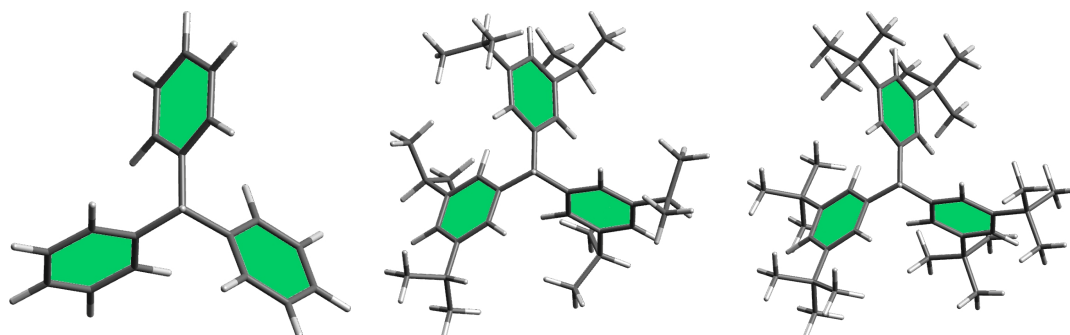


FIGURE 4.2: Structures of TPM, ⁱPrTPM and ^tBuTPM, with increasing size of dispersion energy donors.

4.2.1 DFT calculations

The results of the pre-optimization using B97D reveal that, in contrast to the TPM and ^tBuTPM dimer, the head-to-tail structure seems to be the preferred motif. The head-to-head motif is only several kJ/mol higher in electronic energy and is nearly isoenergetic including the zero-point vibrational energy (ZPVE). The tail-to-tail motif is strongly disfavored, similar to the situation in the ^tBuTPM dimer. The energy difference between the two most stable structures, head-to-head and head-to-tail, is quite small and depends strongly on the inclusion of ZPVE. The observed head-to-head structure exhibits a slightly bent C-H...H-C contact whereas it was linear for the ^tBuTPM dimer (see fig. 4.3).

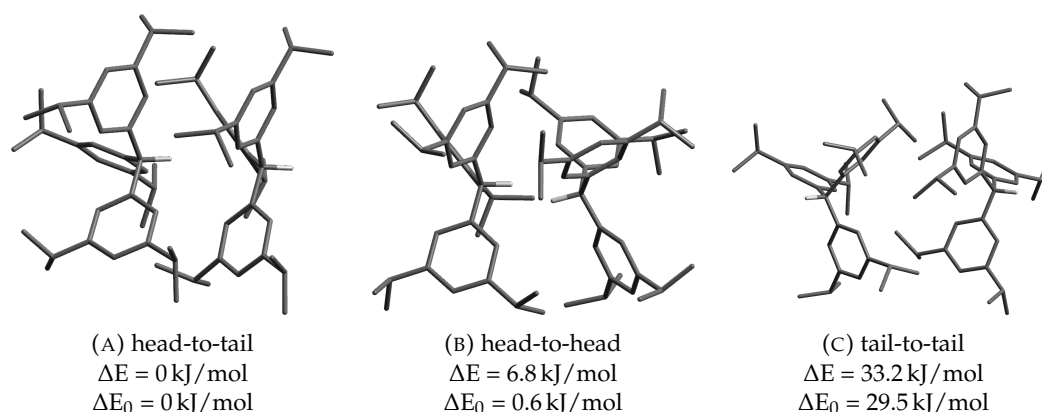


FIGURE 4.3: Different structures of the ⁱPrTPM dimer calculated at B97D/def2-TZVP level. For clarity, most hydrogen atoms are omitted.

The shown minimum geometries as well as several other less stable geometries of the respective motif were optimized with B3LYP-D3(BJ)/def2-TZVP confirming the initial order of motifs. Interestingly, a new minimum was found using the determined

crystal structure as starting geometry.^[255] Indeed, this staggered head-to-tail structure is the most stable one. The head-to-head motif is around 25 kJ/mol higher in energy, while the tail-to-tail motif is strongly disadvantaged with a ΔE of over 50 kJ/mol. For all three motifs, multiple optimizations with different starting geometries were carried out. A multitude of local minima exist due to the high flexibility of the twelve *iso*-propyl groups and possible methyl rotations. Thus, it is possible that a slightly more stable isomer exists for each motif but the overall ordering should be preserved regarding the significant energetic differences. The lowest structure of each motif is shown in detail in figures 4.4 - 4.6. The main attractive interaction responsible for stabilizing these alkyl dimers is certainly London dispersion as was shown for the ^tBuTPM dimer (see section 4.1). Thus, the stability or rather lack thereof for the tail-to-tail motif can be easily rationalized by the large distances between the two monomer units. The sterically crowded head-to-head and head-to-tail structures can be stabilized by the *iso*-propyl groups acting as dispersion energy donors. The head-to-head motif is slightly shifted and does not exhibit a high degree of symmetry in contrast to the ^tBuTPM dimer. This could be a first indicator of the weaker dispersion interaction for ⁱPrTPM₂ which leads to adoption of a slightly distorted geometry to reduce the Pauli repulsion caused by the central C-H...H-C contact. The ideal interlocking of the *tert*-butyl groups is not present for the *iso*-propyl groups. A more detailed analysis will be performed in the following subsection together with discussion of the SAPT results.

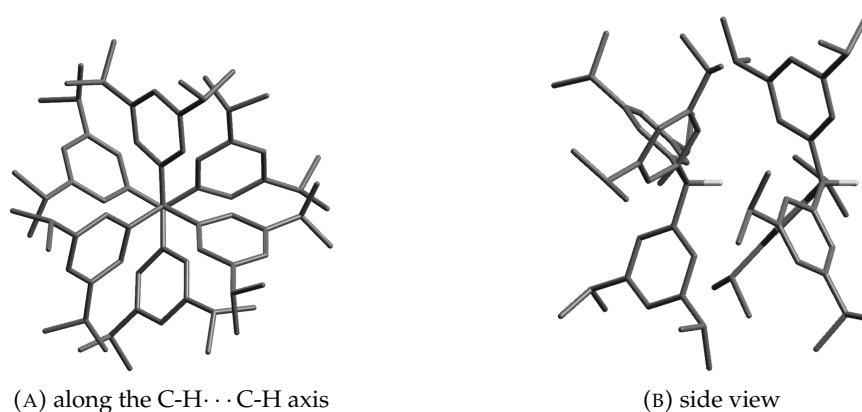


FIGURE 4.4: Head-to-tail motif of the ⁱPrTPM dimer calculated at B3LYP-D3(BJ)/def2-TZVP level. For clarity, most hydrogen atoms are omitted.

$$\Delta E = 0 \text{ kJ/mol}, \Delta E_0 = 0 \text{ kJ/mol}$$

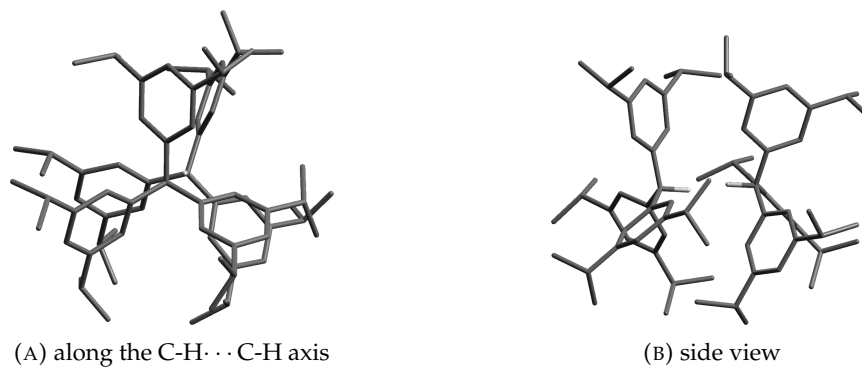


FIGURE 4.5: Head-to-head motif of the ${}^i\text{PrTPM}$ dimer calculated at B3LYP-D3(BJ)/def2-TZVP level. For clarity, most hydrogen atoms are omitted.

$$\Delta E = 27.6 \text{ kJ/mol}, \Delta E_0 = 21.6 \text{ kJ/mol}$$

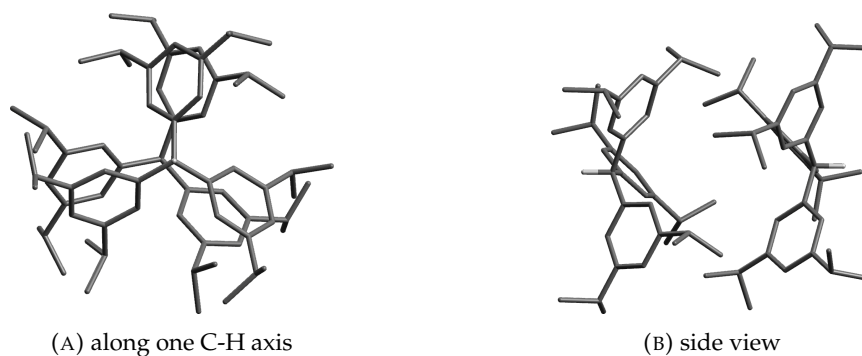


FIGURE 4.6: Tail-to-tail motif of the ${}^i\text{PrTPM}$ dimer calculated at B3LYP-D3(BJ)/def2-TZVP level. For clarity, most hydrogen atoms are omitted.

$$\Delta E = 52.6 \text{ kJ/mol}, \Delta E_0 = 47.1 \text{ kJ/mol}$$

On the experimental side, a crystal structure¹ of ⁱPrTPM was measured by the Schreiner group and strongly hints that the solid-state structure indeed exhibits a head-to-tail structure, although the structure could not be solved completely due to weak diffraction (see fig. 4.7).^[255] Of course, the solid-state structure is influenced by packing effects and interactions between the respective dimers but nevertheless supports the occurrence of the head-to-tail motif. For the ^tBuTPM dimer, the determined crystal structure was also similar to the gas phase structure which together with the strong energetic preference supports the hypothesis of a head-to-tail structure for (ⁱPrTPM)₂.

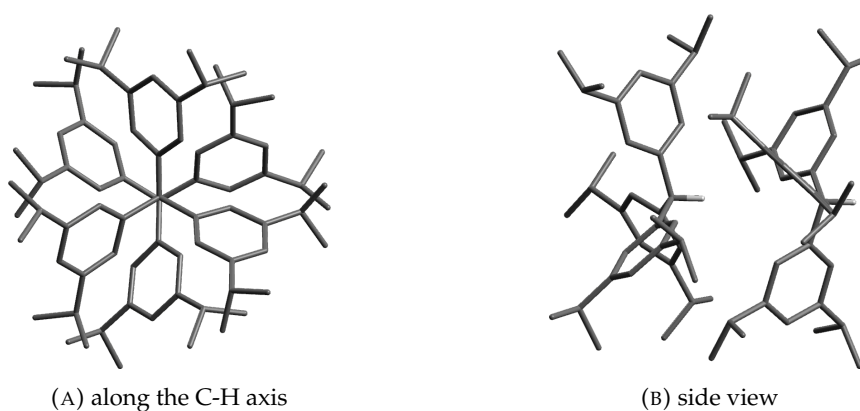


FIGURE 4.7: Crystal structure of ⁱPrTPM. For clarity, most hydrogen atoms and all disordered atoms are omitted.

Complementing the solid state structure, a determination of the gas phase structure would certainly support the initial support. To achieve this, combined IR/UV spectroscopy is not suited due to the low IR intensities of the structure-sensitive C-H stretching vibrations (see table 4.1). The stimulated Raman methods can overcome this problem because the Raman activities are much larger. This was already successfully applied for the ^tBuTPM dimer as described in the previous section. Analysis of the Raman spectra of the different motifs reveal that the transitions of the central C-H group overlap with those of the *iso*-propyl groups (see figs. 4.8 to 4.10). For an unambiguous identification of the preferred binding motif, deuteration of the central C-H bond is necessary. This would shift the C-D stretching frequency to the much less populated region around 2200 cm⁻¹ (see table 4.1).

The central aliphatic C-H bonds exhibit significant amount of Pauli repulsion in

¹CSD No: 1851907

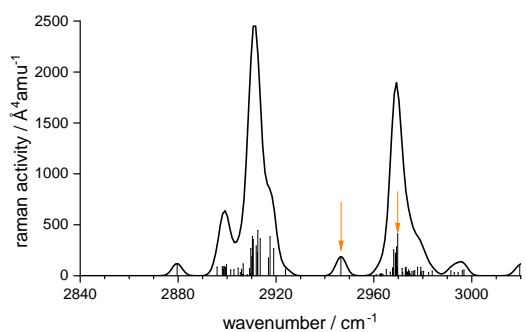


FIGURE 4.8: Calculated harmonic C-H stretching frequencies for the head-to-head motif of the ${}^i\text{PrTPM}$ dimer (gaussian envelope, FWHM=5 cm^{-1} , scaled by 0.96). The orange arrows indicate the stretching vibration of the central aliphatic C-H groups.

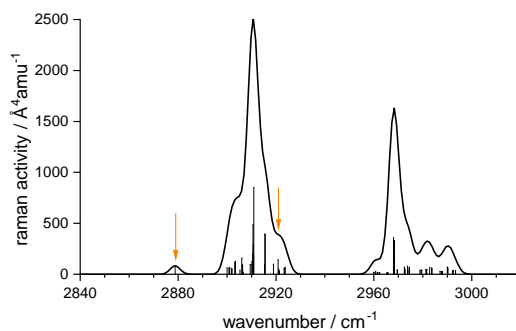


FIGURE 4.9: Calculated harmonic C-H stretching frequencies for the head-to-tail motif of the ${}^i\text{PrTPM}$ dimer (gaussian envelope, FWHM=5 cm^{-1} , scaled by 0.96). The orange arrows indicate the stretching vibration of the central aliphatic C-H groups.

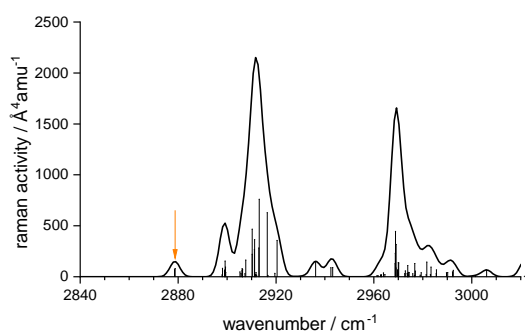


FIGURE 4.10: Calculated harmonic C-H stretching frequencies for the tail-to-tail motif of the ${}^i\text{PrTPM}$ dimer (gaussian envelope, FWHM=5 cm^{-1} , scaled by 0.96). The orange arrows indicate the stretching vibration of the central aliphatic C-H groups.

TABLE 4.1: Vibrational data for the three different motifs of ${}^1\text{PrTPM}$ with and without deuteration of the central C-H bond. The low IR intensities make IR/UV experiments unfeasible, thus stimulated Raman methods are more promising. The C-H and C-D frequencies are scaled by 0.96.

motif	$\tilde{\nu} / \text{cm}^{-1}$		IR int. / km mol^{-1}		Raman act. / $\text{\AA}^4 \text{u}^{-1}$	
	C-H	C-D	C-H	C-D	C-H	C-D
head-to-head	2947	2161	2	1	190	159
	2970	2179	14	3	409	78
head-to-tail	2879	2115	9	6	82	49
	2921	2146	9	1	142	69
tail-to-tail	2879	2115	9	5	70	50
	2879	2115	5	5	80	46
monomer	2898	2130	8	5	57	38

the head-to-head motif and should be significantly blueshifted. Due to the unsatisfactory description of this vibration in the harmonic approximation for the ${}^t\text{BuTPM}$ dimer, a one-dimensional anharmonic calculation is used to describe the vibrational frequency. The resulting frequencies are plotted in figures 4.11 and 4.12. The shifted nature of the head-to-head structure leads to a decoupled situation of both C-D stretching modes with two Raman-active bands. Thus, the induced blue-shift is significantly smaller (${}^t\text{BuTPM}$: 2248 cm^{-1}) and both harmonic and anharmonic frequencies agree well aside from a slight redshift of the anharmonic values which was also observed for the TPM and ${}^t\text{BuTPM}$ dimer.

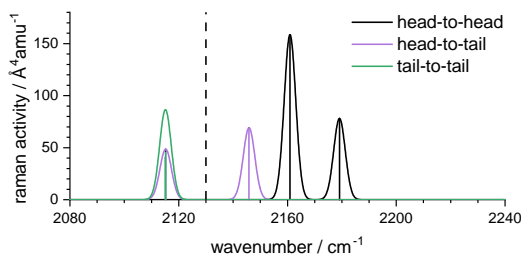


FIGURE 4.11: Calculated **harmonic** C-D stretching frequencies for all three motifs of the ${}^1\text{PrTPM}$ dimer (gaussian envelope, $\text{FWHM}=5 \text{ cm}^{-1}$). The tail-to-tail motif exhibits two close-lying transitions which overlap. The monomer frequency is indicated with a dashed line.

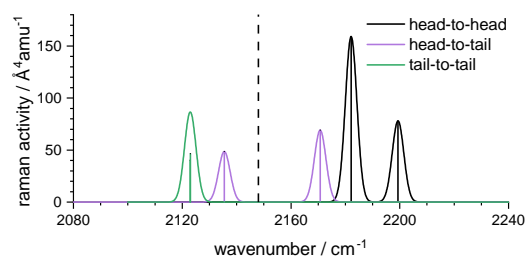


FIGURE 4.12: Calculated **anharmonic** C-D stretching frequencies for all three motifs of the ${}^i\text{PrTPM}$ dimer (gaussian envelope, FWHM=5 cm^{-1}). The anharmonic frequencies are the result of one-dimensional variational calculation. The tail-to-tail motif exhibits two close-lying transitions which overlap. The monomer frequency is indicated with a dashed line.

4.2.2 SAPT calculations

Based on the obtained DFT geometries, SAPT0 calculations were performed to estimate the interaction energy for each dimer and quantify the different contributions (see table 4.2). The results confirm the assignment of the head-to-tail dimer as the most stable structure. ZPVE is not included and might decrease the difference to the less stable head-to-head motif. The energetic ordering should not change because the additional stabilization is limited to around 5-6 kJ/mol. As expected, the interaction energy for all motifs is dominated by London dispersion counterbalanced by strong exchange repulsion. The head-to-tail motif exhibits the strongest dispersion interaction while it is around 15 % weaker for the head-to-head motif. The tail-to-tail structure is even weaker with a reduction of 35 %. Electrostatic and induction interaction also play a significant role but only account for one third of the interaction energy for all motifs. This result can be easily rationalized by the lack of polar C-X bonds ($X=\text{N}, \text{O}, \text{F}, \text{I}, \dots$) resulting in an overall weak dipole moment and polarizability.

TABLE 4.2: Results of energy decomposition analysis by SAPT0/junc-pVDZ based on geometries obtained with DFT. The values for each interaction for the respective motif are given, as well as the energy difference Δ between the motifs. All values are given in kJ/mol.

interaction	head-to-tail	head-to-head	tail-to-tail
Electrostatics	-86.7	-49.4	-45.3
Exchange	204.7	159.7	142.2
Induction	-22.8	-19.4	-13.4
Dispersion	-241.7	-202.6	-158.6
Total energy	-146.5	-111.7	-75.0
ΔE	0.0	34.8	71.4

A very interesting question is the reason for the stability of the head-to-tail over the head-to-head motif. As discussed above, the head-to-tail motif was the second most stable arrangement for the TPM and the ^tBuTPM dimers with similar energies as the head-to-head motif. The dispersion interaction is certainly the key factor influencing the stability of each motif and can be partitioned into three parts: phenyl-phenyl, methyl-methyl and phenyl-methyl. An attempt was made to quantify these parts by analyzing the average distances between the respective groups. For each monomer of a dimer AB the center of the three phenyl groups (A1-A3 and B1-B3) and the *meta*-substituents (C1-C6 and D1-D6) were located (see fig. 4.13). The *meta*-substituents are represented by the hydrogen or carbon atom in the *meta*-position of the respective benzene ring. For the phenyl-phenyl contacts, the 9 intermolecular distances between the three phenyl groups (A1-B3;B1-B3) were analyzed. Similarly, the 36 distances for the methyl-methyl contacts (C1-C6;D1-D6) and the phenyl-methyl contacts (A1-A3;D1-D6 and B1-B3;C1-C6) were obtained. In case of the TPM dimer, the hydrogen atoms in *meta*-position are assumed for the methyl groups. The intramolecular distances were excluded because they do not depend strongly on the structural motif and would skew the distribution towards a common mean. Additionally, the r^{-6} weighted average is given to include the distance dependency of the dispersion energy because closer contact contribute significantly more to the stabilization.

TABLE 4.3: Correlation of energy, dispersion and geometry for TPM, ⁱPrTPM and ^tBuTPM dimer calculated at B3LYP-D3(BJ)/def2-TZVP level. The average r^{-6} -weighted distances d between p(henyl) and m(ethyl) are given together with the regular average in brackets. All values are given in Å. The total SAPT0 energy and the dispersion contribution are given in kJ/mol.

derivative	structure	ΔE	E_{disp}	$d(p,p)$	$d(m,m)$	$d(p,m)$
TPM dimer	head-to-head	8.3	78.7	5.7 (6.6)	5.3 (8.4)	5.9 (7.6)
	head-to-tail	8.2	87.5	5.5 (6.1)	5.0 (7.6)	4.7 (6.9)
	tail-to-tail	0.0	93.0	5.4 (5.8)	4.7 (6.9)	4.5 (6.4)
ⁱ PrTPM dimer	head-to-head	34.8	202.6	5.9 (6.4)	6.4 (8.7)	6.1 (7.7)
	head-to-tail	0.0	241.7	5.7 (6.0)	5.7 (8.0)	5.2 (7.1)
	tail-to-tail	71.4	158.6	7.1 (7.4)	6.0 (8.6)	6.6 (8.0)
^t BuTPM dimer	head-to-head	0.0	253.2	6.2 (6.5)	6.6 (8.8)	6.2 (7.7)
	head-to-tail	17.1	252.0	5.9 (6.4)	6.5 (8.6)	6.0 (7.6)
	tail-to-tail	86.7	125.8	8.3 (8.7)	7.0 (9.6)	7.3 (9.2)

For the TPM dimer, the dispersion energy only results from the phenyl-phenyl interaction since no methyl groups are present in the system. Because the dispersion

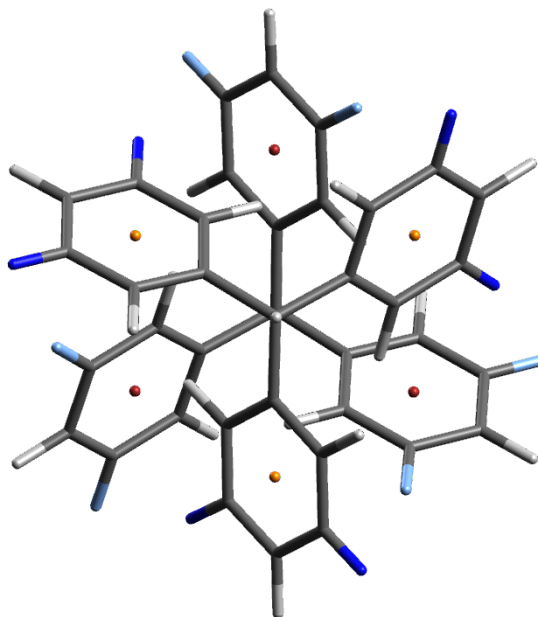


FIGURE 4.13: Visualization of the methyl and phenyl distances for the TPM dimer. The phenyl groups are represented by the orange (A1-A3) and red points (B1-B3). The methyl groups are represented by the dark blue (C1-C6) and light blue points (D1-D6).

interaction is strongly range-dependent (r^{-6}) the distance between the interacting moieties is a central parameter. Continuing this line of thought, the trend for the TPM dimer can be explained. In the absence of *meta*-substituents, the tail-to-tail motif is the ideal arrangement avoiding the Pauli repulsion of a central C-H...H-C contact while minimizing the phenyl-phenyl distance. This is not reproduced for the ⁱPrTPM and ^tBuTPM dimer due to the presence of the mentioned substituents and leads to much higher phenyl-phenyl distances. The methyl-methyl and phenyl-methyl contacts are also mostly longer explaining the worse stabilization for these derivatives. Differentiating between the head-to-head and head-to-tail motif is more difficult because the values are quite similar for all three dimers. For the ^tBuTPM dimer, the values are nearly identical for both arrangements which results in similar values for the dispersion energy according to SAPT0. In this case, referring back to section 4.1, the smaller exchange repulsion is responsible for the head-to-head preference. The smaller Pauli repulsion could be due to the ideal interlocking of the *tert*-butyl groups generating a highly symmetric structure. Considering the ⁱPrTPM dimer, the analysis is easier because all distances are slightly larger, especially the phenyl-methyl contacts which are around 1 Å shorter. Consequently, the calculated

dispersion energy is around 40 kJ/mol higher. The value of 241.7 kJ/mol is close to the values for the ^tBuTPM dimer indicating that the *iso*-propyl groups are already very potent dispersion energy donors. Nevertheless, they are not quite strong enough to achieve the ideal head-to-head motif dimer due to the stronger exchange repulsion. A closer look at the actual distribution of the distances might give further insight into the substituent-dependent preferences. Shorter contacts are much more important than longer contacts due to the strong distance dependence of London dispersion. The corresponding distributions are depicted in figures 4.14 - 4.16. The phenyl-phenyl distances for the unsubstituted TPM show the near the S₆ symmetry of the tail-to-tail motif with a tight grouping of the distances. The head-to-tail values are significantly skewed towards lower values resulting in stronger dispersion interaction which is in line with the calculated dispersion energy (87.5 kJ/mol and 78.7 kJ/mol). Adding substituents in *meta*-position strongly shifts the phenyl-phenyl distances to higher values for the tail-to-tail motif while the effect on the head-to-tail and head-to-head motif is significantly smaller. The high symmetry of the head-to-tail (ⁱPrTPM) and head-to-head motif (^tBuTPM) are again visible. The methyl-methyl and phenyl-methyl distances allow similar comparisons showing tight grouping for the symmetric structures. The stabilization of the head-to-tail motif for ⁱPrTPM can be partially explained by the "condensation" of methyl-methyl contacts to the lowest value observed in the head-to-head structure. Similarly, the ^tBuTPM dimer converges the broad distribution of the head-to-tail motif into six tight groups. Nevertheless, the neglected angle dependence of the benzene-benzene interaction could also play an important role which was not analyzed in detail. Additionally, a more granular approach considering the individual methyl groups could describe the system even better but increases the considered distances significantly complicating the discussion. Finally, it can be stated that the head-to-tail motif is not so much a "hybrid" structure between both binding motifs. The head-to-head and head-to-tail structures could be characterized as "cousins" while the tail-to-tail structure takes a special role. If any dispersion energy donors are present, only the two former motifs are competing for the global minimum. The winning structure seems certainly to be decided by the strength of the DED, weaker ones might prefer the head-to-tail motif.

Finally, the additional stabilization of each substituent can be quantified for the

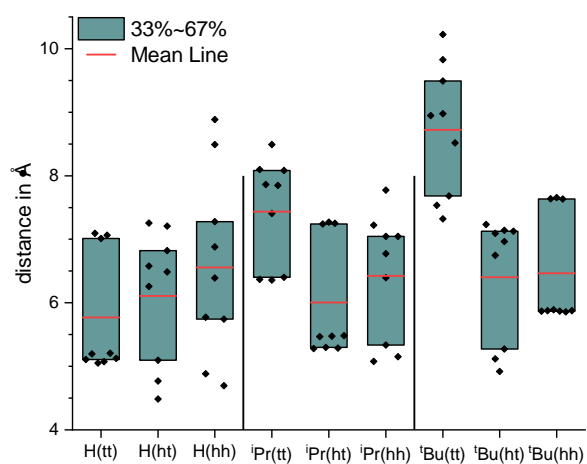


FIGURE 4.14: Box plot of the phenyl-phenyl distances for the different dimer motifs of TPM derivatives. The individual data points are represented by black points and the mean by a red line. The box describes an interval containing the middle third of the distribution.

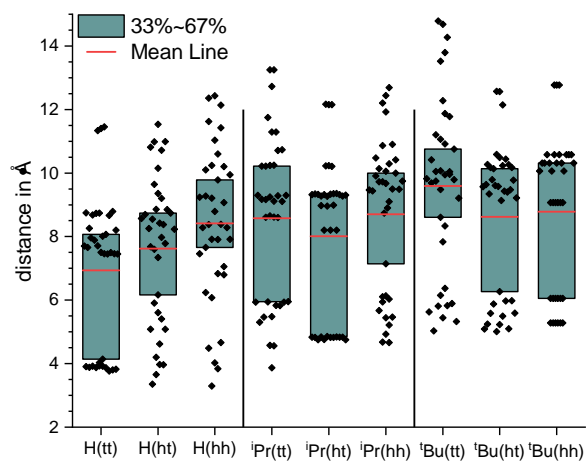


FIGURE 4.15: Box plot of the methyl-methyl distances for the head-to-head and head-to-tail motif of TPM derivatives. The individual data points are represented by black points, the mean by a red line and the median by an orange line. The box describes an interval containing the middle third of the distribution.

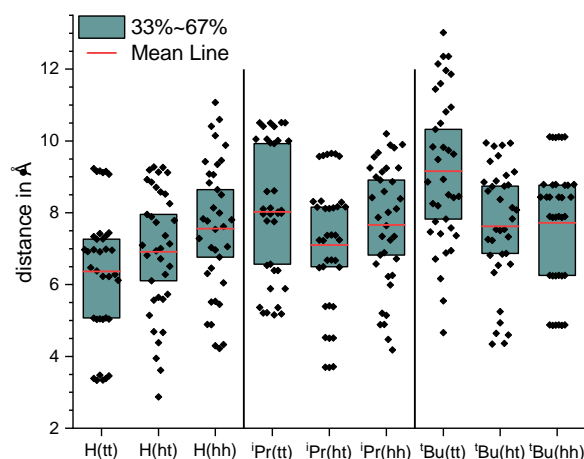


FIGURE 4.16: Box plot of the phenyl-methyl distances for the head-to-head and head-to-tail motif of TPM derivatives. The individual data points are represented by black points, the mean by a red line and the median by an orange line. The box describes an interval containing the middle third of the distribution.

ⁱPrTPM and ^tBuTPM dimer by comparing their interaction and dispersion energy with those of the unsubstituted TPM dimer using the SAPT0 values (see also publication I, appendix B). This results in 12 kJ/mol ($\frac{241.7-93.0}{12}$) additional dispersion energy for the *iso*-propyl derivative per substituent. Similarly, a value of 13 kJ/mol ($\frac{253.2-93.0}{12}$) is obtained for the *tert*-butyl derivative although the amount of methyl groups increases by 50 %. The dispersion energy in these systems is not easily additive as revealed by these values. This comparison is certainly slightly flawed because the most stable structures are compared (head-to-tail and head-to-head) but still reveals a significant "saturation" of the system. Considering, the head-to-tail motif, whose geometry is similar for all three dimers results in similar values: 13 kJ/mol ($\frac{241.7-87.5}{12}$) between TPM and ⁱPrTPM, and 14 kJ/mol between TPM and ^tBuTPM ($\frac{252.0-87.5}{12}$).

4.3 Benchmark of anharmonic frequencies

Referring back to 4.1, anharmonic vibrational frequencies are paramount to identify the head-to-head motif for the dimer of ^tBuTPM. The regular harmonic approximation for frequencies is not able to describe the Pauli repulsion between the two central

C-H bonds adequately. This leads to a significant underestimation of the resulting blueshift by a factor of around two (harmonic: 72 cm^{-1} , anharmonic: 121 cm^{-1}). The variational approach, as described in section 3.6 was successfully applied to multiple systems including phenol-(H₂O),^[256] phenol-MeOH^[257] and the water trimer.^[258] These examples focus on hydrogen-bonded OH and NH stretching frequencies. In this work, the scope is extended to the triphenylmethane dimers and CH stretching modes. Thus, it was necessary to validate this approach for the investigated dispersion-bound systems. This was done by comparing the anharmonic frequencies $\tilde{\nu}(\text{Ritz})$ with the experimental values for the TPM monomer and the tail-to-tail dimer of TPM. In both cases, the calculated anharmonic values are able to reproduce the calculated harmonic frequencies as well as the experimental values. Consequently, the application of this method for the larger ^tBuTPM dimer seemed reasonable and allowed the interpretation of the experimental spectrum. The broad, strongly blueshifted band could successfully be assigned to the head-to-head motif confirming the crystal structure and quantum chemical calculations. Interestingly, a consistent redshift of around 20 cm^{-1} was observed respective to the experimental data. Thus, the question arises whether this redshift is an effect of the variational method or caused by the triphenylmethane system. Furthermore, the power of this approach concerning predicting CH stretching is of interest. Calculating anharmonic CH frequencies for a broader range of molecules with well known literature values should elucidate both questions. The chosen molecules were supposed to fulfill a variety of characteristics: They should be small (under 20 atoms) to reduce the computational effort and well characterized to avoid errors on the side of the literature values. Furthermore, the normal modes should exhibit a range of "locality". The one-dimensional approach usually only provides a good approximation if the investigated normal mode is strongly localized meaning that a large portion of the amplitude is allotted to one atom. In the following, different frequencies are compared for this benchmark. All values refer to the energy difference $G(v=1)-G(v=0)$ which are either calculated by an anharmonic calculation $\tilde{\nu}(\text{Ritz})$ or obtained experimentally $\tilde{\nu}(\text{lit.})$. Harmonic values in the form of $\tilde{\nu}_0$ or anharmonic corrections x_e to a harmonic value are not mentioned.

The anharmonic frequency calculation is performed in the same way for each

system. A geometry optimization is performed using a Gaussian/TURBOMOLE hybrid using B3LYP-D3(BJ)/def2-TZVP (see section 3.4). A one-dimensional potential energy curve is calculated by displacing the minimum geometry along the normal mode. The potential was usually sampled in steps of 0.02 Å. The variational algorithm uses a basis of ten eigenfunctions which should result in an adequate description of the first two eigenstates resulting in a meaningful value for the $v = 0 \rightarrow v = 1$ transition. To achieve this, the potential should be calculated in a way that the maximum energy is significantly higher than the energy of the highest eigenstate ($v = 9$). Since the fundamental frequency of nearly all vibrations is under 4000 cm^{-1} , the highest eigenstate should not be over 40000 cm^{-1} as a lower bound. To improve the description, the potential curve is calculated up to the twice this value, namely 80000 cm^{-1} . This is unfortunately not possible for all cases because problems in the description of the electronic structure (SCF convergence) can occur or the dissociation energy does not exceed this value. Two approximations are made for the sampling. Firstly, the calculation is carried out by TURBOMOLE using the B3LYP_Gaussian density functional, the wrongly implemented B3LYP functional of Gaussian. This is necessary to sample the repulsive region of the potential with short interatomic distances. Secondly, no subsequent relaxation of the geometry is performed in a kind of "mean-geometry" approximation. A constrained optimization of the remaining geometry would be possible for the smaller molecules but is not feasible for larger systems as ^tBuTPM. Thus, no optimization is carried out to ensure a meaningful comparison. Afterwards, the obtained data points are interpolated with a cubic spline which is used for the variational procedure. The reduced mass of the normal mode is taken from the harmonic calculation. The used basis set (force constant) is optimized for each normal mode but is not critical in obtaining a meaningful value for the anharmonic frequency. Due to the use of ten eigenfunctions, larger deviations from the "ideal" value are tolerated. The calculated anharmonic frequencies $\tilde{\nu}(\text{Ritz})$ and the literature values $\tilde{\nu}(\text{lit.})$ with a descriptor of the vibrational mode are presented in table 4.4. The relative error $\Delta \%$ between both values is also given ($\Delta = \frac{\tilde{\nu}(\text{lit.}) - \tilde{\nu}(\text{Ritz})}{\tilde{\nu}(\text{lit.})}$).

It is noticeable that the error of the anharmonic values is quite significant for several vibrational modes, *e.g.*, for ethylene, pyrrole, ammonia or methane. The origin of this deviation is probably an unsatisfactory description of the potential energy

TABLE 4.4: Anharmonic frequencies calculated with a one-dimensional variational method. The calculations were carried out at B3LYP-D3(BJ)/def2-TZVP level.

molecule	mode	$\tilde{\nu}(\text{Ritz}) / \text{cm}^{-1}$	$\tilde{\nu}(\text{lit.}) / \text{cm}^{-1}$	$\Delta / \%$
methane ^[259]	CH sym	2994	2917	2.6
	CH asym	3100	3019	2.7
	CH asym	3163	3019	4.8
	CH asym	3213	3019	6.4
acetylene ^[259]	CH asym	3512	3289	6.8
	CH sym	3478	3374	3.1
ethylene ^[259]	CH sym	3216	2989	7.6
	CH sym	3079	3026	1.8
	CH asym	3225	3103	3.9
ammonia ^[259]	CH asym	3248	3106	4.6
	NH sym	3407	3337	2.1
	NH asym	3616	3444	5.0
methylamine ^[259]	NH asym	3690	3444	7.1
	CH sym	2877	2820	2.0
	CH sym	3032	2961	2.4
	CH asym	3170	2985	6.2
pyrrole ^[260]	NH sym	3410	3361	1.4
	NH asym	3620	3427	5.6
	CH asym	3049	3119	-2.2
	CH sym	3162	3128	1.1
	CH asym	3314	3143	5.4
water ^[259]	CH sym	3303	3149	4.9
	NH	3529	3531	0.0
	bending	1594	1595	-0.1
	OH sym	3701	3657	1.2
methanol ^[259]	OH asym	3976	3756	5.9
	OH	3654	3681	-0.7
phenol ^[261]	OH	3648	3704	-1.5
H ₂ ^[262]	HH	4169	4161	0.2
CO ^[263]	CO	2189	2143	2.2
furan ^[264]	CH asym	3326	3129	6.3
	CH sym	3264	3140	4.0
	CH asym	3347	3161	5.9
	CH sym	3237	3167	2.2
CF ₃ H ^[259]	CH	3000	3036	-1.2
CCl ₃ H ^[259]	CH	3041	3034	0.2
CBr ₃ H ^[259]	CH	3064	3042	0.7
fluoroethyne ^[259]	CH	3390	3355	1.1
chloroethyne ^[259]	CH	3389	3340	1.5
bromoethyne ^[259]	CH	3385	3325	1.8

surface (PES). This can be due to the used method because density functional theory, especially B3LYP is certainly not optimized to describe non-equilibrium geometries. Additionally, the one-dimensional approach can be problematic for vibrational modes with large amplitudes on multiple atoms. As pointed out above, an optimization of the remaining geometry would probably improve the description but can be computationally demanding and was not possible for the ^tBuTPM and ⁱPrTPM dimer. Neglecting the subsequent constrained optimization increases the energy of each calculated data point which should lead to an overall blueshift of the anharmonic frequency. This effect should be stronger for the smaller molecules where changing one or two bond lengths has the largest impact on the overall molecular geometry and energy. Comparing the calculated values with literature reveals a good agreement indicating that the anharmonic values can indeed reproduce the standard harmonic procedure for a larger variety of molecules with a slope close to 1 (see fig. 4.17). Nevertheless, a significant blue shift is present in the data expressed in the intercept of the linear regression. The blue shift exhibits a value of 63 cm^{-1} and a large error of 107 cm^{-1} . It can be stated that the general trend of the harmonic frequencies is reproduced but with significant absolute deviations showing that certain conditions have to be met to obtain useful results. Considering the origin or dependence of this error on different variables, no dependence on the overall literature frequency could be determined although the investigated window of $3000\text{ to }3800\text{ cm}^{-1}$ is certainly not large enough to derive a general statement (see figure 4.18). Analyzing the data in dependence of the locality of the normal mode, namely the largest amplitude of a single amplitude, reveals the limits of the one-dimensional approximation (see fig. 4.19). A second categorization was carried out by color coding the amount of atoms which contribute significantly to the normal mode (over 0.2). The vibrational modes which exhibit a strongly localized character meaning that one atom contributes over 90 % to the total normal mode are all within a $\pm 2\%$ window of the reference. Consequently, this group also contains all modes where only a single atom exhibits an amplitude of over 0.2. If the largest contribution decreases, the deviation increases although only two data points (NH_3 , CH_4) are available to describe the intermediate region between 0.9 and 0.6. Further decrease below 0.6 leads to a significant increase in the deviation. In this region, most vibrational modes cannot be described well in

one-dimensional manner because two atoms contribute in a meaningful way to the normal mode. For these cases, a two-dimensional approach would probably decrease the error. For even smaller values of the largest contribution below 0.3 the error increases even further. The missing multidimensionality is especially apparent investigating degenerate vibrational modes, *e.g.*, for methane and ammonia which exhibit large differences between their "degenerate" anharmonic frequencies. Nevertheless, for vibrational modes which exhibit a strong local character as is the case for the investigated alkyl dimers, the variational calculation provides a good estimate for the vibrational frequency. To reiterate on the observed red shift of the triphenylmethane system, this red shift is not observed for these well-behaved modes and is probably an effect of the system itself and not caused by a systematic methodical error.

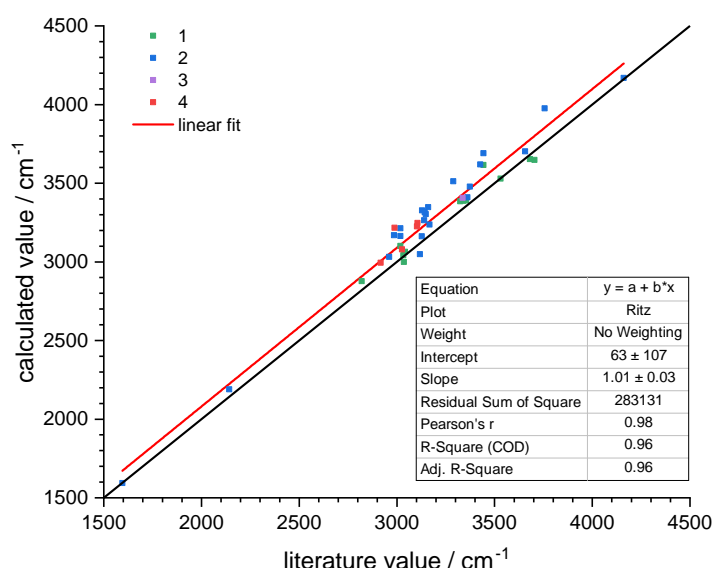


FIGURE 4.17: Comparison of anharmonic frequencies (B3LYP) with literature values. The ideal correspondence is achieved if all values lie on the bisecting straight. The amount of atoms with an amplitude of over 0.2 is indicated with different colors.

To investigate a possible influence of the used functional, the same analysis was also carried out using the Minnesota functional M06-2X^[265] with the D3-dispersion correction (see table 4.5). Becke-Johnson damping was not used because it is not currently parameterized for this functional. The M06-2X functional was chosen because it should improve upon B3LYP-D3(BJ) since it includes an additional dependence

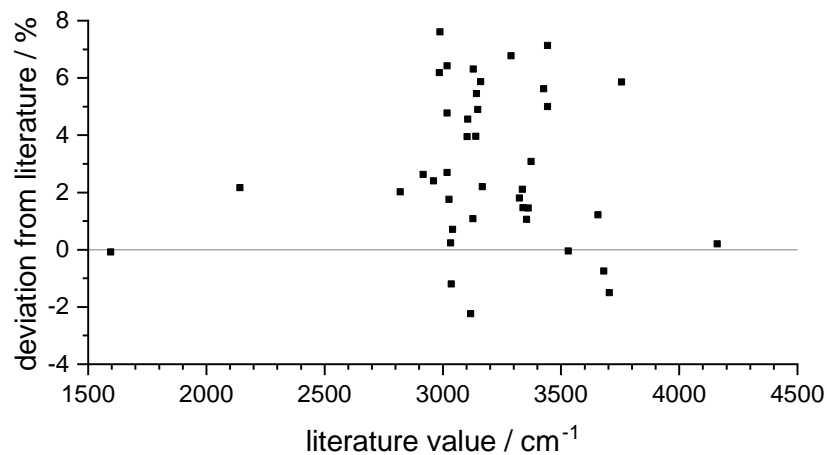


FIGURE 4.18: Deviation of anharmonic frequencies (B3LYP) from literature values.

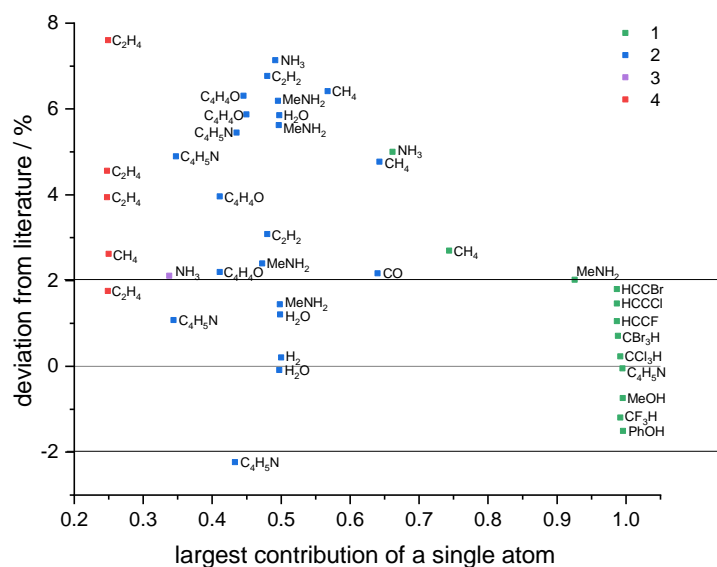


FIGURE 4.19: Deviation of anharmonic frequencies (B3LYP) from literature values in dependence of the locality of the normal mode. The amount of atoms with an amplitude of over 0.2 is indicated with different colors.

on the second derivative of the electronic density. Nevertheless, this approach gives analogous results (see figs. 4.20,4.21 and 4.22). The deviation from literature depends strongly on the locality of the mode and a significant blue shift is observed if this condition is not met. Consideration of wavefunction methods (MPn or CC) can be addressed in future work and was not carried in the scope of this thesis.

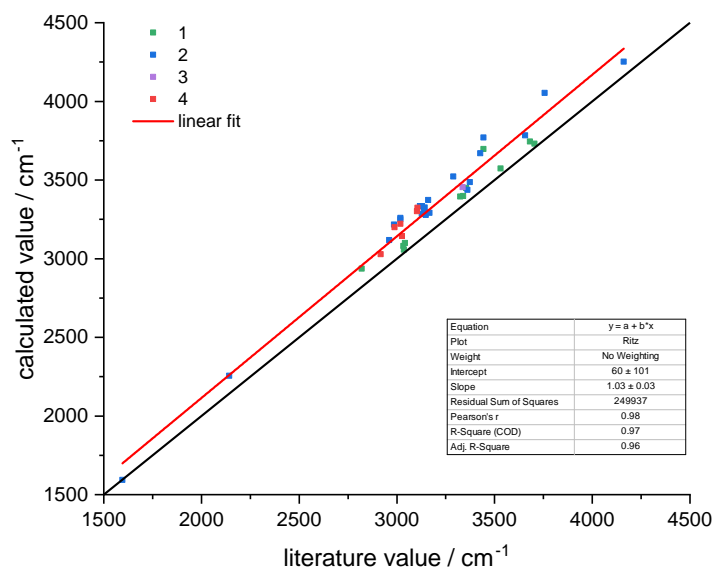


FIGURE 4.20: Comparison of anharmonic frequencies (M06-2X) with literature values. The ideal correspondence is achieved if all values lie on the bisecting straight. The amount of atoms with an amplitude of over 0.2 is indicated with different colors.

TABLE 4.5: Anharmonic frequencies calculated with a one-dimensional variational method. The calculations were carried out at the M06-2X-abD3/def2-TZVP level.

molecule	mode	$\tilde{\nu}(\text{Ritz}) / \text{cm}^{-1}$	$\tilde{\nu}(\text{lit.}) / \text{cm}^{-1}$	$\Delta / \%$
methane ^[259]	CH sym	3029	2917	3.8
	CH asym	3221	3019	6.7
	CH asym	3259	3019	7.9
	CH asym	3251	3019	7.7
acetylene ^[259]	CH asym	3523	3289	7.1
	CH sym	3486	3374	3.3
ethylene ^[259]	CH sym	3200	2989	7.1
	CH sym	3144	3026	3.9
	CH asym	3302	3103	6.4
ammonia ^[259]	CH asym	3323	3106	7.0
	NH sym	3454	3337	3.5
	NH asym	3770	3444	9.5
methylamine ^[259]	NH asym	3697	3444	7.4
	CH sym	2937	2820	4.1
	CH sym	3118	2961	5.3
	CH asym	3217	2985	7.8
pyrrole ^[260]	NH sym	3438	3361	2.3
	NH asym	3669	3427	7.1
	CH asym	3334	3119	6.9
	CH sym	3284	3128	5.0
	CH asym	3325	3143	5.8
water ^[259]	CH sym	3278	3149	4.1
	NH	3572	3531	1.2
	bending	1594	1595	-0.1
	OH sym	3783	3657	3.4
methanol ^[259]	OH asym	4053	3756	7.9
	OH	3745	3681	1.7
phenol ^[261]	OH	3732	3704	0.7
H ₂ ^[262]	HH	4251	4161	2.2
CO ^[263]	CO	2256	2143	5.3
furan ^[264]	CH asym	3333	3129	6.5
	CH sym	3300	3140	5.1
	CH asym	3373	3161	6.7
	CH sym	3290	3167	3.9
CF ₃ H ^[259]	CH	3056	3036	0.7
CCl ₃ H ^[259]	CH	3080	3034	1.5
CBr ₃ H ^[259]	CH	3099	3042	1.9
fluoroethyne ^[259]	CH	3449	3355	2.8
chloroethyne ^[259]	CH	3398	3340	1.7
bromoethyne ^[259]	CH	3394	3325	2.1

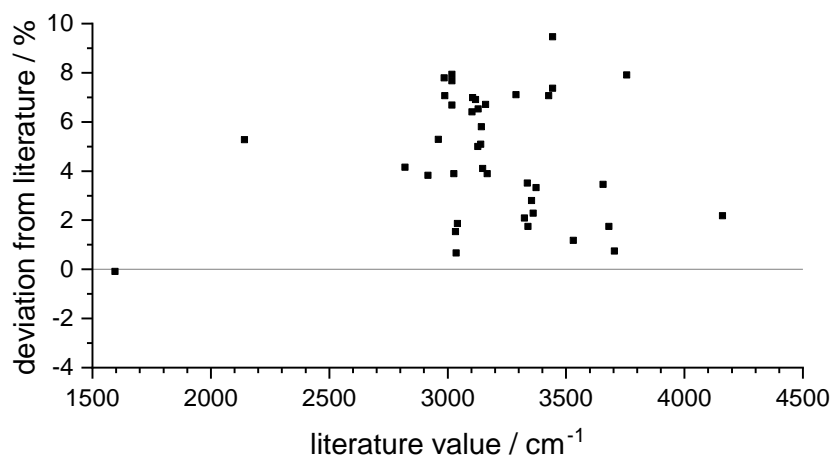


FIGURE 4.21: Deviation of anharmonic frequencies (M06-2X) from literature values.

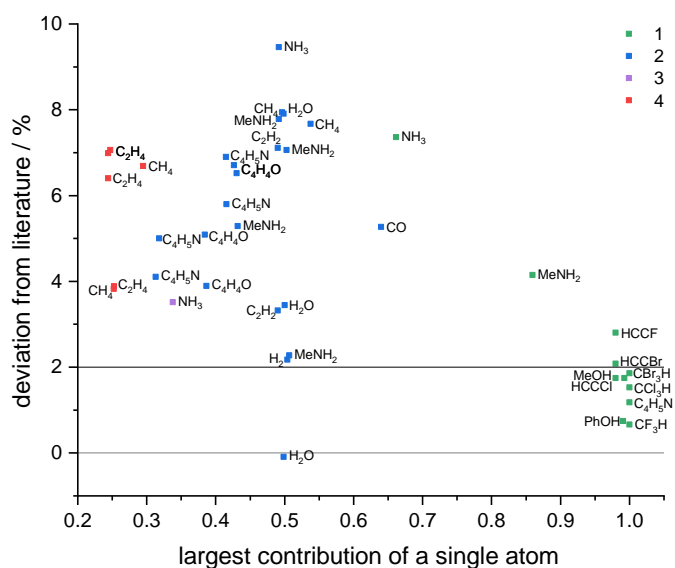


FIGURE 4.22: Deviation of anharmonic frequencies (M06-2X) from literature values in dependence of the locality of the normal mode. The amount of atoms with an amplitude of over 0.2 is indicated with different colors.

4.4 Dispersion in excited states: Chromone-methanol cluster

Prior research on aromatic ether-solvent clusters (diphenyl ether, dibenzofuran, phenyl vinyl ether)^[46–52] was very successful in probing the delicate intermolecular interactions. The resulting small energetic differences between the possible binding motifs OH-O and OH- π could be elucidated by the means of gas phase spectroscopy. The influence of London dispersion was controlled by the introduced solvent which ranged from water to adamantanol. To expand the scope of the research, the aromatic ether is swapped for an aromatic ketone, namely chromone. The chromone-methanol cluster provides, similar to the investigated ether system, two binding sites. The important difference lies in the fact that both binding sites exhibit the same binding motif (OH-O) and are located at the same functional group. The carbonyl group of the chromone molecule presents two possible docking sites (inside/outside) for alcohol molecules, in this case methanol (see fig. 4.23). The energy difference between both arrangements is small and strongly influenced by the interplay of non-covalent interactions. Thus, the chromone-methanol cluster serves as a “molecular balance”, which is studied with combined IR/R2PI and UV/IR/UV laser spectroscopy. Interpretation of the experimental data is supported by strong quantum-chemical calculations, including dispersion-corrected DFT and energy decomposition methods like SAPT0 and LED/DLPNO-CCSD(T) to investigate the non-covalent interactions, especially the role of dispersion. Since the cluster undergoes an intersystem crossing upon electronic excitation, the electronic ground (S_0) and the excited triplet state (T_1) can be probed. To the best of my knowledge, this constitutes the first structural study of a molecular cluster both in the electronic ground and electronically excited triplet state in the gas phase with laser spectroscopic methods.

The experimental results together with the quantum-chemical calculations confirm the occurrence of both outside and inside motif for the electronic ground and the excited triplet state. The energy difference comparing the S_0 and the T_1 state increases while the overall chromone-MeOH binding energy decreases. Utilizing the energy decomposition methods, it was possible to quantify the non-covalent interactions in both electronic states. Electrostatic, induction and exchange interaction are the primary factors influencing this balance and are significantly weakened in the T_1

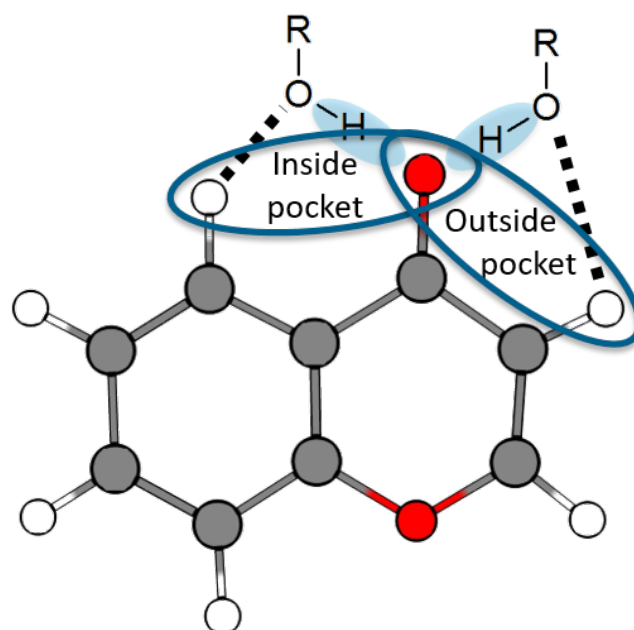


FIGURE 4.23: Schematic depiction of the chromone–solvent cluster with the “inside” and “outside” pocket, stabilized by secondary C–H···O contacts. Reproduced from Ref. [266] with permission from the PCCP Owner Societies.

state with a distinct site selectivity. This is also confirmed by the observed blueshift of the OH stretching vibration, indicating a weaker hydrogen bond. London dispersion contributes significantly to the overall binding energy, but does not influence the balance. Interestingly, contrary to the other non-covalent interactions, the dispersion interaction is only attenuated slightly when comparing the T_1 and the S_0 state.

This study serves as a first stepping stone for quantifying and understanding dispersion in the electronically excited state and should serve as inspiration for further investigations as laid out in the following section 4.5. The results of this work have been published in *Physical Chemistry Chemical Physics*, the manuscript (publication II) can be found in appendix A, page 127.

4.5 Dispersion in excited states: Cluster of chromone derivatives with methanol

4.5.1 Identification of suitable candidates

Based on the investigation performed on the chromone-methanol cluster presented in section 4.4, the chromone-methanol system was identified as a powerful model system to probe non-covalent interactions in the electronic ground and excited triplet state. To expand the scope of this model system, two possible routes can be taken. Firstly, one might change the coordinating solvent molecule from methanol to water or *tert*-butanol similar to prior investigations on aromatic ether-solvent complexes carried out in the Gerhards group.^[46,48–50,52,267] Introduction of *tert*-butanol would certainly enhance the effect of dispersion on the binding energy as was already observed.^[46] Water on the other hand would exhibit less dispersion interaction with the chromone moiety than methanol (see ref. [46]). However, another possibility of influencing this carbonyl balance is adequate derivatization of the chromone molecule. This is comparable to investigations on substituted acetophenone-solvent complexes by the Suhm group.^[268,269]

These two approaches can be certainly combined but in the context of this work the focus lies on the investigation of clusters formed by chromone derivatives and methanol. Considering unsubstituted chromone, the chromone-methanol cluster prefers occupation of the outside pocket by around 1.2 kJ/mol according to DFT in the S_0 state. The first step is to investigate whether the energy difference ΔE between both binding sites can be tuned systematically with respect to the electronic ground and excited triplet state. Finally, the goal is to swap the overall binding preference from the outside to the inside pocket or achieve an equilibrium between both motifs. This allows potent benchmarking studies probing the binding preference experimentally and subsequent comparison with quantum-chemical calculations similar to the benchmarking efforts of the Suhm group.^[54,56,126] Therefore, the accuracy of quantum-chemical methods, especially with regard to hydrogen-bonded clusters, can be improved and the role of dispersion in excited states elucidated.

At first, suitable derivatives of chromone have to be proposed. For this, the electronic situation in the chromone molecule has to be modulated in a way to selectively improve the stabilization for the inside motif. Since both motifs share the carbonyl bond, differentiation between the two free electron pairs of the carbonyl oxygen is difficult. Introduction of electron-withdrawing groups (F, CF₃, NO₂,...) could be an option, weakening the hydrogen bond. This could stabilize the inside motif because the outside motif exhibits the stronger hydrogen bond, accounting for a larger portion of the binding energy. However, the negative inductive and/or mesomeric effect could decrease the polarizability of the system, weakening the influence of dispersion. Furthermore, the newly introduced group must not provide an energetically more attractive binding site for the methanol molecule. Thus carboxylic acids, esters or amides are not feasible, restricting the possible chemical space. This approach could lead to experimental difficulties in forming the desired cluster and only increases the dispersion influence on a "second-hand" basis by destabilizing the outside motif more than the inside motif. Thus, this strategy only plays a secondary role.

This leaves the C-H...O contacts and the dispersion interaction as the primary targets to shift this balance. The main strategy employed to achieve the desired result was stabilizing the inside pocket by introducing dispersion-energy donors to the benzene ring, *e.g.*, methyl, ethyl or methoxy which can also serve as electron-donating groups increasing the electron density of the benzene ring. However, this would probably reduce the polarity of the C-H bond leading to weaker C-H...O contacts. Concerning the position of the group, the 4-pyrone ring containing the outside pocket contains a single suitable C-H group since the second one is required for the C-H...O contact. The benzene ring containing the inside pocket offers three C-H groups for substitution, enabling the introduction of multiple substituents with varying distance to the C-H...O contact and the methanol molecule in general.

Multiple derivatives were generated *in silico* and inside- and outside-bound structures were optimized with DFT/CAM-B3LYP-D3(BJ)/def2-TZVP using the Gaussian/TURBOMOLE hybrid described in section 3.4. The results of these calculations are summarized in table 4.6. The nomenclature is deviating from the IUPAC recommendation with the substituent at the 6-position mentioned first for easier comparison. Images and geometric parameters of all structures can be found in the

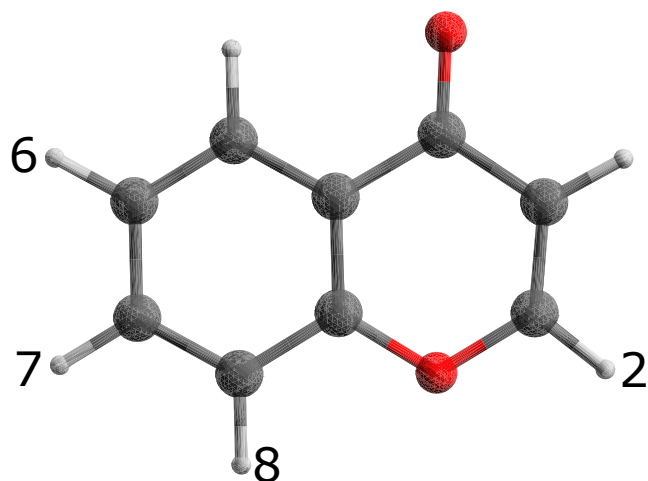


FIGURE 4.24: Structure of the unsubstituted chromone molecule with possible substitution positions.

appendix B.

TABLE 4.6: Energy difference with and without zero-point vibrational energy between inside and outside motif for multiple derivatives of chromone calculated at CAM-B3LYP-D3(BJ)/def2-TZVP level. A positive ΔE indicates preference for the outside pocket (bottom of the table) and *vice versa*. The molecules marked in bold are chosen for further investigation.

Nr.	Derivative	ΔE / kJ/mol	ΔZPE / kJ/mol
1	6-SiMe ₃ , 2-Nitro	-6.6	-5.8
2	6- ^t Bu, 2-Nitro	-6.3	-5.9
3	6-SiMe ₃	-5.2	-4.5
4	6-Methoxy	-5.0	-4.9
5	6- ^t Bu	-4.6	-4.4
6	6-Ethyl, 2-Nitro	-4.0	-3.7
7	6-Methyl, 2-Nitro	-1.6	-1.4
8	6,7,8-Methyl, 2-Nitro	-1.4	-1.3
9	6-SiH ₃ , 2-Nitro	-0.9	-0.7
10	6-Ethyl	-0.8	-0.6
11	6-Methyl, 2-CF ₃	-0.4	-0.3
12	2-Nitro	-0.2	-0.1
13	6-Methyl	-0.1	0.1
14	6,7,8-Methyl	0.0	0.5
15	6-SiH ₃	0.5	0.5
16	2-Chlor	0.9	0.9
17	7-Methyl	1.0	1.0
18	2-Fluor	1.0	0.9
19	2-CF₃	1.0	1.0
20	7-Methoxy	1.1	1.1
-	Chromone	1.2	1.2
21	2-Isocyanide	1.4	1.4
22	2-Cyanide	1.5	1.4
23	8-Methoxy	1.6	1.6
24	8-Methyl	1.7	1.7
25	2-Cyanate	1.9	1.8
26	2-Isocyanate	2.8	2.7

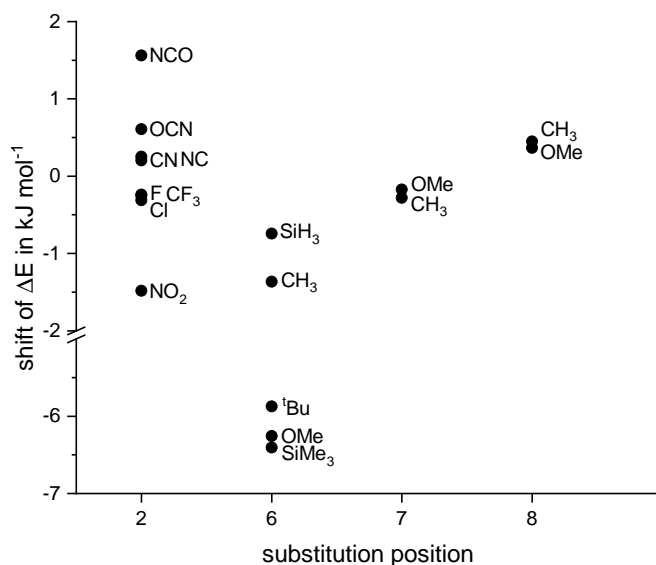


FIGURE 4.25: Change of ΔE between inside and outside pocket for different monosubstituted chromone derivatives with respect to unsubstituted chromone. Positive values indicate an increased preference for the outside pocket and *vice versa*. For better visualization of the data, the y-axis is interrupted between -2 and -5 kJ/mol.

Analyzing table 4.6 exhaustively would exceed the scope of this thesis, nevertheless several key observations can be made. Firstly, the influence of the zero-point vibrational energy (ZPVE) is quite marginal for most molecules. This indicates that the ZPVE nearly cancels and can thus be neglected in this case, similar to the results presented in section 4.4. To ease comparison, the shift in ΔE for all monosubstituted chromone derivatives has been calculated (see fig. 4.25). Introduction of alkyl or silyl groups at position 6 seems to be effective to shift the balance towards the inside pocket, especially with increasing size of the group, indicating its role as a dispersion energy donor ($\text{SiH}_3 < \text{Methyl} < \text{Ethyl} < {}^t\text{Bu} < \text{SiMe}_3$). Out of this row of derivatives, the 6-methyl derivative is predicted to be nearly equal-energetic with respect to the two binding sites, making it an ideal candidate for further investigations. Introduction of further methyl groups at position 7 or 8 does not influence the balance in the same manner: The 7- and 8-methylchromone have a similar ΔE as unsubstituted chromone, whereas the 6,7,8-methylchromone is close to the 6-methylchromone. This indicates that the dispersion interaction between the methyl group and methanol

molecule might dominate the observed additional stabilization. Consequently, substitutions at positions 7 or 8 are too far away from the methanol molecule to induce a significant stabilization since the strength of dispersion interaction decreases strongly with distance. This is also supported by analyzing the methoxy derivatives, with the 6-methoxychromone exhibiting a shift comparable to 6-*tert*-butylchromone while substitution at position 7 or 8 does not stabilize the inside motif. This supports the hypothesis that substitutions at positions 7 and 8 could be less important for this carbonyl balance, at least based on the obtained data. The dispersion effect seems to be much stronger than the changes in polarizability or the C-H...O contact. A thorough analysis of the substituent effects for chromone-MeOH cluster would require a systematic search of a pool of substituents at each position. This was not the goal of the investigation and would incur performing lots of DFT calculations (2 isomers * 4 positions * N substituents * Y optimizations). Assuming two optimizations are necessary to find the global minimum which is already quite optimistic, a data base for 8 substituents would already require 128 calculations.

This first analysis shows that the 6-position is the ideal position to influence the carbonyl balance in favor of the inside pocket. Nevertheless, with regards to disubstituted derivatives, the system can be further tuned by varying the 2-position, located in the 4-pyrone ring. The largest effect, resulting in a near-equilibrium situation, is predicted for 2-nitrochromone. Substituting the hydrogen atom with a F, CF₃ or Cl group leads to, if only, a small effect. The (iso)cyanide and (iso)cyanate even seem to shift the balance in the wrong direction. In general, the calculated shifts in ΔE are smaller than for position 6 (limited to a range of -2 to 2 kJ/mol), although it has to be noted that the investigated substituents are not the same. This can also be attributed to the restricted choice of electron-withdrawing substituents, since ester, amide or carboxyl groups were not considered. A suitable substitution combination at the 2- and 6-position can yield significant energetic shifts, as can be seen, *e.g.*, in the 6-ethyl,2-nitro derivative with an predicted ΔE of -4.0 kJ/mol. The sole 6-ethyl and 2-nitro substitutions lead to smaller ΔE values (-0.8 and -0.2). Adding the resulting shifts of 2.0 and 1.4 kJ/mol would result in a hypothetical energy of -2.2 kJ/mol for the disubstituted derivative indicating some cooperativity in the system. Analysis of these cooperative effects exceeds the scope of this work and would best be carried out

together with the aforementioned database-like approach together with experimental data to confirm the formulated hypotheses.

Finally, the goal of this search is the identification of one or more suitable chromone derivatives for further analysis, with the 6-methyl derivative being an ideal candidate. The 2-nitrochromone would also be a sensible choice but will most likely not exhibit strong dispersion interactions. A huge advantage of 6-methylchromone is the fact that it is commercially available.^[270] Nevertheless, the effect of a substituted 2-position with regards to the excited triplet state is investigated with the 2-CF₃ and combined 2-CF₃,6-methylchromone. They exhibit a smaller energy gap between both binding motifs in the electronic ground state with the CF₃ serving as a small additional increment to further shift the balance.

4.5.2 Analysis of suitable candidates

All candidate molecules (chromone, 6-methylchromone, 2-CF₃chromone and the combined 2-CF₃,6-methylchromone) were analyzed as clusters with methanol. The binding energy difference between both isomers (inside and outside) was calculated using DFT, UDFT, TD-DFT, SAPT0, DLPNO-CCSD(T), SCS-CC2 and SCS-ADC(2) to improve upon the results from the pre-screening in section above. The TD-DFT calculations are carried out using the Tamm-Dancoff approximation (see section 3.2). In the first part, the analysis of the ground state will be presented followed by an investigation of the excited triplet states. The latter part will focus on the T₁ state with regards to the energetic order of the binding motifs and the puckering of the 4-pyrone ring, which was observed for the chromone-methanol cluster (see section 4.4 and fig. 4.27). Starting geometries were generated with Avogadro^[252] and pre-optimized using the implemented force field MMFF94s.^[271] Subsequent geometry optimizations were performed using the Gaussian/TURBOMOLE hybrid for DFT, UDFT and TD-DFT. For SCS-CC2 and SCS-ADC(2), the geometry optimization was done by TURBOMOLE. All IR frequencies, spin densities, natural transition orbitals etc. were calculated using TURBOMOLE. The SAPT0 calculations were carried out using Psi4 while Orca 5.0 was used for the DLPNO-CCSD(T) results.

Analysis of the ground state (S_0)

For the ground state analysis, the energy difference between inside and outside isomer was calculated using DFT, SCS-CC2, SCS-ADC(2), SAPT0 and DLPNO-CCSD(T) with the results depicted in table 4.7. It should be noted that SCS-ADC(2) corresponds to SCS-MP2 for a ground state calculation. All energies are given as electronic energies because the influence of the ZPVE can be neglected as shown above. Otherwise, SAPT0 and DLPNO-CCSD(T) would be difficult to compare since no frequency calculation is currently possible for these methods and thus a frequency calculation of another method would have to be considered.

TABLE 4.7: Energy difference ΔE between inside and outside motif for multiple derivatives of chromone in the S_0 state calculated with different quantum chemical methods using a def2-TZVP basis set. The SAPT0 calculations are based on the final DFT geometries. A positive ΔE indicates preference for the outside pocket and *vice versa*. All values are given in kJ/mol.

ΔE with method	Chromone	6-Me	2-CF ₃	2-CF ₃ ,6-Me
DFT	1.2	-0.1	1.0	-0.4
SCS-CC2	1.6	3.1	1.5	0.0
SCS-ADC(2)	1.6	3.1	1.4	0.1
SAPT0/DFT	0.6	-0.3	2.5	-0.5
DLPNO-CCSD(T)/DFT	1.5	0.1	1.5	-0.1
DLPNO-CCSD(T)/CC2	1.5	0.1	1.3	-0.1

Generally, all methods give similar results but some deviations regarding SCS-CC2, SCS-ADC(2) and SAPT0 have to be addressed. Both SCS methods differ slightly from the results obtained by DFT, especially for the 6-methylchromone. Here, DFT predicts an isoenergetic situation (-0.1 kJ/mol), whereas SCS-CC2 and SCS-ADC(2) determine a considerable preference for the outside pocket (3.1 kJ/mol). This is not a method-specific effect, at least according to the investigated small sample, because the deviations for methanol clusters of chromone, 2-CF₃chromone and 2-CF₃,6-methylchromone are significantly smaller (around 0.5 kJ/mol). The effect of the 6-methyl group is even more puzzling when comparing the 2-CF₃ and combined 2-CF₃,6-methyl derivative since here the same substitution shifts the balance in favor of the inside pocket. The SAPT0 and especially DLPNO-CCSD(T) values should give further insight into the the "correct" values and agree with the DFT prediction, indicating that SCS-CC2 and SCS-ADC(2) might provide a worse description for the ground state

energies with respect to 6-methylchromone. Nevertheless, SAPT0 deviates slightly from all other methods for chromone and 2-CF₃chromone. DLPNO-CCSD(T) should represent the energy of the highest quality and does not exhibit a clear outlier. Thus, DLPNO-CCSD(T) is used as the benchmark energy for the electronic ground state to identify outliers of other methods. Omitting these "wrong" values, it can be stated that all methods generally agree that the 6-methyl substitution results in a shift of around 1 kJ/mol in favor of the inside pocket. Introduction of the CF₃ group achieves, if only, a small effect regarding the electronic ground state.

To shed more light on the deviations of the SCS-CC2 and SCS-ADC(2) calculations, DLPNO-CCSD(T) calculations were conducted on basis of the SCS-CC2 geometries to obtain a better description of the electronic energy. Because both methods give nearly identical values for ΔE , this analysis concentrates on the SCS-CC2 geometries, expecting similar results for SCS-ADC(2). The DLPNO-CCSD(T) results confirm that the values for the 6-methylchromone are indeed outliers. They arise from a faulty description of the electronic structure of a correct geometry since DLPNO-CCSD(T) predicts a more reasonable ΔE . Interestingly, the absolute DLPNO-CCSD(T)/CC2 energy is lower than the DLPNO-CCSD(T)/DFT energy. This indicates that the SCS-CC2 geometry is a better approximation at DLPNO-CCSD(T) level. Nevertheless, the consequence of this assessment is that SCS-CC2 and SCS-ADC(2) values have to be checked carefully and seem less robust than those obtained with DFT. This could be caused by the strong error compensation exploited by DFT methods. Thus, for easier comparison DFT will be used as the "main" method providing the geometry for the energy decomposition methods [SAPT0, LED/DLPNO-CCSD(T)].

The identification and investigation of suitable derivatives is only the first step. The following goal is the successful characterization by experiments. In reference to the IR/UV experiments conducted for the unsubstituted chromone-MeOH cluster (see section 4.4), a similar approach could be applied for these molecules. This requires that the IR frequencies for the inside and outside motif are sufficiently separated (by around 20 cm⁻¹), although this strongly depends on the actual spectrum (fragmentation effects, FWHM of the respective bands, etc.). The quantum chemical predictions show that the transitions are indeed well separated (see table 4.8). The introduction of a scaling factor for the vibrational frequencies is disregarded because

all three methods would require a separate scaling factor to compensate for the neglected anharmonicity, complicating the analysis. Additionally, derivation of a scaling factor would rely on the two measured transitions of the chromone-MeOH cluster which is quite a small data base. Nevertheless, the calculated differences are quite similar and should not change drastically upon introduction of a scaling factor (DFT value for chromone-MeOH: 0.953). This suggests that discrimination of both isomers using IR/UV laser spectroscopy seems feasible.

TABLE 4.8: OH stretching frequencies of chromone (derivative)-methanol clusters calculated with different methods. The values are given in the format X/Y, with X denoting the value for the inside motif and Y for the outside motif. All values are unscaled and are given in cm^{-1} . $\Delta(\text{method})$ describes the difference between the wavenumber of the OH stretching band for the inside and the outside motif.

$\tilde{\nu}(\text{OH})$ in cm^{-1}	Chromone	6-Methyl	2-CF ₃	2-CF ₃ ,6-Me
DFT	3649/3601	3643/3596	3675/3639	3671/3633
SCS-CC2	3673/3624	3666/3620	3693/3651	3685/3647
SCS-ADC(2)	3716/3670	3708/3667	3735/3696	3728/3691
ΔDFT	48	47	36	38
$\Delta\text{SCS-CC2}$	49	46	42	38
$\Delta\text{SCS-ADC(2)}$	46	41	39	37

The OH stretching frequencies also give a first hint concerning the binding energy of the cluster. A lower OH stretching frequency indicates a stronger hydrogen bond between the methanol and chromone (derivative) weakening the O-H bond. Consequently, it can be deduced that introduction of the methyl group does not strongly influence the hydrogen bonding because the OH stretching frequency only changes slightly. This supports the hypothesis that the methyl group mainly acts a dispersion energy donor and does not influence the hydrogen bond significantly. The CF₃ group on the other hand significantly weakens the hydrogen bond for both motifs, resulting in a blueshift of around 20 cm^{-1} . This could be due to its negative inductive effect, leading to a less polarized carbonyl group, although this is only speculative. For the combined substitution pattern, the situation is similar to the CF₃ substitution, exhibiting a blueshift of around 20 cm^{-1} with respect to chromone. Again, the methyl group does not seem to influence the hydrogen bond in a significant manner. These first observations, derived from the OH stretching frequencies, can be further investigated by analyzing the binding energy with SAPT0 and LED/DLPNO-CCSD(T) (see tables 4.9 - 4.11). SAPT0 normally only gives interaction energies

neglecting the geometric distortion of the relaxed monomers. As shown below, the geometric distortion is negligible for these systems. As a result the SAPT0 interaction energies are treated as equivalent to binding energies.

TABLE 4.9: Results of energy decomposition analysis by SAPT0/junc-cc-pVDZ based on geometries obtained with DFT. The values for each interaction for the respective motif are given, as well as the energy difference Δ between both motifs. All values are given in kJ/mol. A positive Δ refers to stabilization of the outside structure relative to the inside isomer.

	Chromone			6-Me			2-CF ₃		
	In	Out	Δ	In	Out	Δ	In	Out	Δ
Electrostatics	-57.9	-60.4	2.5	-58.3	-60.6	2.3	-54.8	-58.6	3.7
Exchange	57.5	58.7	-1.2	58.2	59.0	-0.8	54.7	55.1	-0.4
Induction	-18.2	-18.9	0.6	-18.4	-19.1	0.6	-16.9	-16.6	-0.3
Dispersion	-16.4	-15.2	-1.3	-17.8	-15.3	-2.4	-15.7	-15.2	-0.5
Total energy	-35.1	-35.7	0.6	-36.2	-35.9	-0.3	-32.7	-35.2	2.5

Comparing the values to the baseline of unsubstituted chromone, the influence of the methyl and the CF₃ group can be analyzed. Starting with 6-methylchromone, it is apparent that the situation for the outside motif does not change significantly. The effect of the methyl group is constrained to a stabilization of the inside motif by around 1 kJ/mol. This is due to an increase in the attractive dispersion interaction, supporting the first observations by analyzing the OH stretching frequency. The methyl group seems to act primarily as a dispersion energy donor, stabilizing the methanol molecule in the inside pocket. Consequently, the effect of the methyl group can be characterized as somewhat "double-local", only influencing the inside pocket and the dispersion interaction.

The CF₃ group on the other hand destabilizes the inside motif by 1.5 kJ/mol, while no significant destabilization is observed for the outside motif because the shift of 0.5 kJ/mol should be well within the accuracy of the method. However, the value for ΔE of 2.5 kJ/mol was already identified as an outlier (see table 4.7), which suggests that the destabilization for the outside motif is not modeled properly by SAPT0. This is again supported by the OH stretching frequencies, indicating that both motifs are destabilized. Of course, a blueshift in the OH stretching frequency does not need to result in a lower overall binding energy. Nevertheless, this assumption is not unfounded because the main attractive interaction is electrostatic and thus mainly due to the hydrogen bond.

TABLE 4.10: Results of energy decomposition analysis by SAPT0/jun-cc-pVDZ based on geometries obtained with DFT. The values the combined 2-CF₃,6-methylchromone for each interaction for the respective motif are given, as well as the energy difference Δ between both motifs. All values are given in kJ/mol. Positive values refer to stabilization of the outside structure relative to the inside isomer.

	6-Me			2-CF ₃ ,6-Me		
	In	Out	Δ	In	Out	Δ
Electrostatics	-58.3	-60.6	2.3	-54.5	-57.7	3.1
Exchange	58.2	59.0	-0.8	54.8	57.4	-2.6
Induction	-18.4	-19.1	0.6	-16.8	-17.2	0.5
Dispersion	-17.8	-15.3	-2.4	-17.0	-15.5	-1.5
Total energy	-36.2	-35.9	-0.3	-33.5	-33.0	-0.5

Analysis of the combined derivative should be more fruitful because the calculated ΔE agrees very well with the other methods (see table 4.7). Compared to the 6-methylchromone, the binding energy is significantly reduced for both motifs by around 3 kJ/mol which is more in line what one would expect considering the strong negative inductive effect of the CF₃ group (see table 4.10). This effect should reduce the electron density of the carbonyl group, especially the carbonyl oxygen due to the competition with the CF₃ group. Interestingly, this mostly effects the electrostatic and induction interaction which is counterbalanced by a decrease in the repulsive exchange. The dispersion interaction is weakened slightly and leads to a distinct stabilization of the inside motif. The values for the inside motif of 2-CF₃ and 2-CF₃,6-Me are comparable indicating that the values for of combined derivative are indeed described incorrectly by SAPT0 for the outside case.

To sum up, the SAPT0 results suggest that the methyl group mainly influences the dispersion interaction, specifically for the inside isomer, while the CF₃ group influences the hydrogen bond and weakens the electrostatic and induction interaction. A similar analysis was conducted using LED/DLPNO-CCSD(T), although this method does not give a specific value for the induction interaction. Nevertheless, comparisons of the overall binding energy and dispersion influence are possible (see table 4.11).

In general, the LED values are significantly smaller than the corresponding SAPT0 values. It seems that the binding energy is overestimated by SAPT0 compared to DLPNO-CCSD(T). This is not due to the neglect of the geometric preparation in the

TABLE 4.11: Results of energy decomposition analysis by LED/DLPNO-CCSD(T) based on geometries obtained with DFT. The values for each interaction for the respective motif are given, as well as the energy difference Δ between both motifs. All values are given in kJ/mol. Positive values refer to stabilization of the outside structure relative to the inside isomer. C stands for chromone (derivative), M for methanol.

	Chromone			6-Me			2-CF ₃		
	In	Out	Δ	In	Out	Δ	In	Out	Δ
Geo-prep C	0.6	0.3	0.3	0.6	0.4	0.2	0.5	0.2	0.2
Geo-prep M	0.1	0.2	-0.2	0.1	0.2	-0.2	0.0	0.2	-0.2
Geo-prep C+M	0.6	0.5	0.1	0.6	0.6	0.0	0.5	0.4	0.1
El-prep C	92.5	95.9	-3.4	94.4	96.1	-1.8	88.6	92.5	-3.9
El-prep M	82.0	81.8	0.3	82.1	82.2	-0.1	78.2	78.5	-0.3
El-prep C+M	174.6	177.7	-3.1	176.5	178.4	-1.9	166.8	171.1	-4.2
Elstat	-166.1	-171.3	5.1	-167.5	-172.1	4.6	-157.9	-162.4	4.6
Exch	-29.1	-29.1	0.0	-29.7	-29.2	-0.5	-27.8	-28.4	0.5
Non-disp	3.9	3.3	0.5	2.0	2.1	-0.1	2.4	1.5	0.9
Disp	-13.7	-12.7	-1.1	-13.3	-11.5	-1.8	-11.8	-11.5	-0.3
Triples	-2.0	-2.0	-0.1	-2.3	-2.0	-0.3	-2.0	-2.0	0.1
Total energy	-31.9	-33.4	1.5	-33.7	-33.8	0.1	-29.9	-31.4	1.5

SAPT0 method because no strong deformation takes place forming the methanol-chromone (derivative) complex. Negative values of geometric preparation are unphysical and caused by numeric errors of the DLPNO-CCSD(T) method. The non-dispersive part of the correlation energy as well as the triples correction are quite small and will thus be not discussed further. The electronic preparation incurs the largest energetic penalty but is mostly counterbalanced by subsequent electrostatic attraction and some **intermolecular** exchange. Interestingly, the LED method predicts a distinct stabilization of the inside motif by around 2 kJ/mol upon introduction of the methyl group but the dispersion contribution is less negative for both motifs. This result is a bit puzzling because substitution of a hydrogen with a methyl group should increase the dispersion contribution not decrease it. In the LED picture, the additional stabilization of the inside motif is distributed over several contributions including electrostatics, exchange, dispersive and non-dispersive part of the correlation energy as well as the triples correction. In fact, only the electronic preparation of the chromone moiety is shifted in favor of the outside motif when comparing chromone and 6-methylchromone. An explanation of the different partitioning between LED and SAPT0 is difficult to give and would certainly require a more sophisticated approach concerning the geometry of the cluster. Additionally, a complete basis set

extrapolation for DLPNO-CCSD(T) and application of DFT-SAPT or higher order SAPT methods could provide more insight but is not within the scope of this work.

Turning to the 2-CF₃chromone, the total binding energy for both motifs is reduced by 2 kJ/mol. The negative inductive effect of the CF₃ group seems to reduce the electron density of the interacting carbonyl group, especially the free electron pairs. The hydrogen bond seems to be weaker indicated by a reduced electronic preparation and subsequent electrostatic attraction. In this case, the electrostatic contribution is lowered by around 10 kJ/mol for both motifs. The decrease in the dispersion interaction mainly effecting the inside motif could be due to a reduced polarizability of the chromone moiety.

TABLE 4.12: Results of energy decomposition analysis by LED/DLPNO-CCSD(T) based on geometries obtained with DFT. The values for each interaction for the respective motif are given, as well as the energy difference Δ between both motifs. All values are given in kJ/mol. Positive values refer to stabilization of the outside structure relative to the inside isomer. C stands for chromone (derivative), M for methanol.

	6-Me			2-CF ₃ ,6-Me		
	In	Out	Δ	In	Out	Δ
Geo-prep C	0.6	0.4	0.2	0.4	0.2	0.2
Geo-prep M	0.1	0.2	-0.2	0.0	0.2	-0.2
Geo-prep C+M	0.6	0.6	0.0	0.3	0.3	0.0
El-prep C	94.4	96.1	-1.8	89.2	93.1	-3.9
El-prep M	82.1	82.2	-0.1	77.4	79.3	-1.9
El-prep C+M	176.5	178.4	-1.9	166.6	172.4	-5.8
Elstat	-167.5	-172.1	4.6	-157.2	-163.5	6.4
Exch	-29.7	-29.2	-0.5	-28.2	-28.6	0.4
Non-disp	2.0	2.1	-0.1	1.5	1.4	0.1
Disp	-13.3	-11.5	-1.8	-12.7	-11.7	-1.0
Triples	-2.3	-2.0	-0.3	-2.2	-2.1	-0.1
Total energy	-33.7	-33.8	0.1	-31.8	-31.8	-0.1

The combined substitution pattern shows similar binding energies as the 2-CF₃-chromone, analogous to the SAPT0 results. Comparing with 6-methylchromone, the introduction of the CF₃ group lowers the binding energy for both motifs by 2 kJ/mol, similar to the difference between chromone and 2-CF₃chromone. The near equilibrium between both motifs is again achieved by a delicate interplay of all interactions. The outside motif requires more electronic preparation but is compensated by the electrostatic and exchange interaction. The dispersion interaction is weaker for the inside motif while the outside motif retains the value. As speculated above, this could

be caused by a reduced polarizability of the chromone moiety.

Analysis of excited triplet states (T_1 , T_2)

Based on the ground state calculations, the excited triplet states of the clusters (chromone derivative - MeOH) were investigated with TD-DFT, UDFT, SCS-CC2, SCS-ADC(2) and SAPT0. The central questions are whether similar effects occur, namely weakening of the hydrogen-bond indicated by a blueshift of the OH stretching band and the puckering of the 4-pyrone ring. Further information about the observed changes for the chromone-methanol complex can also be found in section 4.4 (see above). With respect to the puckering, the introduction of the CF_3 group at the 2-position might influence the triplet state geometry. Due to the close proximity of the CF_3 group to the puckered atoms, the triplet state geometry could be influenced whereas the ground state was not influenced significantly. Furthermore, the behavior of the intermolecular interaction upon electronic excitation is of interest. Considering the photophysics, it is assumed that the chromone derivatives undergo a similar intersystem crossing upon electronic excitation. Itoh showed that 6-fluorochromone^[74] shows similar behavior as unsubstituted chromone so that it is reasonable to expect that at least 6-methylchromone behaves in a comparable manner. Nevertheless, only experiments would give insight into the actual photophysics of the system. A hint for the analogous behavior can be derived from the vertical electronic excitations for the electronic ground state. If the lowest electronic transitions match in energy and character, it is possible that the overall photophysics are not changed significantly. Therefore, the vertical excitation energies starting from a relaxed ground state geometry were calculated using TD-DFT (see fig. 4.26). Comparing the respective relative energies, it is apparent that the energetic landscape does not change significantly upon introduction of the methyl or CF_3 group.

Furthermore, the natural transitions orbitals (NTO) for all three derivatives were analyzed, considering the two lowest singlet and triplet states (see figs. C.27 to C.38). The NTOs are nearly identical for all three derivatives and match those of the unsubstituted chromone (see appendix A). They indicate a π, π^* character for the $S_0 \rightarrow S_2$ and $S_0 \rightarrow T_1$ transitions and a n, π^* character for the $S_0 \rightarrow S_1$ and $S_0 \rightarrow T_2$

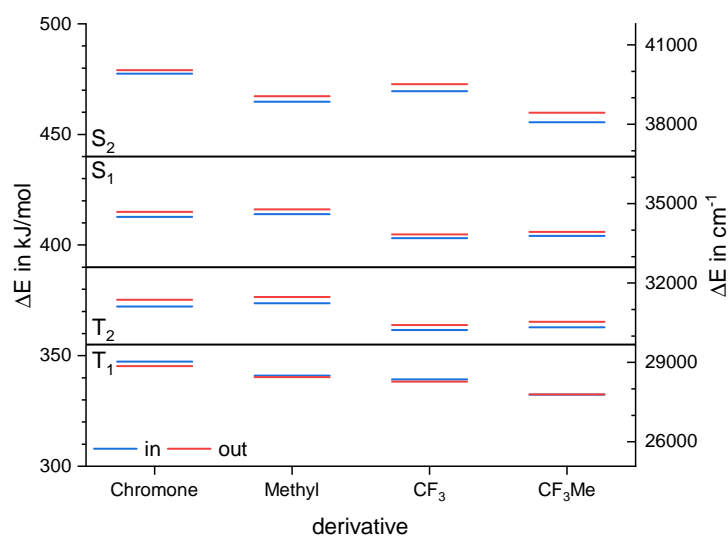


FIGURE 4.26: Jablonski term scheme for the clusters of methanol with different chromone derivatives showing the first two singlet and triplet excited states. The excited states were calculated with (TDA)-TD-DFT/CAM-B3LYP/def2-TZVP.

transitions. This rough analysis supports the assumption of a similar photophysical behavior of the investigated chromone derivatives.

At this point, it should be pointed out that the puckering of the chromone moiety leads to the situation that four possible isomers exist. Apart from the inside/outside differentiation, the puckering can also occur towards the methanol group or away from it. For the chromone-methanol cluster, the energetic difference between both structures as well as the interconversion barrier is very small (see section 4.4 and appendix A). For the sake of simplicity, only one puckered structure is considered for each binding motif (inside/outside). Usually, the structure with carbon atom puckered away from the methanol molecule is considered, as shown in fig. 4.27. In certain cases, the other structure exhibiting puckering towards the methanol molecule was obtained. These cases will be marked specifically but should not change the energy difference significantly.

Analogous to the ground state section, the energy difference for the lowest triplet state was investigated using different quantum-chemical methods (see table 4.13). To achieve this, relaxed geometries of the clusters were calculated for the outside and inside motif. In general, ΔE considerably increases compared to the ground state

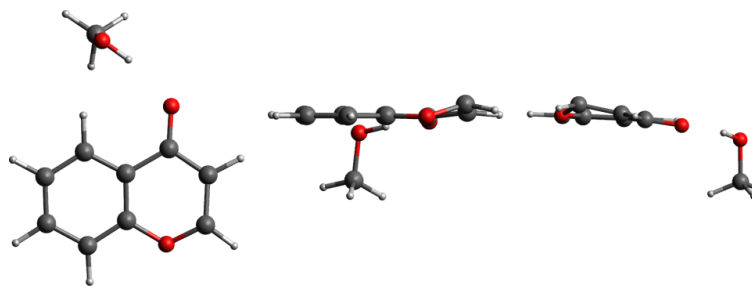


FIGURE 4.27: Geometry of the chromone-methanol cluster showing the puckering effect in the excited triplet state. The loss of planarity of the 4-pyrone ring is clearly visible in the images taken from above (left), the front (middle) and the right of (right) the cluster.

going from a nearly balanced situation to a slight preference for the outside pocket. Interestingly, the methods agree quite well and no clear outlier can be identified. In contrast to the ground state, DLPNO-CCSD(T) calculations were not performed for the triplet state. The investigation was limited to SAPT0 but can certainly be extended to include (LED/)DLPNO-CCSD(T) calculations in further work.

TABLE 4.13: Energy difference between inside and outside motif for multiple derivatives of chromone in the T_1 state calculated with different quantum chemical methods with a def2-TZVP basis set. The SAPT0 calculations are based on the final UDFT geometries. A positive ΔE indicates preference for the outside pocket and *vice versa*. All values in kJ/mol.

Method	Chromone	6-Methyl	2-CF ₃	2-CF ₃ ,6-Me
ΔE (UDFT)	3.2	1.9	2.4	0.9
ΔE (TD-DFT)	3.6	2.4 ^a	2.6	1.3
ΔE (SCS-CC2)	2.5	0.8 ^b	1.8	0.1
ΔE (SCS-ADC(2))	2.5 ^b	0.8 ^b	1.6	0.0
ΔE (SAPT0/UDFT)	2.4	1.2	2.0	-14.2

^a Both structures are planar. ^b Outside structure puckered towards methanol.

Generally, UDFT will be used as the reference geometry/energy due to its excellent performance in describing the chromone methanol cluster, especially compared to TD-DFT. TD-DFT was mainly included to describe the vertical excitation from the ground state. SCS-CC2 and SCS-ADC(2) were included to compare DFT approaches with wavefunction methods. Starting with chromone as reference, UDFT, TD-DFT and SCS-CC2 predict two puckered structures (out/in) as shown exemplary in fig. 4.27. For these methods, the geometry optimization converges without a special starting geometry into the expected puckered structure. Generally, the geometry optimization converges smoothly into a puckered structure even when a planar structure

is chosen as starting geometry. However, as will be described in the following, all methods sometimes converge to geometries which are not necessarily realistic and have problems in converging towards the correct minimum. A starting geometry close to the final geometry including considerable puckering of the 4-pyrone ring is required to converge to the right minimum structure. Already for the unsubstituted chromone-MeOH cluster, it is difficult to obtain the puckered structure with SCS-ADC(2). For the inside motif, the expected puckered structure is obtained while a weird geometry with the methanol molecule located next to the aromatic π -system is found for the outside motif (see fig. 4.28). Interestingly, the planar structure exhibits a lower energy with a ΔE of -17.0 kJ/mol compared to the puckered outside structure. Importantly, the puckered structures obtained with SCS-CC2 and SCS-ADC(2) are nearly identical to the UDFT structures and are thus not shown separately. This planar structure is most likely the result of a bad starting geometry, resulting in the optimization of a "wrong" T_x state. In this case, SCS-ADC(2) identifies a HOMO-4 to LUMO transition for the T_1 , whereas the T_1 state for the puckered structure is usually a HOMO to LUMO transition (regardless of the method). It is possible, that in the planar starting geometry the lowest triplet state is not the same as for the puckered structure resulting in the unexpected optimization behavior (see fig. 4.29). This value is thus identified as an artifact of the calculation, the low energy is probably due to an insufficient description of the highly excited triplet state. Interestingly, the D_1 diagnostic for this calculation, which describes the single-determinant character, is fine with 0.07 (see p. 31 with eq. 3.23 for details) indicating that careful checking is always necessary. The OH stretching frequency is strongly blue-shifted (3807 cm^{-1}) and is close to the one of free methanol (3836 cm^{-1}). This would indicate a very weak hydrogen bond, which is not observed in the experiment (see 4.4). It is also very difficult to imagine how the methanol and the chromone molecule are bound because a strong hydrogen bond is not realistic for this arrangement. Thus, the planar structure is discarded and the given ΔE refers to the two puckered structures. Similar artifacts with other quantum-chemical methods are observed for other chromone derivatives and will be discussed in the following.

Introducing a methyl group at position 6 leads to a shift in favor of the inside motif by around 1 kJ/mol, which is similar to the value for the electronic ground

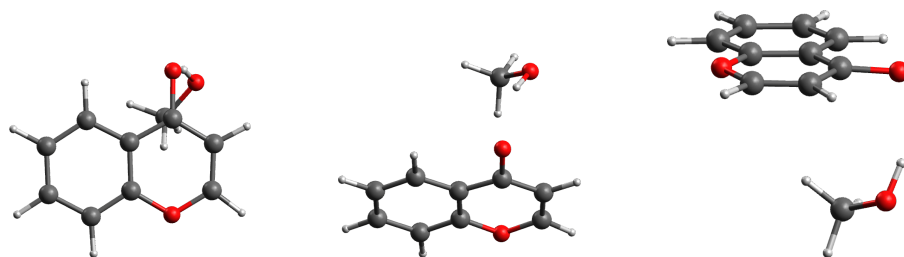


FIGURE 4.28: Planar structure of the chromone-methanol cluster calculated with SCS-ADC(2)/def2-TZVP, shown from a) above, b) the front and c) the right.

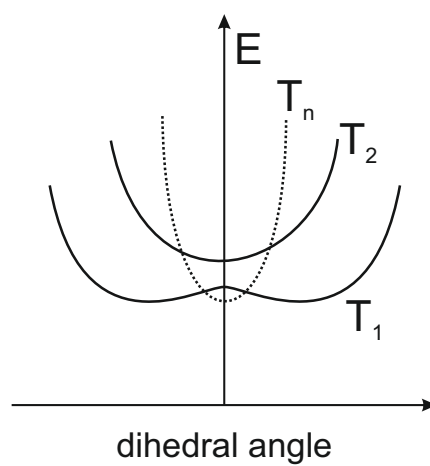


FIGURE 4.29: An exemplary cartoon explaining how for a certain starting geometry the wrong triplet state (dashed line) can be chosen as T_1 state. It is also possible that the T_n state is the T_2 state, a case which is not depicted here.

state. There, a distinct local effect was observed, which seems to be conserved in the excited triplet state. The SCS-CC2 and SCS-ADC(2) values are close together and generally prefer the inside motif by around 1 kJ/mol compared to the UDFT values for all derivatives. For 6-methylchromone, similar problems considering the minimum geometry occur as described before. UDFT, TD-DFT, SCS-CC2 and SCS-ADC(2) all predict the occurrence of planar minimum structures. For UDFT, even two different planar structures are found although both are significantly higher in energy than the puckered structures. It is probable that optimizations in the "wrong" T_1 state were carried out (see fig. 4.29). In this case, this even happened twice showing that geometry optimizations in the excited state have to be treated carefully to find the right minimum. Without the knowledge of the puckered structure for chromone-methanol, the correct starting geometry would have been difficult to guess. This shows that even quantum chemical calculations are sometimes an experiment themselves (see fig. 4.30). For structure c, the spin density is mostly localized in a p-type orbital on the carbonyl oxygen. In contrast, for structure d a significant portion of spin density is present on the benzene ring. These planar structures are only observed for the outside motif although it is possible that a specific starting geometry for the inside motif could lead to similar results. Nevertheless, the planar structures can be disregarded due to their high energy ($\Delta E > 19$ kJ/mol, see fig. 4.30). It is possible that structure c or d describes the T_2 state which is close-lying in energy but this is only speculative.

The planar geometries predicted by SCS-CC2 and SCS-ADC(2) are different to those obtained with UDFT but show strong similarities to the faulty geometry obtained for the unsubstituted chromone (see figs. 4.28 and 4.31). For SCS-CC2, this planar structure exhibits a low ΔE of only 1.5 kJ/mol (see table 4.14). This would normally suggest that this structure should be taken into consideration. Again, it has to be assumed that this triplet state is not well described which is also visible in the high D_1 diagnostic of 0.14 compared to the values for the puckered structures (both 0.10). Thus, this structure will be disregarded. For SCS-ADC2, the planar geometry is strongly preferred over the puckered structures by around 18 kJ/mol. Similarly, this value is most likely the result of a highly excited triplet state and is described insufficiently. As a result, the structure is disregarded. The D_1 diagnostic is not so

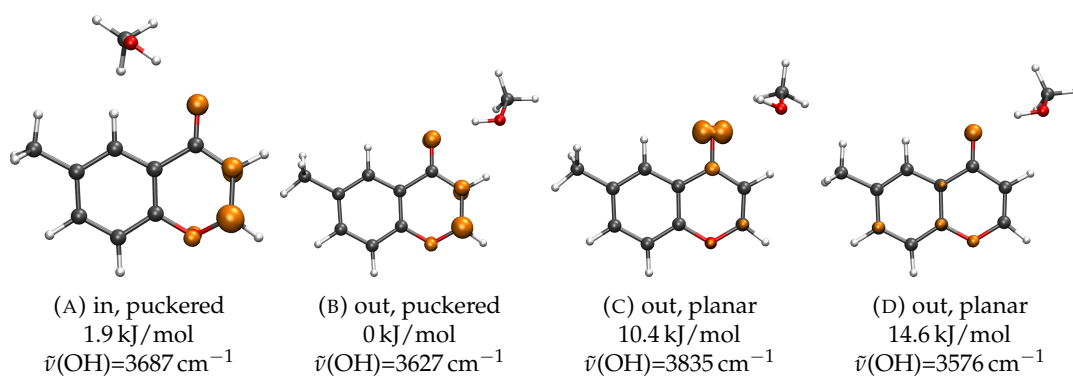


FIGURE 4.30: Structures of the 6-methylchromone-methanol cluster in the triplet state calculated with UDFT/CAM-B3LYP. The spin densities (cutoff=95 %) are shown in orange. The two structures on the left have most of the spin density distributed on the puckered carbon atoms. In contrast, the carbonyl oxygen carries most of the spin density for the outside planar structures. The relative energies and the respective OH stretching frequencies are given below the structure.

indicative in this case with a value of 0.07 compared to the values for the puckered geometry (both 0.05).

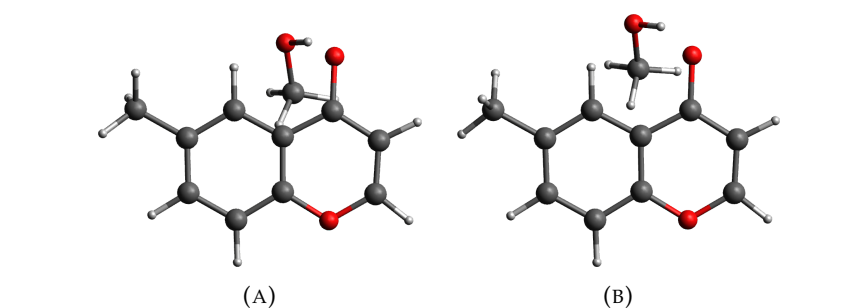


FIGURE 4.31: Planar structure of the 6-methylchromone-methanol cluster calculated with (a) SCS-CC2 and (b) SCS-ADC(2) using the basis set def2-TZVP, shown from above.

TABLE 4.14: Relative electronic energies ΔE for different structures of 6-methylchromone-methanol. All values are given in kJ/mol.

motif	SCS-CC2	SCS-ADC(2)
π , planar	1.5	0.0
in, puckered	0.8	18.2
out, puckered	0.0	17.4

TD-DFT only finds planar structures for both motifs with a energy difference of 0.8 kJ/mol between both structures. Even starting the optimization with a puckered starting geometry leads to a planar structure, which is quite confusing. Most likely, due to a small energy difference between the two lowest triplet states, their order interchanges. Though it cannot be ruled out that a specific starting geometry could

result in a puckered minimum with the "correct" order of the triplet states but this was not investigated in detail.

To sum up, 6-methylchromone seems to be a difficult case to describe with quantum chemical methods. Every method would predict a different situation if isomers with a relative energy of up to 5 kJ/mol were considered: TD-DFT predicts two planar structures, UDFT two puckered structures, SCS-CC2 two puckered and a planar inside structure and SCS-ADC(2) strongly favors a planar inside structure. 6-methylchromone is certainly an interesting candidate for experimental studies to determine for certain whether it is planar or puckered. The UV/IR/UV method could be able to distinguish between the planar and puckered structures because their OH stretching frequencies are vastly different, as shown for UDFT in figure 4.30. Similar differences are also present for TD-DFT, SCS-CC2 and SCS-ADC(2) (see table 4.15). Nevertheless, 6-methylchromone is quite problematic in the excited state according to the quantum-chemical methods. This cluster seems to be difficult to describe requiring a thorough analysis maybe even including multireference methods.

The influence of the 2-CF₃ group was insignificant for the electronic ground state but is much more pronounced for the T₁ state. All methods indicate a decrease in ΔE , which ranges from 0.4 to 1.0 kJ/mol, right on the edge of the statistical error which should be around 1 kJ/mol. Although it can be argued that the error compensation for so similar situations could be very powerful. In contrast to 6-methylchromone, no planar structure was observed for the lowest triplet state, simplifying the interpretation considerably. TD-DFT and UDFT agree nicely on a value of around 2.5 kJ/mol while the SCS-CC2 and SCS-ADC(2) predict a lower value around 1.7 kJ/mol. The SAPT0 value of 2.0 kJ/mol lies in the middle of those values, which are all within 1 kJ/mol of each other. Consequently, the introduction of the 2-CF₃ group to influence the triplet state was successful. Of course, this only constitutes one example and would certainly require experimental proof but the fact that the triplet state can be influenced specifically is quite promising. However, no special influence of the CF₃ group on the puckering or spin density could be found. The spin densities are similar to those of chromone-MeOH and 6-methylchromone-MeOH, considering the puckered structures (see fig. 4.32).

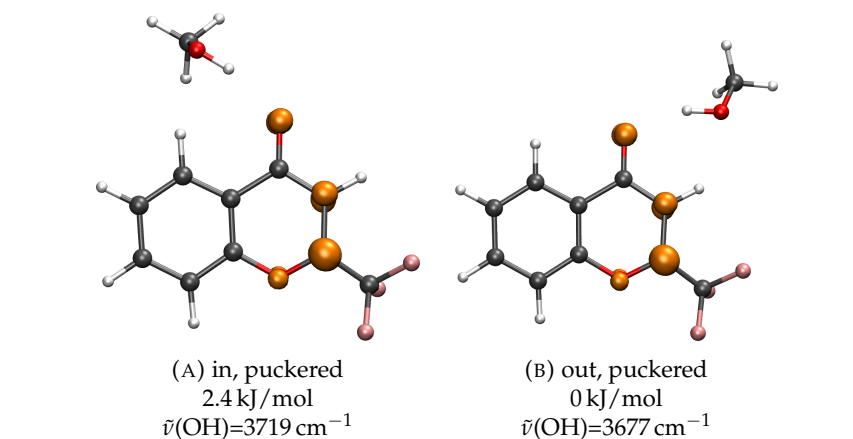


FIGURE 4.32: Structures of the 2-CF₃chromone-methanol cluster in the triplet state calculated with UDFT/CAM-B3LYP. The spin densities (cutoff=95 %) are shown in orange. The relative energies and the respective OH stretching frequencies are given below the structure.

Turning to the third derivative, the combined 2-CF₃,6-methylchromone is also predicted to shift towards the inside motif compared to the unsubstituted chromone. Analogous to the 6-methylchromone, planar minimum structures are obtained using SCS-CC2 and SCS-ADC(2) for the inside motif. These planar structures are around 20 kJ/mol higher in energy than their puckered counterparts. As described above, these structures are most likely the result of a bad starting geometry resulting in an optimization in a higher triplet state. The calculated UDFT energies are nearly additional with respect to the observed shifts for the mono-substituted derivatives. Concretely, the 6-methyl substitution leads to a shift of 1.3 kJ/mol, the 2-CF₃ substitution to a shift of 0.8 kJ/mol. The combined shift of 2.1 kJ/mol would result in a ΔE of 1.1 kJ/mol which is quite close to the observed value of 0.9 kJ/mol indicating only weak cooperativity of both groups. The spin densities are nearly identical to those shown for the other puckered structures while the IR frequencies are close to those of the 2-CF₃ derivative (see fig. 4.33).

The IR frequencies in general show a significant blueshift respective to the electronic ground state. This was also confirmed experimentally for the chromone-MeOH cluster so that the observed trend is reasonable. In table 4.15 only the IR frequencies for the puckered structures are given, except when noted otherwise. The IR frequencies of the planar structures behave unpredictably (often strongly blueshifted) and are well separated from those for the puckered structure. This excludes TD-DFT predicting only planar structures for the 6-methylchromone clusters with somewhat

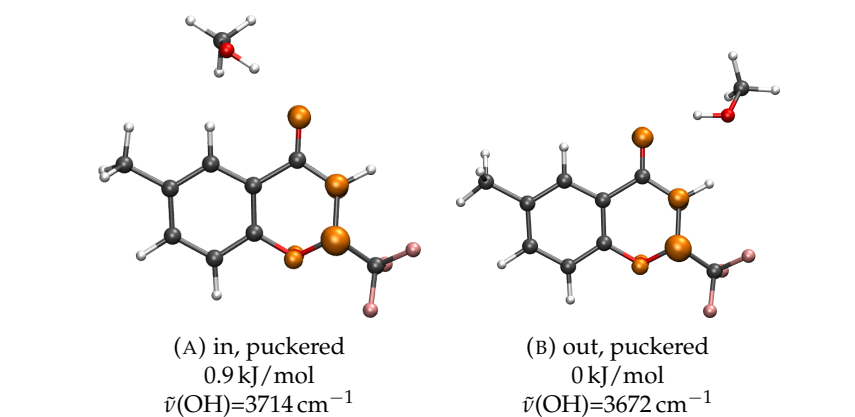


FIGURE 4.33: Structures of the 2-CF₃,6-methylchromone-methanol cluster in the lowest triplet state calculated with UDFT/CAM-B3LYP. The spin densities (cutoff=95 %) are shown in orange. The relative energies and the respective OH stretching frequencies are given below the structure.

reasonable values. Since the planar structure does not occur for every derivative or every method, a comparison of those values is not carried out. Nevertheless, if the planar structure occurs in the experiment, a discrimination using UV/IR/UV spectroscopy should be possible. Analysis of the IR frequencies in the triplet state shows that even when ΔE gets close to zero, indicating a near-equilibrium between inside and outside motif, the OH stretching frequencies are still well separated. Thus, all considered chromone derivatives should be distinguishable by combined IR/UV laser spectroscopy. Regarding spin contamination for the UDFT calculations, the amount of undesired mixing with higher order spin states can be estimated with the S^2 expectation values. No strong contamination could be observed with all S^2 values being under 2.04.

A short analysis of the binding energy for the triplet state was also performed using SAPT0 based on the UDFT geometries (see table 4.16). Only the values for the puckered structures could be obtained, for the planar structures the SCF procedure of Psi4 broke down and did not converge despite considerable effort. SAPT0 confirms that the overall binding energy is lower for the triplet state compared to the ground state. This was already visible in the blueshift of the IR frequencies. The trend derived from the energetic shifts observed for the S_0 state is reproduced in the T_1 state. Introduction of the 6-methyl group leads to a distinct stabilization of the inside motif by around 1.2 kJ/mol while the outside motif is not influenced significantly.

TABLE 4.15: OH stretching frequencies of the investigated chromone derivatives calculated with different methods. The values are given in the format X/Y, with X denoting the value for the inside motif and Y for the outside motif. All values are unscaled and are given in cm^{-1} . $\Delta(\text{method})$ describes the difference between the wavenumber of the OH stretching band for the inside and the outside motif.

$\tilde{\nu}(\text{OH})$ in cm^{-1}	Chromone	6-Methyl	2-CF ₃	2-CF ₃ ,6-Me
UDFT	3693/3632	3687/3627	3719/3677	3714/3672
TD-DFT	3682/3616	3657 ^a /3600 ^a	3714/3671	3708/3663
SCS-CC2	3706/3657	3699/3654 ^b	3722/3681	3716/3679
SCS-ADC(2)	3743/3694	3737/3693 ^b	3758/3720	3753/3717
ΔUDFT	61	60	43	42
$\Delta\text{TD-DFT}$	65	58	43	44
$\Delta\text{SCS-CC2}$	49	45	41	37
$\Delta\text{SCS-ADC(2)}$	49	44	38	36

^a Structure planar. ^b Structure puckered towards methanol.

TABLE 4.16: Results of energy decomposition analysis by SAPT0/junc-cc-pVDZ based on geometries obtained with UDFT. The values for each interaction for the respective motif are given, as well as the energy difference Δ between both motifs. All values are given in kJ/mol. Positive values refer to stabilization of the outside structure relative to the inside isomer.

	Chromone			6-Me			2-CF ₃		
	In	Out	Δ	In	Out	Δ	In	Out	Δ
Electrostatics	-43.5	-50.8	7.3	-44.1	-51.0	6.8	-41.0	-47.5	6.5
Exchange	50.4	56.5	-6.1	51.1	56.9	-5.8	47.9	53.4	-5.5
Induction	-13.5	-16.0	2.4	-13.7	-16.2	2.4	-12.4	-14.2	1.8
Dispersion	-15.2	-14.0	-1.2	-16.3	-14.1	-2.2	-14.7	-13.9	-0.7
Total energy	-21.8	-24.2	2.4	-23.0	-24.3	1.2	-20.1	-22.2	2.0

Comparison of the respective Δ for each interaction reveals that the dispersion interaction seems to be responsible for this effect. Nevertheless, the overall interaction is still dominated by the electrostatic and exchange interaction. Nevertheless, the dispersion interaction is able to play a deciding role in this carbonyl balance and can induce the same shift of around 1 kJ/mol regardless of the electronic state according to SAPT0. Turning to 2-CF₃-chromone, the outside motif is still preferred over the inside motif. Compared to chromone, only a weak shift of 0.4 kJ/mol is predicted which is within the error of the SAPT0 method. Nevertheless, the other quantum chemical methods all predict that the CF₃ group leads to a smaller ΔE between both motifs. Thus, maybe this small value can be considered somewhat realistic due to large amounts of error compensation because the two structures are so similar.

To compare the interaction strength between the two electronic states, a second table with relative values is shown below (see table 4.17). The interaction energy for the T₁ state is expressed as multiple of the corresponding value for the S₀ state. The general strength of the dispersion interaction is retained in the T₁ state, according to SAPT0. This can be seen in the high relative values of over 0.9, while all other attractive interactions are significantly weakened (electrostatics and induction). A similar side-selective effect which was observed for the chromone-MeOH cluster is also present for the mono-substituted derivatives. The modulation is much more pronounced for the inside motif than for the outside motif which might be due to the locality of the puckering effect and the spin densities being much closer to the outside pocket. A more detailed explanation of this effect can be found in the respective publication. Overall the observed modulation does not seem to depend strongly on the substitution pattern and is somewhat intrinsic to the chromone scaffold.

Unfortunately, the SAPT0 calculations for the disubstituted 2-CF₃,6-methylchromone could not be carried out successfully. This was due to unsatisfactory convergence of the HF algorithm, similar to the planar structures, and leads to unphysical values for nearly all interactions (see table 4.18). It is highly unlikely that the inside motif is 14.2 kJ/mol more stable than the outside structure. Furthermore, stronger electrostatic attraction should also result in a higher exchange repulsion which is also not observed. This clearly indicates that the SAPT0 method breaks down for this case for no obvious reason. Application of the more sophisticated LED method based on

TABLE 4.17: Results of energy decomposition analysis by SAPT0/jun-cc-pVDZ based on geometries obtained with UDFT. The values for each interaction for the respective motif are given, calculated as percentage of the S_0 value. A value close to 1 indicates that the interaction has the same strength in the T_1 state as in the electronic ground state.

	Chromone		6-Me		2-CF ₃	
	In	Out	In	Out	In	Out
Electrostatics	0.75	0.84	0.76	0.84	0.75	0.81
Exchange	0.88	0.96	0.88	0.96	0.88	0.97
Induction	0.74	0.85	0.75	0.85	0.74	0.86
Dispersion	0.93	0.92	0.92	0.92	0.93	0.91
Total energy	0.62	0.68	0.64	0.68	0.62	0.63

DLPNO-CCSD(T) might result in meaningful values for the binding energy and their decomposition due to the larger basis set used. Additionally, the HF program in Orca could also be more robust than the implementation in Psi4. This again shows that the mutual improvement and challenge of theory and experiment is vital to elucidate the effect of dispersion in the excited state.

TABLE 4.18: Results of energy decomposition analysis by SAPT0/jun-cc-pVDZ based on geometries obtained with UDFT. The values for each interaction for the respective motif are given, as well as the energy difference Δ between both motifs. All values are given in kJ/mol. Positive values refer to stabilization of the outside structure relative to the inside isomer.

	Chromone			2-CF ₃ ,6-Me		
	In	Out	Δ	In	Out	Δ
Electrostatics	-43.5	-50.8	7.3	-70.6	-65.4	-5.2
Exchange	50.4	56.5	-6.1	51.8	56.9	-5.1
Induction	-13.5	-16.0	2.4	-22.2	-19.7	-2.5
Dispersion	-15.2	-14.0	-1.2	-16.9	-15.5	-1.4
Total energy	-21.8	-24.2	2.4	-57.9	-43.7	-14.2

Finally, not only the T_1 state but also the T_2 state was analyzed using TD-DFT, SCS-CC2 and SCS-ADC(2). It is of special interest to calculate the optimized T_2 geometries to differentiate between both triplet states. For chromone-methanol, both states lie in close proximity of each other (<35 kJ/mol with TD-DFT). This could enable incomplete internal conversion into the T_2 state but this was not observed for chromone-MeOH cluster. Concerning the chromone derivatives, TD-DFT generally predicts a planar structure with strongly blueshifted OH stretching frequencies. For 2-CF₃ and 2-CF₃,6-methylchromone the optimization for the outside motif does not

converge due to oscillations. SCS-CC2 fails for all cases to converge to a local minimum. Instead, a planar geometry with two close-lying triplet states are obtained ($<20 \text{ cm}^{-1}$) which could indicate a conical intersection between the T_2 and T_1 state. SCS-ADC(2) can in some cases overcome these problems due to its symmetric formulation of the Jacobian (see section 3.3) but only reproduces the SCS-CC2 results of two close-lying triplet states.

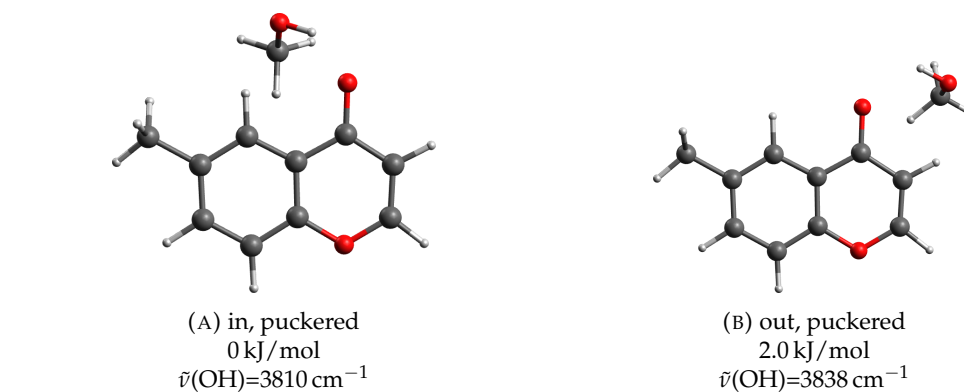


FIGURE 4.34: Structures of 6-methylchromone-methanol cluster in the T_2 state calculated with TD-DFT/CAM-B3LYP. The relative energies and the respective OH stretching frequencies are given below the structure.

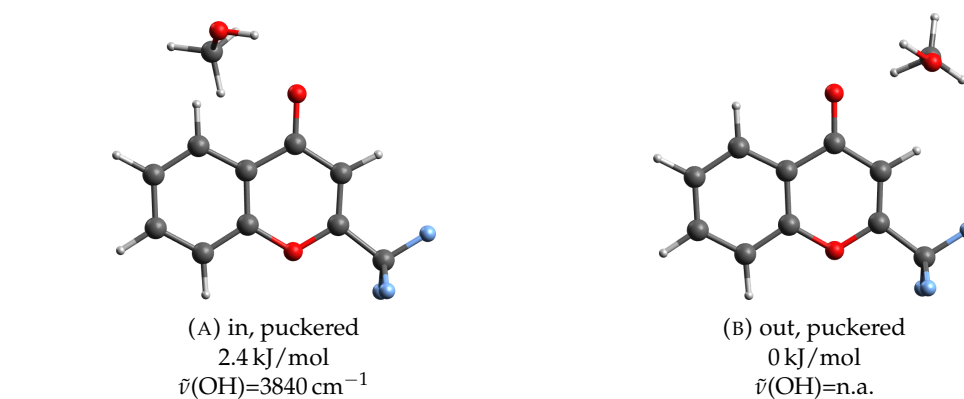


FIGURE 4.35: Structures of 2- CF_3 chromone-methanol cluster in the T_2 state calculated with TD-DFT/CAM-B3LYP. Concerning the outside motif, the calculation does not converge and oscillates. Thus, the shown structure represents the best approximation for comparison. The relative energies and the respective OH stretching frequencies are given below the structure.

To sum up the whole topic briefly, the chromone-methanol system was introduced as a molecular balance in form of a ketone-solvent cluster. The two possible binding sites allow probing the strength of $\text{CO} \cdots \text{H}$ and $\text{CH} \cdots \text{O}$ contacts. The experimental investigation with combined IR/UV methods was supported by quantum chemical

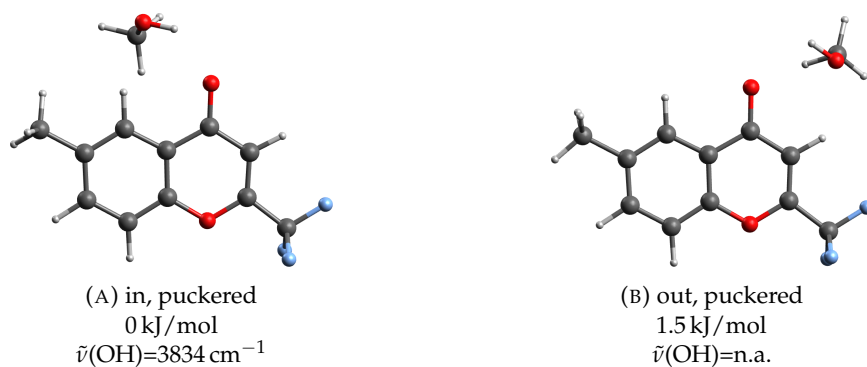


FIGURE 4.36: Structures of 2-CF₃,6-methylchromone-methanol cluster in the T₂ state calculated with TD-DFT/CAM-B3LYP. Concerning the outside motif, the calculation does not converge and oscillates. Thus, the shown structure represents the best approximation for comparison. The relative energies and the respective OH stretching frequencies are given below the structure.

calculations with DFT and UDFT resulting in a comparison of experimental and theoretical vibrational spectra. The preference for the outside pocket could be confirmed for the electronic ground state as well as the electronically excited state. The analysis of the binding energy with SAPT0 and LED/DLPNO-CCSD(T) showed that electrostatics and induction are the most important factors for the balance between both motifs. London dispersion contributes significantly but does not influence the balance in a consequential manner. The electronically excited state was identified as the T₁ state with interesting geometry changes, especially a puckering motion of a single carbon atom leading to the deplanarization of the 4-pyrone ring.

In order to expand the scope of the system, cluster of chromone derivatives with methanol were investigated *in silico*. A suitable derivative, 6-methylchromone, exhibits a nearly isoenergetic situation between both binding motifs compared to the outside preference of the unsubstituted chromone. Additionally, the 2-CF₃chromone and the disubstituted 2-CF₃,6-methylchromone were included as well to investigate the effect of a functional group at the puckered carbon atom. Application of more sophisticated theoretical methods (SCS-CC2, DLPNO-CCSD(T), SAPT0) confirmed that the methyl group in 6-position leads to a additional stabilization of the inside pocket. Furthermore, the additional stabilization is mostly concentrated in the dispersion interaction, while electrostatics and induction are not effected significantly. The description of the excited state was quite problematic for 6-methylchromone-MeOH, but the additional stabilization by London dispersion is also present in the T₁ state.

For the 2-CF₃ derivatives, the overall binding energy is lowered compared the respective unsubstituted chromone-MeOH cluster. The hypothetical influence on the geometry of the cluster in the excited triplet state could not be confirmed. Finally, the chromone-MeOH system provides an interesting starting point for investigations of London dispersion in electronically excited states. The results presented in this thesis can be understood as a first stepping stone into this interesting topic.

Chapter 5

Summary and Outlook

In this work, London dispersion interactions are investigated over multiple electronic states with experimental and quantum chemical methods.

In the first part, concentrating on strongly dispersion-bound alkyl dimers, London dispersion is examined in the electronic ground state. The model system of triphenylmethane-based dimers is introduced in order to probe the strength of dispersion with varying alkyl residues. This work was supported by a cooperation with the Schreiner group in Gießen who synthesized the ^tBuTPM molecule and its mono-deuterated variant. The cooperation with the Schreiner group is embedded in the context of the Priority Programm SPP 1807 "Control of London dispersion interactions in molecular chemistry". In principle, these molecules can adopt three different arrangements when forming a dimer: tail-to-tail, head-to-tail and head-to-head depending on the orientation of the central C-H bond (the head). For the unsubstituted TPM dimer, a tail-to-tail arrangement was identified as the most stable structure by application of combined IR/UV and stimulated Raman/UV spectroscopy. Caused by the lack of dispersion energy donors, the head-to-tail and head-to-head motif are energetically strongly disadvantaged. For the ^tBuTPM dimer, introducing *tert*-butyl groups at all *meta*-positions, a head-to-head arrangement was found for the solid structure by neutron diffraction. This crystal structure also represents the shortest measured C-H...H-C contact to date. Stimulated Raman spectroscopy was required to elucidate the gas phase structure, because the dipole moment does not change significantly during the vibration. Furthermore, due to the vast amount of CH stretching vibrations, deuteration of structure-sensitive central C-H bond was necessary to isolate those modes. An anharmonic approach describing the corresponding C-D(H)

stretching vibrations was necessary because the harmonic approximation does not describe the strong Pauli repulsion occurring in the head-to-head motif correctly. The anharmonic calculation is able to reproduce the strong blueshift observed in the experiment and led to an unambiguous assignment of the structure. Thus, the gas phase experiments confirmed that this structure is indeed stabilized by strong London dispersion interactions and is not caused by external effects, *e.g.*, packing effects. As an intermediate point, the ¹PrTPM dimer with *iso*-propyl at each *meta*-position was investigated. The *iso*-propyl group represents a weaker dispersion energy donor and prefers a head-to-tail structure according to quantum chemical calculations. Crystal structure data for the ¹PrTPM confirm the assignment of a staggered head-to-tail structure. Using symmetry-adapted perturbation theory (SAPT), the intermolecular interaction was analyzed for all systems and confirms the crucial importance of London dispersion stabilizing these systems. Especially for the ¹PrTPM and ^tBuTPM dimers, London dispersion achieves a stabilization of around 250 kJ/mol, an impressive value for a molecule of this size. Varying the dispersion energy donor, all three arrangements can take the position of the global minimum, so that the structure can indeed be controlled by dispersion.

Regarding the variational one-dimensional approach to calculate the anharmonic frequencies, a distinct validation was carried out. A database of 41 vibrational modes of 18 small, well characterized molecules exhibiting C-H, N-H and O-H stretching modes. The anharmonic values show good agreement with the benchmark data if the described vibrational mode is local in character which is true for the investigated alkyl dimers (TPM, ¹PrTPM and ^tBuTPM). The one-dimensional variational method was validated using both an internal standard (TPM and TPM dimer) and an external standard (database).

In the second part, the influence of London dispersion in the electronic ground state and the electronically excited state is probed. A molecular balance in the form of the chromone-MeOH cluster is introduced providing two similar binding sites in form of the free electron pairs of the carbonyl oxygen (inside and outside motif). Comparison of the results obtained by combined IR/UV experiments with quantum chemical calculations reveal that the outside structure is more stable in the S₀ state. Going to the T₁ state, the general structure of the cluster is retained and the outside

motif stays the global minimum. Energy decomposition analysis and the experimental data agree that the binding energy is lower than in the electronic ground state. The energy difference between both motifs is significantly increased which is attributed to the loss of planarity of the chromone molecule. The outside pocket is much more flexible and contains the vast amount of spin density while the inside pocket stays planar and rigid. The preference between both motifs is decided by the delicate interplay of intermolecular interactions with London dispersion playing a small but important role in stabilizing the inside pocket. Interestingly, electrostatic, inductive and exchange interaction are significantly weakened upon electronic excitation while the dispersion interaction retains its strength. Although it is not the deciding factor for the molecular balance, a promising model system for probing intermolecular interaction in multiple electronic states could be established.

In an attempt to expand the scope of the chromone-MeOH balance, several chromone derivatives were analyzed regarding the energetic difference to probe a larger bandwidth of energy difference between both motifs. Out of over 20 possible molecules, the 6-methylchromone was identified as an ideal candidate for further experiments. The methyl group in 6-position enables a distinct stabilization of the inside motif with dispersion which is also present for the electronically excited state. A near equilibrium situation is achieved for the electronic ground state and possible discrimination between both motifs by combined IR/UV spectroscopy is predicted. Furthermore, the 2-CF₃ and combined 2-CF₃,6-methylchromone were investigated to examine a possible coupling between the substitution pattern and the loss of planarity, but no significant effect could be determined.

Looking forward, new questions arise and old questions remain unanswered. Considering the alkyl dimers, the experimental investigation of the ¹PrTPM dimer with the combined stimulated Raman/UV methods would be very promising to confirm the assignment of the head-to-tail structure. There is also the possibility of investigating other triphenylmethane derivatives which were synthesized in the Schreiner group, e.g., molecules where the central aliphatic C-H bond is substituted by halogens (C-X) or OH (C-OH). Additionally, dimers with larger groups like cyclohexyl, phenyl and adamantyl are also possible targets for further research, computationally as well as experimentally. The identification of the small, sharp

feature in the ILSRS spectrum of the ^tBuTPM dimer remains open. It is not clear if this results from an overtone of the C-D bending vibrations or kinetic trapping of other isomers. Experimentally, this could be answered by developing a stimulated Raman/IR/UV triple resonance method, which would certainly be challenging.

The chromone-MeOH cluster opens new possibilities to investigate London dispersion in excited states. The extension of the chromone-MeOH system to include other solvents like water, ethanol, *tert*-butanol, cyclohexanol would be able to modulate the influence of London dispersion for the system. This approach can also be combined with the different chromone derivatives, especially the 6-methylchromone is a promising candidate for experimental investigations due to the site-selective stabilization. Application of more sophisticated SAPT variants for these open-shell systems should also lead to a fruitful combination of theory and experiment. The question whether the theoretical model or the experiment is right leads to a close, intertwined relationship resulting in better experimental methods as well as quantum chemical methods. Finally, this allows the interpretation of more complicated effects and phenomena which is also the reason for the chosen citation at the beginning of my thesis (“through measuring to knowledge”).

Chapter 6

Zusammenfassung und Ausblick

In dieser Arbeit wird die London-Dispersion in mehreren elektronischen Zuständen mit experimentellen und quantenchemischen Methoden untersucht.

Im ersten Teil, der sich auf stark dispersionsgebundene Alkyl-Dimere konzentriert, wird die London-Dispersion im elektronischen Grundzustand untersucht. Ein Modellsystem von Dimeren aus Triphenylmethan-Derivaten wird eingeführt, um die Stärke der Dispersion mit variierenden Alkylresten zu untersuchen. Diese Arbeit wurde durch eine Kooperation mit der Schreiner-Gruppe in Gießen unterstützt, die das ^tBuTPM-Molekül und die mono-deuterierte Variante synthetisiert hat. Die Kooperation mit der Schreiner-Gruppe ist eingebettet in das Schwerpunktprogramm SPP 1807 "Kontrolle von London-Dispersion in der molekularen Chemie". Grundsätzlich können diese Moleküle bei der Bildung eines Dimers drei verschiedene Anordnungen in Abhängigkeit der Orientierung der zentralen C-H-Bindungen (dem Kopf) einnehmen: Kopf-Kopf, Kopf-Schwanz und Schwanz-Schwanz. Für das unsubstituierte TPM-Dimer wurde durch kombinierte IR/UV- und stimulierte Raman/UV-Spektroskopie eine Schwanz-Schwanz-Anordnung als die stabilste Struktur identifiziert. Aufgrund des Fehlens von starken Dispersionsenergie-Donoren sind das Kopf-Schwanz- und das Kopf-Kopf-Motiv energetisch stark benachteiligt. Für das ^tBuTPM-Dimer, bei dem *tert*-Butylgruppen an allen *meta*-Positionen sitzen, wurde die Kristallstruktur durch Neutronenbeugung aufgeklärt. Dabei wurde eine Kopf-Kopf-Anordnung zugeordnet, die sich durch den bisher kürzesten gemessenen C-H...H-C-Kontakt in der Literatur auszeichnet. Die Verwendung der stimulierten Raman-Spektroskopie war erforderlich, um die Struktur *in vacuo* aufzuklären, da sich das Dipolmoment im Verlauf der betrachteten Schwingungen nicht signifikant

änert. Außerdem war aufgrund der großen Anzahl an CH-Streckschwingungen eine Deuterierung der struktursensiblen, zentralen C-H-Bindungen erforderlich, um diese Moden zu isolieren. Ein anharmonisches Modell zur Beschreibung der entsprechenden C-D-Streckschwingungen war notwendig, da die harmonische Näherung die starke Pauli-Abstoßung, die im Kopf-an-Kopf-Motiv auftritt, unzureichend beschreibt. Das anharmonische Modell ist in der Lage, die im Experiment beobachtete starke Blauverschiebung zu reproduzieren und ermöglichte eine eindeutige Zuordnung der Struktur. So bestätigten die Gasphasenexperimente, dass die Kopf-Kopf-Struktur tatsächlich durch starke London-Dispersionswechselwirkungen stabilisiert wird und nicht durch äußere Effekte, wie z.B. Packungseffekte, verursacht wird. Als Mittelpunkt der Dimerreihe wurde das ¹PrTPM-Dimer mit *iso*-propyl-Resten in den *meta*-Positionen untersucht. Die *iso*-propyl-Gruppe stellt einen schwächeren Dispersionsenergie-Donor als die *tert*-butyl-Gruppe dar und bevorzugt laut quantenchemischen Rechnungen eine Kopf-Schwanz-Struktur. Kristallstrukturdaten für das ¹PrTPM bestätigen die Zuordnung einer gestaffelten Kopf-Schwanz-Struktur. Mit Hilfe der symmetrieangepassten Störungstheorie (SAPT) wurden die intermolekulare Wechselwirkungen für alle Systeme analysiert. Dadurch konnte die entscheidende Bedeutung der London-Dispersion zur Stabilisierung dieser Systeme aufgezeigt werden. Insbesondere für die Dimere von ¹PrTPM und ¹BuTPM sorgt die London-Dispersion für eine Stabilisierung von etwa 250 kJ/mol, ein beeindruckender Wert für ein Molekül dieser Größe. Durch geeignete Variation des Dispersionsenergie-Donors kann jedes der drei Struktur motive als globales Minimum stabilisiert werden. Die molekulare Struktur dieser Dimere kann also, wie der Name des SPP sagt, durch Dispersion kontrolliert werden kann.

Für den eindimensionalen variationellen Ansatz zur Berechnung der anharmonischen Frequenzen wurde zunächst eine Validierung durchgeführt. Hierzu wurde eine Datenbank erstellt, welche 41 Schwingungsmoden von 18 kleinen, gut charakterisierten Molekülen, die C-H-, N-H- und O-H-Streckungsmoden aufweisen, umfasst. Die berechneten anharmonischen Werte zeigen eine gute Übereinstimmung mit den Referenzdaten, wenn die jeweilige Schwingungs mode einen stark lokalen Charakter hat, was bei den untersuchten Alkyl-Dimeren (TPM, ¹PrTPM und ¹BuTPM) der Fall ist. Die eindimensionale Variationsmethode wurde somit sowohl mit einem internen

Standard (TPM und TPM-Dimer) als auch mit einem externen Standard (Datenbank) validiert.

Im zweiten Teil wird der Einfluss der London-Dispersion im elektronischen Grundzustand und im elektronisch angeregten Zustand untersucht. Es wird eine molekulare Waage in Form des Chromon-MeOH-Clusters eingeführt, das zwei ähnliche Bindungstaschen in Form der freien Elektronenpaare des Carbonylsauerstoffes bietet (innere und äußere Tasche). Ein Vergleich der Ergebnisse kombinierter IR/UV-Experimente mit quantenchemischen Berechnungen zeigt, dass die äußere Tasche im S_0 -Zustand vom Methanol bevorzugt wird. Im T_1 -Zustand bleibt die allgemeine Struktur des Clusters erhalten und das äußere Motiv bleibt das globale Minimum. Die quantenchemische Analyse der Interaktionsenergie und die experimentellen Daten bestätigen, dass die Bindungsenergie niedriger ist als im elektronischen Grundzustand. Der Energieunterschied zwischen beiden Motiven ist erheblich größer, was auf den Verlust der Planarität des Chromonmoleküls zurückzuführen ist. Die äußere Tasche ist viel flexibler und enthält einen großen Anteil der Spindichte, während die innere Tasche planar und starr bleibt. Die Präferenz zwischen beiden Motiven wird durch das delikate Zusammenspiel der intermolekularen Wechselwirkungen bestimmt, wobei die London-Dispersion eine kleine, aber wichtige Rolle bei der Stabilisierung der inneren Tasche spielt. Interessanterweise werden Elektrostatik, Induktion und Austauschwechselwirkung bei elektronischer Anregung erheblich geschwächt, während die London-Dispersion ihre Stärke beibehält. Obwohl sie nicht der entscheidende Faktor für das molekulare Gleichgewicht ist, konnte ein vielversprechendes Modellsystem für die Untersuchung intermolekularer Wechselwirkungen in mehreren elektronischen Zuständen gefunden werden.

In einem Versuch, die Bandbreite des Chromon-MeOH-Systems zu erweitern, wurden mehrere Chromon-Derivate hinsichtlich des energetischen Unterschieds analysiert, um eine größere Bandbreite des Energieunterschieds zwischen beiden Motiven zu untersuchen. Aus über 20 formulierten Derivaten wurde das 6-Methylchromon als idealer Kandidat für weitere Experimente identifiziert. Die Methylgruppe in 6-Position ermöglicht eine signifikante Stabilisierung der inneren Tasche mittels London-Dispersion, die auch für den elektronisch angeregten Zustand vorhergesagt wird. Für den elektronischen Grundzustand wird eine nahezu äquivalente Situation

erzielt und eine mögliche experimentelle Unterscheidung zwischen beiden Isomeren durch kombinierte IR/UV-Spektroskopie vorhergesagt. Darüber hinaus wurden das 2-CF₃ und das kombinierte 2-CF₃,6-Methylchromon untersucht, um eine mögliche Kopplung zwischen dem Substitutionsmuster und dem Verlust der Planarität zu untersuchen.

Mit Blick auf die Zukunft werden neue Fragen aufgeworfen, einige alte Fragen bleiben noch unbeantwortet. Hinsichtlich der Alkyl-Dimere ist die experimentelle Untersuchung des ¹PrTPM-Dimers mit den kombinierten stimulierten Raman/UV-Methoden vielversprechend, um die Zuordnung der Kopf-Schwanz-Struktur zu bestätigen. Es besteht auch die Möglichkeit, andere Triphenylmethan-Derivate zu untersuchen, die in der Schreiner-Gruppe synthetisiert wurden, z.B. Moleküle, bei denen die zentrale aliphatische C-H Bindung durch Halogene (C-X) oder OH (C-OH) substituiert ist. Ausgehend vom TPM-Dimer, sind Dimere mit größeren Resten wie Cyclohexyl, Phenyl und Adamantyl ebenfalls mögliche Ziele für weitere Untersuchungen, sowohl quantenchemisch als auch experimentell. Die Identifikation der kleinen, scharfen Bande im ILSRS-Spektrum des ^tBuTPM-Dimers bleibt offen. Es ist nicht klar, ob hier ein Oberton der C-D-Biegeschwingungen oder das Ausfrieren weiterer Isomere vorliegt. Experimentell könnte dies durch die Entwicklung einer stimulierten Raman/IR/UV-Dreifachresonanzmethode geklärt werden, was sicherlich eine Herausforderung darstellt.

Der Chromon-MeOH-Cluster eröffnet neue Möglichkeiten zur Untersuchung der London-Dispersion in angeregten Zuständen. Durch die Erweiterung des Chromon-MeOH-Systems auf andere Lösungsmittel wie Wasser, Ethanol, Butanol und Cyclohexanol könnte der Einfluss der London-Dispersion auf das System moduliert werden. Dieser Ansatz kann auch mit den verschiedenen Chromonderivaten kombiniert werden, insbesondere das 6-Methylchromon ist aufgrund der selektiven Stabilisierung ein vielversprechender Kandidat für experimentelle Untersuchungen. Die Anwendung anspruchsvollerer SAPT-Varianten für diese Systeme mit Tripletcharakter dürfte ebenfalls zu einer fruchtbaren Kombination von Theorie und Experiment führen. Die Frage, ob das theoretische Modell oder das Experiment richtig liegt, führt zu einer engen, verflochtenen Beziehung, die zu besseren experimentellen Methoden und quantenchemischen Methoden führt. Letztlich erlaubt dies die Interpretation

komplizierterer Effekte und Phänomene, was auch der Grund für das gewählte Zitat am Anfang meiner Arbeit ist ("durch Messen zu Wissen").

Bibliography

- [1] Y.-R. Luo, *Comprehensive Handbook of Chemical Bond Energies*, CRC Press, **2007**.
- [2] J. D. van der Waals, PhD thesis, Leiden, **1873**.
- [3] P. Muller, *Pure Appl. Chem.* **1994**, *66*, 1077–1184.
- [4] P. Hobza, K. Müller-Dethlefs, *Non-covalent interactions: Theory and experiment*, Royal Society of Chemistry, Cambridge, **2010**.
- [5] K. Müller-Dethlefs, P. Hobza, *Chem. Rev.* **2000**, *100*, 143–168.
- [6] F. London, *Z. Phys.* **1930**, *63*, 245–279.
- [7] R. Eisenschitz, F. London, *Z. Phys.* **1930**, *60*, 491–527.
- [8] J. P. Wagner, P. R. Schreiner, *Angew. Chem. Int. Ed.* **2015**, *54*, 12274–12296.
- [9] N. O. B. Lüttschwager, T. N. Wassermann, R. A. Mata, M. A. Suhm, *Angew. Chem. Int. Ed.* **2013**, *52*, 463–466.
- [10] K. Autumn, M. Sitti, Y. A. Liang, A. M. Peattie, W. R. Hansen, S. Sponberg, T. W. Kenny, R. Fearing, J. N. Israelachvili, R. J. Full, *Proc. Natl. Acad. Sci. U.S.A.* **2002**, *99*, 12252–12256.
- [11] K. Autumn, P. H. Niewiarowski, J. B. Puthoff, *Annual Review of Ecology Evolution and Systematics* **2014**, *45*, 445–470.
- [12] A. P. Russell, T. E. Higham, *Proc. Biol. Sci.* **2009**, *276*, 3705–3709.
- [13] G. Huber, H. Mantz, R. Spolenak, K. Mecke, K. Jacobs, S. N. Gorb, E. Arzt, *Proc. Natl. Acad. Sci. U.S.A.* **2005**, *102*, 16293–16296.
- [14] H. Izadi, K. M. E. Stewart, A. Penlidis, *Journal of the Royal Society Interface* **2014**, *11*, 20140371.
- [15] R. Skitterians, P. Skitterians, **2015**, <https://pixabay.com/de/photos/gecko-hand-klebrig-natur-reptil-800887/>.

- [16] R. Pollice, M. Bot, I. J. Kobylanskii, I. Shenderovich, P. Chen, *J. Am. Chem. Soc.* **2017**, *139*, 13126–13140.
- [17] R. Pollice, F. Fleckenstein, I. Shenderovich, P. Chen, *Angew. Chem. Int. Ed.* **2019**, *58*, 14281–14288.
- [18] V. Gorbachev, A. Tsybizova, L. Miloglyadova, P. Chen, *J. Am. Chem. Soc.* **2022**, *144*, 9007–9022.
- [19] D. H. Zaitsau, V. N. Emel'yanenko, P. Stange, C. Schick, S. P. Verevkin, R. Ludwig, *Angew. Chem. Int. Ed.* **2016**, *55*, 11682–11686.
- [20] A.-M. Bansa, D. Paschek, D. H. Zaitsau, V. N. Emel'yanenko, S. P. Verevkin, R. Ludwig, *Chemphyschem* **2017**, *18*, 1242–1246.
- [21] D. H. Zaitsau, V. N. Emel'yanenko, P. Stange, S. P. Verevkin, R. Ludwig, *Angew. Chem. Int. Ed.* **2019**, *58*, 8589–8592.
- [22] H. Eyring, *J. Chem. Phys.* **1936**, *4*, 283–291.
- [23] R. H. Ewell, H. Eyring, *J. Chem. Phys.* **1937**, *5*, 726–736.
- [24] B. S. Harrap, E. Heymann, *Chem. Rev.* **1951**, *48*, 45–67.
- [25] F. M. Wilming, J. Becker, P. R. Schreiner, *J. Org. Chem.* **2022**, *87*, 1874–1878.
- [26] L. Rummel, M. H. J. Domanski, H. Hausmann, J. Becker, P. R. Schreiner, *Angew. Chem. Int. Ed.* **2022**, *61*, e202204393.
- [27] J. M. Schümann, J. P. Wagner, A. K. Eckhardt, H. Quanz, P. R. Schreiner, *J. Am. Chem. Soc.* **2021**, *143*, 41–45.
- [28] M. A. Strauss, H. A. Wegner, *Angew. Chem. Int. Ed.* **2019**, *58*, 18552–18556.
- [29] M. A. Strauss, H. A. Wegner, *Angew. Chem. Int. Ed.* **2021**, *60*, 779–786.
- [30] I. K. Mati, S. L. Cockroft, *Chem. Soc. Rev.* **2010**, *39*, 4195–4205.
- [31] M. A. Strauss, H. A. Wegner, *Eur. J. Org. Chem.* **2019**, *2019*, 295–302.
- [32] S. Paliwal, S. Geib, C. S. Wilcox, *J. Am. Chem. Soc.* **1994**, *116*, 4497–4498.
- [33] M. H. Lyttle, A. Streitwieser, R. Q. Kluttz, *J. Am. Chem. Soc.* **1981**, *103*, 3232–3233.
- [34] H. F. König, L. Rummel, H. Hausmann, J. Becker, J. M. Schümann, P. R. Schreiner, *J. Org. Chem.* **2022**, *87*, 4670–4679.

- [35] M. Bot, V. Gorbachev, A. Tsybizova, P. Chen, *J. Phys. Chem. A* **2020**, *124*, 8692–8707.
- [36] E. Detmar, V. Müller, D. Zell, L. Ackermann, M. Breugst, *Beilstein J. Org. Chem.* **2018**, *14*, 1537–1545.
- [37] L. Ackermann, A. Althammer, R. Born, *Angew. Chem. Int. Ed.* **2006**, *45*, 2619–2622.
- [38] A. Hansen, C. Bannwarth, S. Grimme, P. Petrović, C. Werlé, J.-P. Djukic, *ChemistryOpen* **2014**, *3*, 177–189.
- [39] G. Lu, R. Y. Liu, Y. Yang, C. Fang, D. S. Lambrecht, S. L. Buchwald, P. Liu, *J. Am. Chem. Soc.* **2017**, *139*, 16548–16555.
- [40] Q. Lu, F. Neese, G. Bistoni, *Angew. Chem. Int. Ed.* **2018**, *57*, 4760–4764.
- [41] R. C. Wende, A. Seitz, D. Niedek, S. M. M. Schuler, C. Hofmann, J. Becker, P. R. Schreiner, *Angew. Chem. Int. Ed.* **2016**, *55*, 2719–2723.
- [42] V. R. Yatham, W. Harnying, D. Kootz, J.-M. Neudörfl, N. E. Schlörer, A. Berkessel, *J. Am. Chem. Soc.* **2016**, *138*, 2670–2677.
- [43] T. Ikawa, Y. Yamamoto, A. Heguri, Y. Fukumoto, T. Murakami, A. Takagi, Y. Masuda, K. Yahata, H. Aoyama, Y. Shigeta, H. Tokiwa, S. Akai, *J. Am. Chem. Soc.* **2021**, *143*, 10853–10859.
- [44] C. Eschmann, L. Song, P. R. Schreiner, *Angew. Chem. Int. Ed.* **2021**, *60*, 4823–4832.
- [45] S. Grimme, R. Huenerbein, S. Ehrlich, *Chemphyschem* **2011**, *12*, 1258–1261.
- [46] F. Dietrich, D. Bernhard, M. Fatima, C. Pérez, M. Schnell, M. Gerhards, *Angew. Chem. Int. Ed.* **2018**, *57*, 9534–9537.
- [47] C. Medcraft, S. Zinn, M. Schnell, A. Poblitzki, J. Altnöder, M. Heger, M. A. Suhm, D. Bernhard, A. Stamm, F. Dietrich, M. Gerhards, *Phys. Chem. Chem. Phys.* **2016**, *18*, 25975–25983.
- [48] D. Bernhard, C. Holzer, F. Dietrich, A. Stamm, W. Klopper, M. Gerhards, *Chemphyschem* **2017**, *18*, 3634–3641.

- [49] D. Bernhard, F. Dietrich, M. Fatima, C. Perez, A. Poblitzki, G. Jansen, M. A. Suhm, M. Schnell, M. Gerhards, *Phys. Chem. Chem. Phys.* **2017**, *19*, 18076–18088.
- [50] D. Bernhard, M. Fatima, A. Poblitzki, A. L. Steber, C. Pérez, M. A. Suhm, M. Schnell, M. Gerhards, *Phys. Chem. Chem. Phys.* **2019**, *21*, 16032–16046.
- [51] M. Fatima, A. L. Steber, A. Poblitzki, C. Pérez, S. Zinn, M. Schnell, *Angew. Chem. Int. Ed.* **2019**, *58*, 3108–3113.
- [52] D. Bernhard, F. Dietrich, M. Fatima, C. Pérez, H. C. Gottschalk, A. Wuttke, R. A. Mata, M. A. Suhm, M. Schnell, M. Gerhards, *Beilstein J. Org. Chem.* **2018**, *14*, 1642–1654.
- [53] H. C. Gottschalk, J. Altnöder, M. Heger, M. A. Suhm, *Angew. Chem. Int. Ed.* **2016**, *55*, 1921–1924.
- [54] H. C. Gottschalk, A. Poblitzki, M. A. Suhm, M. M. Al-Mogren, J. Antony, A. A. Auer, L. Baptista, D. M. Benoit, G. Bistoni, F. Bohle, R. Dahmani, D. Firaha, S. Grimme, A. Hansen, M. E. Harding, M. Hochlaf, C. Holzer, G. Jansen, W. Klopper, W. A. Kopp, L. C. Kröger, K. Leonhard, H. Mouhib, F. Neese, M. N. Pereira, I. S. Ulusoy, A. Wuttke, R. A. Mata, *J. Chem. Phys.* **2018**, *148*, 014301.
- [55] H. C. Gottschalk, A. Poblitzki, M. Fatima, D. A. Obenchain, C. Pérez, J. Antony, A. A. Auer, L. Baptista, D. M. Benoit, G. Bistoni, F. Bohle, R. Dahmani, D. Firaha, S. Grimme, A. Hansen, M. E. Harding, M. Hochlaf, C. Holzer, G. Jansen, W. Klopper, W. A. Kopp, M. Krasowska, L. C. Kröger, K. Leonhard, M. Mogren Al-Mogren, H. Mouhib, F. Neese, M. N. Pereira, M. Prakash, I. S. Ulusoy, R. A. Mata, M. A. Suhm, M. Schnell, *J. Chem. Phys.* **2020**, *152*, 164303.
- [56] A. Poblitzki, H. C. Gottschalk, M. A. Suhm, *J. Phys. Chem. Lett.* **2017**, *8*, 5656–5665.
- [57] D. Maué, PhD thesis, Technische Universität Kaiserslautern, **2021**.
- [58] W. Meyer, *J. Chem. Phys.* **1973**, *58*, 1017–1035.
- [59] P. Pulay, H.-J. Werner, *Mol. Phys.* **2020**, *118*, e1730993.
- [60] D. I. Sharapa, J. T. Margraf, A. Hesselmann, T. Clark, *J. Chem. Theory Comput.* **2017**, *13*, 274–285.
- [61] Q. Lu, F. Neese, G. Bistoni, *Phys. Chem. Chem. Phys.* **2019**, *21*, 11569–11577.

- [62] J. A. Frey, C. Holzer, W. Klopper, S. Leutwyler, *Chem. Rev.* **2016**, *116*, 5614–5641.
- [63] A. Altun, F. Neese, G. Bistoni, *Beilstein J. Org. Chem.* **2018**, *14*, 919–929.
- [64] P. S. Zuchowski, R. Podeszwa, R. Moszyński, B. Jeziorski, K. Szalewicz, *J. Chem. Phys.* **2008**, *129*, 084101.
- [65] M. Hapka, P. S. Żuchowski, M. M. Szcześniak, G. Chałasiński, *J. Chem. Phys.* **2012**, *137*, 164104.
- [66] J. F. Gonthier, C. D. Sherrill, *J. Chem. Phys.* **2016**, *145*, 134106.
- [67] S. Bhattacharjee, M. Isegawa, M. Garcia-Ratés, F. Neese, D. A. Pantazis, *J. Chem. Theory Comput.* **2022**, *18*, 1619–1632.
- [68] V. Barone, M. Biczysko, M. Pavone, *Chem. Phys.* **2008**, *346*, 247–256.
- [69] E. A. Briggs, N. A. Besley, *Phys. Chem. Chem. Phys.* **2014**, *16*, 14455–14462.
- [70] A. Fabrizio, C. Corminboeuf, *J. Phys. Chem. Lett.* **2018**, *9*, 464–470.
- [71] X. Feng, A. Otero-de-la-Roza, E. R. Johnson, *Can. J. Chem.* **2018**, *96*, 730–737.
- [72] Y. Ikabata, H. Nakai, *J. Chem. Phys.* **2012**, *137*, 124106.
- [73] K. Bartl, A. Funk, M. Gerhards, *Chemphyschem* **2009**, *10*, 1882–1886.
- [74] T. Itoh, *J. Photochem. Photobiol. A: Chem.* **2010**, *214*, 10–15.
- [75] A. C. Hancock, L. Goerigk, *RSC Adv.* **2022**, *12*, 13014–13034.
- [76] E. Gloaguen, M. Mons, K. Schwing, M. Gerhards, *Chem. Rev.* **2020**, *120*, 12490–12562.
- [77] S. Bakels, M.-P. Gaigeot, A. M. Rijs, *Chem. Rev.* **2020**, *120*, 3233–3260.
- [78] A. M. Rijs, J. Oomens, *Top. Curr. Chem.* **2015**, *364*, 1–42.
- [79] K. Schwing, M. Gerhards, *Bunsen-Magazin* **2014**, *16*, 116–131.
- [80] K. Schwing, M. Gerhards, *Int. Rev. Phys. Chem.* **2016**, *35*, 569–677.
- [81] D. L. Feldman, R. K. Lengel, R. N. Zare, *Chem. Phys. Lett.* **1977**, *52*, 413–417.
- [82] U. Boesl, H. J. Neusser, E. W. Schlag, *Z. Naturforsch. A.* **1978**, *33*, 1546–1548.
- [83] L. Zandee, R. B. Bernstein, *J. Chem. Phys.* **1979**, *71*, 1359–1371.

- [84] T. R. Rizzo, Y. D. Park, L. Peteanu, D. H. Levy, *J. Chem. Phys.* **1985**, *83*, 4819–4820.
- [85] E. Condon, *Phys. Rev.* **1926**, *28*, 1182–1201.
- [86] J. Franck, E. G. Dymond, *Trans. Faraday Soc.* **1926**, *21*, 536.
- [87] E. U. Condon, *Phys. Rev.* **1928**, *32*, 858–872.
- [88] S. Tanabe, T. Ebata, M. Fujii, N. Mikami, *Chem. Phys. Lett.* **1993**, *215*, 347–352.
- [89] T. Ebata, A. Fujii, N. Mikami, *Int. J. Mass Spectrom. Ion Processes* **1996**, *159*, 111–124.
- [90] J. R. Carney, F. C. Hagemeister, T. S. Zwier, *J. Chem. Phys.* **1998**, *108*, 3379–3382.
- [91] R. H. Page, Y. R. Shen, Y. T. Lee, *J. Chem. Phys.* **1988**, *88*, 4621–4636.
- [92] C. Riehn, C. Lahmann, B. Wassermann, B. Brutschy, *Chem. Phys. Lett.* **1992**, *197*, 443–450.
- [93] L. Snoek, E. Robertson, R. Kroemer, J. Simons, *Chem. Phys. Lett.* **2000**, *321*, 49–56.
- [94] C. Unterberg, A. Gerlach, T. Schrader, M. Gerhards, *J. Chem. Phys.* **2003**, *118*, 8296–8300.
- [95] M. Gerhards, S. Schumm, C. Unterberg, K. Kleinermanns, *Chem. Phys. Lett.* **1998**, *294*, 65–70.
- [96] P. M. Palmer, Y. Chen, M. R. Topp, *Chem. Phys. Lett.* **2000**, *318*, 440–447.
- [97] J. A. Stearns, A. Das, T. S. Zwier, *Phys. Chem. Chem. Phys.* **2004**, *6*, 2605.
- [98] K. Bartl, A. Funk, M. Gerhards, *J. Chem. Phys.* **2008**, *129*, 234306.
- [99] P. Esherick, A. Owyong, *Chem. Phys. Lett.* **1983**, *103*, 235–240.
- [100] P. Esherick, A. Owyong, J. Plíva, *J. Chem. Phys.* **1985**, *83*, 3311–3317.
- [101] G. V. Hartland, B. F. Henson, V. A. Venturo, R. A. Hertz, P. M. Felker, *J. Opt. Soc. Am. B* **1990**, *7*, 1950.
- [102] P. M. Felker, P. M. Maxton, M. W. Schaeffer, *Chem. Rev.* **1994**, *94*, 1787–1805.
- [103] A. Golan, N. Mayorkas, S. Rosenwaks, I. Bar, *J. Chem. Phys.* **2009**, *131*, 024305.
- [104] N. Mayorkas, I. Malka, I. Bar, *Phys. Chem. Chem. Phys.* **2011**, *13*, 6808–6815.

- [105] A. Shachar, N. Mayorkas, I. Bar, *Phys. Chem. Chem. Phys.* **2017**, *19*, 23999–24008.
- [106] A. Shachar, I. Kallos, M. S. de Vries, I. Bar, *J. Phys. Chem. Lett.* **2021**, *12*, 11273–11279.
- [107] D. Maué, P. H. Strebert, D. Bernhard, S. Rösel, P. R. Schreiner, M. Gerhards, *Angew. Chem. Int. Ed.* **2021**, *60*, 11305–11309.
- [108] G. Eckhardt, R. W. Hellwarth, F. J. McClung, S. E. Schwarz, D. Weiner, E. J. Woodbury, *Phys. Rev. Lett.* **1962**, *9*, 455–457.
- [109] M. Hippler, M. Quack, *Chem. Phys. Lett.* **1994**, *231*, 75–80.
- [110] T. Omi, H. Shitomi, N. Sekiya, K. Takazawa, M. Fujii, *Chem. Phys. Lett.* **1996**, *252*, 287–293.
- [111] S.-i. Ishiuchi, H. Shitomi, K. Takazawa, M. Fujii, *Chem. Phys. Lett.* **1998**, *283*, 243–250.
- [112] B. Fehrensens, M. Hippler, M. Quack, *Chem. Phys. Lett.* **1998**, *298*, 320–328.
- [113] C. Unterberg, A. Jansen, M. Gerhards, *J. Chem. Phys.* **2000**, *113*, 7945–7954.
- [114] L. Dunoyer, *J. phys. radium* **1911**, *8*, 142–146.
- [115] O. Stern, *Z. Phys.* **1926**, *39*, 751–763.
- [116] A. Kantrowitz, J. Grey, *Rev. Sci. Instrum.* **1951**, *22*, 328–332.
- [117] R. E. Smalley, L. Wharton, D. H. Levy, *Acc. Chem. Res.* **1977**, *10*, 139–145.
- [118] D. H. Levy, *Annu. Rev. Phys. Chem.* **1980**, *31*, 197–225.
- [119] G. Meijer, M. S. de Vries, H. E. Hunziker, H. R. Wendt, *Appl. Phys. B* **1990**, *51*, 395–403.
- [120] W. Demtröder in *Laserspektroskopie 2*, (Ed.: W. Demtröder), Springer Berlin Heidelberg, Berlin, Heidelberg, **2013**, p. 149.
- [121] W. C. Wiley, I. H. McLaren, *Rev. Sci. Instrum.* **1955**, *26*, 1150–1157.
- [122] L. Goerigk, S. Grimme, *J. Chem. Theory Comput.* **2011**, *7*, 291–309.
- [123] N. O. C. Winter, N. K. Graf, S. Leutwyler, C. Hättig, *Phys. Chem. Chem. Phys.* **2013**, *15*, 6623–6630.
- [124] S. Grimme, M. Steinmetz, *Phys. Chem. Chem. Phys.* **2013**, *15*, 16031–16042.

- [125] R. A. Mata, M. A. Suhm, *Angew. Chem. Int. Ed.* **2017**, *56*, 11011–11018.
- [126] T. L. Fischer, M. Bödecker, A. Zehnacker-Rentien, R. A. Mata, M. A. Suhm, *Phys. Chem. Chem. Phys.* **2022**, *24*, 11442–11454.
- [127] W. Kutzelnigg, *Einführung in die Theoretische Chemie*, Wiley-VCH Verlag, Weinheim, **2002**, <http://onlinelibrary.wiley.com/book/10.1002/9783527663804>.
- [128] A. Szabo, N. S. Ostlund, *Modern Quantum Chemistry: Introduction to Advanced Electronic Structure Theory*, Dover Publications, Newburyport, **2012**, <http://subhh.ebib.com/patron/FullRecord.aspx?p=1894806>.
- [129] D. A. McQuarrie, *Quantum Chemistry*, VIVA Books, **2016**.
- [130] P. Hohenberg, W. Kohn, *Phys. Rev.* **1964**, *136*, B864–B871.
- [131] W. Kohn, L. J. Sham, *Phys. Rev.* **1965**, *140*, A1133–A1138.
- [132] J. P. Perdew, K. Burke, M. Ernzerhof, *Phys. Rev. Lett.* **1997**, *78*, 1396.
- [133] Becke, *Phys. Rev. A* **1988**, *38*, 3098–3100.
- [134] Lee, Yang, Parr, *Phys. Rev. B Condens. Matter* **1988**, *37*, 785–789.
- [135] P. J. Stephens, F. J. Devlin, C. F. Chabalowski, M. J. Frisch, *J. Phys. Chem.* **1994**, *98*, 11623–11627.
- [136] A. D. Becke, *J. Chem. Phys.* **1993**, *98*, 5648–5652.
- [137] D. J. Tozer, R. D. Amos, N. C. Handy, B. O. Roos, L. Serrano-ANDRES, *Mol. Phys.* **1999**, *97*, 859–868.
- [138] A. Dreuw, J. L. Weisman, M. Head-Gordon, *J. Chem. Phys.* **2003**, *119*, 2943–2946.
- [139] A. Dreuw, M. Head-Gordon, *J. Am. Chem. Soc.* **2004**, *126*, 4007–4016.
- [140] Y. Tawada, T. Tsuneda, S. Yanagisawa, T. Yanai, K. Hirao, *J. Chem. Phys.* **2004**, *120*, 8425–8433.
- [141] T. Yanai, D. P. Tew, N. C. Handy, *Chem. Phys. Lett.* **2004**, *393*, 51–57.
- [142] S. Grimme, J. Antony, S. Ehrlich, H. Krieg, *J. Chem. Phys.* **2010**, *132*, 154104.
- [143] S. Grimme, S. Ehrlich, L. Goerigk, *J. Comput. Chem.* **2011**, *32*, 1456–1465.
- [144] S. Grimme, *J. Comput. Chem.* **2006**, *27*, 1787–1799.
- [145] F. Weigend, R. Ahlrichs, *Phys. Chem. Chem. Phys.* **2005**, *7*, 3297–3305.

- [146] D. G. A. Smith, L. A. Burns, K. Patkowski, C. D. Sherrill, *J. Phys. Chem. Lett.* **2016**, *7*, 2197–2203.
- [147] E. Runge, E. K. U. Gross, *Phys. Rev. Lett.* **1984**, *52*, 997–1000.
- [148] R. van Leeuwen, *Phys. Rev. Lett.* **1999**, *82*, 3863–3866.
- [149] M. E. Casida in *Recent Advances in Density Functional Methods*, (Ed.: D. P. Chong), *Recent Advances in Computational Chemistry*, WORLD SCIENTIFIC, **1995**, pp. 155–192.
- [150] F. Furche, R. Ahlrichs, *J. Chem. Phys.* **2002**, *117*, 7433–7447.
- [151] A. L. Fetter, J. D. Walecka, *Quantum theory of many-particle systems*, McGraw-Hill, New York, NY, **1971**.
- [152] S. Hirata, M. Head-Gordon, *Chem. Phys. Lett.* **1999**, *314*, 291–299.
- [153] C.-P. Hsu, S. Hirata, M. Head-Gordon, *J. Phys. Chem. A* **2001**, *105*, 451–458.
- [154] A. Chantzis, A. D. Laurent, C. Adamo, D. Jacquemin, *J. Chem. Theory Comput.* **2013**, *9*, 4517–4525.
- [155] A. Dreuw, M. Head-Gordon, *Chem. Rev.* **2005**, *105*, 4009–4037.
- [156] A. V. Luzanov, A. A. Sukhorukov, V. Umanskii, *Theor. Exp. Chem.* **1976**, *10*, 354–361.
- [157] R. L. Martin, *J. Chem. Phys.* **2003**, *118*, 4775–4777.
- [158] A. T. Amos, G. G. Hall, H. Jones, *Proc. R. Soc. A: Math. Phys. Eng. Sci.* **1961**, *263*, 483–493.
- [159] R. J. Bartlett, M. Musiał, *Reviews of Modern Physics* **2007**, *79*, 291–352.
- [160] K. Raghavachari, G. W. Trucks, J. A. Pople, M. Head-Gordon, *Chem. Phys. Lett.* **1989**, *157*, 479–483.
- [161] O. Christiansen, H. Koch, P. Jørgensen, *Chem. Phys. Lett.* **1995**, *243*, 409–418.
- [162] C. L. Janssen, I. M. Nielsen, *Chem. Phys. Lett.* **1998**, *290*, 423–430.
- [163] M. Korth, S. Grimme, *J. Chem. Theory Comput.* **2009**, *5*, 993–1003.
- [164] C. Hättig, F. Weigend, *J. Chem. Phys.* **2000**, *113*, 5154.
- [165] C. Hättig, K. Hald, *Phys. Chem. Chem. Phys.* **2002**, *4*, 2111–2118.

- [166] C. Hättig, A. Hellweg, A. Köhn, *Phys. Chem. Chem. Phys.* **2006**, *8*, 1159–1169.
- [167] A. Hellweg, S. A. Grün, C. Hättig, *Phys. Chem. Chem. Phys.* **2008**, *10*, 4119–4127.
- [168] F. Weigend, *Phys. Chem. Chem. Phys.* **2002**, *4*, 4285–4291.
- [169] C. Hättig, *J. Chem. Phys.* **2003**, *118*, 7751–7761.
- [170] M. von Arnim, R. Ahlrichs, *J. Chem. Phys.* **1999**, *111*, 9183–9190.
- [171] A. Köhn, C. Hättig, *J. Chem. Phys.* **2003**, *119*, 5021–5036.
- [172] C. Hättig, A. Köhn, *J. Chem. Phys.* **2002**, *117*, 6939–6951.
- [173] F. Weigend, M. Häser, H. Patzelt, R. Ahlrichs, *Chem. Phys. Lett.* **1998**, *294*, 143–152.
- [174] J. Schirmer, *Phys. Rev. A* **1982**, *26*, 2395–2416.
- [175] A. B. Trofimov, J. Schirmer, *J. Phys. B: At. Mol. Opt. Phys.* **1995**, *28*, 2299–2324.
- [176] J. Schirmer, *Phys. Rev. A* **1991**, *43*, 4647–4659.
- [177] J. Schirmer, A. B. Trofimov, *J. Chem. Phys.* **2004**, *120*, 11449–11464.
- [178] A. B. Trofimov, I. L. Krivdina, J. Weller, J. Schirmer, *Chem. Phys.* **2006**, *329*, 1–10.
- [179] A. Dreuw, M. Wormit, *Wiley Interdiscip. Rev. Comput. Mol. Sci.* **2015**, *5*, 82–95.
- [180] C. Hättig in *Response Theory and Molecular Properties*, (Ed.: H. J. Å. Jensen), *Advances in Quantum Chemistry*, Academic Press, **2005**, pp. 37–60, <https://www.sciencedirect.com/science/article/pii/S0065327605500030>.
- [181] S. Grimme, *J. Chem. Phys.* **2003**, *118*, 9095–9102.
- [182] A. Szabados, *J. Chem. Phys.* **2006**, *125*, 214105.
- [183] A. Tajti, P. G. Szalay, *J. Chem. Theory Comput.* **2019**, *15*, 5523–5531.
- [184] A. Tajti, L. Tulipán, P. G. Szalay, *J. Chem. Theory Comput.* **2020**, *16*, 468–474.
- [185] A. Tajti, B. Kozma, P. G. Szalay, *J. Chem. Theory Comput.* **2021**, *17*, 439–449.
- [186] D. G. Liakos, F. Neese, *J. Chem. Theory Comput.* **2015**, *11*, 4054–4063.
- [187] Y. Guo, U. Becker, F. Neese, *J. Chem. Phys.* **2018**, *148*, 124117.
- [188] F. Neese, *Wiley Interdiscip. Rev. Comput. Mol. Sci.* **2012**, *2*, 73–78.

- [189] F. Neese, *Wiley Interdiscip. Rev. Comput. Mol. Sci.* **2018**, *8*, 33.
- [190] F. Neese, F. Wennmohs, U. Becker, C. Riplinger, *J. Chem. Phys.* **2020**, *152*, 224108.
- [191] C. Riplinger, B. Sandhoefer, A. Hansen, F. Neese, *J. Chem. Phys.* **2013**, *139*, 134101.
- [192] C. Riplinger, P. Pinski, U. Becker, E. F. Valeev, F. Neese, *J. Chem. Phys.* **2016**, *144*, 024109.
- [193] P. Pulay, *Chem. Phys. Lett.* **1983**, *100*, 151–154.
- [194] S. Saebo, P. Pulay, *J. Chem. Phys.* **1988**, *88*, 1884–1890.
- [195] S. Saebo, P. Pulay, *Annu. Rev. Phys. Chem.* **1993**, *44*, 213–236.
- [196] M. Schütz, G. Hetzer, H.-J. Werner, *J. Chem. Phys.* **1999**, *111*, 5691–5705.
- [197] G. Hetzer, M. Schütz, H. Stoll, H.-J. Werner, *J. Chem. Phys.* **2000**, *113*, 9443–9455.
- [198] M. Schütz, H.-J. Werner, *Chem. Phys. Lett.* **2000**, *318*, 370–378.
- [199] M. Schütz, H.-J. Werner, *J. Chem. Phys.* **2001**, *114*, 661.
- [200] W. Meyer, *Int. J. Quantum Chem.* **1971**, *5*, 341–348.
- [201] J. Pipek, P. G. Mezey, *J. Chem. Phys.* **1989**, *90*, 4916–4926.
- [202] S. F. Boys, *Reviews of Modern Physics* **1960**, *32*, 296–299.
- [203] P. Pracht, F. Bohle, S. Grimme, *Phys. Chem. Chem. Phys.* **2020**, *22*, 7169–7192.
- [204] S. Grimme, C. Bannwarth, P. Shushkov, *J. Chem. Theory Comput.* **2017**, *13*, 1989–2009.
- [205] C. Bannwarth, S. Ehlert, S. Grimme, *J. Chem. Theory Comput.* **2019**, *15*, 1652–1671.
- [206] M. J. Frisch, G. W. Trucks, H. B. Schlegel, G. E. Scuseria, M. A. Robb, J. R. Cheeseman, G. Scalmani, V. Barone, G. A. Petersson, H. Nakatsuji, X. Li, M. Caricato, A. V. Marenich, J. Bloino, B. G. Janesko, R. Gomperts, B. Mennucci, H. P. Hratchian, J. V. Ortiz, A. F. Izmaylov, J. L. Sonnenberg, D. Williams-Young, F. Ding, F. Lipparini, F. Egidi, J. Goings, B. Peng, A. Petrone, T. Henderson, D. Ranasinghe, V. G. Zakrzewski, J. Gao, N. Rega, G. Zheng, W. Liang, M. Hada, M. Ehara, K. Toyota, R. Fukuda, J. Hasegawa, M. Ishida, T. Nakajima,

- Y. Honda, O. Kitao, H. Nakai, T. Vreven, K. Throssell, J. J. A. Montgomery, J. E. Peralta, F. Ogliaro, M. J. Bearpark, J. J. Heyd, E. N. Brothers, K. N. Kudin, V. N. Staroverov, T. A. Keith, R. Kobayashi, J. Normand, K. Raghavachari, A. P. Rendell, J. C. Burant, S. S. Iyengar, J. Tomasi, M. Cossi, J. M. Millam, M. Klene, C. Adamo, R. Cammi, J. W. Ochterski, R. L. Martin, K. Morokuma, O. Farkas, J. B. Foresman, D. J. Fox, Gaussian~16 Revision A.03, **2016**.
- [207] S. G. Balasubramani, G. P. Chen, S. Coriani, M. Diedenhofen, M. S. Frank, Y. J. Franzke, F. Furche, R. Grotjahn, M. E. Harding, C. Hättig, A. Hellweg, B. Helmich-Paris, C. Holzer, U. Huniar, M. Kaupp, A. Marefat Khah, S. Karbalaie Khani, T. Müller, F. Mack, B. D. Nguyen, S. M. Parker, E. Perlt, D. Rappoport, K. Reiter, S. Roy, M. Rückert, G. Schmitz, M. Sierka, E. Tapavicza, D. P. Tew, C. van Wüllen, V. K. Voora, F. Weigend, A. Wodyński, J. M. Yu, *J. Chem. Phys.* **2020**, *152*, 184107.
- [208] H. B. Schlegel, *J. Comput. Chem.* **1982**, *3*, 214–218.
- [209] Gaussian 16 Documentation, <https://gaussian.com/opt/>.
- [210] E. G. Hohenstein, C. D. Sherrill, *J. Chem. Phys.* **2010**, *132*, 184111.
- [211] E. G. Hohenstein, R. M. Parrish, C. D. Sherrill, J. M. Turney, H. F. Schaefer, *J. Chem. Phys.* **2011**, *135*, 174107.
- [212] J. M. Turney, A. C. Simmonett, R. M. Parrish, E. G. Hohenstein, F. A. Evangelista, J. T. Fermann, B. J. Mintz, L. A. Burns, J. J. Wilke, M. L. Abrams, N. J. Russ, M. L. Leininger, C. L. Janssen, E. T. Seidl, W. D. Allen, H. F. Schaefer, R. A. King, E. F. Valeev, C. D. Sherrill, T. D. Crawford, *Wiley Interdiscip. Rev. Comput. Mol. Sci.* **2012**, *2*, 556–565.
- [213] G. Berthier, M. J. S. Dewar, H. Fischer, K. Fukui, G. G. Hall, H. Hartmann, H. H. Jaffé, J. Jortner, W. Kutzelnigg, K. Ruedenberg, E. Scrocco, P. Arrighini, *Intermolecular Forces and Their Evaluation by Perturbation Theory*, Vol. 25, Springer Berlin Heidelberg, Berlin, Heidelberg, **1981**.
- [214] K. Szalewicz, Patkowski Konrad, Jeziorski Bogumil in *Intermolecular Forces and Clusters II*, (Ed.: D. J. Wales), Springer Berlin Heidelberg, Berlin, Heidelberg, **2005**, pp. 43–117, https://doi.org/10.1007/430_004.

- [215] T. Korona in *Recent Progress in Coupled Cluster Methods: Theory and Applications*, (Eds.: P. Cársky, P. Josef, P. Jirí), Springer Netherlands, Dordrecht, **2010**, pp. 267–298, https://doi.org/10.1007/978-90-481-2885-3_11.
- [216] K. Szalewicz, *Wiley Interdiscip. Rev. Comput. Mol. Sci.* **2012**, *2*, 254–272.
- [217] E. G. Hohenstein, C. D. Sherrill, *Wiley Interdiscip. Rev. Comput. Mol. Sci.* **2012**, *2*, 304–326.
- [218] B. Jeziorski, R. Moszynski, K. Szalewicz, *Chem. Rev.* **1994**, *94*, 1887–1930.
- [219] T. M. Parker, L. A. Burns, R. M. Parrish, A. G. Ryno, C. D. Sherrill, *J. Chem. Phys.* **2014**, *140*, 094106.
- [220] P. Jurecka, J. Spöner, J. Cerný, P. Hobza, *Phys. Chem. Chem. Phys.* **2006**, *8*, 1985–1993.
- [221] C. D. Sherrill, T. Takatani, E. G. Hohenstein, *J. Phys. Chem. A* **2009**, *113*, 10146–10159.
- [222] K. S. Thanthiriwatte, E. G. Hohenstein, L. A. Burns, C. D. Sherrill, *J. Chem. Theory Comput.* **2011**, *7*, 88–96.
- [223] J. C. Faver, M. L. Benson, X. He, B. P. Roberts, B. Wang, M. S. Marshall, M. R. Kennedy, C. D. Sherrill, K. M. Merz, *J. Chem. Theory Comput.* **2011**, *7*, 790–797.
- [224] E. Papajak, J. Zheng, X. Xu, H. R. Leverentz, D. G. Truhlar, *J. Chem. Theory Comput.* **2011**, *7*, 3027–3034.
- [225] W. B. Schneider, G. Bistoni, M. Sparta, M. Saitow, C. Riplinger, A. A. Auer, F. Neese, *J. Chem. Theory Comput.* **2016**, *12*, 4778–4792.
- [226] G. Bistoni, A. A. Auer, F. Neese, *Chemistry* **2017**, *23*, 865–873.
- [227] G. Bistoni, *Wiley Interdiscip. Rev. Comput. Mol. Sci.* **2020**, *10*, 1.
- [228] A. Altun, M. Saitow, F. Neese, G. Bistoni, *J. Chem. Theory Comput.* **2019**, *15*, 1616–1632.
- [229] A. Altun, F. Neese, G. Bistoni, *J. Chem. Theory Comput.* **2019**, *15*, 215–228.
- [230] A. Altun, R. Izsák, G. Bistoni, *Int. J. Quantum Chem.* **2021**, *121*, 919.
- [231] B. G. Johnson, M. J. Fisch, *J. Chem. Phys.* **1994**, *100*, 7429–7442.
- [232] A. P. Scott, L. Radom, *J. Phys. Chem.* **1996**, *100*, 16502–16513.

- [233] W. Ritz, *J. Reine Angew. Math.* **1909**, 1909, 1–61.
- [234] W. Ritz, *Ann. Phys.* **1909**, 333, 737–786.
- [235] J. K. L. MacDonald, *Phys. Rev.* **1933**, 43, 830–833.
- [236] T. Martin, *Schwingungsspektroskopie und DFT-Rechnungen zu Protonentransferkoordinaten*, **2010**.
- [237] A. Funk, *Quantenchemische Studien zu Schwingungsspektren wasserstoffbrückengebundener Systeme im elektronischen Grundzustand und in elektronisch angeregten Zuständen*, <http://nbn-resolving.de/urn:nbn:de:hbz:386-kluedo-28757>.
- [238] J. M. Bowman, *J. Chem. Phys.* **1978**, 68, 608–610.
- [239] K. Yagi, T. Taketsugu, K. Hirao, M. S. Gordon, *J. Chem. Phys.* **2000**, 113, 1005–1017.
- [240] G. Rauhut, *J. Chem. Phys.* **2004**, 121, 9313–9322.
- [241] M. Keçeli, S. Hirata, *J. Chem. Phys.* **2011**, 135, 134108.
- [242] L. S. Norris, M. A. Ratner, A. E. Roitberg, R. B. Gerber, *J. Chem. Phys.* **1996**, 105, 11261–11267.
- [243] G. M. Chaban, J. O. Jung, R. B. Gerber, *J. Chem. Phys.* **1999**, 111, 1823–1829.
- [244] O. Christiansen, *J. Chem. Phys.* **2003**, 119, 5773–5781.
- [245] J. M. Bowman, K. Christoffel, F. Tobin, *J. Phys. Chem.* **1979**, 83, 905–912.
- [246] K. M. Dunn, J. E. Boggs, P. Pulay, *J. Chem. Phys.* **1986**, 85, 5838–5846.
- [247] M. Neff, G. Rauhut, *J. Chem. Phys.* **2009**, 131, 124129.
- [248] P. Carbonnière, A. Dargelos, C. Pouchan, *Theor. Chem. Acc.* **2010**, 125, 543–554.
- [249] O. Christiansen, *J. Chem. Phys.* **2004**, 120, 2140–2148.
- [250] O. Christiansen, *J. Chem. Phys.* **2004**, 120, 2149–2159.
- [251] G. Schaftenaar, J. H. Noordik, *J. Comput.-Aided Mol. Des.* **2000**, 14, 123–134.
- [252] M. D. Hanwell, D. E. Curtis, D. C. Lonie, T. Vandermeersch, E. Zurek, G. R. Hutchison, *J. Cheminform.* **2012**, 4, 17.
- [253] W. Humphrey, A. Dalke, K. Schulten, *J. Mol. Graph. Model.* **1996**, 14, 33–38.

- [254] S. Rösel, H. Quanz, C. Logemann, J. Becker, E. Mossou, L. Cañadillas-Delgado, E. Caldeweyher, S. Grimme, P. R. Schreiner, *J. Am. Chem. Soc.* **2017**, *139*, 7428–7431.
- [255] S. Rösel, J. Becker, W. D. Allen, P. R. Schreiner, *J. Am. Chem. Soc.* **2018**, *140*, 14421–14432.
- [256] A. Jansen, M. Gerhards, *J. Chem. Phys.* **2001**, *115*, 5445–5453.
- [257] M. Gerhards, K. Beckmann, K. Kleinerhanns, *Z. Phys. D* **1994**, *29*, 223–229.
- [258] M. Schütz, T. Bürgi, S. Leutwyler, H. B. Bürgi, *J. Chem. Phys.* **1993**, *99*, 5228–5238.
- [259] T. Shimanouchi, *Tables of molecular vibrational frequencies, consolidated volume i*, National Bureau of Standards, Gaithersburg, MD, **1972**.
- [260] A. Mellouki, J. Liévin, M. Herman, *Chem. Phys.* **2001**, *271*, 239–266.
- [261] V. Williams, R. Hofstadter, R. C. Herman, *J. Chem. Phys.* **1939**, *7*, 802–805.
- [262] G. D. Dickenson, M. L. Niu, E. J. Salumbides, J. Komasa, K. S. E. Eikema, K. Pachucki, W. Ubachs, *Phys. Rev. Lett.* **2013**, *110*, 193601.
- [263] R. T. Lagemann, A. H. Nielsen, F. P. Dickey, *Phys. Rev.* **1947**, *72*, 284–289.
- [264] M. Rico, M. Barrachina, J. M. Orza, *J. Mol. Spectrosc.* **1967**, *24*, 133–148.
- [265] Y. Zhao, D. G. Truhlar, *Theor. Chem. Acc.* **2008**, *120*, 215–241.
- [266] P. Boden, P. H. Strebert, M. Meta, F. Dietrich, C. Riehn, M. Gerhards, *Phys. Chem. Chem. Phys.* **2022**, DOI 10.1039/D2CP01341J.
- [267] M. Fatima, D. Maué, C. Pérez, D. S. Tikhonov, D. Bernhard, A. Stamm, C. Medcraft, M. Gerhards, M. Schnell, *Phys. Chem. Chem. Phys.* **2020**, *22*, 27966–27978.
- [268] C. Zimmermann, H. C. Gottschalk, M. A. Suhm, *Phys. Chem. Chem. Phys.* **2020**, *22*, 2870–2877.
- [269] C. Zimmermann, M. Lange, M. A. Suhm, *Molecules* **2021**, *26*, DOI 10.3390/molecules26164883.
- [270] ThermoFisher Scientific, 6-Methylchromon, 98 %, <https://www.thermofisher.com/order/catalog/product/H27002.06> (visited on 07/11/2022).

- [271] T. A. Halgren, *J. Comput. Chem.* **1999**, *20*, 720–729.

Appendix A

Publications

A.1 Publication I

Dispersion-Bound Isolated Dimers in the Gas Phase: Observation of the Shortest Intermolecular C-H · · · H-C Distance via Stimulated Raman Spectroscopy

D. Maué, P. H. Strebert, D. Bernhard, S. Rösel, P. R. Schreiner, M. Gerhards

Angew. Chem. Int. Ed., **2021**, *60*, 11305–11309.

DOI: 10.1002/anie.202016020

The singly deuterated ^tBuTPM was synthesized by S. Rösel in the group of P. R. Schreiner. The combined IR/UV and stimulated Raman/UV investigations were carried out by D. Maué in the context of her doctoral thesis. Based on DFT calculations (B97D) by D. Bernhard, which were redone by myself at higher computational level (B3LYP-D3(BJ)). The calculation of the anharmonic vibrational frequencies, analysis and analysis of the intermolecular binding energy by DFT and SAPT0 was performed by myself. P. R. Schreiner and M. Gerhards assisted in discussion and interpretation of the results as well as writing and editing the manuscript. M. Gerhards was my supervisor.

Reproduced with permission from the PCCP Owner Societies.

Dispersion-Bound Isolated Dimers in the Gas Phase: Observation of the Shortest Intermolecular CH...H–C Distance via Stimulated Raman Spectroscopy

Dominique Maué,* Patrick H. Strebart, Dominic Bernhard, Sören Rösel, Peter R. Schreiner,* and Markus Gerhards†

Abstract: The triphenylmethane and all-*meta* tert-butyl triphenylmethane dimers, (TPM)₂ and (T^tBuPM)₂, respectively, were studied with ionization loss stimulated Raman spectroscopy in molecular beam experiments to resolve structure sensitive vibrations. This answers the question whether the recently reported linear head-to-head arrangement in (T^tBuPM)₂ results from crystal packing or prevails also in the gas phase, and therefore must result from extraordinarily strong London dispersion (LD) interactions. Our study clearly demonstrates that the head-to-head arrangement is maintained even under isolated molecular beam conditions in the absence of crystal packing effects. The central Raman-active aliphatic C–D vibration of appropriately deuterated (T^tBuPM)₂ associated with an unusually short C–D...D–C distance exhibits a strong blue-shift compared to the undisturbed case. As the LD stabilizing tert-butyl groups are absent in (TPM)₂, it displays an approximately S₆-symmetric tail-to-tail arrangement.

London dispersion (LD) interactions^[1] are of fundamental importance for many facets of chemistry and biology, yet they have been neglected for a long time^[2] due to their supposedly “weak” nature. However, the latter is only true regarding individual interactions between two atoms, whereas the interaction strength grows rapidly with increasing size of the interacting molecules or moieties due to the (nearly) pairwise additivity.^[3] This leads to significant steric attraction already for medium-sized molecules, becoming even the dominant

factor determining the shape of supramolecular structures such as DNA^[4] or proteins.^[5] LD interactions furthermore explain macroscopic phenomena such as the existence of condensed matter and the remarkable adhesion effect of gecko setae,^[6] utilized in glue research.

Another important and frequently disregarded aspect is the balance between Pauli repulsion and noncovalent attraction, which has recently been shown to be pushed towards the attractive side by utilizing “dispersion energy donors”^[2,7] (DEDs), stabilizing unusual intra- or intermolecular bonding arrangements. Remarkable examples include, e.g., diamondoids connected via very long C–C bonds^[8] as well as alkyl-substituted triphenylmethyl (TPM) derivatives^[9] and all-*meta* tert-butyl hexaphenylethane.^[10–12] The latter one is an extraordinary example of a sterically crowded system that nevertheless forms a stable molecule at room temperature exhibiting a melting point of 210 °C and of which even an X-ray structure could be obtained.^[11] Conversely, unsubstituted hexaphenylethane is not stable despite the early assumption of its existence by Gomberg.^[13] It rather equilibrates between the triphenylmethyl radical dimer, and a quinoid structure.^[14] An explanation for the unexpected stability of (T^tBuPM)₂ originates from the enormous magnitude of LD interactions that outbalance Pauli repulsion.^[10]

In order to gain insights into the intrinsic properties of these LD-bound systems (Figure 1), investigations at the molecular level are required without environmental effects. This can be achieved with molecular beam experiments, generating isolated molecules or defined molecular aggregates at low temperatures. Combining these experiments with, for instance, vibrational or rotational spectroscopy yields valuable structural information, as the spectra represent a fingerprint of the three-dimensional molecular structure, which can be compared to quantum chemical computations. Due to the low sample concentration in the molecular beam the measurement of direct light absorption is not

[*] Dr. D. Maué, P. H. Strebart, Dr. D. Bernhard, Prof. Dr. M. Gerhards
Fachbereich Chemie and Research Center Optimas, TU Kaiserslautern

Erwin-Schrödinger-Str. 52, 67663 Kaiserslautern (Germany)

E-mail: ak_gerhards@chemie.uni-kl.de

Dr. S. Rösel, Prof. Dr. P. R. Schreiner

Institute of Organic Chemistry, Justus-Liebig University

Heinrich-Buff-Ring 17, 35392 Giessen (Germany)

E-mail: prs@uni-giessen.de

[†] Deceased 28.12.2020

Supporting information and the ORCID identification number(s) for the author(s) of this article can be found under:

https://doi.org/10.1002/anie.202016020.

© 2021 The Authors. *Angewandte Chemie International Edition* published by Wiley-VCH GmbH. This is an open access article under the terms of the Creative Commons Attribution Non-Commercial NoDerivs License, which permits use and distribution in any medium, provided the original work is properly cited, the use is non-commercial and no modifications or adaptations are made.

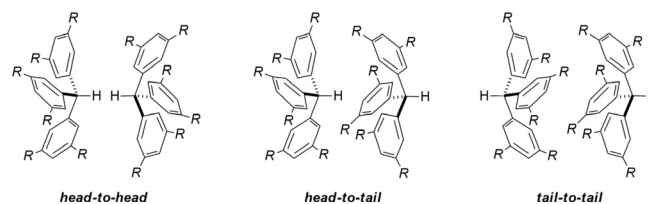


Figure 1. Different dimer motifs of triphenylmethane derivatives (R = H, ^tBu).

possible. Thus, action spectroscopic methods are performed, recording the effect of light (e.g., ionization with subsequent mass detection) on the molecule. An established powerful IR spectroscopic method is combined IR/UV spectroscopy^[15] in combination with time-of-flight mass spectrometry. In the mass- and isomer-selective IR/R2PI method a vibrational excitation (via IR) is recorded as a depletion of an ion signal generated by resonant UV excitation followed by ionization via a second UV photon (R2PI = resonant two-photon ionization process, for details see SI).

Notwithstanding these technical advances, the structural analysis of symmetric molecules or aggregates is often hard or even impossible for infrared and/or rotational spectroscopy due to vanishing transition dipole moments or the lack of a permanent dipole moment. In such cases, Raman spectroscopy is an ideal method since such systems commonly exhibit highly Raman-active vibrational transitions. Spontaneous Raman scattering itself is an inefficient process in molecular beam experiments due to low sample concentrations in the gas phase. Stimulated Raman scattering^[16] uses a pump/dump process, which increases the sensitivity by orders of magnitude. In analogy to the IR/R2PI method, stimulated Raman scattering can be combined with R2PI, a method labeled ionization loss stimulated Raman spectroscopy (ILSRS).^[17] ILSRS allows a combination of vibrational spectroscopy and

mass selectivity via time-of-flight mass spectrometry. In case of ILSR (see inset in Figure 2) the UV laser is set on an electronic transition within the corresponding R2PI spectrum, thereby generating a constant ion signal. A frequency-fixed pump photon ν_p depopulates the ground state (S_0) and the vibrational spectrum is obtained by monitoring the stimulated Raman-induced depletion of the ion signal as a function of $(\nu_p - \nu_s)$ with ν_s being the wavenumber of the tunable Stokes Raman photon. In addition to the ILSRS, ionization gain stimulated Raman spectroscopy (IGSRS)^[18] is almost background-free since the ionization starts only from the vibrational states populated by the stimulated Raman process (and not from the vibrational ground state). A detailed description of this method is given in the Supporting Information.

This communication presents the first stimulated Raman investigations on isolated triphenylmethane-based dimers in the gas phase using our newly modified laser setup (see section 1.2, Supporting Information). The capability of the applied techniques is demonstrated by clearly identifying the isolated dimer structures exhibiting structurally sensitive, Raman-active vibrations.

Figure 2 shows the ILSR spectrum of the $(\text{TPM})_2$ mass trace in the aromatic C–H stretching region obtained via the electronic resonance of 37212 cm^{-1} , the R2PI spectrum of $(\text{TPM})_2$ is depicted in Figure S24. In case of the TPM

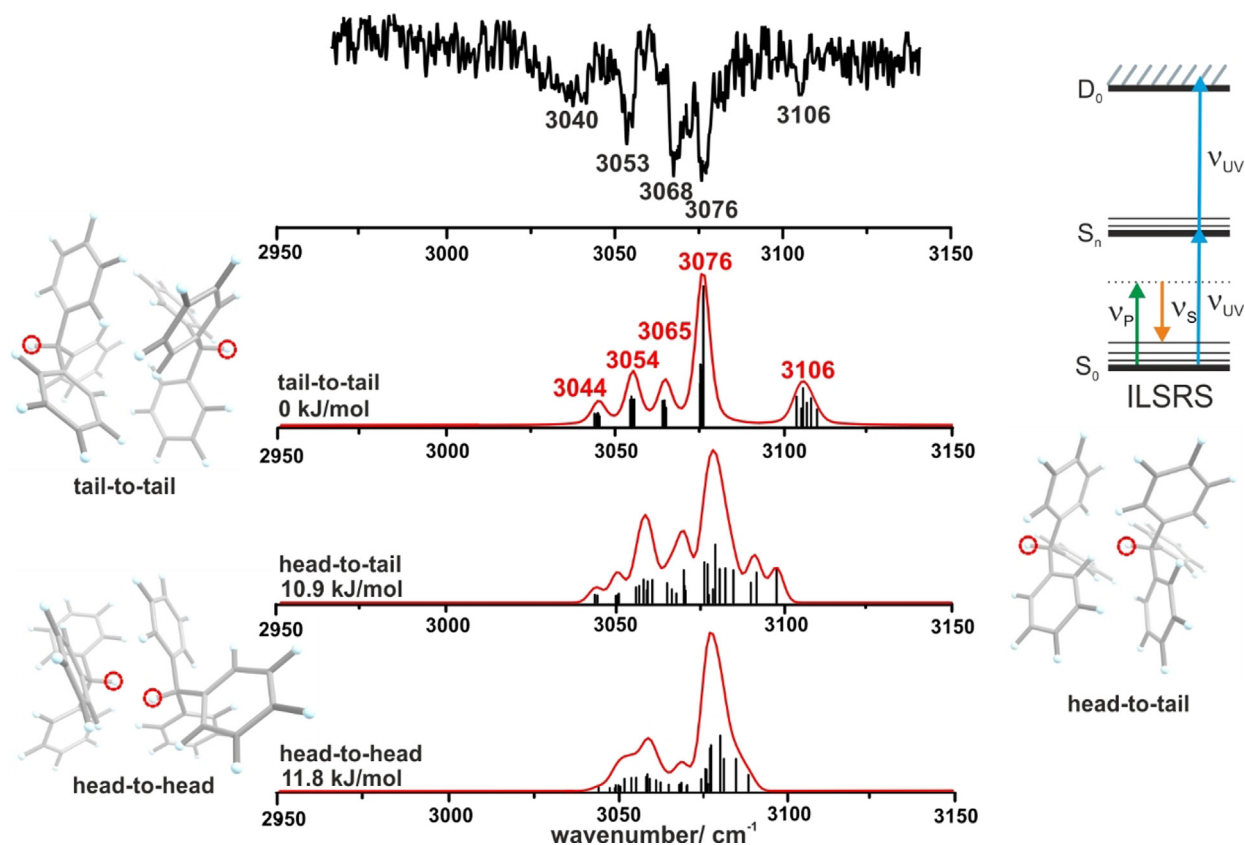


Figure 2. ILSR spectrum of $(\text{TPM})_2$ in the aromatic C–H stretching region compared to calculated vibrational frequencies with Raman intensities at B3LYP-D3(BJ)/def2-TZVP level for the tail-to-tail, head-to-tail, and head-to-head arrangements, scaling factor 0.963 (arom. C–H); factor obtained with respect to CH vibrations of the TPM monomer (see Figure S25). The energy values refer to E_0 , the relative BSE-corrected energy of the respective dimer, including ZPVE. The calculated vibration spectra of the three different isomers all have the same intensity scale. The red dotted marks characterize the aliphatic C–H groups.

monomer it was possible to record the corresponding IGS spectrum in the C–H stretching region (*cf.* Figure S25). These experimentally observed vibrational transitions in combination with DFT calculations are the basis for the structural assignments. There are tail-to-tail, head-to-tail, and head-to-head dimers (Figure 1). Despite the significantly lower S/N ratio, similarities of the ILSR spectrum (Figure 2) of the dimer to the IGS spectrum of the TPM monomer (Figure S25) are obvious: With a difference of not more than 3 cm^{-1} , the transitions at 3041 (3040), 3052 (3053), 3068 (3068), and 3079 (3076) cm^{-1} occur in the monomer (and dimer) spectra, implying some symmetry for the TPM dimer as well. Merely the blue-shifted transition at 3106 cm^{-1} appears as a noticeable additional feature within the aromatic C–H stretching region of the dimer spectrum. Good agreement exists between the ILSR spectrum and the calculated vibrational frequencies including Raman intensities for the tail-to-tail arrangement in $(\text{TPM})_2$ (Figure 2). Six aromatic C–H stretching vibrations are significantly blue-shifted compared to the remaining ones (*cf.* Section 2.1 in the SI). This is not observed for the head-to-tail and head-to-head arrangements. This significant difference in the tail-to-tail structure is due to a bond compression induced by the balance of Pauli repulsion and LD in the dimer (Figure 2). Furthermore, nearly degenerate frequencies in the symmetric tail-to-tail structure result in formation of four groups of C–H stretching frequencies leading to a structured ILSR spectrum with four peaks between 3000 and 3100 cm^{-1} . In case of the head-to-tail and head-to-head structures the remaining C–H stretching vibrations are much more spread. This spreading (resulting in a broadening of the spectrum) is not directly observed in the experimental spectrum. There are more possible arrangements which are in between the three limiting

types but only for the symmetric tail-to-tail geometry a structured spectrum with a clearly separated group of C–H stretching vibrations at about 3106 cm^{-1} is obtained. The assignment of the tail-to-tail structure is further supported by IR/R2PI spectra in the aliphatic C–H region (*cf.* Figure S27). Despite this unambiguous assignment the presence of a small fraction ($<30\%$) of the energetically strongly disfavored head-to-tail and head-to-head isomers due to kinetic trapping cannot be excluded since in this case their vibrational pattern would be hidden below the spectrum of the dominant tail-to-tail isomer.

Turning to $(\text{T}^t\text{BuPM})_2$, head-to-head, head-to-tail, and tail-to-tail structures are shown in Figure 3 (see also Figures S7–S9 and S13–S15). The linear head-to-head structure observed in the crystal^[19] exhibits an intermolecular C–H...H–C distance of $1.566(5)\text{ \AA}$ obtained by neutron diffraction at 20 K , the shortest intermolecular C–H...H–C distance measured to date. As there are no crystal packing effects influencing the structure in the gas phase, the structure is expected to be somewhat “relaxed” compared to the solid state, resulting in a slightly larger C–H...H–C distance of 1.571 \AA (B3LYP-D3(BJ)/def2-TZVP). Compared to the head-to-head arrangement the competing head-to-tail and

Table 1: Relative energies for $(\text{T}^t\text{BuPM})_2$ obtained at different computational levels. The ΔE -values and D_0 -values refer to BSSE-corrected values for the deuterated dimer. All values are given in kJ mol^{-1} .

	B3LYP-D3(BJ)/def2-TZVP			B97-D/def2-TZVP		
	ΔE	ΔE_0	D_0	ΔE	ΔE_0	D_0
head-to-head	0	0	115.3	0	0	110.5
head-to-tail	22.8	28.5	86.8	11.8	14.0	96.5
tail-to-tail	68.6	67.2	48.2	51.6	46.7	63.8

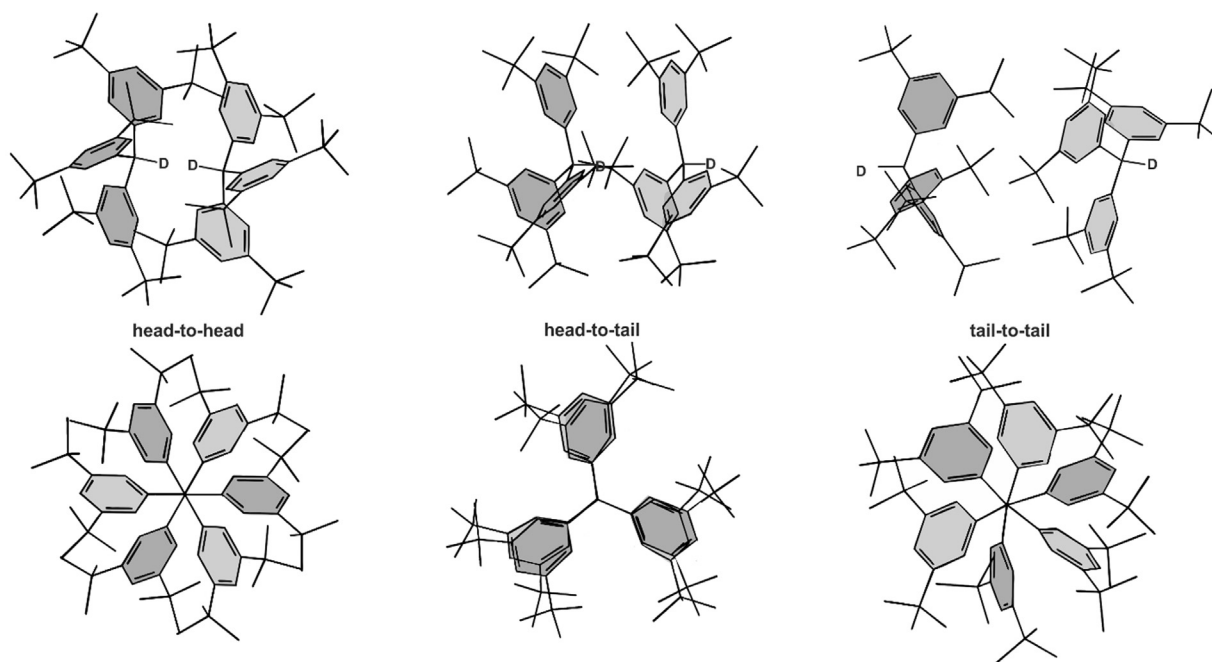


Figure 3. Computed three geometries for the all-*meta* *tert*-butyl triphenylmethane dimer $(\text{T}^t\text{BuPM})_2$ at B3LYP-D3(BJ)/def2-TZVP. In the second row the view in direction of the C–D...D–C bond of the head-to-head, head-to-tail and tail-to-tail structure are depicted.

tail-to-tail structures are energetically disfavored (Table 1). This results from the sterically demanding *tert*-butyl moieties in (T¹BuPM)₂ leading to a larger distance between the phenyl rings and thus a lack of interaction surface compared to the head-to-head arrangement. Within the head-to-head structure, the *tert*-butyl moieties enable an ideal interlocking between the two T¹BuPM molecules in which LD is able to outbalance Pauli repulsion.

To obtain a structural identification of (T¹BuPM)₂ a vibrational analysis of the C–H stretching modes has been performed. The two C–H stretching vibrations of the dimer involving the C–H moieties at the central carbon atom of each TPM unit should be structurally sensitive with respect to the head-to-head, head-to-tail, and tail-to-tail arrangements. The remarkably short C–H...H–C distance in the head-to-head arrangement should create a unique structural identifier differing from all other arrangements. Remarkably large Raman intensities are theoretically predicted especially for the plethora of aliphatic C–H stretching vibrations (*cf.* Figure S10). Unfortunately, the structurally sensitive C–H vibrations overlap with parts of the aliphatic C–H stretching modes of the 12 *tert*-butyl groups (*cf.* Figure S10). This problem is solved by preparing and investigating the singly deuterated T¹BuPM and its dimer, in which a deuterium atom replaces the hydrogen atom of the central C–H moiety. The C–D vibrations shift to a spectral region around 2200 cm⁻¹ where no spectral overlaps are expected.

The two aliphatic C–D stretching vibrations of the tail-to-tail and head-to-tail isomers calculated harmonically at B3LYP-D3(BJ)/def2-TZVP are completely localized. The head-to-head arrangement (almost S₆-symmetry) displays a Raman-active (IR-inactive) symmetric and a Raman-inactive (and vanishingly small IR active) asymmetric stretching normal mode of the two coupled C–D vibrations. Thus, the stimulated Raman techniques are an ideal tool to investigate the asymmetric structure sensitive C–D vibration. For a better theoretical description of the symmetric C–D stretching mode, a one-dimensional potential energy curve along the normal coordinate (*cf.* Figures S18–S23) was computed at B3LYP-D3(BJ)/def2-TZVP. The same procedure has been performed for the localized C–D vibrations of the tail-to-tail and head-to-tail isomers (Figures S21 and S23). The calculations confirm the assumption that the symmetric C–D vibration in the head-to-head dimer is significantly blue-shifted compared to the isolated C–D vibrations in the other dimers (Figure 4).

The demanding ILSR method could be applied with respect to the isolated C–D vibrations. The experimentally obtained spectrum (recorded via an UV excitation at 36958 cm⁻¹, Figure S28) is given in Figure 4 and is compared to the computed data. A strong transition at 2270 cm⁻¹ and a weaker one at 2134 cm⁻¹ are observed in the ILSR spectrum. The band at 2270 cm⁻¹ is strongly blue-shifted in agreement with the prediction for the head-to-head structure and in contrast to the C–D frequencies computed for the other dimer structures (Figure 4; Tables S6 and S8; Figures S12 and S17). Thus, in agreement with the theoretical prediction, the strong transition at 2270 cm⁻¹ can unambig-

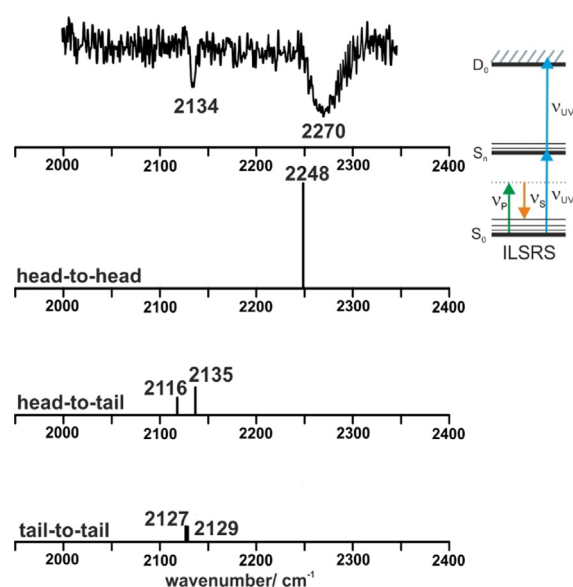


Figure 4. ILSR spectrum of (T¹BuPM-*d*₁)₂ in the region of the aliphatic C–D stretching vibrations compared to the calculated anharmonic values (obtained from one-dimensional potential energy curves along the normal coordinates at B3LYP-D3(BJ)/def2-TZVP, see text and Figures S18–S23). The computed relative Raman intensities (arbitrary units) are taken from the normal mode analyses and are indicated by the heights of the bars. The calculated vibration spectra of the three different isomers all have the same intensity scale.

uously be assigned to the most stable head-to-head structure, clearly indicating its formation under isolated conditions.

The second sharper transition at 2134 cm⁻¹ could originate from a C–D bending overtone of the central aliphatic carbon atoms of the T¹BuPM moieties (see section 3.2 in the SI). Coupled bending vibrations are calculated at 1062 and 1065 cm⁻¹ (harmonic approximation, B3LYP-D3(BJ)/def2-TZVP, scaled by 0.99^[20]). However, another explanation for the transition at 2134 cm⁻¹ is that it arises from the tail-to-tail isomer (as an overlap of the two C–D frequencies which are almost identical). It would also be possible that the vibrations of the tail-to-tail structure and one of the more stable head-to-tail arrangement overlap (the remaining transition of the head-to-tail structure may be too weak to be observed). The formation of the energetically disfavored head-to-tail and/or tail-to-tail isomers, which can hardly be distinguished from the head-to-head isomer by their UV resonance might be explained by kinetic trapping during the supersonic expansion (*cf.* Section 3.2 of the SI).

The main goal of this communication is to demonstrate that the linear head-to-head arrangement in (T¹BuPM)₂ observed in the condensed phase is also found under isolated conditions in the gas phase. Ionization loss stimulated Raman experiments unambiguously identify the structure through the Raman-active C–D vibration of the dimer composed of monodeuterated monomers. This vibration is characteristically blue-shifted compared to competing structures due to significant C–H(D) bond compression in this peculiar dimer arrangement involving an extremely short C–H(D)...(D)H–C distance. In (TPM)₂ Pauli repulsion exceeds LD attraction when the two TPM moieties approach each other head-to-

head, leading to the preference of the tail-to-tail structure. By introducing the *tert*-butyl substituents as large DEDs, the balance is tipped towards LD attraction within the head-to-head arrangement. The clear spectroscopic identification of the (T^tBuPM)₂ structure in the gas phase proves that crystal packing effects play a negligible role for the observed head-to-head arrangement in the condensed phase. Thus, this text book example shows that the arrangement is driven by LD originating from a multitude of *tert*-butyl groups outbalancing steric repulsion. In unsubstituted (TPM)₂ no comparable LD stabilization is possible and a tail-to-tail structure forms. Likewise, this study demonstrates the remarkable ability of stimulated Raman techniques within molecular beam experiments to elucidate the structure of large, symmetric, and nonpolar molecular aggregates by their Raman-active vibrations.

Acknowledgments

The authors would like to acknowledge funding from the Deutsche Forschungsgemeinschaft (DFG, Ge 961/9-2 and Schr 597/27-2) within the priority program SPP 1807 “Dispersion” for funding. Furthermore the authors thank Prof. C. van Wüllen for performing part of the dimer calculations on his high performance computer cluster. The authors also want to thank PD C. Riehn and Dr. K. Schwing for the fruitful discussion. This work is part of the doctoral thesis of D.M. and P.H.S. Open access funding enabled and organized by Projekt DEAL.

Conflict of interest

The authors declare no conflict of interest.

Keywords: combined IR/UV experiments · density functional theory · molecular beam experiments · non-covalent interactions · vibrational spectroscopy

-
- [1] F. London, *Z. Phys.* **1930**, *63*, 245–279.
 [2] J. P. Wagner, P. R. Schreiner, *Angew. Chem. Int. Ed.* **2015**, *54*, 12274–12296; *Angew. Chem.* **2015**, *127*, 12446–12471.
 [3] A. J. Stone, *The theory of intermolecular forces*, Oxford Univ. Press, Oxford, **2013**.
 [4] S. Hanlon, *Biochem. Biophys. Res. Commun.* **1966**, *23*, 861–867.
 [5] *Advances in Protein Chemistry* (Eds.: S. K. Burley, G. A. Petsko), Academic Press, New York, **1988**.
 [6] K. Autumn, M. Sitti, Y. A. Liang, A. M. Peattie, W. R. Hansen, S. Sponberg, T. W. Kenny, R. Fearing, J. N. Israelachvili, R. J. Full, *Proc. Natl. Acad. Sci. USA* **2002**, *99*, 12252–12256.

- [7] L. Goerigk, S. Grimme, *Phys. Chem. Chem. Phys.* **2011**, *13*, 6670–6688.
 [8] a) P. R. Schreiner, L. V. Chernish, P. A. Gunchenko, E. Y. Tikhonchuk, H. Hausmann, M. Serafin, S. Schlecht, J. E. P. Dahl, R. M. K. Carlson, A. A. Fokin, *Nature* **2011**, *477*, 308–311; b) A. A. Fokin, L. V. Chernish, P. A. Gunchenko, E. Y. Tikhonchuk, H. Hausmann, M. Serafin, J. E. P. Dahl, R. M. K. Carlson, P. R. Schreiner, *J. Am. Chem. Soc.* **2012**, *134*, 13641–13650.
 [9] S. Rösel, J. Becker, W. D. Allen, P. R. Schreiner, *J. Am. Chem. Soc.* **2018**, *140*, 14421–14432.
 [10] a) S. Rösel, C. Balestrieri, P. R. Schreiner, *Chem. Sci.* **2017**, *8*, 405–410; b) N. Yannoni, B. Kahr, K. Mislow, *J. Am. Chem. Soc.* **1988**, *110*, 6670–6672.
 [11] S. Grimme, P. R. Schreiner, *Angew. Chem. Int. Ed.* **2011**, *50*, 12639–12642; *Angew. Chem.* **2011**, *123*, 12849–12853.
 [12] B. Kahr, D. van Engen, K. Mislow, *J. Am. Chem. Soc.* **1986**, *108*, 8305–8307.
 [13] M. Gomberg, *J. Am. Chem. Soc.* **1900**, *22*, 757–771.
 [14] H. Lankamp, W. T. Nauta, C. MacLean, *Tetrahedron Lett.* **1968**, *9*, 249–254.
 [15] a) E. G. Robertson, M. R. Hockridge, P. D. Jelfs, J. P. Simons, *J. Phys. Chem. A* **2000**, *104*, 11714–11724; b) E. G. Robertson, J. P. Simons, M. Mons, *J. Phys. Chem. A* **2001**, *105*, 9990–9992; c) P. Çarçabal, R. T. Kroemer, L. C. Snoek, J. P. Simons, J. M. Bakker, I. Compagnon, G. Meijer, G. v. Helden, *Phys. Chem. Chem. Phys.* **2004**, *6*, 4546–4552; d) T. S. Zwier, *Annu. Rev. Phys. Chem.* **1996**, *47*, 205–241; e) S. Tanabe, T. Ebata, M. Fujii, N. Mikami, *Chem. Phys. Lett.* **1993**, *215*, 347–352; f) C. Riehn, C. Lahmann, B. Wassermann, B. Brutschy, *Chem. Phys. Lett.* **1992**, *197*, 443–450; g) R. H. Page, Y. R. Shen, Y. T. Lee, *J. Chem. Phys.* **1988**, *88*, 4621–4636; h) M. Gerhards, C. Unterberg, *Phys. Chem. Chem. Phys.* **2002**, *4*, 1760–1765.
 [16] G. Eckhardt, R. W. Hellwarth, F. J. McClung, S. E. Schwarz, D. Weiner, E. J. Woodbury, *Phys. Rev. Lett.* **1962**, *9*, 455–457.
 [17] a) M. Felker, P. M. Maxton, M. W. Schaeffer, *Chem. Rev.* **1994**, *94*, 1787–1805; b) G. V. Hartland, B. F. Henson, V. A. Ventura, R. A. Hertz, P. M. Felker, *J. Opt. Soc. Am. B* **1990**, *7*, 1950.
 [18] a) P. Esherick, A. Owyong, J. Plíva, *J. Chem. Phys.* **1985**, *83*, 3311–3317; b) P. Esherick, A. Owyong, *Chem. Phys. Lett.* **1983**, *103*, 235–240.
 [19] S. Rösel, H. Quanz, C. Logemann, J. Becker, E. Mossou, L. Cañadillas-Delgado, E. Caldeweyher, S. Grimme, P. R. Schreiner, *J. Am. Chem. Soc.* **2017**, *139*, 7428–7431.
 [20] a) C. W. Bauschlicher, S. R. Langhoff, *Spectrochim. Acta Part A* **1997**, *53*, 1225–1240; b) M. D. Halls, J. Velkovski, H. B. Schlegel, *Theor. Chem. Acc.* **2001**, *105*, 413–421; c) P. Sinha, S. E. Boesch, C. Gu, R. A. Wheeler, A. K. Wilson, *J. Phys. Chem. A* **2004**, *108*, 9213–9217; d) K. Bartl, A. Funk, K. Schwing, H. Fricke, G. Kock, H.-D. Martin, M. Gerhards, *Phys. Chem. Chem. Phys.* **2009**, *11*, 1173–1179.

Manuscript received: December 1, 2020

Revised manuscript received: February 13, 2021

Accepted manuscript online: March 11, 2021

A.2 Supporting Information of Publication I

Supporting Information

Dispersion-Bound Isolated Dimers in the Gas Phase: Observation of the Shortest Intermolecular CH...H-C Distance via Stimulated Raman Spectroscopy

Dominique Maué, Patrick H. Strebert, Dominic Bernhard, Sören Rösel, Peter R. Schreiner,* and Markus Gerhards†*

anie_202016020_sm_miscellaneous_information.pdf

Supporting Information

Contents

1. Computational as well as Experimental Methods and Set-up	2
1.1. Computational Methods	2
1.2. Raman and IR/UV Spectroscopy.....	2
2. Theoretical Results	4
2.1. Triphenylmethane (TPM) dimer	4
2.2. All- <i>meta tert</i> -butyl triphenylmethane dimer (T ^t BuPM) ₂	10
2.2.1 Geometries and aliphatic C–H stretching frequencies (B3LYP-D3(BJ)/def2-TZVP level) ...	10
2.2.2 Geometries and aliphatic C–H stretching frequencies (B97D/def2-TZVP level)	14
2.2.3 Anharmonic calculations.....	17
2.2.4 Dissociation energies and SAPT(0) calculations.....	21
3. Experimental Results.....	23
3.1. Triphenylmethane and triphenylmethane dimer	23
3.2. All- <i>meta tert</i> -butyl triphenylmethane dimer (T ^t BuPM) ₂	27

1. Computational as well as Experimental Methods and Set-up

1.1. Computational Methods

Input structures (without using symmetry constraints) were manually created using Avogadro^[1] while applying the MMFF94s^[2] force field for pre-optimization of the geometries. Further structures were generated using the simulated annealing routine available within the GFN-xTB program.^[3] Regarding the all-*meta tert*-butyl triphenylmethane dimer, initial geometries for the linear head-to-head structure were taken from Ref.^[4]. All computations were performed at the density functional theory (DFT) level using the hybrid functional B3LYP along with the D3 dispersion correction^[5] and Becke-Johnson damping^[6] with the def2-TZVP basis set.^[7] Further DFT computations were carried out with the B97-D functional^[8] using the basis set def2-TZVP. Geometry optimizations and harmonic frequency calculations including Raman activities were performed with Gaussian 09.^[9]

Raman activities (S_i) calculated *via* Gaussian 09 were converted to Raman intensities (I_i) by the formula adapted from Ref.^[10]:

$$I_i = \frac{f(\tilde{\nu}_0 - \tilde{\nu}_i)^4 S_i}{\tilde{\nu}_i (1 - \exp(-\frac{hc\tilde{\nu}_i}{kT}))} \quad (1)$$

with f as normalization factor of all peak intensities, the wavenumber of the exciting laser $\tilde{\nu}_0$, the respective vibrational wavenumber $\tilde{\nu}_i$ as well as the temperature T . The respective values were chosen according to the molecular beam conditions of the applied ionization gain/loss stimulated Raman method: $f=1$, $\tilde{\nu}_0=18797 \text{ cm}^{-1}$ and $T=30 \text{ K}$, whereas $\tilde{\nu}_i$ and S_i are obtained from the harmonic frequency calculations.

1.2. Raman and IR/UV Spectroscopy

Figure S1 illustrates the concepts of the applied ionization loss and ionization gain stimulated Raman spectroscopy (ILSRS and IGSRS). These stimulated Raman methods introduced by Owyong *et al.*,^[11] extended by Felker *et al.*^[12,13] and further established by Bar *et al.*^[14] take advantage of the resonant 2-photon ionization (R2PI),^[15] allowing for mass-selective ionization detection. For the ILSR technique (*cf.* Figure S1a), the UV laser is set on an electronic transition within the corresponding R2PI spectrum, thereby generating a constant ion signal. The vibrational spectrum is obtained by monitoring the stimulated Raman-induced depletion of the ion signal as a function of the wavenumber of the respective tuneable Stokes beam ν_s . Specifically, the frequency-fixed pump photon ν_p depopulates the ground state (S_0) in a non-resonant process, moving population into a “virtual state”. In contrast to spontaneous Raman scattering, a simultaneously arriving Stokes photon ν_s is able to dump the molecules from this “virtual state” to a vibrationally excited state of the ground state, if the energy difference between ν_p and ν_s is in resonance with the respective vibrational state. After the stimulated Raman process, less molecules are available for the R2PI process occurring several nanoseconds afterwards, resulting in a depletion of the ion signal. The ILSR method is the stimulated Raman equivalent to the IR/R2PI technique^[16] as a complementary infrared technique and might also be seen as a non-resonant variant of the stimulated emission pumping (SEP)-R2PI method.^[17]

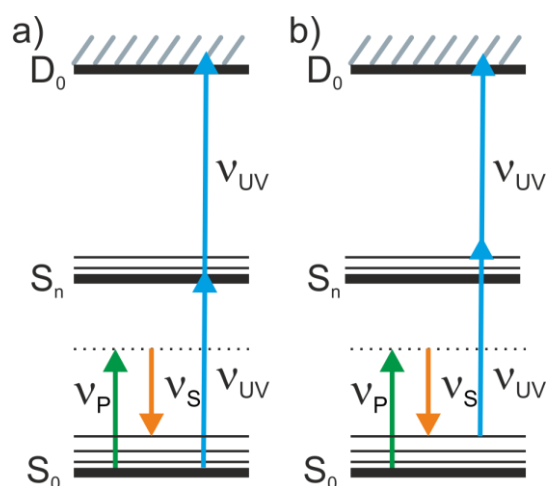


Figure S1: Term schemes for a) the ionization-loss stimulated Raman spectroscopy (ILSRS) and b) the ionization-gain stimulated Raman spectroscopy (IGSRS).

Conversely, the IGSR method is based on a signal gain due to stimulated Raman scattering (*cf.* Figure S1b). For this purpose, the UV laser is detuned from any resonance in the R2PI spectrum to a lower energy being insufficient for electronic excitation and ionization. If now a vibrational state is populated *via* stimulated Raman scattering, the sum of the vibrational energy and UV photon energy might be sufficient for electronic excitation and ionization, leading to an ion signal. The success of this technique strongly depends on the respective molecule and the excited vibration, as it relies on a sufficient lifetime of the excited vibrational state^[12] as well as on Franck-Condon factors,^[18] related to the density of vibrational states in the electronically excited state. This technique might be roughly comparable to the IR+UV technique^[19] as an equivalent infrared technique.

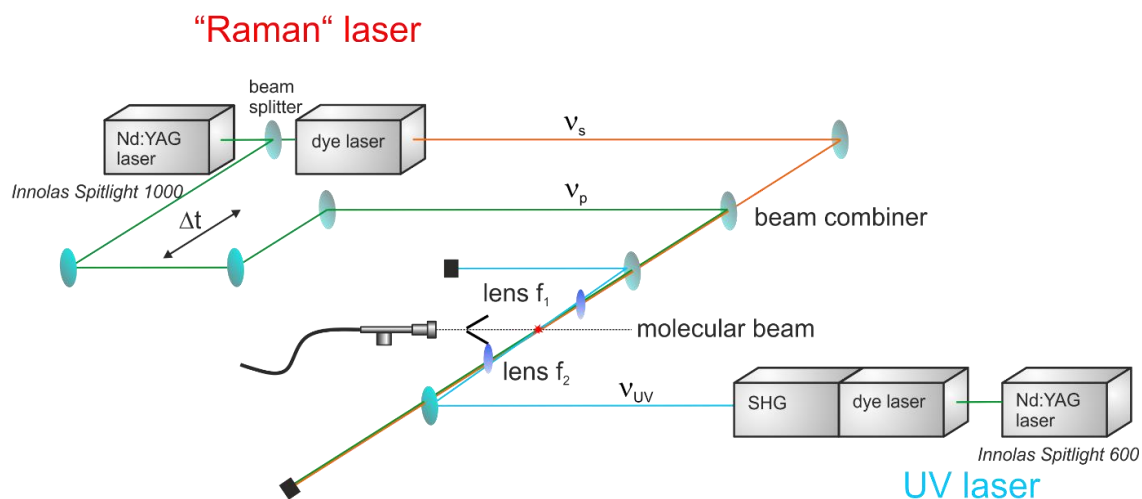


Figure S2 Experimental setup for the stimulated Raman techniques.

The mass-selective one-color R2PI as well as the IGSR and ILSR spectra were measured using nanosecond laser systems. The tunable UV laser system consists of a frequency-tripled (355 nm) Nd:YAG laser (Innolas, Spitlight 600) pumping a dye laser (Sirah, Cobra-Stretch), yielding tunable laser radiation in the visible region. In a subsequent frequency conversion unit, the radiation is frequency-doubled within a BBO crystal, generating tunable UV laser radiation. For the pump (ν_P) and Stokes beams (ν_S) required for stimulated Raman scattering, one single Nd:YAG laser (Innolas, Spitlight 1000) has been used. The second harmonic (532 nm) of the Nd:YAG laser is split *via* a 1:4 beam

divider, using 20% as the frequency-fixed pump beam (ν_p). The tunable Stokes beam (ν_s) in the visible region is obtained as the output of a further dye laser (Sirah, PrecisionScan) pumped by the remaining 80% of the 532 nm beam. For all ILSR and IGSR experiments, the pump (ν_p) and Stokes (ν_s) beams were irradiated 30 ns prior to the UV beam.

All experiments were carried out in a molecular beam apparatus consisting of a differentially pumped linear time-of-flight mass spectrometer (TOF-MS) that has been described elsewhere.^[20] The samples were heated (64 °C for TPM and 152 °C for T^tBuPM, respectively) and thereby seeded into the carrier gas (neon or helium) for supersonic jet expansion *via* a pulse valve (Series 9 and pulse driver Iota One, General Valve, 500 μ m orifice). The triphenylmethane (TPM) sample was purchased from Sigma Aldrich (99%). The synthesis of Tri(3,5-di-*tert*-butylphenyl)methane and the singly deuterated Tri(3,5-di-*tert*-butylphenyl)methane-*d*₁ is described in Ref. ^[4].

As shown in Figure S2, the pump beam ν_p (pulse energy of \approx 30 mJ) and Stokes beam ν_s (pulse energy of \approx 18 mJ) were spatially and temporally overlapped *via* a beam combiner (SEM-LPD02-532RU-25, Semrock) and focused by the same plano-convex lens (f_1) with a focal length of 300 mm into the molecular beam. The UV laser beam (energies from \approx 20 μ J for ILSR and \approx 40 μ J for IGSR-experiments) entered the ionization chamber from the opposite side and was focused by a plano-convex lens (f_2) with a focal length of 400 mm. The position of the lenses f_1 and f_2 was adjusted to ensure ideal overlap of the foci. This experimental setup differs from those of Felker, Ito and Bar by using a dichroic beam combiner for combining pump and Stokes beam, whereas the UV laser is irradiated from the opposite side.

2. Theoretical Results

2.1. Triphenylmethane (TPM) dimer

Figure S3 shows optimized structures of the triphenylmethane dimer at the B3LYP-D3(BJ)/def2-TZVP level. Each structure is shown in a simplified form, in the perspectives on the right the phenyl planes are highlighted in order to support the perspective view. The tail-to-tail structure is nearly S_6 -symmetric, involving a staggered conformation of the phenyl rings considering the view along the aligned central aliphatic C–H bonds (Figure S3, upper right). This allows for a maximization of LD interactions between the two TPM units, “interlocking” each other. Within this particular arrangement, the effect of Pauli repulsion is reflected in the compression of three aromatic *ortho*-C–H bonds of each TPM monomer (*cf.* Figure S4), pointing towards another C–H moiety. This bond compression leads to a blue-shift of the corresponding CH stretching vibrations compared to those involving undisturbed C–H moieties and will be further discussed in the Experimental Results section.

The structure shown in Figure S3b is denoted as head-to-tail (*cf.* Figure S5). One central C–H moiety points towards the “tail” of the second TPM unit and the C–H moiety of the second TPM molecule points away from the first TPM unit. Furthermore, a head-to-head structure is obtained as a further minimum conformation (*cf.* Figure S6). Within that dimer arrangement, the central C–H moieties are pointing towards each other. However, they arrange not linearly but slightly shifted, dodging each other avoiding Pauli repulsion. Thereby, the TPM units get closer to each other enabling stronger dispersion interactions. Nevertheless, this arrangement does not allow for an ideal “interlocking” of the propeller-like TPM molecules as it is observed in the tail-to-tail structure.

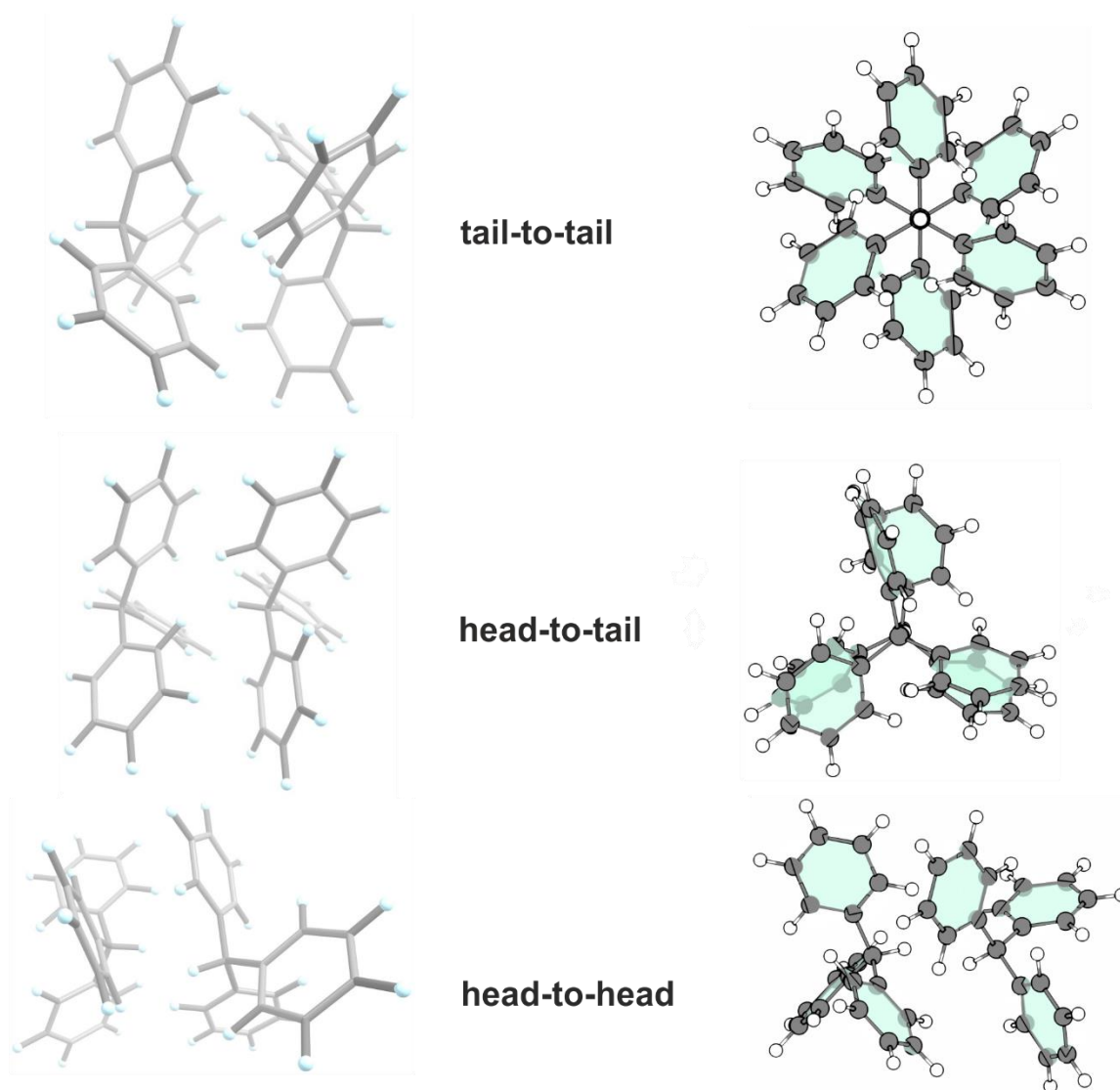


Figure S3: Calculated lowest energy isomers of TPM_2 at the B3LYP-D3(BJ)/def2-TZVP level.

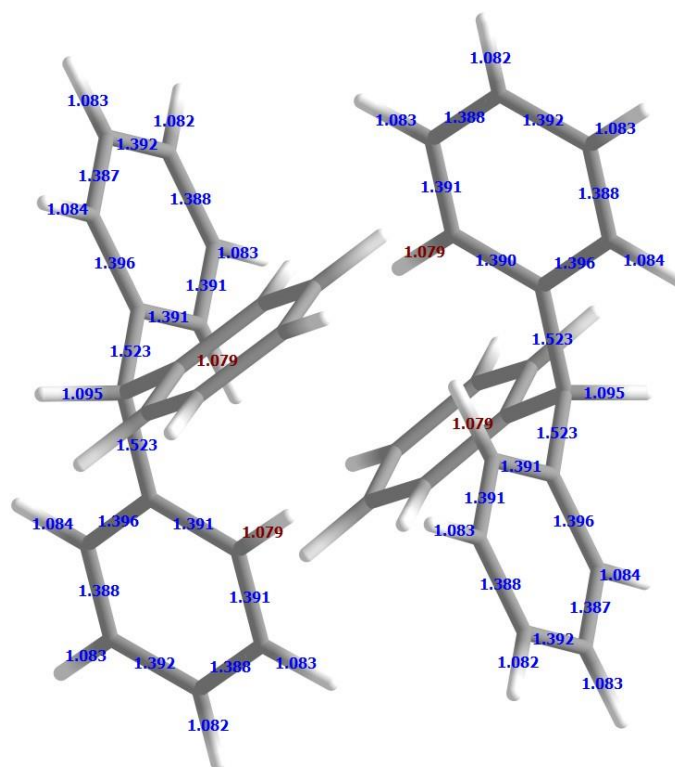


Figure S4a: Selected bond distances given in Å within the *tail-to-tail* structure of the triphenylmethane dimer calculated at the B3LYP-D3(BJ)/def2-TZVP level. The red numbers indicate four of the six compressed *ortho*-C–H bonds.

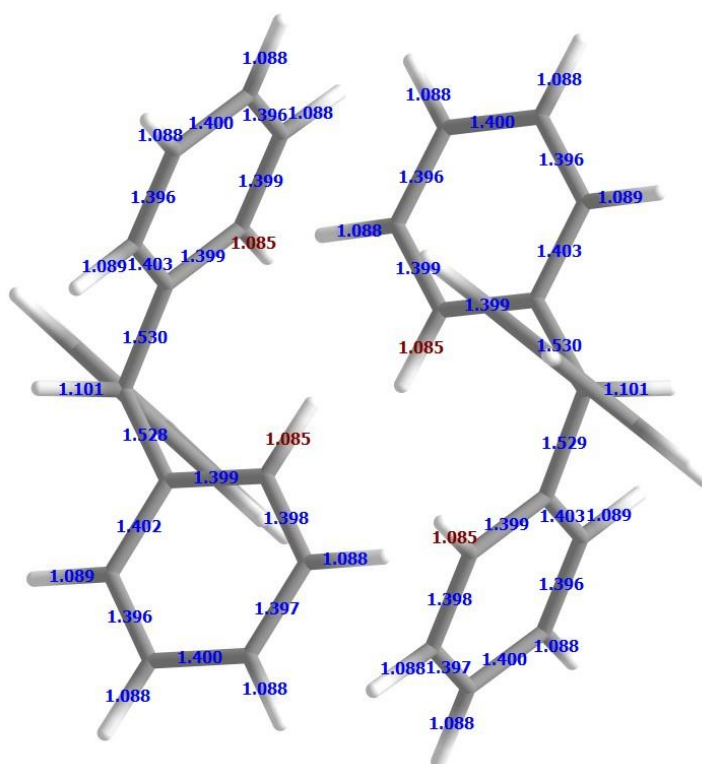


Figure S4b: Selected bond distances given in Å within the *tail-to-tail* structure of the triphenylmethane dimer calculated at the B97-D/def2-TZVP level. The red numbers indicate four of the six compressed *ortho*-C–H bonds.

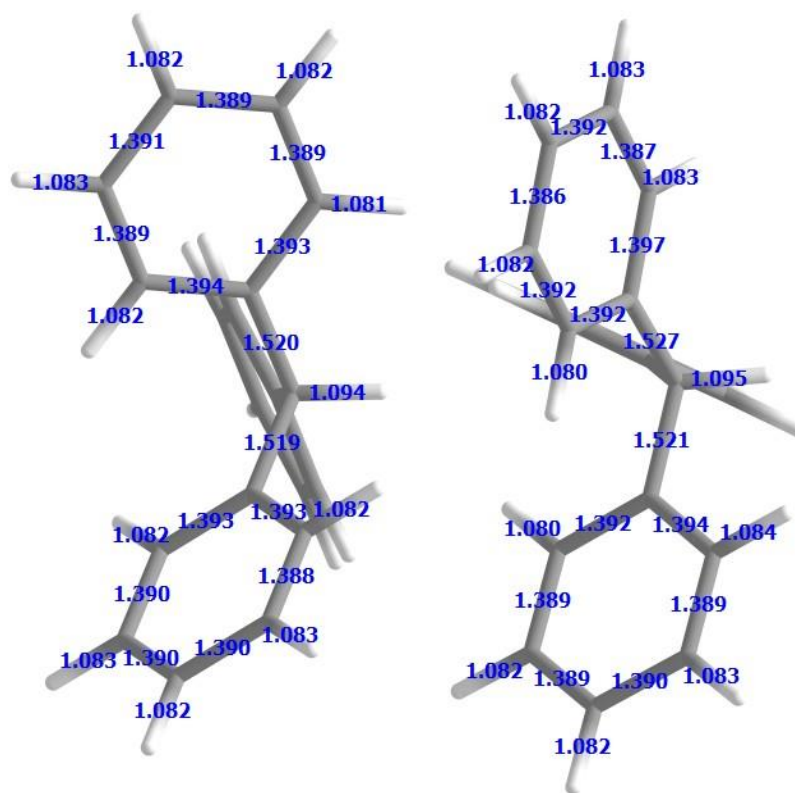


Figure S5a: Selected bond distances in Å within the **head-to-tail** structure of the triphenylmethane dimer calculated at the B3LYP-D3(BJ)/def2-TZVP level.

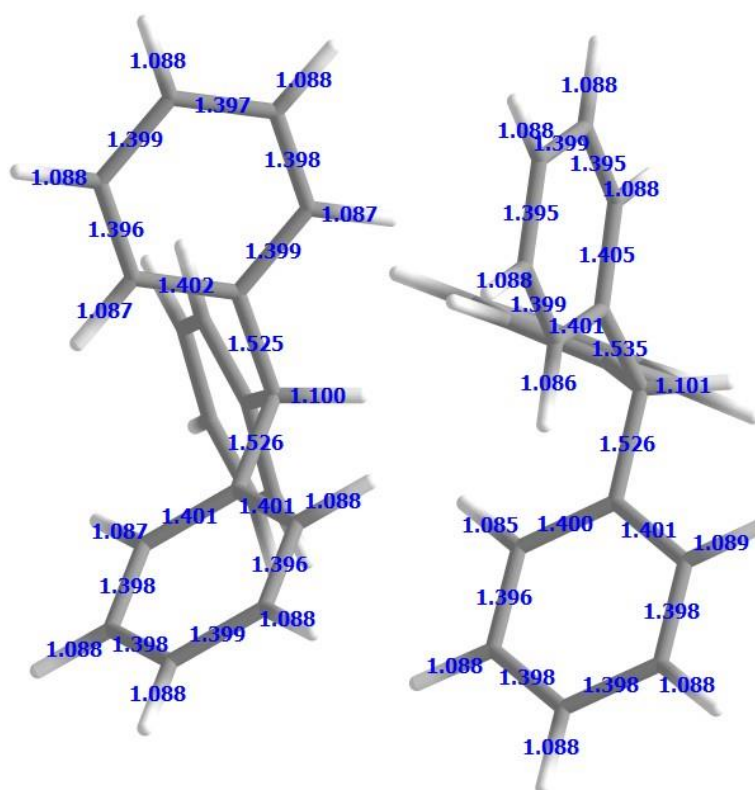


Figure S5b: Selected bond distances in Å within the **head-to-tail** structure of the triphenylmethane dimer calculated at the B97-D/def2-TZVP level.

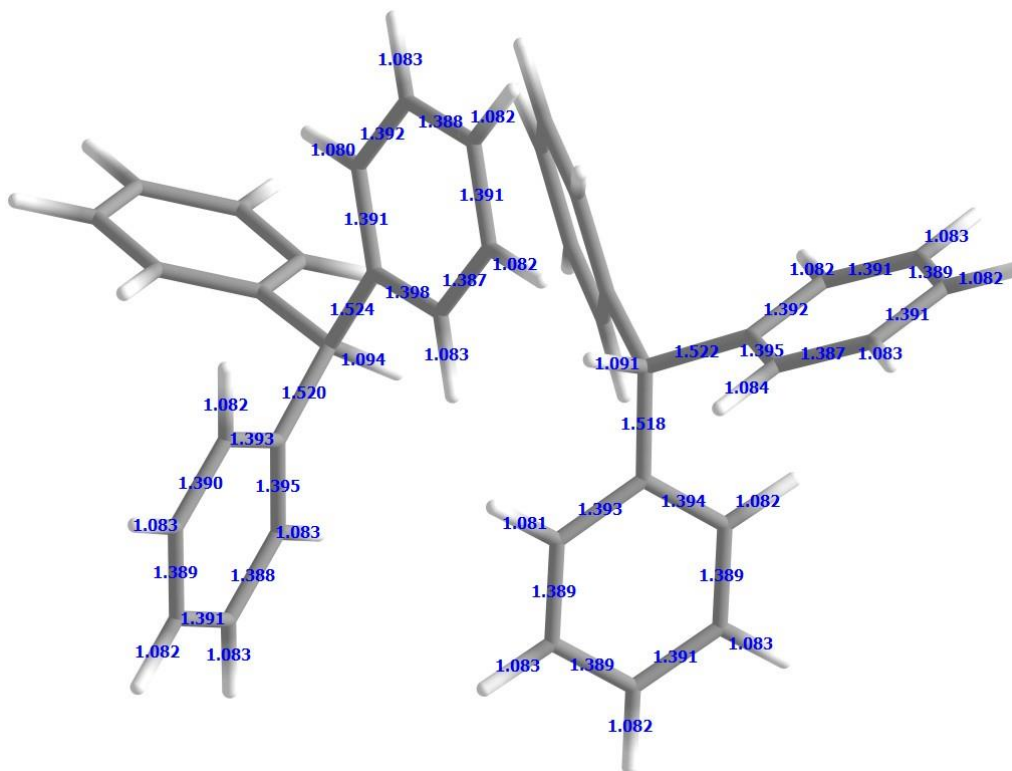


Figure S6a: Selected bond distances in Å within the **head-to-head** structure of the triphenylmethane dimer calculated at the B3LYP-D3(BJ)/def2-TZVP level.

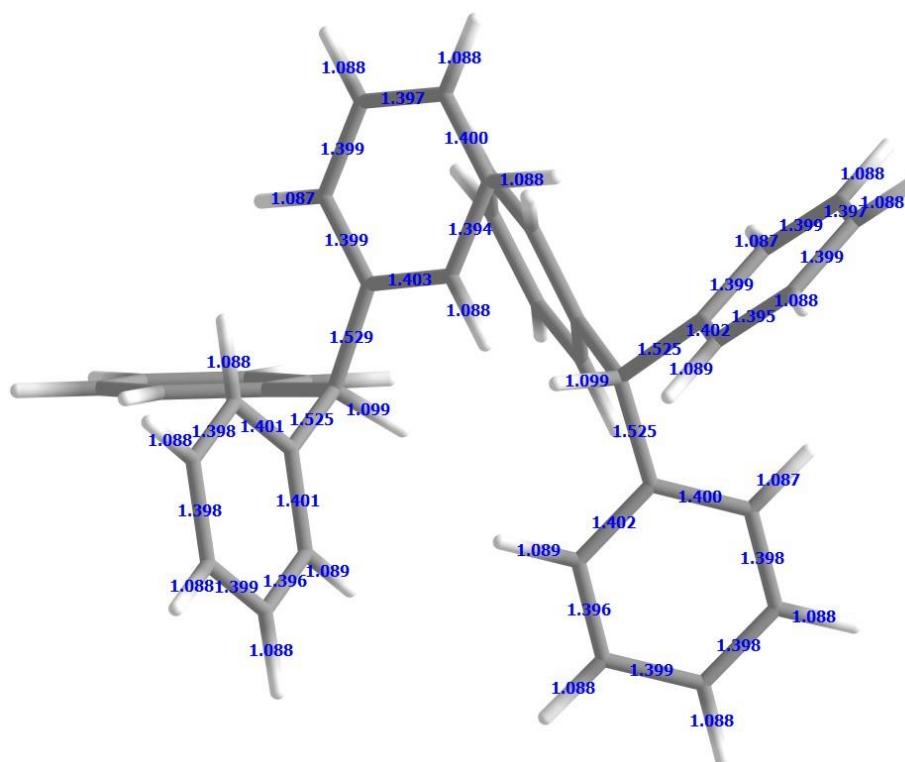


Figure S6b: Selected bond distances in Å within the **head-to-head** structure of the triphenylmethane dimer calculated at the B97-D/def2-TZVP level.

Table S1: Relative electronic energies ΔH as well as zero-point energy (ZPVE)-corrected relative energies ΔH_0 obtained at different computational levels. All energies have been corrected for the basis set superposition error (BSSE). All values are given in kJ/mol.

geometry	B3LYP-D3(BJ)/def2-TZVP		B97-D/def2-TZVP	
	ΔH	ΔH_0	ΔH	ΔH_0
head-to-head	12.8	11.8	10.2	11.0
head-to-tail	12.6	10.9	8.6	11.0
tail-to-tail	0.0	0.0	0.0	0.0

The obtained relative energies between the three isomers tail-to-tail, head-to-tail, and head-to-head at different computational levels are found in Table S1. All computations uniformly predict the tail-to-tail arrangement to be the most stable minimum structure, followed by the head-to-tail structure and the head-to-head geometry. This is in line with the initial considerations, assuming the strongest interaction within the ideally interlocked tail-to-tail structure and less stabilization in the head-to-tail and head-to-head isomers due to pronounced Pauli repulsion.

SAPT(0)/jun-cc-pVDZ^[21] computations yield further insight into the respective energy contributions composing the total interaction energy of all discussed structures (*cf.* Table S2): in all structures, LD is by far the dominant attractive contribution to the total interaction energy and its magnitude is decreasing from tail-to-tail *via* head-to-tail to head-to-head, as expected. The head-to-tail structure has about 6% less dispersion contribution than the tail-to-tail dimer, whereas it is 15% less in the head-to-head structure. Similarly, the electrostatic as well as induction contributions are decreasing from tail-to-tail *via* head-to-tail to head-to-head. The repulsive exchange contributions reflecting Pauli repulsion are of similar magnitude as the dispersion contribution for tail-to-tail and head-to-head just with reversed sign, whereas it is clearly smaller in the head-to-tail arrangement. In summary, all types of intermolecular interactions, including dispersion, are strongest within the tail-to-tail arrangement, yielding the largest total interaction of all competing motifs.

Table S2: Energy contributions obtained from SAPT(0)/jun-cc-pVDZ calculations. All values are given in kJ/mol.

geometry	E_{elst}	E_{exch}	E_{ind}	E_{disp}	E_{total}	ΔE_{total}
head-to-head	-31.1	69.2	-9.9	-78.7	-50.4	8.3
head-to-tail	-26.6	72.2	-8.6	-87.5	-50.5	8.2
tail-to-tail	-42.2	86.4	-10.0	-93.0	-58.7	0.0

2.2. All-*meta* *tert*-butyl triphenylmethane dimer (T^tBuPM)₂

2.2.1 Geometries and aliphatic C–H stretching frequencies (B3LYP-D3(BJ)/def2-TZVP level)

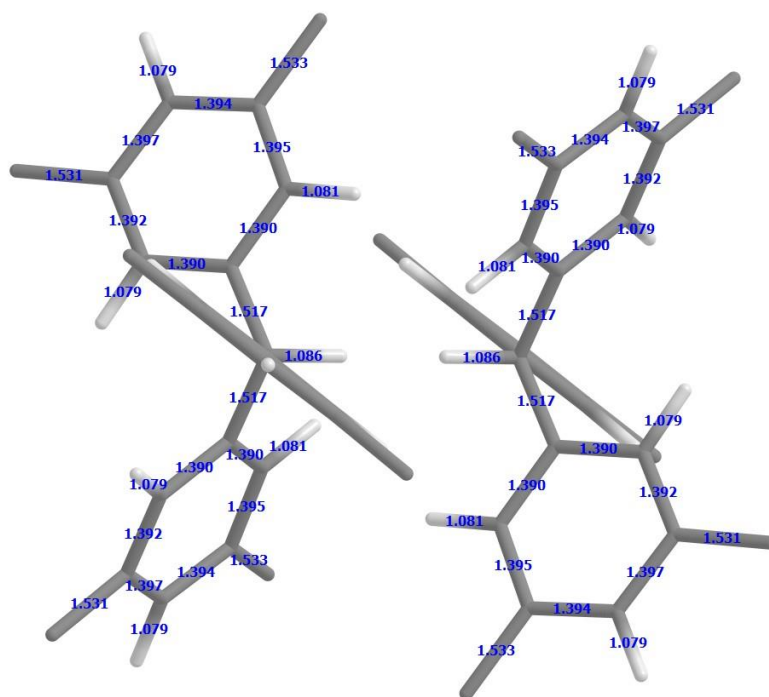


Figure S7: Selected bond distances in Å within the **head-to-head** structure of the all-*meta* *tert*-butyl triphenylmethane dimer calculated at the B3LYP-D3(BJ)/def2-TZVP level. Methyl groups are omitted for clarity.

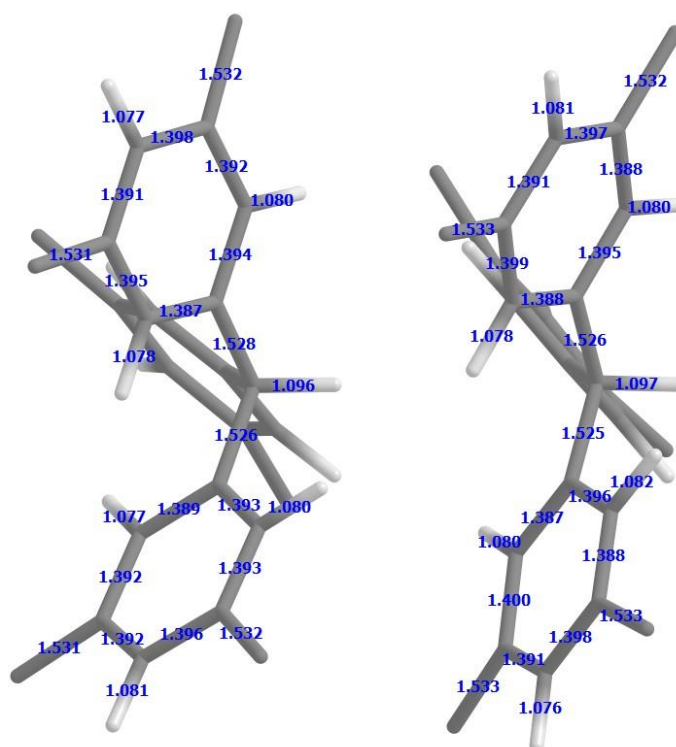


Figure S8: Selected bond distances in Å within the **head-to-tail** structure of the all-*meta* *tert*-butyl triphenylmethane dimer calculated at the B3LYP-D3(BJ)/def2-TZVP level. Methyl groups are omitted for clarity.

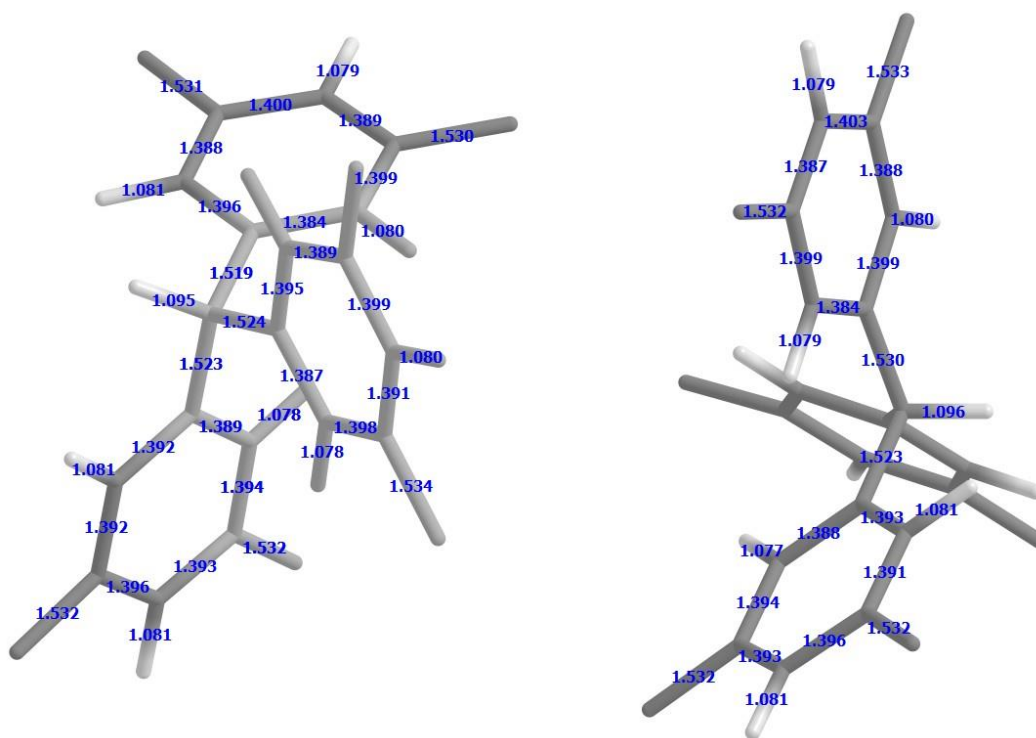


Figure S9: Selected bond distances in Å within the **tail-to-tail** structure of the all-*meta* *tert*-butyl triphenylmethane dimer calculated at the B3LYP-D3(BJ)/def2-TZVP level. Methyl groups are omitted for clarity.

Table S3: Geometry parameters for different dimer motifs of all-*meta* *tert*-butyl triphenylmethane at B3LYP-D3(BJ)/def2-TZVP level. The C-H distance in the monomer is 1.094 Å.

geometry	d(C,H) / Å	d(C,H) / Å	d(H,H) / Å
head-to-head	1.086	1.086	1.571
head-to-tail	1.096	1.097	4.675
tail-to-tail	1.095	1.096	11.376

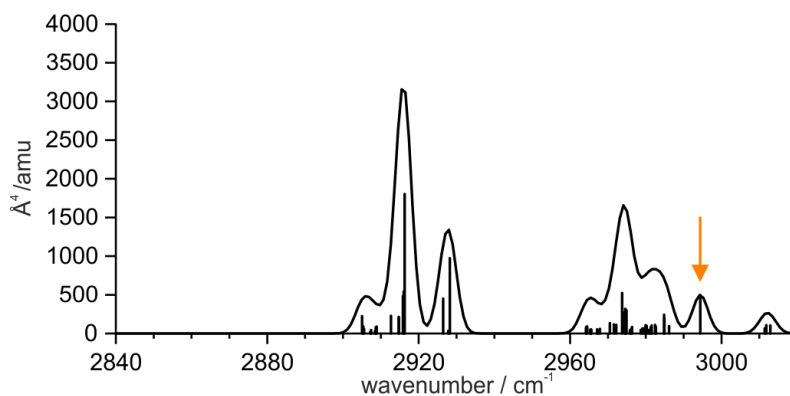


Figure S10a: Calculated harmonic C–H stretching frequencies with Raman intensities as obtained at the B3LYP-D3(BJ)/def2-TZVP level (FWHM = 5 cm⁻¹, Gaussian profile), for the all-*meta tert*-butyl triphenylmethane dimer **head-to-head** motif; scaling factor 0.96. The orange arrow indicates the aliphatic Raman active C–H-stretching vibration of the central C–H groups. This transition cannot be isolated, thus the central hydrogen atoms have been exchanged by deuterium.

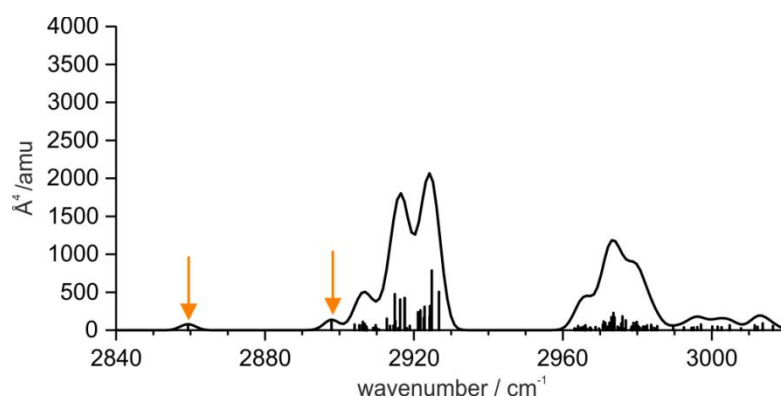


Figure S10b: Calculated harmonic C–H stretching frequencies with Raman intensities as obtained at the B3LYP-D3(BJ)/def2-TZVP level (FWHM = 5 cm⁻¹, Gaussian profile), for the all-*meta tert*-butyl triphenylmethane dimer **head-to-tail** motif; scaling factor 0.96. The orange arrows indicate the aliphatic C–H-vibrations of the central C–H groups. At least the more intense transition at 2898 cm⁻¹ cannot be isolated, thus the hydrogen atoms have been exchanged by deuterium.

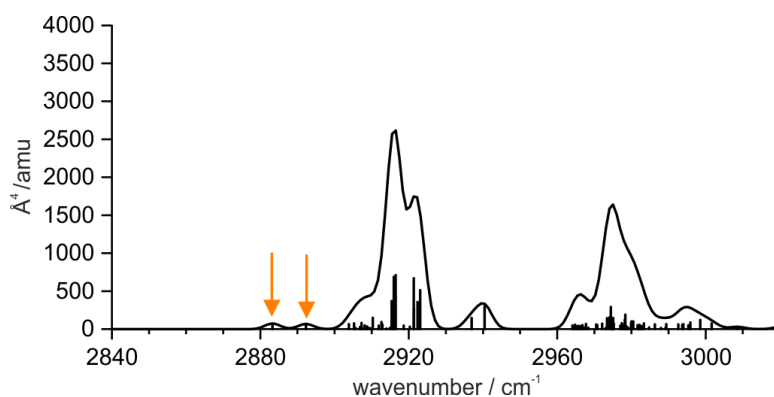


Figure S10c Calculated harmonic C–H stretching frequencies with Raman intensities as obtained at the B3LYP-D3(BJ)/def2-TZVP level (FWHM = 5 cm⁻¹, Gaussian profile), for the all-*meta tert*-butyl triphenylmethane dimer **tail-to-tail** motif; scaling factor 0.96. The orange arrows indicate the aliphatic C–H-vibrations of the central C–H groups. These transitions are very weak and very close to more intense vibrations. Thus again the exchange of the central hydrogen atoms against deuterium yields an isolation of the important stretching vibrations.

Table S4: IR intensities and Raman activities for the deuterated all-*meta tert*-butyl triphenylmethane dimer motifs calculated at B3LYP-D3(BJ)/def2-TZVP. The calculated transitions are scaled by 0.96.

geometry	wavenumber 1 / cm^{-1}	wavenumber 2 / cm^{-1}	IR intensity 1 / $(\text{km} \cdot \text{mol}^{-1})$	IR intensity 2 / $(\text{km} \cdot \text{mol}^{-1})$	Raman activity 1 / $\text{\AA}^4 \text{amu}^{-1}$	Raman activity 2 / $\text{\AA}^4 \text{amu}^{-1}$
head-to-head	2191	2198	0	2	292	0
head-to-tail	2100	2129	3	4	46	75
tail-to-tail	2119	2126	5	6	42	41

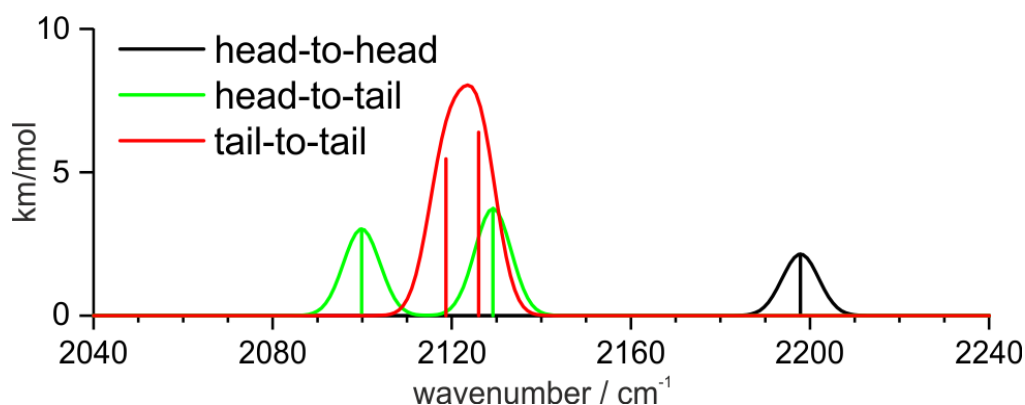


Figure S11: IR spectra of the deuterated all-*meta tert*-butyl triphenylmethane dimer motifs calculated at the B3LYP-D3(BJ)/def2-TZVP level (FWHM = 10 cm^{-1} , Gaussian profile), scaling factor of 0.96.

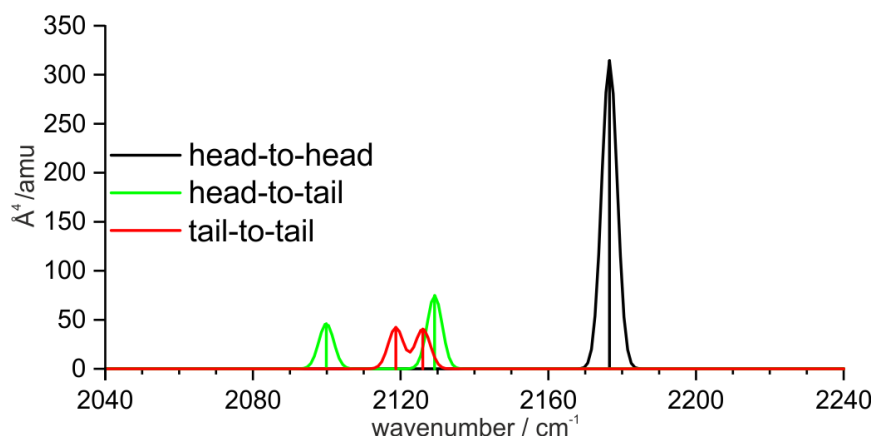


Figure S12: Raman spectra of the deuterated all-*meta tert*-butyl triphenylmethane dimer motifs calculated at the B3LYP-D3(BJ)/def2-TZVP level (FWHM = 5 cm^{-1} , Gaussian profile), scaling factor of 0.96.

The head-to-head and head-to-tail motifs exhibit a certain degree of symmetry considering the axis through the central aliphatic C–H bond. In the head-to-head motif we observe an S_6 -symmetric structure, whereas the head-to-tail motif is approximately C_3 -symmetric. The tail-to-tail motif is less symmetric, the slight bend in the CH–HC axis, which is close to linear in the other two motifs, leads to a decrease in symmetry. Compared to the structures of the unsubstituted triphenylmethane dimers (*cf.* Figure S3), we can observe some significant differences between corresponding structures. In the

unsubstituted case the six phenyl groups want to interlock with each other, which is best facilitated in a tail-to-tail arrangement, whereas in the substituted dimer a geometry that allows ideal interactions between the twelve *tert*-butyl groups is more favored. Thus the head-to-head motif is preferred.

In the head-to-head arrangement the strong contraction of the central aliphatic C–H units, caused by the Pauli repulsion, has a significant effect on the bond length, which is considerably shortened in comparison to the head-to-tail and tail-to-tail motifs (1.086 Å /1.096 Å). This results in a significant blue shift of the C–H (C–D) vibration. The scaled harmonic C–D stretching frequencies of this structure are at 2191 and 2198 cm^{-1} (see Table S4). Compared to the deuterated monomer (calculated at 2138 cm^{-1}), a blue-shift of about 56 cm^{-1} is predicted.

2.2.2 Geometries and aliphatic C–H stretching frequencies (B97D/def2-TZVP level)

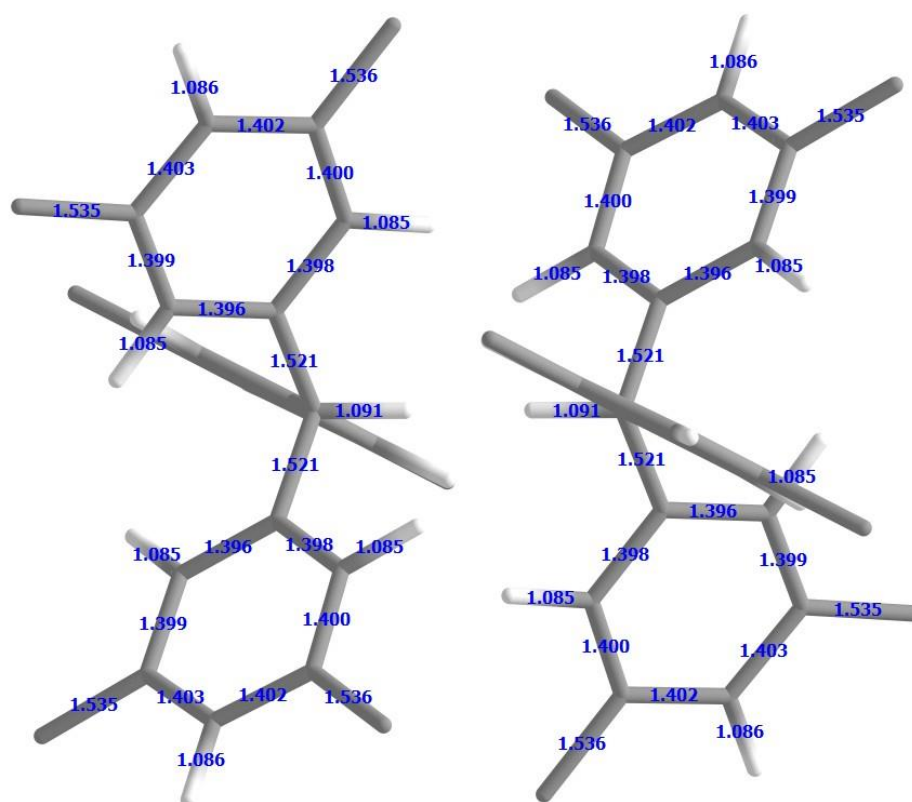


Figure S13: Selected bond distances in Å within the **head-to-head** structure of the all-*meta* *tert*-butyl triphenylmethane dimer calculated at the B97-D/def2-TZVP level. Methyl groups are omitted for clarity.

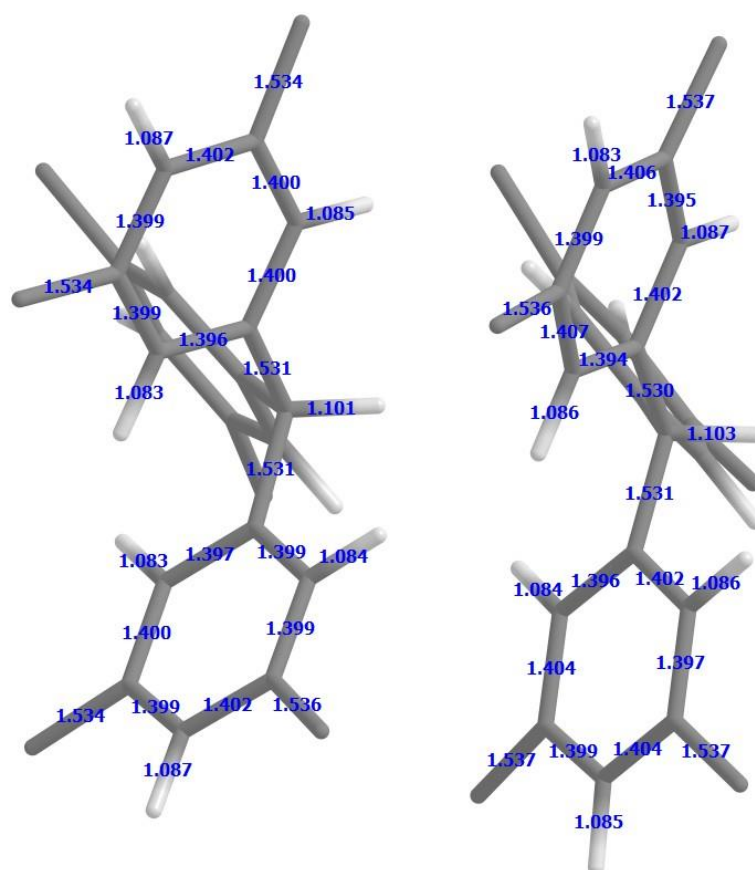


Figure S14: Selected bond distances in Å within the **head-to-tail** structure of the all-*meta* *tert*-butyl triphenylmethane dimer calculated at the B97D/def2-TZVP level. Methyl groups are omitted for clarity.

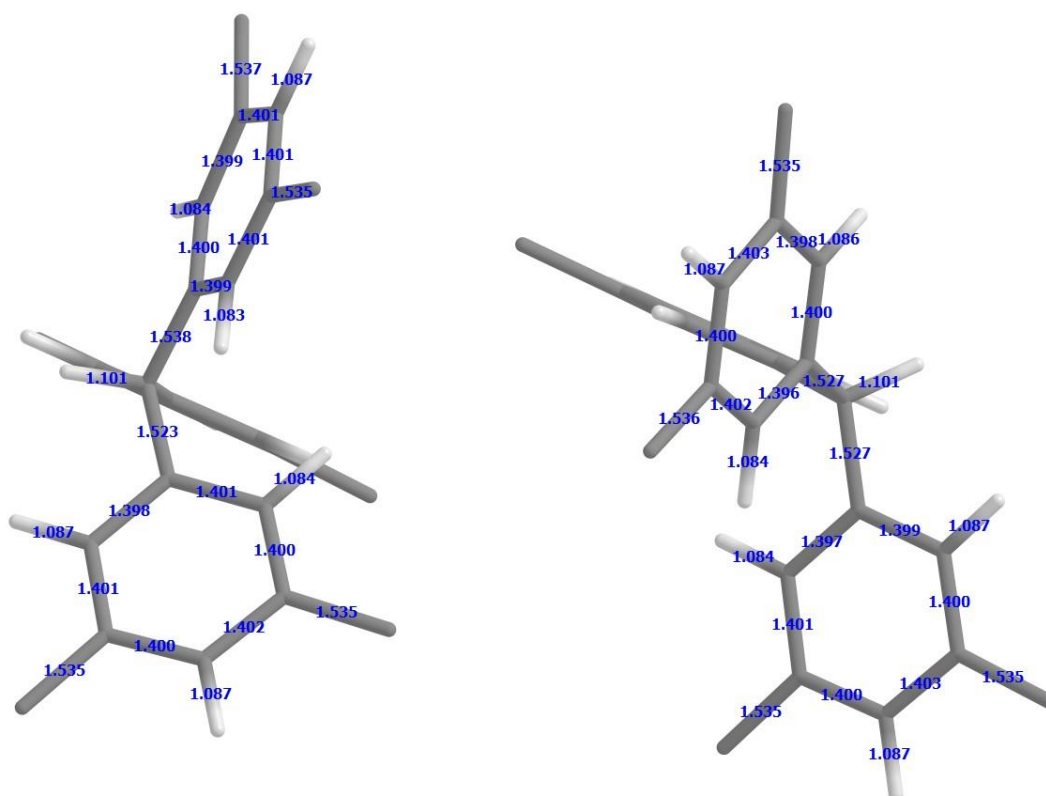


Figure S15: Selected bond distances in Å within the **tail-to-tail** structure of the all-*meta* *tert*-butyl triphenylmethane dimer calculated at the B97D/def2-TZVP level. Methyl groups are omitted for clarity.

Table S5: Geometry parameters for different dimer motifs of all-*meta tert*-butyl triphenylmethane at B97D/def2-TZVP level. The C-H distance in the monomer is 1.099 Å.

geometry	d(C,H) / Å	d(C,H) / Å	d(H,H) / Å
head-to-head	1.091	1.091	1.549
head-to-tail	1.101	1.103	4.627
tail-to-tail	1.101	1.101	11.512

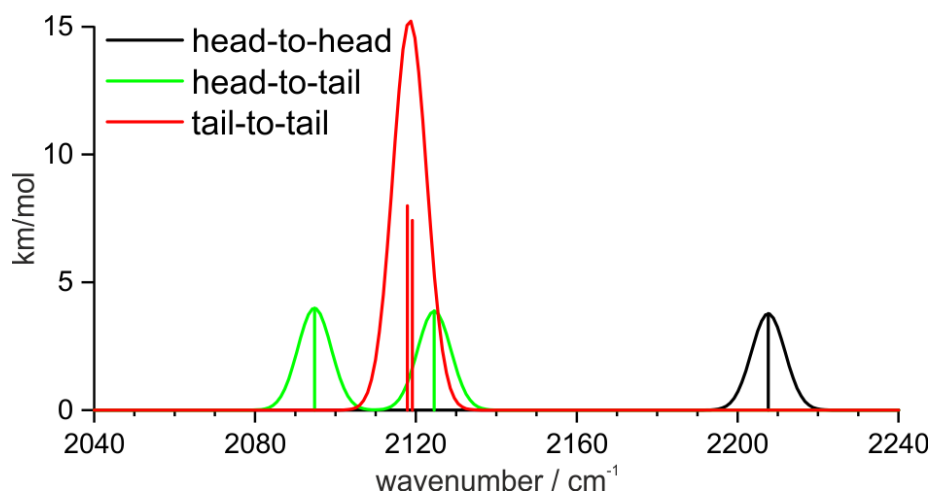


Figure S16: IR spectra of the deuterated all-*meta tert*-butyl triphenylmethane dimer motifs calculated at the B97D/def2-TZVP level (FWHM = 10 cm⁻¹, Gaussian profile); scaling factor of 0.98.

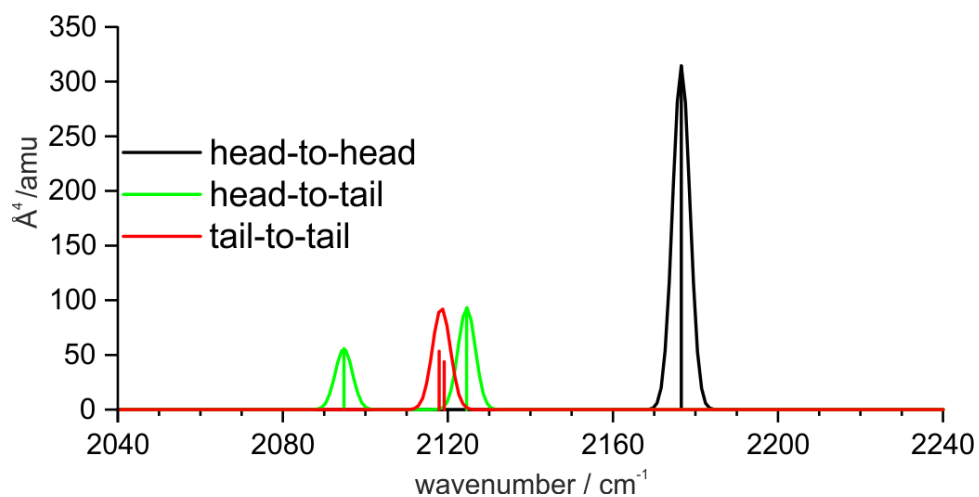


Figure S17: Raman spectra of the deuterated all-*meta tert*-butyl triphenylmethane dimer motifs calculated at the B97D/def2-TZVP level (FWHM = 5 cm⁻¹, Gaussian profile); scaling factor of 0.98.

Table S6: IR intensities and Raman activities for the deuterated all-*meta tert*-butyl triphenylmethane dimer motifs calculated at B97D/def2-TZVP level. The calculated transitions are scaled by 0.98.

geometry	wavenumber 1 / cm ⁻¹	wavenumber 2 / cm ⁻¹	IR intensity 1 /(km [*] mol ⁻¹)	IR intensity 2 /(km [*] mol ⁻¹)	Raman activity 1 / Å ⁴ amu ⁻¹	Raman activity 2 / Å ⁴ amu ⁻¹
head-to-head	2177	2208	0	4	314	0
head-to-tail	2095	2125	4	4	56	93
tail-to-tail	2118	2119	8	7	53	44

2.2.3 Anharmonic calculations

To get a better description of the aliphatic C–D/H vibrations, especially with respect to the observed spectral blue-shift in case of the head-to-head structure, anharmonic calculations along the localized normal modes Q are performed. The corresponding Hamilton operator (with reduced mass μ taken from the normal mode analyses) is:

$$\hat{H} = -\frac{\hbar^2}{2\mu} \frac{d^2}{dQ^2} + V(Q) \quad (2)$$

The potential energy curves $V(Q)$ of the head-to-head isomer, head-to-tail, and tail-to-tail isomers are presented in Figures S18-S23 (B3LYP-D3(BJ)/def2-TZVP level) respectively, together with the corresponding harmonic oscillator potentials obtained from the normal mode analyses. By using the Ritz variational method, harmonic oscillator functions are taken as basis. Already with six basis functions the expectation (eigen) values converge with an uncertainty of less than 1 cm⁻¹.

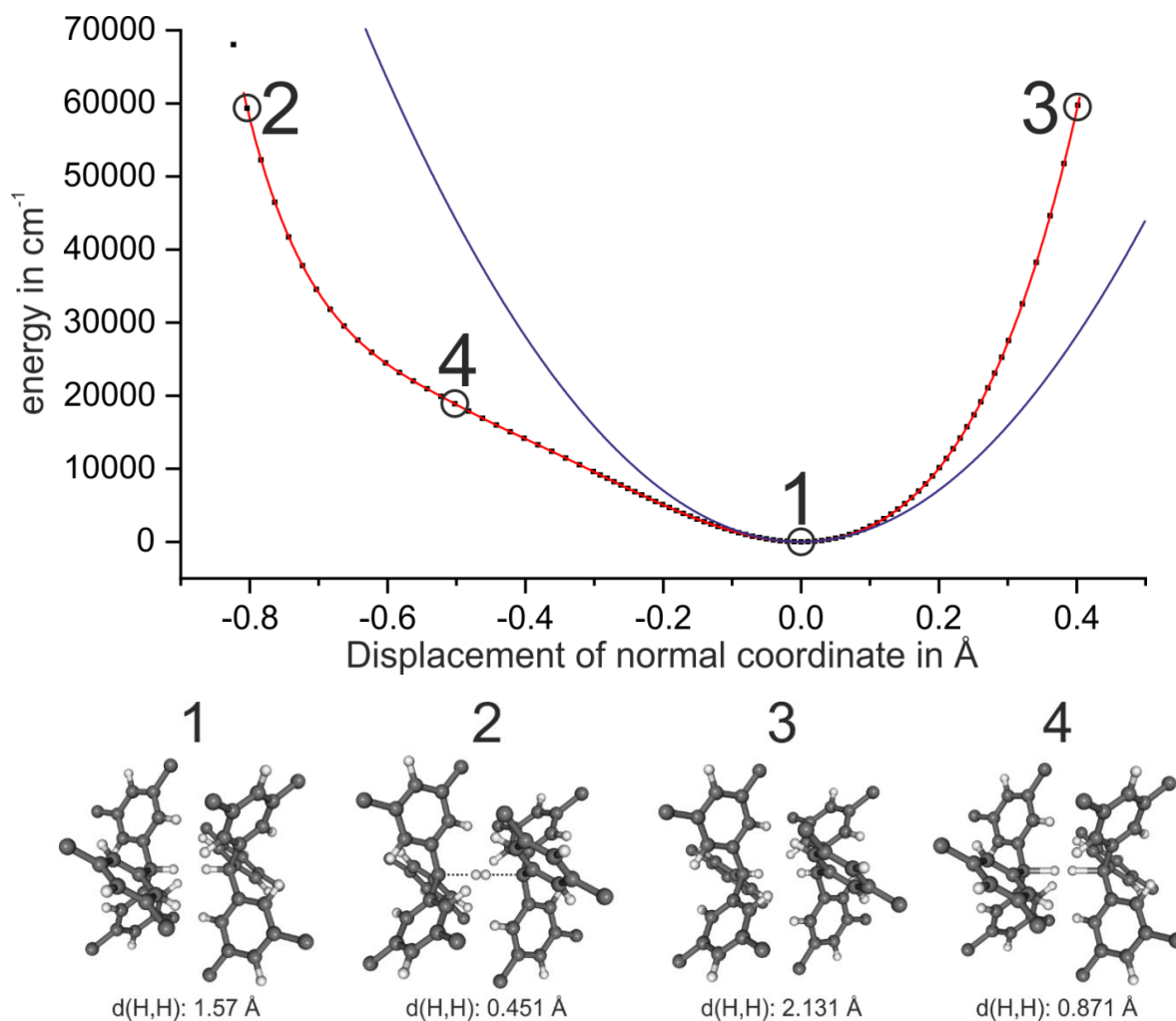


Figure S18: Potential curve of the **head-to-head** structure of the deuterated all-*meta tert*-butyl triphenylmethane dimer along the symmetric C–D vibration of the two C–D groups. Calculations are performed at the B3LYP-D3(BJ)/def2-TZVP level. The potential curve corresponding to the harmonic case is drawn in blue. Selected geometries are marked in the curve and shown below. Methyl groups are omitted for clarity.

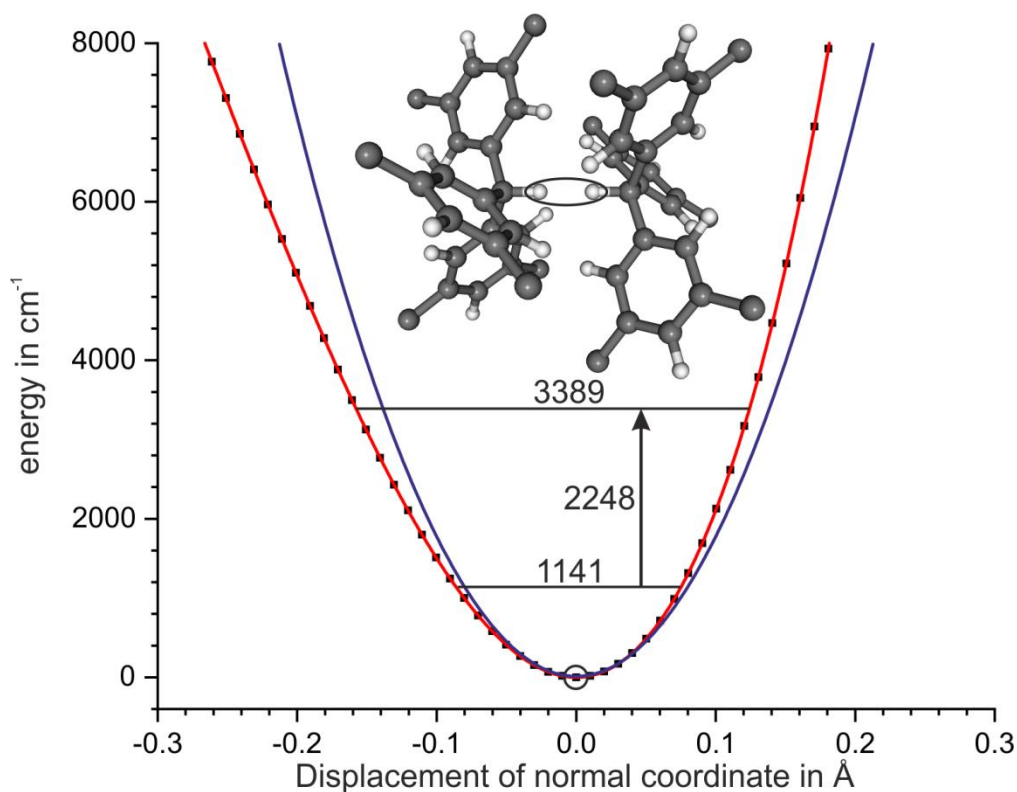


Figure S19: Inset of the potential curve of the **head-to-head** structure of the deuterated all-*meta tert*-butyl triphenylmethane dimer along the symmetric C–D vibration of the two C–D groups (indicated by the circle.) The potential energy is calculated at the B3LYP-D3(BJ)/def2-TZVP level. The potential curve corresponding to the harmonic case is drawn in blue. Methyl groups are omitted for clarity.

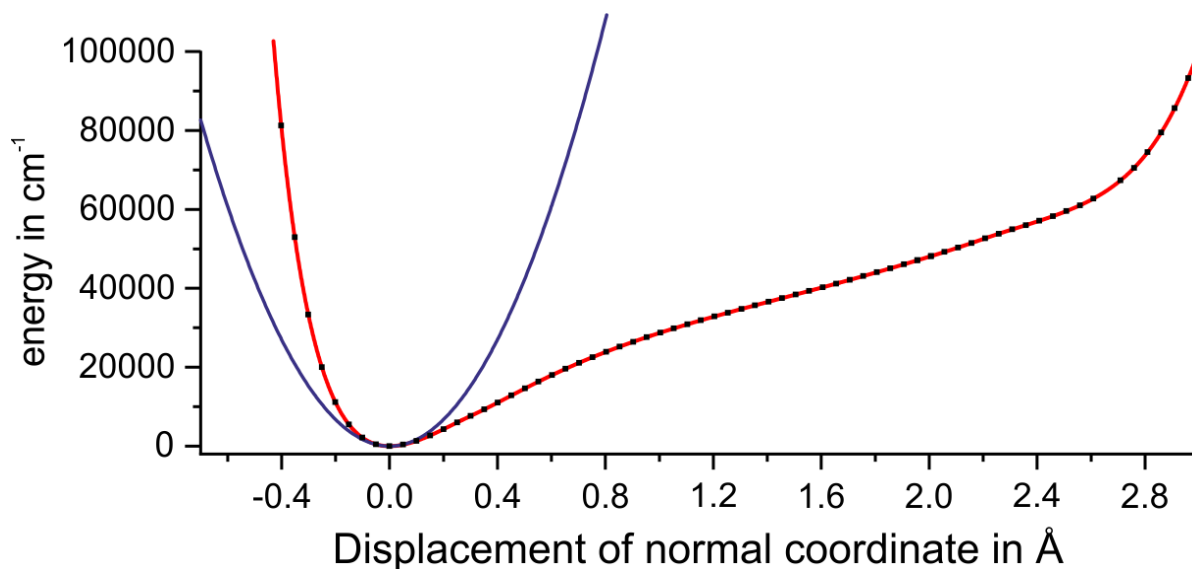


Figure S20: Potential energy curve of the **head-to-tail** structure of the deuterated all-*meta tert*-butyl triphenylmethane dimer calculated at the B3LYP-D3(BJ)/def2-TZVP level. The anharmonic calculations refer to the indicated C–D stretching group (cf. Figure S21). The potential curve corresponding to the harmonic case is drawn in blue.

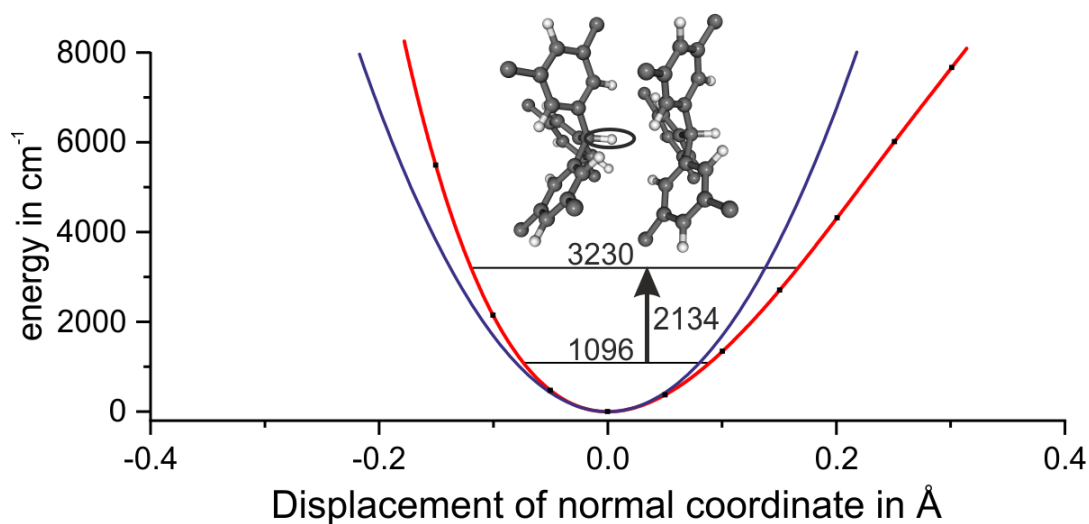


Figure S21: Inset of the potential curve of the **head-to-tail** structure of the deuterated all-*meta tert*-butyl triphenylmethane dimer calculated at the B3LYP-D3(BJ)/def2-TZVP level. The anharmonic calculations refer to the indicated C–D stretching group. The potential curve corresponding to the harmonic case is drawn in blue.

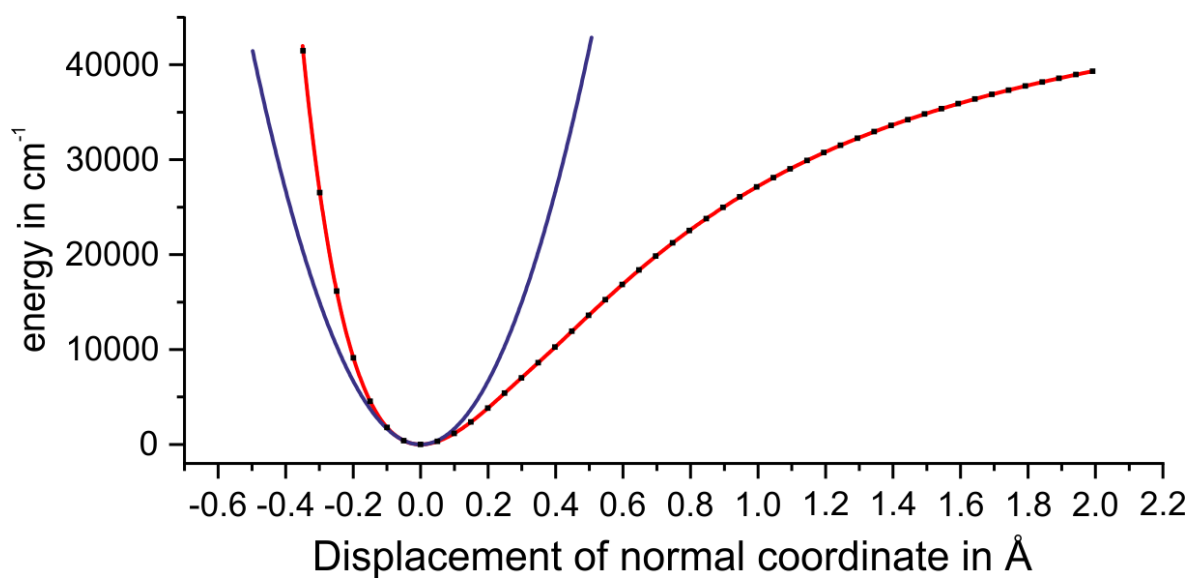


Figure S22: Potential energy curve of the **tail-to-tail** structure of the deuterated all-*meta tert*-butyl triphenylmethane dimer calculated at the B3LYP-D3(BJ)/def2-TZVP level. The anharmonic calculations refer to the indicated C–D stretching groups (cf. Figure S23) which have almost identical vibrational frequencies. The potential curve corresponding to the harmonic case is drawn in blue.

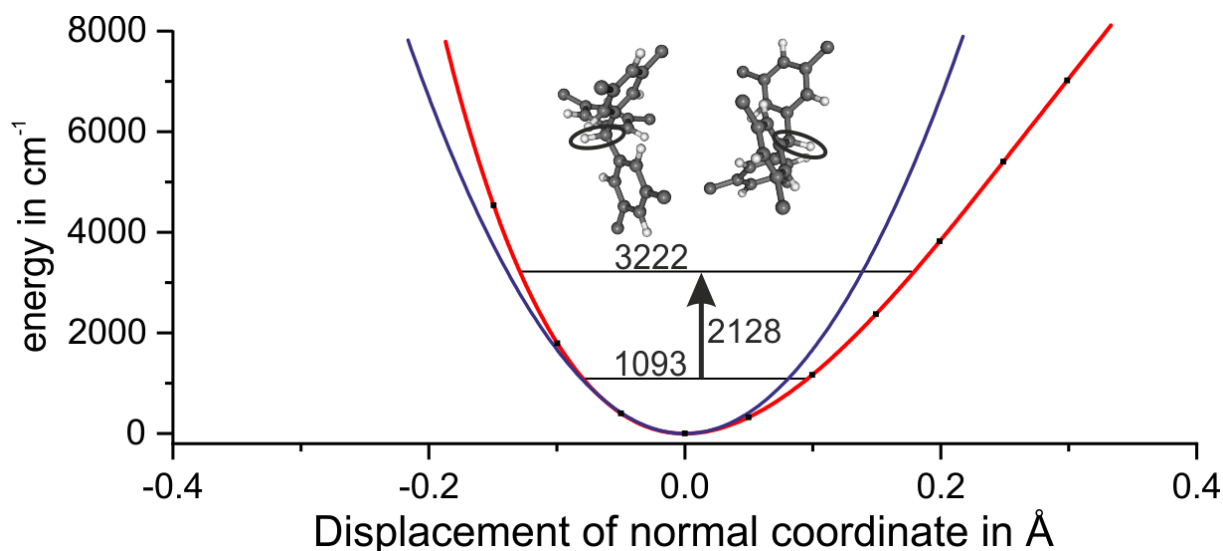


Figure S23: Inset of the potential curve of the **tail-to-tail** structure of the deuterated all-*meta tert*-butyl triphenylmethane dimer calculated along the symmetric C–D vibration of the two C–D groups (indicated by the circles). The calculations are performed at the B3LYP-D3(BJ)/def2-TZVP level. The potential curve corresponding to the harmonic case is drawn in blue.

2.2.4 Dissociation energies and SAPT(0) calculations

BSSE-corrected calculations allow the determination of dissociation and deformation energies which are given in Table S7 and S8 for the B97D/def2-TZVP and B3LYP-D3(BJ)/def2-TZVP level, respectively. The deformation energy describes the difference between the optimized geometry of the T^tBuPM monomer and the energy of the monomer as obtained in the dimer. The head-to-head motif exhibits the highest dissociation energy, whereas the dissociation energy of the tail-to-tail structure is 60%/53% lower. The difference to the head-to-tail motif is considerably smaller with a dissociation energy which is only 9%/18% lower than in the head-to-head arrangement. By comparing the deformation energies, we observe that the head-to-tail structure requires the most reorganization upon dimer formation with the larger contribution of monomer B (monomer on right side of Figure S14). For symmetry reasons both monomers of the head-to-head arrangement exhibit the same amount of deformation energy.

Table S7: Dissociation and deformation energies from BSSE-corrected DFT/B97-D/def2-TZVP calculations. All values are given in kJ/mol.

geometry	Dissociation energy of Dimer AB	Deformation energy of Monomer A	Deformation energy of Monomer B
head-to-head	132.0	12.0	12.0
head-to-tail	120.2	4.7	22.6
tail-to-tail	80.5	9.5	1.0

Table S8: Dissociation and deformation energies from BSSE-corrected DFT/B3LYP-D3(BJ)/def2-TZVP calculations. All values are given in kJ/mol.

geometry	Dissociation energy of Dimer AB	Deformation energy of Monomer A	Deformation energy of Monomer B
head-to-head	127.2	11.5	11.5
head-to-tail	104.4	5.6	24.9
tail-to-tail	58.6	7.9	5.2

As mentioned above (chapter 2.1.), SAPT(0)/jun-cc-pVDZ calculations yield further insight into the respective energy contributions composing the total interaction energy of all discussed structures (*cf.* Table S9 and S10). For B97-D, the head-to-tail motif exhibits the largest amount of dispersion energy but this attractive contribution is overcompensated by the repulsive exchange term reflecting the Pauli repulsion. The same behavior is observed for the tail-to-tail case, the repulsive exchange term is larger than the attractive dispersion term. The electrostatic as well as the induction contributions are decreasing from head-to-head to tail-to-tail.

The SAPT(0) calculations for the geometries optimized with B3LYP-D3(BJ) follow a similar trend but show some key differences (*cf.* Table S10). The contribution of the dispersion energy is now nearly equal between the head-to-head and head-to-tail motif. By comparing these values to the exchange terms the sum has a negative sign, so no overcompensation as in the B97-D case takes place. It should be noted that the exchange energy for the head-to-tail motif is 3% larger in comparison to the head-to-head motif. This suggests that the dimer retains most of its dispersion energy by turning one unit by 180 ° but the ideal interlocking of the *tert*-butyl group is lost and leads to an increase in Pauli-repulsion and thus in exchange energy.

In summary, the SAPT(0) calculations estimate the same ordering of the three binding motifs with no dependence on the chosen functional. The disparity of exchange energy and dispersion energy in the B97-D case seems to indicate that these geometries are less “relaxed” in comparison to the B3LYP geometries. This is also supported by comparison of the total energies which are considerably lower for B3LYP-D3(BJ)/def2-TZVP.

Table S9: Energy contributions obtained from SAPT(0)/jun-cc-pVDZ calculations for the B97-D/def2-TZVP geometries. All values are given in kJ/mol.

geometry	E_{elst}	E_{exch}	E_{ind}	E_{disp}	E_{total}	ΔE_{total}
head-to-head	-98.6	269.4	-36.0	-273.5	-138.7	0
head-to-tail	-98.3	285.7	-28.4	-283.9	-124.9	13.8
tail-to-tail	-52.3	163.2	-15.1	-162.4	-66.6	72.2

Table S10: Energy contributions obtained from SAPT(0)/jun-cc-pVDZ calculations for the DFT/B3LYP-D3(BJ)/def2-TZVP geometries. All values are given in kJ/mol.

geometry	E_{elst}	E_{exch}	E_{ind}	E_{disp}	E_{total}	ΔE_{total}
head-to-head	-79.1	213.7	-28.6	-253.2	-147.1	0
head-to-tail	-75.7	219.8	-22.0	-252.0	-130.0	17.1
tail-to-tail	-33.1	107.5	-9.1	-125.8	-60.5	86.7

3. Experimental Results

3.1. Triphenylmethane and triphenylmethane dimer

In order to obtain detailed structural information on the triphenylmethane-based aggregates by using IR/R2PI, IGSR and ILSR spectroscopy, knowledge of relevant UV excitation energies is required. Therefore, R2PI spectra have been recorded in the range of 36800–37800 cm^{-1} .

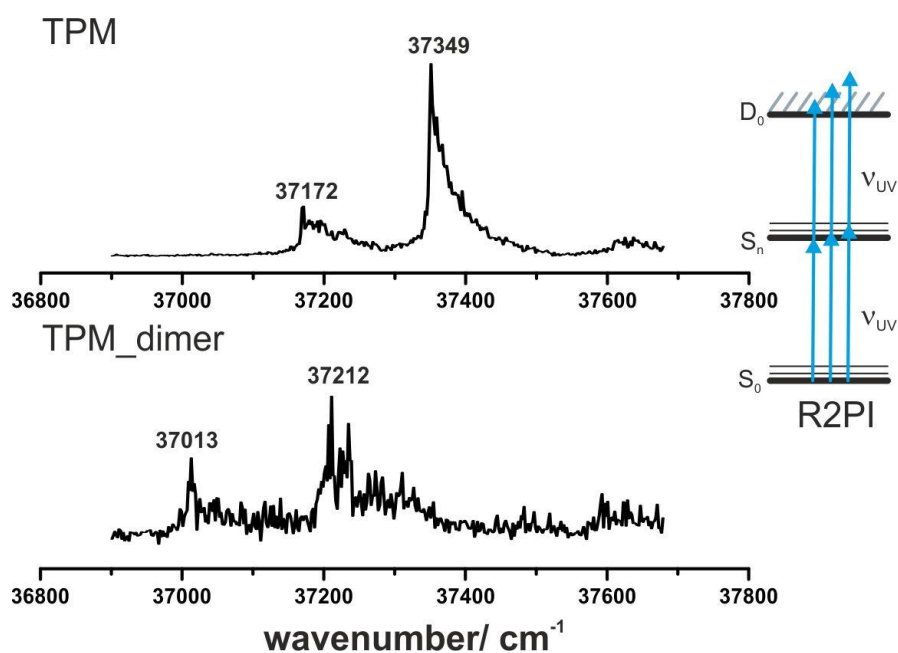


Figure S24: R2PI spectra for TPM and TPM₂, carrier gas neon.

The R2PI spectrum of the TPM monomer (cf. Figure S24 upper trace) exhibits an electronic origin at 37172 cm^{-1} along with a second transition at 37349 cm^{-1} , being blue-shifted by 177 cm^{-1} with respect to the electronic origin. The R2PI spectrum of the TPM dimer (cf. Figure S24 lower trace) shows its electronic origin at 37013 cm^{-1} , indicating a red-shift of 159 cm^{-1} compared to the electronic origin of the monomer.

The IGSR spectrum of the **TPM monomer** was recorded by fixing the exciting UV laser at 36765 cm^{-1} , which is 407 cm^{-1} below the $S_1 \leftarrow S_0$ transition. The spectrum is depicted in Figure S25.

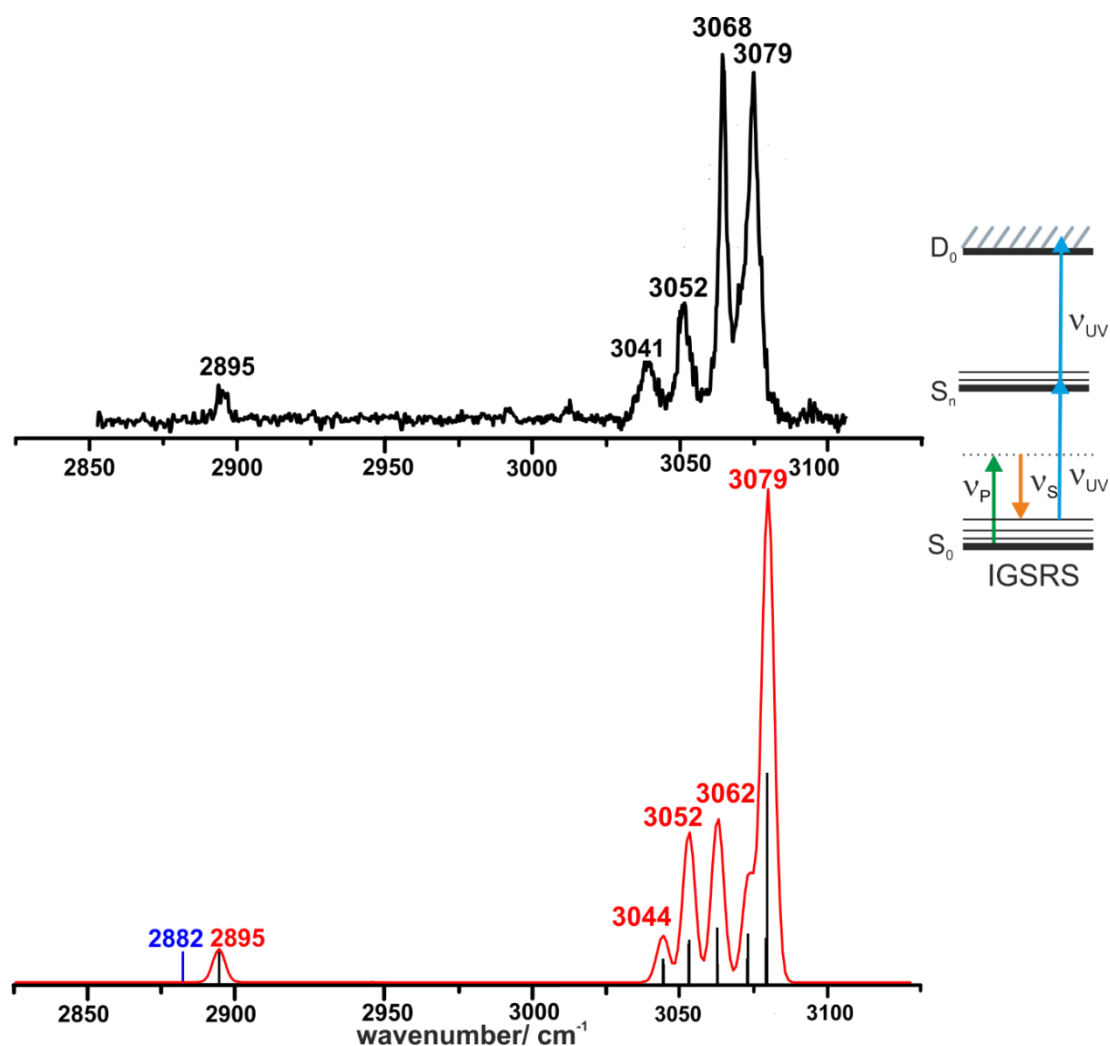


Figure S25: IGSR spectrum of TPM in the C–H stretching region using neon as carrier gas compared to calculated vibrational frequencies with corresponding relative Raman intensities obtained at the B3LYP-D3(BJ)/def2-TZVP level (FWHM = 5 cm^{-1} , Gaussian profile). The scaling factors of 0.958 (aliph. C–H) and 0.963 (arom. C–H) for the harmonic vibrational frequencies are obtained with respect to the aliphatic C–H stretching vibration at 2895 cm^{-1} and the aromatic C–H stretching vibration at 3079 cm^{-1} . The anharmonically calculated aliphatic C–H stretching vibration is indicated in blue.

The IGSR spectrum of the TPM monomer exhibits a sharp transition at 2895 cm^{-1} corresponding to the single aliphatic C–H stretching vibration of TPM (anharmonic calculation as described in section 2.2.). Regarding the aromatic C–H stretching region, the vibrations corresponding to the C–H moieties within the three phenyl rings are observed at 3041 , 3052 and 3068 and 3079 cm^{-1} ,

respectively. This clearly structured spectrum already indicates degenerate vibrations due to the expected C_3 -symmetry of the TPM molecule. All transitions exhibit a sufficient agreement to the calculated C–H stretching vibrations for the C_3 -symmetric TPM molecule at the B3LYP-D3(BJ)/def2-TZVP level. Merely the relative intensities are deviating from the prediction, especially regarding the intense transitions at 3068 cm^{-1} . This is the same behaviour as in the case of the ILSR spectrum of the TPM dimer (cf. Figure 2). By comparing the recorded IGSR spectrum of the isolated molecule to a condensed phase spontaneous Raman spectrum,^[22] discrepancies regarding relative intensities are obvious: the prominent transitions at 3068 and 3079 cm^{-1} occur with much less intensity in the condensed phase spectrum.^[22] This leads to the conclusion that the stimulated Raman process somehow strongly promotes these transitions compared to the spontaneous case.

In Figure S26 the IR/R2PI spectrum of the TPM monomer is depicted. The experimental spectrum exhibits the same transitions as the Raman spectrum (Figure S25). The aliphatic C–H stretching vibration at 2895 cm^{-1} is again clearly visible. In a direct comparison a very good agreement of the position of the C–H stretching vibrations of both spectroscopic methods can be obtained. Only the intensities differ. This may result from a coupling of IR active C–H bending overtone transitions with C–H stretching modes. The transition at 3096 cm^{-1} is also observed in Ref. ^[22] and supports our interpretation as an overtone vibration of the fundamental transition of 1558 cm^{-1} . This vibration represents a C–C framework vibration of the TPM monomer.

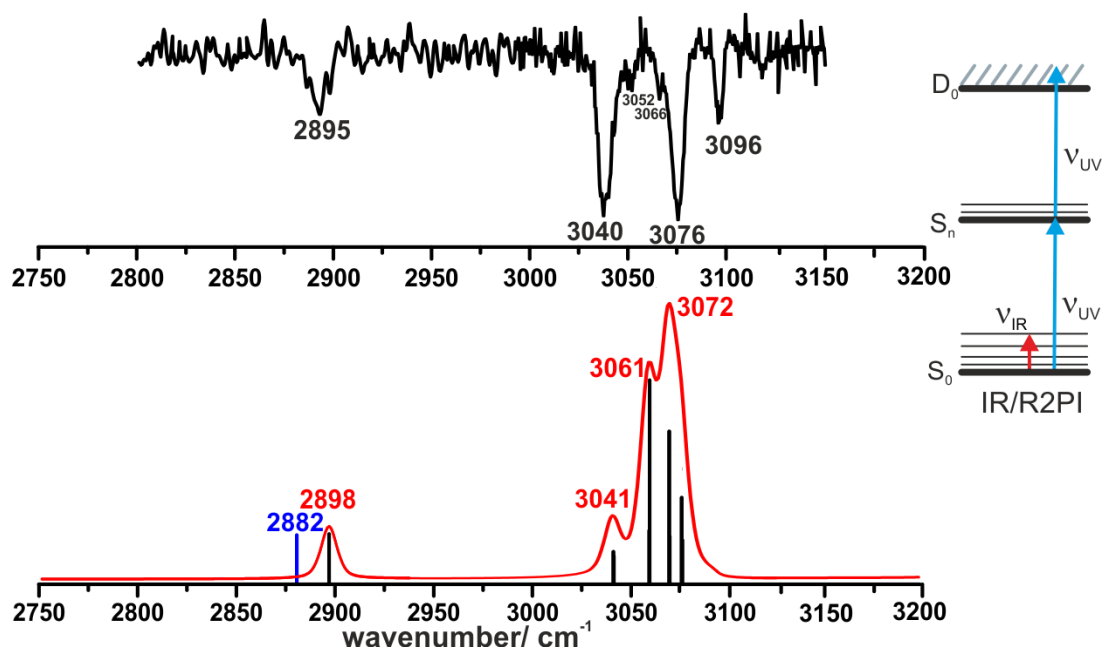


Figure S26: IR/R2PI spectrum of TPM in the C–H stretching region using neon as carrier gas compared to calculated vibrational frequencies with corresponding relative IR intensities obtained at the B3LYP-D3(BJ)/def2-TZVP level (FWHM = 10 cm^{-1} , Gaussian profile). The IR/R2PI spectrum of the TPM monomer was recorded by fixing the exciting UV laser on 37349 cm^{-1} ; scaling factors for the harmonic vibrational frequencies are 0.958 (aliph. C–H) and 0.963 (arom. C–H); see Figure S25. The anharmonically calculated aliphatic C–H vibrational frequency is given in blue.

For the **TPM dimer** also IR/R2PI measurements were carried out (Figure S27) and compared to the Raman spectrum (shown in Figure 2). As in the case of the TPM monomer the band positions of the aromatic C–H stretching modes are well described. Similar to the TPM monomer (vibration at 3096 cm^{-1} , see Figure S26), the vibration at 3094 cm^{-1} is assigned to an overtone transition.

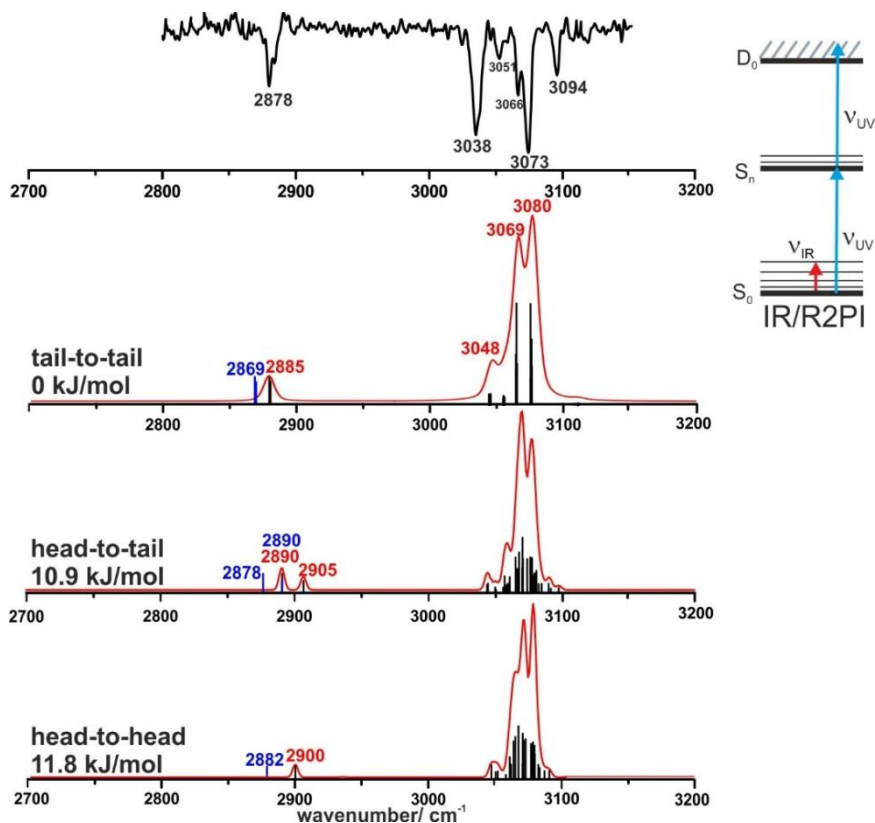


Figure S27: IR/R2PI spectrum of the TPM dimer in the C–H stretching region using neon as carrier gas compared to calculated vibrational frequencies with corresponding relative IR intensities obtained at the B3LYP-D3(BJ)/def2-TZVP level (FWHM = 10 cm^{-1} , Gaussian profile). The IR/R2PI spectrum of the TPM dimer was recorded by fixing the exciting UV laser at 37212 cm^{-1} ; scaling factors for the harmonic vibrational frequencies are 0.958 (aliph. C–H) and 0.963 (arom. C–H); see Figure S25. The anharmonically calculated aliphatic C–H vibrational frequencies are given in blue.

By comparing the three different arrangements, the central C–H moieties of the TPM units are in different environments. This is reflected in the corresponding aliphatic C–H stretching vibrations: Within the nearly S_6 -symmetric tail-to-tail structure, the two degenerated aliphatic C–H stretching vibrations are anharmonically predicted at 2869 cm^{-1} (see Figure S27), i.e. these vibrations are slightly red-shifted compared to the TPM monomer (anharmonically predicted at 2882 cm^{-1} , see Figure S26). The same red-shift is observed with respect to harmonic calculations (2885 cm^{-1} in the dimer compared to 2898 cm^{-1} in the monomer). This is in excellent agreement to the experimental results, indicating a red-shift of 17 cm^{-1} (2895 cm^{-1} for the monomer vs 2878 cm^{-1} for the dimer). In case of the head-to-head arrangement one frequency of the two aliphatic C–H stretching vibrations is predicted to be identical with respect to the monomer. This vibration at 2882 cm^{-1} has a small IR intensity, the second transition is anharmonically predicted at 2925 cm^{-1} and has no IR intensity. (Thus the transition is not shown in Figure S27). Finally, within the head-to-tail arrangement, a splitting of the two vibrations is expected with one frequency being blue-shifted and the other one

slightly red-shifted to the monomer-frequency. Both with respect to the predicted vibrational frequencies and the relative intensities of the aliphatic C–H stretching modes only the tail-to-tail arrangement agrees with the experimentally observed vibrational transition at 2878 cm^{-1} . These results with respect to the aliphatic C–H stretching modes clearly support the assignment of the tail-to-tail arrangement as already discussed on the basis of the Raman (ILSR) spectrum, see Figure 2. It should be mentioned that the aliphatic C–H stretching vibrations have not been observed in the Raman spectra. This may result from their up to a factor of 10 lower Raman activities compared to the one of the aromatic stretching vibrations.

3.2. All-*meta tert*-butyl triphenylmethane dimer (T^tBuPM)₂

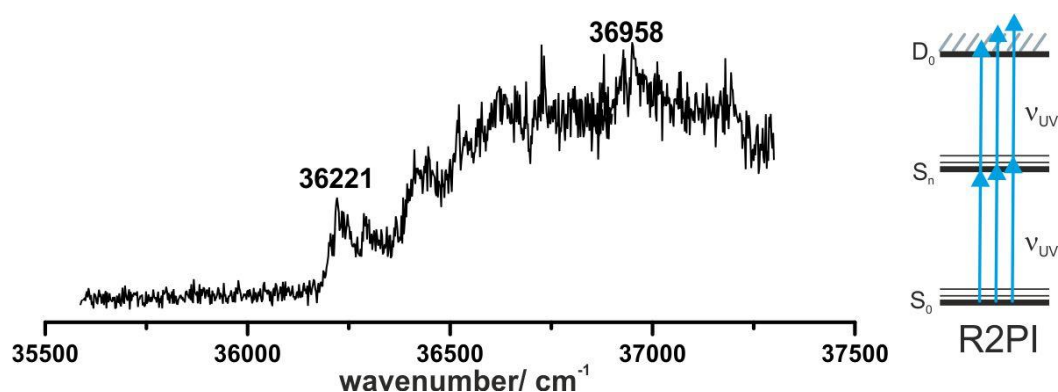


Figure S28: R2PI spectrum of the T^tBuPM dimer, carrier gas neon.

The R2PI spectrum of the T^tBuPM dimer (Figure S28) exhibits a strong electronic transition at 36221 cm^{-1} (the electronic origin of the T^tBuPM dimer is red-shifted to the unsubstituted dimer because of the +I effects of the *tert*-butyl groups^[23]). The ILSR spectrum shown in Figure 4 has been recorded *via* the transition at 36958 cm^{-1} . For this transition a strong ion signal is observed which has been sufficiently high enough to record the very demanding Raman spectra.

Relative Intensities in the ILSR spectrum and assignment of the transition at 2134 cm^{-1} (*cf.* Figure 4 of the Communication):

By comparing the areas under the two bands observed in the ILSR spectrum (*cf.* Figure 4 of the manuscript) a ratio of about 7:1 for the two transitions at 2270 vs. 2134 cm^{-1} is obtained. As mentioned in the manuscript the assignment to the head-to-head structure (with respect to the transition at 2270 cm^{-1}) is unambiguous, but for the second transition at 2134 cm^{-1} different explanations can be discussed:

One explanation for the transition at 2134 cm^{-1} could be derived from an observation of an overtone vibration (see also transitions observed at 3096/3094 cm^{-1} in the TPM monomer/dimer, respectively (Figures S26 and S27)). There are four C–D bending vibrations arising from the central C–D groups, two of them are located at 1062 cm^{-1} (unscaled: 1073 cm^{-1}) and the other at 1065 cm^{-1} (unscaled 1076 cm^{-1}). The scaling factor of 0.99^[24] is a kind of standard factor at the B3LYP-D3/def2-TZVP level in the spectral region around 1000 cm^{-1} . The C–D bending vibrations are localized on the

central binding motif of the head-to-head arrangement but these vibrations are coupled, i.e. both C–D groups are involved in the corresponding bending vibration. The predicted overtone vibration is almost identical to the observed vibration at 2134 cm^{-1} ; anharmonic effects are not included and lead to a (small) deviation from a pure doubling of the harmonic wavenumber. This overtone interpretation fits very well to the experimentally observed vibrational transition. If the transition at 2134 cm^{-1} belongs to an overtone only the thermodynamically most stable head-to-head structure would be formed in the molecular beam expansion.

Another explanation may arise from the existence of a head-to-tail or/and a tail-to tail arrangement. In this case kinetic trapping must occur since the thermodynamic stability should lead to an exclusive population of the head-to-head arrangement. Also, if only one of the two structures (head-to-tail, tail-to-tail) is formed, the relative intensities in the spectrum clearly indicate that the head-to-head arrangement is the one which is formed in largest amount. Of course, an additional general argument against a population analysis via the area of the peaks is the question, if all structures show the same efficiency with respect to the ILSR method. This assumption would be justified since all structures have the same chromophores. However, an exact relative population cannot be derived from the peak intensities.

If kinetic trapping occurs it has to be clarified if an interconversion to the most stable structure would be possible. Thus the energies required for interconversion of the different isomers has to be estimated. A pathway to convert an isomer into another would require to separate both molecules in the dimer far enough to allow rotation by 180° of one or both halves and subsequent stabilization/relaxation of the new arrangement. Considering, e.g., the tail-to-tail motif, the required separation of both monomers probably needs a separation of the twelve *tert*-butyl groups followed by a rearrangement. It can be assumed that the separation process almost necessitates energies in the magnitude of the dissociation energy of the tail-to-tail motif, which is about 60 kJ/mol (see Tables S7 and S8). The dissociation energy of the head-to-tail arrangement is even higher, i.e., there are significant barriers for an interconversion once a molecule is trapped in a local minimum. On the other hand it is difficult to predict if kinetic trapping happens in a molecular beam expansion; it depends on a large variety of expansion parameters. In most cases, the thermodynamically most stable structure is trapped strengthening the assignment of the second transition to an overtone (see above).

Concerning the peak width of the observed vibrational transitions: The width of the transition at 2270 cm^{-1} may arise from coupling of this vibration to the bath of a huge amount of low-lying frequencies, especially those describing the intermolecular vibrations. This is a typical phenomenon observed for hydrogen-bonded vibrations and the C–D vibrations of the two C–D groups of the central carbon atoms, interacting with each other, may lead to a similar situation. The narrow band width of the transition at 2134 cm^{-1} may arise from its low intensity if a head-to-tail or/and a tail-to-tail structure is observed, it is a kind of “tip of the iceberg”. On the other hand the small bandwidth could also be a further indication for the observation of an overtone (of a C–D bending mode, see above). In this case a sharp transition is expected.

References

- [1] M. D. Hanwell, D. E. Curtis, D. C. Lonie, T. Vandermeersch, E. Zurek, G. R. Hutchison, *J. Cheminformatics* **2012**, *4*, 17.
- [2] T. A. Halgren, *J. Comput. Chem.* **1996**, *17*, 490–519.
- [3] S. Grimme, C. Bannwarth, P. Shushkov, *J. Chem. Theory Comput.* **2017**, *13*, 1989–2009.
- [4] S. Rösel, H. Quanz, C. Logemann, J. Becker, E. Mossou, L. Cañadillas-Delgado, E. Caldeweyher, S. Grimme, P. R. Schreiner, *J. Am. Chem. Soc.* **2017**, *139*, 7428–7431.
- [5] S. Grimme, J. Antony, S. Ehrlich, H. Krieg, *J. Chem. Phys.* **2010**, *132*, 154104.
- [6] S. Grimme, S. Ehrlich, L. Goerigk, *J. Comput. Chem.* **2011**, *32*, 1456–1465.
- [7] F. Weigend, R. Ahlrichs, *PCCP* **2005**, *7*, 3297–3305.
- [8] S. Grimme, *J. Comput. Chem.* **2006**, *27*, 1787–1799.
- [9] M. J. Frisch, G. W. Trucks, H. B. Schlegel, G. E. Scuseria, M. A. Robb, J. R. Cheeseman, G. Scalmani, V. Barone, B. Mennucci, G. A. Petersson et al., *Gaussian 09, Revision D.01*, Gaussian, Inc, Wallingford, CT, USA, **2009**.
- [10] a) P. L. Polavarapu, *J. Phys. Chem.* **1990**, *94*, 8106–8112; b) V. Krishnakumar, N. Prabavathi, *J. Raman Spectrosc.* **2008**, *39*, 679–684;
- [11] a) P. Esherick, A. Owyong, J. Plíva, *J. Chem. Phys.* **1985**, *83*, 3311–3317; b) P. Esherick, A. Owyong, *Chem. Phys. Lett.* **1983**, *103*, 235–240;
- [12] G. V. Hartland, B. F. Henson, V. A. Venturo, R. A. Hertz, P. M. Felker, *J. Opt. Soc. Am. B* **1990**, *7*, 1950.
- [13] P. M. Felker, P. M. Maxton, M. W. Schaeffer, *Chem. Rev.* **1994**, *94*, 1787–1805.
- [14] a) A. Golan, N. Mayorkas, S. Rosenwaks, I. Bar, *J. Chem. Phys.* **2009**, *131*, 24305; b) N. Mayorkas, H. Sachs, M. Schütz, S.-i. Ishiuchi, M. Fujii, O. Dopfer, I. Bar, *PCCP* **2016**, *18*, 1191–1201;
- [15] a) P. M. Johnson, *J. Chem. Phys.* **1976**, *64*, 4143–4148; b) U. Boesl, H. J. Neusser, E. W. Schlag, *Z. Naturforsch. A* **1978**, *33*, 1546–1548; c) V. S. Antonov, I. N. Knyazev, V. S. Letokhov, V. M. Matiuk, V. G. Movshev, V. K. Potapov, *Opt. Lett.* **1978**, *3*, 37–39; d) T. R. Rizzo, Y. D. Park, L. Peteanu, D. H. Levy, *J. Chem. Phys.* **1985**, *83*, 4819–4820; e) J. R. Cable, M. J. Tubergen, D. H. Levy, *J. Am. Chem. Soc.* **1988**, *110*, 7349–7355;
- [16] a) R. H. Page, Y. R. Shen, Y. T. Lee, *J. Chem. Phys.* **1988**, *88*, 4621–4636; b) C. Riehn, C. Lahmann, B. Wassermann, B. Brutschy, *Chem. Phys. Lett.* **1992**, *197*, 443–450; c) S. Tanabe, T. Ebata, M. Fujii, N. Mikami, *Chem. Phys. Lett.* **1993**, *215*, 347–352; d) T. S. Zwier, *Annu. Rev. Phys. Chem.* **1996**, *47*, 205–241; e) M. Gerhards, C. Unterberg, *PCCP* **2002**, *4*, 1760–1765;
- [17] T. Bürgi, T. Droz, S. Leutwyler, *Chem. Phys. Lett.* **1994**, *225*, 351–358.
- [18] a) E. Condon, *Phys. Rev.* **1926**, *28*, 1182–1201; b) J. Franck, E. G. Dymond, *Trans. Faraday Soc.* **1926**, *21*, 536;
- [19] a) T. Omi, H. Shitomi, N. Sekiya, K. Takazawa, M. Fujii, *Chem. Phys. Lett.* **1996**, *252*, 287–293; b) B. Fehrensens, M. Hippler, M. Quack, *Chem. Phys. Lett.* **1998**, *298*, 320–328; c) H. Fricke, K. Bartl, A. Funk, A. Gerlach, M. Gerhards, *Chemphyschem* **2008**, *9*, 2592–2600;
- [20] a) C. Unterberg, A. Jansen, M. Gerhards, *J. Chem. Phys. (The Journal of Chemical Physics)* **2000**, *113*, 7945; b) M. Gerhards, C. Unterberg, *Phys. Chem. Chem. Phys.* **2002**, *4*, 1760–1765;
- [21] a) T. M. Parker, L. A. Burns, R. M. Parrish, A. G. Ryno, C. D. Sherrill, *J. Chem. Phys.* **2014**, *140*, 94106; b) E. G. Hohenstein, R. M. Parrish, C. D. Sherrill, J. M. Turney, H. F. Schaefer, *J. Chem. Phys.* **2011**, *135*, 174107; c) E. G. Hohenstein, C. D. Sherrill, *J. Chem. Phys.* **2010**, *132*, 184111;
- [22] N. M. Shishlov, S. L. Khursan, V. V. Lazarev, V. V. Nechaev, *J Appl Spectrosc* **2018**, *85*, 581–587.
- [23] a) C. J. Gruenloh, J. R. Carney, F. C. Hagemeister, C. A. Arrington, T. S. Zwier, S. Y. Fredericks, J. T. Wood, K. D. Jordan, *J. Chem. Phys.* **1998**, *109*, 6601–6614; b) J. G. Philis, C. Kosmidis, *Int. J. Mass Spectrom.* **1999**, *193*, 69–75;

[24] a) M. Gerhards, C. Unterberg, A. Gerlach, *Phys. Chem. Chem. Phys.* **2002**, *4*, 5563–5565; b) K. Bartl, A. Funk, K. Schwing, H. Fricke, G. Kock, H.-D. Martin, M. Gerhards, *Phys. Chem. Chem. Phys.* **2009**, *11*, 1173–1179;

A.3 Publication II

Chromone–methanol clusters in the electronic ground and lowest triplet state: a delicate interplay of non-covalent interactions

P. Boden, P. H. Strebert, M. Meta, F. Dietrich, C. Riehn, M. Gerhards

Phys. Chem. Chem. Phys., **2022**, *24*, 15208-15216.

DOI: 10.1039/D2CP01341J

The combined IR/UV experiments were performed by P. Boden within his doctoral thesis with assistance of myself. Marcel Meta aided in analyzing the experimental data as part of a lab course in the research group. The theoretical work including the (TD)DFT calculations as well as the analysis of the intermolecular binding energy with SAPT0 and LED/DLNPO-CCSD(T) was conducted by myself. P. Boden and myself discussed and interpreted the results and wrote the draft of the manuscript. F. Dietrich and C. Riehn were involved in reviewing and editing the manuscript. M. Gerhards and C. Riehn were my supervisors.

Reproduced with permission from Wiley-VCH GmbH.



Cite this: DOI: 10.1039/d2cp01341j

Chromone–methanol clusters in the electronic ground and lowest triplet state: a delicate interplay of non-covalent interactions†

 Pol Boden,^{‡a} Patrick H. Strebert,^{‡a} Marcel Meta,^a Fabian Dietrich,^{§*ab} Christoph Riehn,^{§*a} and Markus Gerhards,^{§a}

Chromone offers two energetically almost equivalent docking sites for alcohol molecules, in which the hydroxyl group is hydrogen bonded to one of the free electron pairs of the carbonyl O atom. Here, the delicate balance between these two competing arrangements is studied by combining IR/R2PI and UV/IR/UV spectroscopy in a molecular beam supported by quantum-chemical calculations. Most interestingly, chromone undergoes an efficient intersystem crossing into the triplet manifold upon electronic excitation, so that the studies on aromatic molecule–solvent complexes are for the first time extended to such a cluster in a triplet state. As the lowest triplet state (T_1) is of ground state character, powerful energy decomposition approaches such as symmetry-adapted perturbation theory (SAPT) and local energy decomposition using the domain-based local pair natural orbital coupled–cluster method (DLPNO–CCSD(T)/LED) are applied. From the theoretical analysis we infer for the T_1 state a loss of planarity (puckering) of the 4-pyrone ring of the chromone unit, which considerably affects the interplay between different types of non-covalent interactions at the two possible binding sites.

 Received 21st March 2022,
Accepted 11th May 2022

DOI: 10.1039/d2cp01341j

rsc.li/pccp

Introduction

The role of dispersion interactions in chemistry has been underestimated for a long time. However, they have meanwhile turned out to play an important role in understanding the binding behavior of molecules, which is of fundamental importance for, *e.g.*, (bio)chemical processes and catalysis.¹ The so-called “London dispersion” appears as an attractive potential between non-polar molecules or molecular parts and is balanced by Pauli repulsion at short distances. Due to the nature of London dispersion being cumulative and nearly pairwise additive with respect to the size of the molecule, the importance of this interaction for large molecules cannot be understated. For medium-sized molecules, especially molecular clusters, they also represent a key factor to determine structural preferences. Thus, it is imperative to investigate dispersion-bound systems for developing and enhancing theoretical models, which can then be applied to more complex systems. A promising path

is the investigation of molecular clusters, which represent balances for exploration of the different binding motifs and sites for small solvent molecules. For this purpose, so-called “solvation balances” were extensively studied on complexes between aromatic ether molecules (diphenyl ether, phenyl vinyl ether, different furans) and various alcohols,^{2–8} combining several spectroscopic methods (FTIR, IR/UV, MW) in molecular beam experiments. Furthermore, studies of the carbonyl solvation balances have been launched by the Suhm group.⁹ They investigated aggregates between acetophenone derivatives (with varying alkyl substituents) and various alcohols (with different alkyl residues) by FTIR spectroscopy in molecular jet experiments combined with DFT-based theoretical studies.¹⁰ In the same context, they also analyzed pinacolone–alcohol clusters,¹¹ as well as phenol–halogenated acetophenone complexes.¹² Other work on ketone–solvent complexes¹³ in the gas phase comprises studies on complexes between camphor and various H-bond donor molecules¹⁴ and investigations of fenchone–solvent aggregates¹⁵ (phenol/benzene *vs.* water/ethanol).

All these studies are focused on molecular aggregates in the electronic ground state (S_0). In contrast, the studies of dispersion interactions in electronically excited states are scarce.¹⁶ Fabrizio *et al.*¹⁷ show the importance of dispersion for photochemical processes in molecular switches in a computational study. Further theoretical studies on excited state properties are limited to small clusters, *e.g.* ethene–argon or formaldehyde–methane.¹⁸ In that

^a *Fachbereich Chemie & State Research Center OPTIMAS, TU Kaiserslautern, Erwin-Schrödinger-Str. 52, D-67663 Kaiserslautern, Germany*
^b *Núcleo Milenio MultiMat & Departamento de Ciencias Físicas, Universidad de La Frontera, Temuco, Chile. E-mail: fabian.dietrich@ufrontera.cl*
[†] Electronic supplementary information (ESI) available. See DOI: <https://doi.org/10.1039/d2cp01341j>
[‡] P. B. and P. H. S. contributed equally to this work.

[§] In memoriam of Markus Gerhards, who passed away 28.12.2020.

context, a cross-reference should be given to exciplexes, although only weakly-bound in the ground state and often dominated by charge transfer interactions in the excited state, are related to this topic.¹⁹ The aforementioned investigations on diphenyl ether (DPE) with methanol^{8,20} and *tert*-butanol² have also been applied towards the excited state (here S_1). However, a quantification of the dispersion or other interactions was not possible, since the established energy decomposition methods are yet limited to studies on electronic ground states, while their application to electronically excited-states is still under development.

Extending the investigation of microsolvated ketones to electronically excited states, we here study aggregates between chromone, *i.e.*, 1,4-benzopyrone (an isomer of coumarin), and methanol both in the electronic ground state (S_0) as well as in the lowest triplet state (T_1). Similar to the structurally related xanthone,²¹ chromone undergoes a fast and efficient intersystem crossing into the triplet manifold²² after electronic excitation, which may thus also be expected for the chromone–methanol aggregates. The advantage (for theoretical studies) of investigating the T_1 state (in contrast to S_1/S_2) lies in its ground state, *i.e.*, lowest energy triplet state, character giving the opportunity to apply powerful energy decomposition analysis approaches, like SAPT^{23,24} (symmetry-adapted perturbation theory) and DLPNO-CCSD(T)/LED^{25–27} (local energy decomposition domain-based local pair natural orbital coupled-cluster method).

In the chromone–MeOH complexes produced in our molecular beam experiments, the chromone unit acts as a UV chromophore within the complex providing the possibility for two-photon ionization, a prerequisite for the applied R2PI (resonant two-photon ionization) and IR/R2PI (infrared/resonant two-photon ionization) spectroscopy. The electronically excited state is accessible by the related UV(excitation)/IR/UV(ionization) technique, which has been used in our group for the investigation of (among others) xanthone²¹(T_1), 3-hydroxychromone²⁸ (S_1) and DPE–solvent clusters (S_1).^{2,5,6,8,20}

Within the chromone–MeOH complexes, the decisive structural element is given by the two free electron pairs of the carbonyl group, which exhibit distinct stabilization by a fine interplay between electrostatic H-bond stabilization (mainly due to coordination of the OH group to a carbonyl O lone pair) and dispersion interactions (including C–H...O contacts involving the OH group of methanol and the C–H groups of the chromone unit). For illustration, the relevant binding sites, which will be named “inside pocket” and “outside pocket” in the following, are sketched in Fig. 1. The main goals of our investigation are now: is it possible to assign a preference for one of the binding sites by spectroscopy and quantum chemical calculations and does this preference change upon electronic excitation?

The choice of chromone also eliminates a theoretical challenge: due to very similar docking sites on the chromone unit, similar ZPVE (zero point vibrational energy) values can be expected for both binding sites, resulting in nearly complete error cancellation for the ZPVE. This aspect is a major difference compared to previous studies^{2–6,8,20} which elucidate the subtle energetic balances between isomers of the distinct binding motifs OH...O and OH... π .

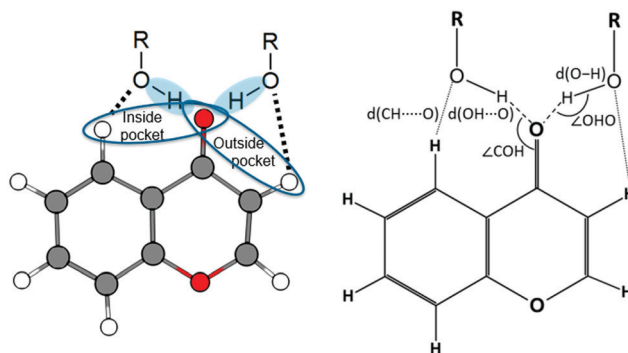


Fig. 1 Left: Schematic depiction of the chromone–solvent cluster with the “inside” and “outside” pocket, stabilized by secondary C–H...O contacts. Right: Lewis structure of the chromone–solvent cluster with selected geometry parameters.

Finally, our studies on the competition between electrostatic, induction and dispersion interactions, combining molecular beam experiments and quantum theory, are for the first time extended to aromatic molecule–solvent complexes in an electronically excited triplet state. The major quest is to compare the importance of these interactions in different electronic states with regards to relative isomer stabilities and the structural consequences for hydrogen-bonded aggregates.

Experimental methods

The experimental setup for IR/UV experiments is described in detail elsewhere,²⁹ thus only a brief description is given here. All experiments were carried out in a molecular beam apparatus consisting of a differentially pumped linear time-of-flight (TOF) mass spectrometer with a pulsed valve (General Valve Iota One, 500 μm orifice) for skimmed jet expansion. Chromone was purchased from Sigma-Aldrich (99%) and used without further purification. Methanol (Merck, 99.9%) was supplied *via* a cooled reservoir (-16°C) and co-expanded with chromone (heated up to 35°C) using neon as carrier gas (3.0 bar).

For the two-color R2PI, IR/R2PI and UV/IR/UV experiments up to three tunable nanosecond laser systems are used: two independent UV laser systems and one IR laser system. The UV laser radiation is generated by second-harmonic generation in a BBO crystal using the output of a dye laser (Sirah, Precision-Scan) pumped by the second or third harmonic ($\lambda = 532, 355\text{ nm}$) of a Nd:YAG laser (Spotlight 1000 or 1000.2, Innolas). IR radiation in the region of $3130\text{--}3750\text{ cm}^{-1}$ is generated with a LiNbO₃ crystal by difference frequency mixing (DFM) of the fundamental ($\lambda = 1064\text{ nm}$) of a seeded Nd:YAG laser (Pro 230, Spectra Physics) and the output of the dye laser pumped by the second harmonic ($\lambda = 532\text{ nm}$) of the same Nd:YAG laser. The obtained IR radiation is amplified by using an optical parametric amplification (OPA) process in a further LiNbO₃ crystal using the DFM output and again the fundamental ($\lambda = 1064\text{ nm}$) of the Nd:YAG laser.

The two-color R2PI spectra were recorded using two unfocused UV lasers. For all experiments, the UV ionization laser

(≈ 0.3 mJ pulse $^{-1}$) is fired 70 ns after the UV excitation laser (≈ 1 mJ pulse $^{-1}$). For the IR/R2PI spectra, the tuned IR laser (≈ 8 mJ pulse $^{-1}$) is fired 50 ns prior to the UV excitation laser, whereas for the UV/IR/UV spectra the IR laser is fired 20 ns after the UV excitation laser to avoid temporal overlap of the laser pulses.

Computational methods

For the theoretical approach, starting geometries for chromone–methanol clusters were obtained using the CREST algorithm³⁰ by the Grimme group. Calculations of the ground state and electronically excited states were performed using (TD)DFT. We choose the CAM-B3LYP³¹ as functional, def2-TZVP^{32–34} as basis set and used Grimme's D3 correction³⁵ with Becke–Johnson damping³⁶ to account for dispersion interaction. Geometry optimizations were carried out using the Bery algorithm in Gaussian 16³⁷ and calculating energies and gradients with Turbomole 7.5.³⁸ A subsequent harmonic frequency calculation was used to check for imaginary frequencies confirming a minimum structure. Harmonic frequencies for excited state geometries were computed using the NumForce script with the option “–central”. All harmonic frequencies were corrected with a scaling factor of 0.95.³⁹

Relaxed scans of the potential energy surface in the electronic ground state and excited triplet state were performed to estimate the isomerization barrier between the “inside” and “outside” structure by variation of the COH angle.

Energy decomposition calculations were performed using the SAPT0^{23,40} method implemented in Psi4⁴¹ using the basis set jun-cc-pVDZ.²⁴ A second approach used the DLPNO-CCSD(T)/LED^{25–27,42} method implemented in Orca 5.0.0.⁴³ As basis set def2-TZVP^{32–34} was chosen, furthermore the “TightPNO” option was selected.

Results and discussion

Theoretical results

Chromone provides multiple possible binding sites for interactions with solvent molecules, namely the carbonyl oxygen, the ether oxygen and the π -system of the aromatic moiety. We thus distinguish between OH \cdots O(carbonyl), OH \cdots O(ether) and OH $\cdots\pi$ structures. As expected from chemical intuition, coordination to the polar carbonyl group, exhibiting a relatively large dipole moment, is energetically preferred over coordination to the ether group or the aromatic π -system. This is confirmed by geometry optimizations using CAM-B3LYP-D3(BJ)/def2-TZVP predicting two nearly isoenergetic OH \cdots O(carbonyl) structures for the chromone–methanol cluster as shown in Fig. 2, omitting the corresponding enantiomers obtained by using the chromone plane as a mirror plane. All other structures show significantly higher relative energies (OH \cdots O(ether), $\Delta E > 19.6$ kJ mol $^{-1}$; OH $\cdots\pi$, $\Delta E > 20.1$ kJ mol $^{-1}$, see Fig. S7, ESI†). Furthermore, as demonstrated in the experimental results section, only the OH stretching frequencies predicted for the carbonyl-bound

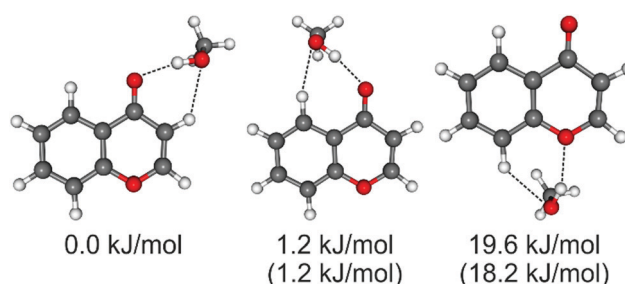


Fig. 2 Optimized structures for the chromone–methanol cluster in the S_0 state with the respective relative electronic energies and zero-point corrected energies (in brackets), as obtained at the DFT/CAM-B3LYP-D3(BJ)/def2-TZVP level.

structures correlate with the experimental IR spectrum. Thus, further discussions are limited to the two OH \cdots O(carbonyl) isomers. As mentioned before, we will refer to these two motifs as the “inside” and “outside” isomers. The main difference between both structures lies in their additional stabilization *via* different CH \cdots O contacts. We observe an 1,2-like contact for the outside isomer and an 1,3-like contact for the inside isomer, leading to different binding angles (especially \angle CO \cdots H and \angle CH \cdots O) for the docking solvent molecule.

We can distinguish both structures by their different calculated OH stretching vibrational frequencies which are 3421 cm $^{-1}$ for the outside isomer and 3467 cm $^{-1}$ for the inside isomer (scaled by 0.95³⁹). This difference is also visible in the corresponding geometric parameters (Table 1) with an OH \cdots O distance of 1.838 Å for the favored outside isomer and 1.842 Å for the inside isomer. For ether coordination, the OH \cdots O distance is considerably larger with 2.054 Å, indicating a weaker hydrogen bond and thus less stabilization of the cluster resulting in a higher energy. Comparing the COH and OHO angles between the two most favorable isomers yields further insight regarding the energetic ordering (see Table 1). The outside (inside) isomer exhibits a COH angle of 113° (135°) and an OHO angle of 165° (166°), the latter deviating considerably from a linear arrangement. The 1,3-contact for the inside isomer leads to this sub-optimal COH angle, with a greater difference to a probably ideal COH angle of 120° than for the outside isomer, which could be a further reason for the energetic preference of the latter. We also calculated the isomerization barrier with a relaxed potential energy surface (PES) scan for the COH angle with values between

Table 1 Selected geometry parameters for the chromone–methanol cluster in different electronic states, with the T_1 state treated at UDFT/CAM-B3LYP-D3(BJ)/def2-TZVP level

	Ground state S_0		Excited state T_1		Difference(S_0, T_1)/%	
	Inside	Outside	Inside	Outside	Inside	Outside
$d(\text{C}=\text{O})/\text{\AA}$	1.222	1.224	1.252	1.255	+2.5	+2.5
$d(\text{OH}\cdots\text{O})/\text{\AA}$	1.842	1.838	1.886	1.869	+2.4	+1.7
$d(\text{OH})/\text{\AA}$	0.972	0.974	0.969	0.972	–0.3	–0.2
$\angle(\text{CO}\cdots\text{H})^\circ$	135.0	112.8	134.5	112.1	–0.4	–0.6
$\angle(\text{OH}\cdots\text{O})^\circ$	167.2	164.6	166.0	160.7	–0.7	–2.4
$d(\text{CH}\cdots\text{O})/\text{\AA}$	2.291	2.425	2.316	2.315	+1.1	–4.5
$\angle(\text{CH}\cdots\text{O})^\circ$	162.4	129.1	159.3	132.6	–1.9	+2.7

110° and 230° resulting in a barrier of 11.5 kJ mol⁻¹ for the electronic ground state (Fig. S18, ESI†).

Furthermore, calculations of excited state properties were carried out using TDA-TDDFT/CAM-B3LYP-D3(BJ)/def2-TZVP. The two lowest singlet and triplet excited states were investigated (see ESI†), with a special focus on the T₁ state, exploiting its “ground state nature” by applying an UDFT/CAM-B3LYP-D3(BJ)/def2-TZVP approach, which provides more reliable results than the TD-DFT method with respect to the obtained geometry (see Table S1, ESI†).

The optimized geometries of the chromone–methanol cluster in the T₁ state keep a strong preference for the OH...O(carbonyl) structures, while the other motifs remain disfavored (Fig. 3). The Δ*E* between the inside and outside isomer increases from 1.2 kJ mol⁻¹ (S₀) to 3.2 kJ mol⁻¹ (T₁).

The main geometric parameters are listed in Table 1 and emphasize that the general geometry is retained, except for the elongation of the hydrogen bond and the carbonyl bond in the T₁ state. This is caused by the loss of planarity (puckering) of the chromone framework in the triplet state leading to a double minimum potential for both motifs, with a barrier of 1.4 kJ mol⁻¹ (outside) and 1.2 kJ mol⁻¹ (inside), respectively (Fig. S21–S22, ESI†). Structurally, the C atom of the CH moiety adjacent to the ether O atom lies outside the plane of the chromone unit (Fig. 4).

For both the inside and outside structures, the puckered C atom is displaced by around 0.3 Å relative to its position in the respective ground state geometry. Consequently, the dihedral angle formed by O(ether)–C(puckered)–C–C(carbonyl) changes from 0° in the S₀ state to around 20° in the T₁ state. For clarity, we limit the discussion to the slightly more stable “down” geometries (see Fig. S16, S17 and Tables S1, S2, ESI†). The isomerization barrier between the inside and outside isomers in the T₁ state is determined to 13.5 kJ mol⁻¹ by a relaxed scan (Fig. S19 and S20, ESI†), similar to the ground state barrier.

The Δ*E* values are compared to other DFT methods, SAPT0 and DLPNO-CCSD(T), as given in Table 2. All methods predict a larger dispersion interaction for the inside isomer. The value obtained from the D3(BJ) dispersion correction used in DFT yields a good approximation compared to the assumably “correct” energy decomposition approaches.

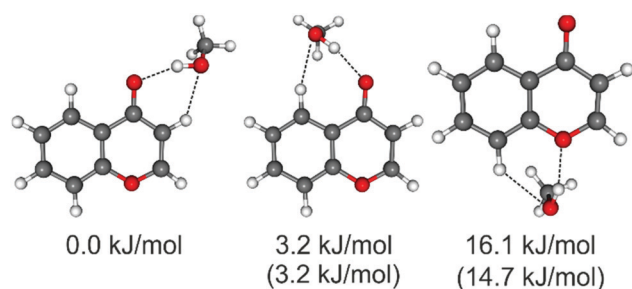


Fig. 3 Optimized structures for the chromone–methanol cluster in the T₁ state with the respective relative electronic energies and zero-point corrected energies (in brackets), as obtained at the UDFT/CAM-B3LYP-D3(BJ)/def2-TZVP level.

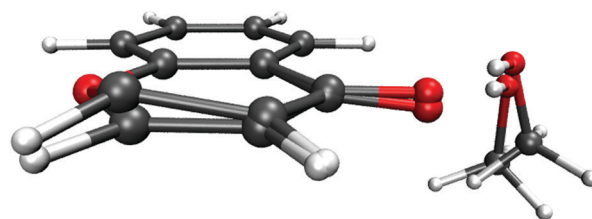


Fig. 4 Overlay of the ground state (S₀) and puckered excited triplet state (T₁) geometry for the inside (“down”) isomer. The puckering of the carbon atom is clearly visible. Structures obtained at (U)DFT/CAM-B3LYP-D3(BJ)/def2-TZVP level.

Table 2 Relative energies and dispersion energies for the chromone–methanol cluster in the S₀ state, as obtained by various theoretical methods

Method	<i>E</i> (in)– <i>E</i> (out)	Δ <i>E</i> _{disp}
CAM-B3LYP/def2-TZVP	1.8	—
CAM-B3LYP-D3(BJ)/def2-TZVP	1.2	–1.1
PBE0-D3(BJ)/def2-TZVP	1.5	–1.2
SAPT0/jun-cc-pVDZ	0.6	–1.3
DLPNO-CCSD(T)/def2-TZVP	1.5	–0.8

As mentioned above, the goal of this study is to investigate the delicate balance between the inside and outside isomers. In order to gain insight into the relevant interactions leading to the energetic ordering of the isomers, energy decomposition calculations were performed to quantify the dispersion and other interactions. The energy values obtained by the SAPT0 calculations are shown in Table 3 (similar analysis for DLPNO-CCSD(T)/LED can be found in Table S4, ESI†). The strongest interaction, as expected for a hydrogen-bonded cluster, is the electrostatic interaction, showing a clear preference for the outside isomer, confirming the hypothesis of its stronger hydrogen-bond. The induction and dispersion interactions are significantly weaker for both isomers. It is important to note that the induction energy does not differ significantly between both motifs, while the dispersion interaction is stronger for the inside isomer, somewhat compensating for the weaker hydrogen bond. This can be rationalized by the shorter center-of-mass distances between the chromone and methanol moieties: 4.76 (inside) and 5.36 Å (outside). The larger dispersion energy in the SAPT approach leads to a reduced Δ*E* of 0.6 kJ mol⁻¹ in comparison to the (dispersion-corrected) DFT value of 1.2 kJ mol⁻¹. Analyzing the energetics for the T₁ state reveals that the strongest interaction is here the repulsive exchange interaction, with the attractive electrostatic contribution being slightly weaker, while induction and dispersion interactions are significantly weaker.

If we compare these values with the ones for the electronic ground state, it is revealed that the electrostatic interaction decreases by 14 kJ mol⁻¹ (inside) and 10 kJ mol⁻¹ (outside), while the induction interaction is reduced by 5 kJ mol⁻¹ (inside) and 3 kJ mol⁻¹ (outside). At the same time, the repulsive exchange is also decreased by 7 kJ mol⁻¹ (inside) and 2 kJ mol⁻¹ (outside). The dispersion interaction is only slightly weaker in the triplet state, reduced by *ca.* 1.2 kJ mol⁻¹ for both isomers.

Table 3 Results of energy decomposition analysis by SAPT0/jun-cc-pVDZ. The raw values for each interaction for the respective electronic state and isomer (col. 2–5), the energy difference between the inside and outside isomer for each interaction (col. 6 and 7), the change in ΔE going from the S_0 to T_1 state (col. 8), giving insight which interactions influence the change in ΔE , and the modulation (col. 9 and 10) of each interaction in the T_1 state expressed in their relative strength compared to the S_0 state. All values are given in kJ mol^{-1} , except col. 9 and 10. Positive values in col. 6–8 refer to stabilization of the outside structure relative to the inside isomer, in col. 9,10 a lower value indicates a weaker interaction in the T_1 state compared to the corresponding value in the S_0 state. A detailed overview of each contribution can be found in the ESI (Table S3)

	Inside isomer (S_0)	Outside isomer (S_0)	Inside isomer (T_1)	Outside isomer (T_1)	ΔE (S_0)	ΔE (T_1)	$\Delta\Delta E$ (S_0, T_1)	E (T_1, in)/ E (S_0, in)	E (T_1, out)/ E (S_0, out)
Electrostatics	−57.9	−60.4	−43.5	−50.8	2.5	7.3	4.8	0.75	0.84
Exchange	57.5	58.7	50.4	56.5	−1.2	−6.1	−4.8	0.88	0.96
Induction	−18.2	−18.9	−13.5	−16.0	0.6	2.4	1.8	0.74	0.85
Dispersion	−16.4	−15.2	−15.2	−14.0	−1.3	−1.2	0.0	0.93	0.92
$E_{\text{tot}}/\text{kJ mol}^{-1}$	−35.1	−35.7	−21.8	−24.2	0.6	2.4	1.8	0.62	0.68

Consequently, the interplay of electrostatics, induction and exchange is responsible for the increased ΔE for the two discussed isomers in the triplet state, while London dispersion does not influence the carbonyl balance. The observed trend is consistent with the increased C=O and O \cdots HO bond distances in the T_1 state, suggesting weaker hydrogen bonding and resulting in overall smaller interaction energies (see Table S5, ESI \dagger). At this point, we propose to analyze the relative instead of the absolute energy differences between the S_0 and T_1 states, unraveling further insights on the interplay of the different interaction terms (Table 3, last two columns). We observe an interesting behavior for the electrostatic and induction terms. Comparing the T_1 values in relation to the S_0 values, we can state that both interactions drop to around 75% for the inside motif, while only dropping to 85% for the outside motif.

This is not a simple geometric effect, since the dispersion energy decreases similarly for both structures to around 92% of its original value. A possible explanation for the energy reduction of the outside structure could be the fact that the distortion of the chromone framework and the spin density is localized strongly onto the 4-pyrone ring, including the bond responsible for the CH \cdots O contact (see Fig. S15, ESI \dagger). Thus, for the outside isomer, both the electronic and geometric structure of the ring can better adapt to the situation in the triplet state, leading to an improved interaction between the methanol and the chromone. This is also manifested by the lowering of the CH \cdots O distance by 4.5% for the outside motif, while it is increased for the inside motif.

Experimental results

R2PI experiments

As mentioned in the introduction, fast ISC is observed for isolated chromone²² and for the structurally related xanthone,²¹ thus similar behavior is expected for chromone–methanol aggregates. The R2PI spectra are obtained *via* a two-color R2PI process, scanning the UV excitation laser and keeping the UV ionization laser frequency-fixed. By varying the time delay between the ns-UV excitation pulse and ns-UV ionization laser pulse the fast (sub-ns) generation of a long-lived excited state (probably a triplet state populated by ISC) could be confirmed: at a delay of 23 μs a strong ion signal of the chromone–methanol clusters is still

present. In the molecular beam expansion not only clusters comprising one single methanol molecule are observed, but at the same time a multitude of higher clusters comprising several (up to 10–15 methanol molecules) are also obtained. As discussed further down, this strong aggregation behavior has some experimental disadvantages, but allows us to estimate a possible excited state lifetime dependence on the cluster size. However, at least for time delays of up to 23 μs between the excitation and ionization laser pulses, the mass signal distribution (and thus cluster size distribution) in the recorded mass spectra is largely unchanged (see Fig. S2, ESI \dagger). This means that all observed cluster sizes should have similar excited state lifetimes. We conclude that most probably an ISC into a triplet state with long lifetime takes place for the chromone–methanol clusters, which is in accordance with the studies of Itoh,²² who reported gas vapor UV and emission spectra for chromone, and also in line with prior studies on xanthone²¹ performed in our group. Finally, we chose a time delay of 70 ns for our experiments to minimize the required spatial shift of the lasers due to the velocity of the molecular beam while still avoiding temporal overlap of the laser pulses.

The R2PI spectrum of chromone, recorded with the UV ionization laser set to a frequency of 46 838 cm^{-1} exhibits a strong band at 33 896 cm^{-1} (see Fig. S1, ESI \dagger). We assign this band to the $S_0 \rightarrow S_2$ transition in correspondence to gas vapor UV spectra from literature²² (33 880 cm^{-1}). It should be pointed out that a UV photoexcitation into the S_1 state (prior to ionization) was not possible due to the weak absorption cross section of the $S_0 \rightarrow S_1$ transition.²² This was further confirmed by TD-DFT calculations (see Fig. S10, ESI \dagger) and is again in accordance with the studies on xanthone.²¹ In the accordingly obtained R2PI spectra of chromone with one or more methanol molecules, a strong shift of the $S_0 \rightarrow S_2$ transition down to 33 292 cm^{-1} (chromone–methanol (1:1) cluster) is observed, corresponding to a red-shift of 604 cm^{-1} relative to the value for chromone, which increases with further addition of methanol molecules (see Fig. S1, ESI \dagger).

IR/UV experiments in the electronic ground state

The IR/R2PI spectra were recorded in the IR frequency range from 3130 cm^{-1} to 3750 cm^{-1} , with the UV excitation laser frequency set to 33 292 cm^{-1} and the UV ionization laser frequency-fixed at 46 838 cm^{-1} . We observe multiple overlapping bands

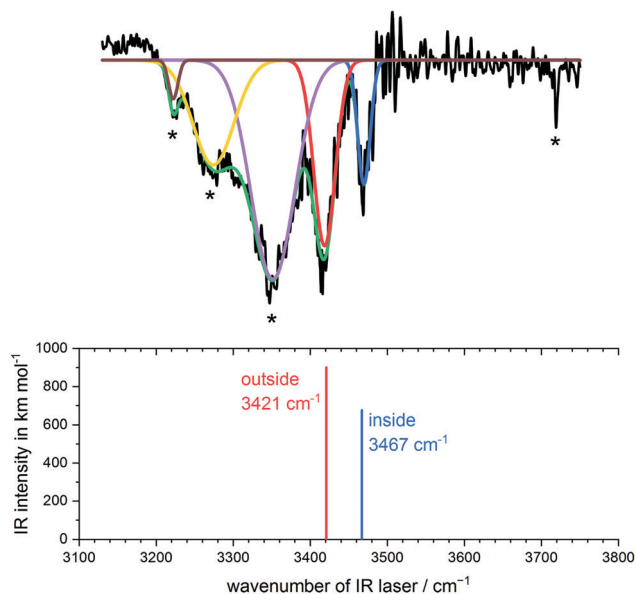


Fig. 5 Experimental and theoretical IR spectra for the chromone–methanol cluster in the S_0 state. Bands marked with asterisks result from UV fragmentation of higher chromone–methanol(–water) clusters. A convolution of five Gaussians (green) is fitted to the spectrum. The red and blue Gaussians were assigned to the outside and inside isomers, respectively. Calculated OH stretching frequencies were obtained at CAM-B3LYP-D3(BJ)/def2-TZVP level and scaled by 0.95.

indicating that more than one species contributes to the IR spectrum of the chromone–MeOH cluster (Fig. 5). By comparing this IR spectrum with the spectra obtained at higher mass traces (see Fig. S3, ESI[†]) corresponding to clusters with two and more methanol (as well as water) molecules, several features marked with asterisks in the IR spectrum of chromone–methanol are assigned to IR transitions of higher clusters (with more than one methanol molecule) or chromone–methanol–water clusters (feature at 3719 cm^{-1}), appearing in the IR spectrum of chromone–methanol due to UV photofragmentation of the respective larger clusters.

Typically, larger alcohol clusters show strong, anharmonic and thus particularly red-shifted OH stretching frequencies, while features around 3720 cm^{-1} (free OH stretching vibration of H_2O) are a hint on the formation of water clusters in the molecular beam expansion which are difficult to avoid for hygroscopic substances. The neutral chromone–methanol complexes are expected to undergo intersystem crossing into the triplet-manifold upon UV photoexcitation, resulting in a large amount of excess energy. This could explain why the discussed photofragmentation effects could not be suppressed in usual ways, like keeping the excess energy in the excitation and ionization step moderate or by varying the expansion conditions. Since the investigated aggregates are probed in the cold, collision-free part of the molecular beam, isolated vibrationally hot triplet state clusters formed upon intersystem crossing cannot undergo vibrational relaxation by colliding with the expansion gas (neon). Therefore, we assume that the chromone–solvent clusters (especially the probably more labile larger clusters)

tend to dissipate energy by evaporative cooling,⁴⁴ specifically detachment of solvent molecules. We calculate the energy difference between the T_1 and S_2 state to be around 160 kJ mol^{-1} (see Fig. S10, ESI[†]), which would require evaporation of multiple methanol molecules for (partial) cooling. This may explain the strong photofragmentation effects observed in the IR/R2PI spectra, since the IR laser is applied temporally prior to the first UV laser and thus before the discussed fragmentation process. Nevertheless, the IR spectrum depicted in Fig. 5 shows two intense features at 3419 and 3470 cm^{-1} that can be assigned with high confidence to two distinct isomers of the chromone–methanol cluster. Indeed, these two bands are in excellent agreement with the OH stretching frequencies predicted by quantum-chemical calculations (CAM-B3LYP-D3(BJ)/def2-TZVP level) for the two energetically favored structures, namely the “outside pocket” (3421 cm^{-1}) and “inside pocket” (3467 cm^{-1}) isomers. This strongly supports the formation of both $\text{OH}\cdots\text{O}$ bound isomers in the molecular beam expansion, moreover because the $\text{OH}\cdots\text{O}(\text{ether})$ and $\text{OH}\cdots\pi$ structures would exhibit resonances at higher wavenumbers (see Fig. S7, ESI[†]), closer to the value for free methanol⁴⁵ at 3686 cm^{-1} . Thus, the presence of both (expected) isomers is highly suggested by the experimental results presented above, whereby isomerizations between both arrangements seem unlikely due to a high interconversion barrier between both local minima. As mentioned in the theoretical results, this barrier was calculated by a relaxed potential energy surface scan (PES) and estimated to be around 11.5 kJ mol^{-1} , a value that makes isomerization during the molecular beam expansion unlikely. Nevertheless, the small energetic difference between both isomers also supports the direct population of both isomers within the adiabatic expansion.

However, even if the inside and outside isomers are both observed in the experiment, both minima may not be populated in equal amounts in the molecular beam. Although quantitative assignments based on our IR/UV experiments are difficult, a tentative estimation should be possible in the specific case treated here, since similar UV oscillator strengths are expected for both isomers in question (see predictions of TDDFT in the ESI[†]). Likewise, the predicted intensities of the respective OH stretching modes are in the same order of magnitude. Thus, it can be claimed that, without indicating any precise value concerning the isomeric ratio between the outside and inside structures, the outside isomer IR-band is clearly more pronounced than the inside isomer band, so that the outside isomer population should predominate in the molecular beam (compared to the inside isomer contribution). This observation is perfectly in accordance with the relative energies of the competing minimum structures (see theoretical results section, further analysis in Fig. S6, ESI[†]).

IR/UV experiments in the electronically excited state (T_1)

The IR spectrum of chromone–methanol in its electronically excited triplet state (T_1), depicted in Fig. 6, was obtained by applying the UV/IR/UV technique. Compared to the ground state IR spectrum discussed above, the UV/IR/UV spectrum shows significantly changed characteristics. First of all, it is

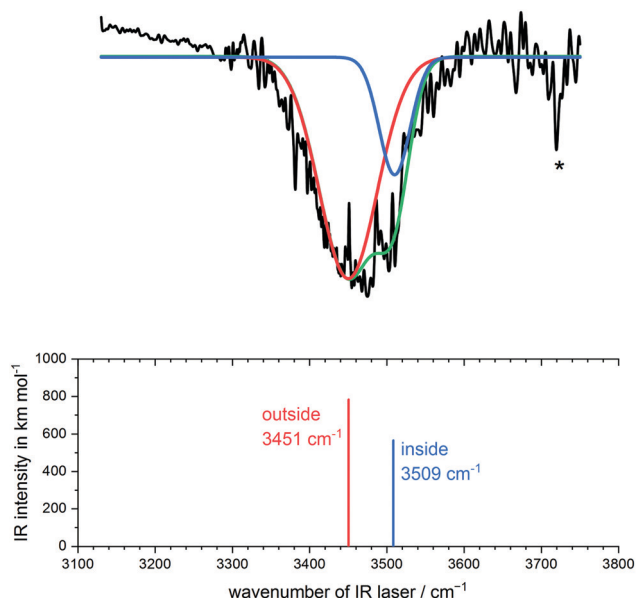


Fig. 6 Experimental and theoretical spectra for the chromone–methanol cluster in the T_1 state. A convolution of two Gaussians (green), representing the outside (red) and inside (blue) isomer peaks, is fitted to the spectrum. Calculated OH stretching frequencies were obtained at CAM-B3LYP-D3(BJ)/def2-TZVP level and scaled by 0.95.

almost free of any features which are caused by UV photofragmentation of larger chromone–methanol clusters. There is one sharp feature at 3720 cm^{-1} , marked with an asterisk, which is again due to UV photofragmentation of chromone–methanol–water clusters, but any further effects related to higher clusters are not observed. This strengthens the hypothesis that strong UV fragmentation of (especially larger) chromone–methanol clusters occurs after intersystem crossing. Since the ISC process can be expected to take place on a ps timescale, the IR laser (fired about 50 ns after the UV excitation laser) is thus irradiating the sample after the ISC and most probably also after the evaporative cooling takes place. Thus, this could present a plausible explanation for the absence of any major features resulting from larger clusters in the UV/IR/UV spectrum of chromone–methanol.

Finally, we observe a strong and structured band from 3330 cm^{-1} to 3600 cm^{-1} that can be deconvoluted into two Gaussians with peak maxima at 3451 cm^{-1} and 3510 cm^{-1} , which are in excellent agreement with the predicted calculated values of 3451 cm^{-1} (outside) and 3508 cm^{-1} (inside), respectively. At this point it should also be noted that the spikes in the measured band around 3450 and 3510 cm^{-1} are caused by dips in the IR laser power curve (see Fig. S5, ESI† for comparison). Thus, both structural motifs assigned for the ground state (S_0) are retained in the T_1 state. As discussed in the theoretical results section, the optimized geometries of the T_1 state isomers are similar compared to those observed for the respective ground state structures. However, the OH...O hydrogen bonds (and C=O bonds) are slightly elongated for both motifs and thus weakened compared to the S_0 state geometries (see Table 1), which explains the blue-shift of the measured as well as the calculated OH

stretching frequencies relative to the ground state OH vibrations and is in line with the calculated lower binding energies (see Table S5, ESI†).

The discussed cluster fragmentation effects upon UV photoexcitation imply that any assumptions regarding isomerization between outside and inside motifs upon ISC into the triplet manifold should be handled carefully. Specifically, the population of both the inside and outside minima may not only be influenced by isomerization processes between both motifs, but also by fragmentation of larger clusters onto the chromone–methanol mass trace prior to IR probing. This means that chromone–methanol clusters initially formed during the adiabatic expansion and kept intact upon ISC, as well as chromone–methanol aggregates generated by UV fragmentation of larger clusters may both contribute to the depicted UV/IR/UV spectrum. Thus, the population ratio between the outside and inside minima in the T_1 state can have different origins. Nevertheless, the outside isomer seems to be again clearly more populated than the inside isomer motif (see deconvolution in Fig. 6).

Another remarkable aspect is that compared to the ground state IR spectrum, the OH stretching bands observed in the UV/IR/UV spectrum are rather broad. As already mentioned, the clusters in the triplet-manifold cannot dissipate any energy by collisions or other interaction with the environment. Thus, it is quite probable that also (vibrationally) hot clusters are probed in the UV/IR/UV experiment. This assumption may explain the large width of the bands observed in the T_1 state spectrum.

An additional rationalization for the broadening of the OH stretching bands (especially for the outside isomer) could be inferred from the fact that, as described in the theoretical results section, the chromone unit in the chromone–methanol cluster forms a puckered 4-pyrone ring when reaching the T_1 state. Consequently, this effect leads to the occurrence of two distinct local minima per binding motif, separated by a very low interconversion barrier (see Fig. S21 and S22, ESI†). The larger binding energy of the outside isomer could lead to the detection of clusters which are structurally and energetically more displaced from the minimum structure. Hereby, a somewhat distorted structure may exhibit a slightly distinct OH stretching frequency (compared to the minimum geometry), leading to a broadening of the measured IR band. In contrast to this, the inside isomer, exhibiting a lower binding energy, might be more likely to undergo fragmentation upon ISC if its structure is slightly off its minimum geometry. For this reason, such hot inside clusters may not contribute to the measured IR spectrum. It should be further noted that the influence of the puckering effect on the cluster stability should be relatively more pronounced for the outside isomer due to the spatial proximity of the puckered 4-pyrone ring and the methanol molecule.

Another reason for the distinct broadness of the two Gaussian peaks could be that the outside isomer, with its red-shifted OH stretching mode (relative to the inside isomer), exhibits a comparatively broad potential well, leading to a relatively increased bandwidth. However, a clear explanation for the observed different broadening of the bands in the triplet-state

is difficult to give, so that the aspects discussed above should be merely considered as possible hypotheses.

Conclusions

We present the first results for IR/UV spectroscopic investigations of molecular clusters in the triplet state in general as well as an analysis of the interplay of non-covalent interactions over multiple electronic states. Slightly different cluster structures (inside/outside pocket binding) for chromone-methanol have been identified by quantum-chemical calculations and IR/UV laser spectroscopic investigations. The presented results provide a case study for the influence of London dispersion interaction in excited states, serving as a stepping stone for further analysis in other molecular cluster systems. For chromone-methanol, the balance is mainly influenced by electrostatic, induction and exchange interaction. It was shown that, although collisional cooling in the cold part of the molecular beam can be ruled out, meaningful UV/IR/UV measurements in the T_1 state on molecular clusters are possible and may be supported by the loss of excess energy after ISC *via* cluster fragmentation effects, *i.e.* evaporative cooling. We observe a significant blue-shift of the OH stretching band (relative to the respective value for the cluster in its electronic ground state) upon electronic excitation, indicating a weakening of the hydrogen bond. This is indeed confirmed by binding energy calculations and energy decomposition analysis (SAPT0).

Furthermore, the electronic excitation leads to a ring puckering of the 4-pyrone unit with the spin density mostly localized on the puckered carbon atom (see Fig. S15, ESI[†]). This leads to a stronger differentiation between the two binding motifs since the outside pocket is part of this flexible non-planar 4-pyrone ring. Consequently, the energy difference between both motifs increases upon electronic excitation. The energy decomposition analysis reveals that the strength of the dispersion interaction is only dampened slightly by the change in electronic and geometric structure, whereas electrostatic, exchange and induction are strongly modulated depending on the binding site. Finally, not the dispersion interaction leads to the increase in ΔE , but stronger electrostatic and induction interaction is the deciding factor on this delicate carbonyl scale.

Author contributions

Pol Boden: investigation, writing: draft, review and editing; Patrick Horst Strebart: investigation, writing: draft, review and editing, formal analysis and visualization; Marcel Meta: formal analysis and visualization; Fabian Dietrich: conceptualization, writing: review and editing; Christoph Riehn: supervision, writing: review and editing; Markus Gerhards: conceptualization, funding acquisition, resources, supervision.

Conflicts of interest

There are no conflicts to declare.

Acknowledgements

The authors thank the German Research Foundation (DFG) for financial support in the context of the Priority Programme SPP 1807 (Ge 961/9-2, Control of London dispersion interactions in molecular chemistry). The authors thank the State Research Center OPTIMAS for financial support. The authors want to thank Dr Kirsten Schwing for fruitful discussion. This work is part of the PhD theses of P. B. and P. H. S.

Notes and references

- (a) J. Cerný and P. Hobza, *Phys. Chem. Chem. Phys.*, 2007, **9**, 5291–5303; (b) J.-M. Lehn, *Angew. Chem., Int. Ed. Engl.*, 1988, **27**, 89–112; (c) E. A. Meyer, R. K. Castellano and F. Diederich, *Angew. Chem., Int. Ed.*, 2003, **42**, 1210–1250; (d) K. Müller-Dethlefs and P. Hobza, *Chem. Rev.*, 2000, **100**, 143–168; (e) J. P. Wagner and P. R. Schreiner, *Angew. Chem., Int. Ed.*, 2015, **54**, 12274–12296; (f) I. K. Mati and S. L. Cockroft, *Chem. Soc. Rev.*, 2010, **39**, 4195–4205.
- D. Bernhard, F. Dietrich, M. Fatima, C. Pérez, A. Poblitzki, G. Jansen, M. A. Suhm, M. Schnell and M. Gerhards, *Phys. Chem. Chem. Phys.*, 2017, **19**, 18076–18088.
- D. Bernhard, M. Fatima, A. Poblitzki, A. L. Steber, C. Pérez, M. A. Suhm, M. Schnell and M. Gerhards, *Phys. Chem. Chem. Phys.*, 2019, **21**, 16032–16046.
- D. Bernhard, F. Dietrich, M. Fatima, C. Pérez, H. C. Gottschalk, A. Wuttke, R. A. Mata, M. A. Suhm, M. Schnell and M. Gerhards, *Beilstein, J. Org. Chem.*, 2018, **14**, 1642–1654.
- F. Dietrich, D. Bernhard, M. Fatima, C. Pérez, M. Schnell and M. Gerhards, *Angew. Chem., Int. Ed.*, 2018, **57**, 9534–9537.
- M. Fatima, D. Maué, C. Pérez, D. S. Tikhonov, D. Bernhard, A. Stamm, C. Medcraft, M. Gerhards and M. Schnell, *Phys. Chem. Chem. Phys.*, 2020, **22**, 27966–27978.
- H. C. Gottschalk, A. Poblitzki, M. Fatima, D. A. Obenchain, C. Pérez, J. Antony, A. A. Auer, L. Baptista, D. M. Benoit, G. Bistoni, F. Bohle, R. Dahmani, D. Firaha, S. Grimme, A. Hansen, M. E. Harding, M. Hochlaf, C. Holzer, G. Jansen, W. Kloppe, W. A. Kopp, M. Krasowska, L. C. Kröger, K. Leonhard, M. Mogren Al-Mogren, H. Mouhib, F. Neese, M. N. Pereira, M. Prakash, I. S. Ulusoy, R. A. Mata, M. A. Suhm and M. Schnell, *J. Chem. Phys.*, 2020, **152**, 164303.
- C. Medcraft, S. Zinn, M. Schnell, A. Poblitzki, J. Altnöder, M. Heger, M. A. Suhm, D. Bernhard, A. Stamm, F. Dietrich and M. Gerhards, *Phys. Chem. Chem. Phys.*, 2016, **18**, 25975–25983.
- A. Poblitzki, H. C. Gottschalk and M. A. Suhm, *J. Phys. Chem. Lett.*, 2017, **8**, 5656–5665.
- C. Zimmermann, H. C. Gottschalk and M. A. Suhm, *Phys. Chem. Chem. Phys.*, 2020, **22**, 2870–2877.
- C. Zimmermann, T. L. Fischer and M. A. Suhm, *Molecules*, 2020, **25**, 5095.
- C. Zimmermann, M. Lange and M. A. Suhm, *Molecules*, 2021, **26**, 4883.
- S. Blanco, A. Macario and J. C. López, *Phys. Chem. Chem. Phys.*, 2019, **21**, 20566–20570.

- 14 P. Banerjee, P. Pandey and B. Bandyopadhyay, *Spectrochim. Acta, Part A*, 2019, **209**, 186–195.
- 15 E. Burevschi, E. R. Alonso and M. E. Sanz, *Chemistry*, 2020, **26**, 11327–11333.
- 16 (a) Y. Ikabata and H. Nakai, *J. Chem. Phys.*, 2012, **137**, 124106; (b) X. Feng, A. Otero-de-la-Roza and E. R. Johnson, *Can. J. Chem.*, 2018, **96**, 730–737; (c) V. Barone, M. Biczysko and M. Pavone, *Chem. Phys.*, 2008, **346**, 247–256.
- 17 A. Fabrizio and C. Corminboeuf, *J. Phys. Chem. Lett.*, 2018, **9**, 464–470.
- 18 E. A. Briggs and N. A. Besley, *Phys. Chem. Chem. Phys.*, 2014, **16**, 14455–14462.
- 19 (a) Q. Ge, Y. Mao and M. Head-Gordon, *J. Chem. Phys.*, 2018, **148**, 64105; (b) R. A. Krueger and G. Blanquart, *J. Phys. Chem. A*, 2019, **123**, 1796–1806; (c) A. Diaz-Andres and D. Casanova, *J. Phys. Chem. Lett.*, 2021, **12**, 7400–7408.
- 20 D. Bernhard, C. Holzer, F. Dietrich, A. Stamm, W. Klopper and M. Gerhards, *ChemPhysChem*, 2017, **18**, 3634–3641.
- 21 K. Bartl, A. Funk and M. Gerhards, *ChemPhysChem*, 2009, **10**, 1882–1886.
- 22 T. Itoh, *J. Photochem. Photobiol., A*, 2010, **214**, 10–15.
- 23 E. G. Hohenstein, R. M. Parrish, C. D. Sherrill, J. M. Turney and H. F. Schaefer, *J. Chem. Phys.*, 2011, **135**, 174107.
- 24 T. M. Parker, L. A. Burns, R. M. Parrish, A. G. Ryno and C. D. Sherrill, *J. Chem. Phys.*, 2014, **140**, 94106.
- 25 A. Altun, R. Izsák and G. Bistoni, *Int. J. Quantum Chem.*, 2021, **121**, 919.
- 26 A. Altun, F. Neese and G. Bistoni, *Beilstein J. Org. Chem.*, 2018, **14**, 919–929.
- 27 A. Altun, M. Saitow, F. Neese and G. Bistoni, *J. Chem. Theory Comput.*, 2019, **15**, 1616–1632.
- 28 A. Stamm, M. Weiler, A. Brächer, K. Schwing and M. Gerhards, *Phys. Chem. Chem. Phys.*, 2014, **16**, 21795–21803.
- 29 (a) M. Gerhards and C. Unterberg, *Phys. Chem. Chem. Phys.*, 2002, **4**, 1760–1765; (b) C. Unterberg, A. Jansen and M. Gerhards, *J. Chem. Phys.*, 2000, **113**, 7945.
- 30 S. Grimme, *J. Chem. Theory Comput.*, 2019, **15**, 2847–2862.
- 31 (a) M. A.-L. Marques, M. J.-T. Oliveira and T. Burnus, *Comput. Phys. Commun.*, 2012, **183**, 2272–2281; (b) S. Lehtola, C. Steigemann, M. J.-T. Oliveira and M. A.-L. Marques, *SoftwareX*, 2018, **7**, 1–5; (c) T. Yanai, D. P. Tew and N. C. Handy, *Chem. Phys. Lett.*, 2004, **393**, 51–57.
- 32 F. Weigend and R. Ahlrichs, *Phys. Chem. Chem. Phys.*, 2005, **7**, 3297–3305.
- 33 F. Weigend, *J. Comput. Chem.*, 2008, **29**, 167–175.
- 34 A. Hellweg, C. Hättig, S. Höfener and W. Klopper, *Theor. Chem. Acc.*, 2007, **117**, 587–597.
- 35 S. Grimme, J. Antony, S. Ehrlich and H. Krieg, *J. Chem. Phys.*, 2010, **132**, 154104.
- 36 S. Grimme, S. Ehrlich and L. Goerigk, *J. Comput. Chem.*, 2011, **32**, 1456–1465.
- 37 M. J. Frisch, G. W. Trucks, H. B. Schlegel, G. E. Scuseria, M. A. Robb, J. R. Cheeseman, G. Scalmani, V. Barone, G. A. Petersson, H. Nakatsuji, X. Li, M. Caricato, A. V. Marenich, J. Bloino, B. G. Janesko, R. Gomperts, B. Mennucci, H. P. Hratchian, J. V. Ortiz, A. F. Izmaylov, J. L. Sonnenberg, D. Williams-Young, F. Ding, F. Lipparini, F. Egidi, J. Goings, B. Peng, A. Petrone, T. Henderson, D. Ranasinghe, V. G. Zakrzewski, J. Gao, N. Rega, G. Zheng, W. Liang, M. Hada, M. Ehara, K. Toyota, R. Fukuda, J. Hasegawa, M. Ishida, T. Nakajima, Y. Honda, O. Kitao, H. Nakai, T. Vreven, K. Throssell, J. A. Montgomery, Jr., J. E. Peralta, F. Ogliaro, M. J. Bearpark, J. J. Heyd, E. N. Brothers, K. N. Kudin, V. N. Staroverov, T. A. Keith, R. Kobayashi, J. Normand, K. Raghavachari, A. P. Rendell, J. C. Burant, S. S. Iyengar, J. Tomasi, M. Cossi, J. M. Millam, M. Klene, C. Adamo, R. Cammi, J. W. Ochterski, R. L. Martin, K. Morokuma, O. Farkas, J. B. Foresman and D. J. Fox, *Gaussian 16*, Gaussian, Inc., Wallingford, CT, USA, 2016.
- 38 TURBOMOLE V7.5 2020. a development of University of Karlsruhe and Forschungszentrum Karlsruhe GmbH, 1989-2007, TURBOMOLE GmbH, since 2007.
- 39 D. O. Kashinski, G. M. Chase, R. G. Nelson, O. E. Di Nallo, A. N. Scales, D. L. VanderLey and E. F.-C. Byrd, *J. Phys. Chem. A*, 2017, **121**, 2265–2273.
- 40 E. G. Hohenstein and C. D. Sherrill, *J. Chem. Phys.*, 2010, **132**, 184111.
- 41 R. M. Parrish, L. A. Burns, D. G.-A. Smith, A. C. Simmonett, A. E. DePrince, E. G. Hohenstein, U. Bozkaya, A. Y. Sokolov, R. Di Remigio, R. M. Richard, J. F. Gonthier, A. M. James, H. R. McAlexander, A. Kumar, M. Saitow, X. Wang, B. P. Pritchard, P. Verma, H. F. Schaefer, K. Patkowski, R. A. King, E. F. Valeev, F. A. Evangelista, J. M. Turney, T. D. Crawford and C. D. Sherrill, *J. Chem. Theory Comput.*, 2017, **13**, 3185–3197.
- 42 (a) W. B. Schneider, G. Bistoni, M. Sparta, M. Saitow, C. Riplinger, A. A. Auer and F. Neese, *J. Chem. Theory Comput.*, 2016, **12**, 4778–4792; (b) G. Bistoni, *Wiley Interdiscip. Rev.: Comput. Mol. Sci.*, 2020, **10**, 1.
- 43 (a) F. Neese, *Wiley Interdiscip. Rev.: Comput. Mol. Sci.*, 2017, **8**, 33; (b) F. Neese, *Wiley Interdiscip. Rev.: Comput. Mol. Sci.*, 2011, **2**, 73–78.
- 44 C. E. Klots, *J. Chem. Phys.*, 1985, **83**, 5854–5860.
- 45 F. Kollipost, K. Papendorf, Y.-F. Lee, Y.-P. Lee and M. A. Suhm, *Phys. Chem. Chem. Phys.*, 2014, **16**, 15948–15956.

A.4 Supporting Information of Publication II

Electronic Supplementary Information

Chromone-methanol cluster in the electronic ground and lowest triplet state: A delicate interplay of non-covalent interactions

Pol Boden^a, Patrick H. Streb^a, Marcel Meta^a, Fabian Dietrich^{a,b}, Christoph Riehn^{a*}, Markus Gerhards^{†a}

^aFachbereich Chemie & State Research Center OPTIMAS, TU Kaiserslautern, Erwin-Schrödinger-Str. 52, D-67663 Kaiserslautern, Germany.

^bNúcleo Milenio MultiMat & Departamento de Ciencias Físicas, Universidad de La Frontera, Temuco, Chile.

Contents

Experimental results.....	2
R2PI experiments on chromone and chromone-methanol clusters.....	2
IR/UV experiments on chromone-methanol	4
IR/R2PI experiments on higher clusters.....	8
Theoretical results.....	10
Further analysis of the excited states for chromone-methanol	10
Further analysis of the T ₁ state	13
Binding and deformation energies.....	18
Barriers for isomer interconversion.....	18
References.....	21

Experimental results

R2PI experiments on chromone and chromone-methanol clusters

R2PI spectra were measured for chromone and the chromone-(MeOH)_n clusters, based on previous experiments on chromone.¹ Since chromone as well as the structurally related xanthone² both undergo intersystem crossing (ISC) into the triplet manifold upon electronic excitation, an ISC is also expected for the chromone-(MeOH)_n clusters. In the R2PI experiments, even at a delay of 23 μs between the excitation and ionization laser pulses, a strong ion signal was observed for the chromone-(MeOH)_n aggregates, which makes an ISC plausible. For successful ionization, a two-color process was required with the excitation laser scanned between 32522 cm⁻¹ and 34784 cm⁻¹. The frequency-fixed ionization laser was set to 46838 cm⁻¹ and irradiated 70 ns after the excitation laser. For isolated chromone we reproduced the 0-0 transition at 33896 cm⁻¹ (figure S1). Coordination of one or more methanol molecules leads to a red-shift, resulting in bands at 33292 cm⁻¹ and 33204 cm⁻¹ for the chromone-MeOH and chromone-(MeOH)₂ clusters, respectively. The band broadens significantly upon methanol coordination leading to unstructured spectra for the higher clusters, which are a first hint for UV fragmentation of larger clusters exhibiting similar UV absorption.

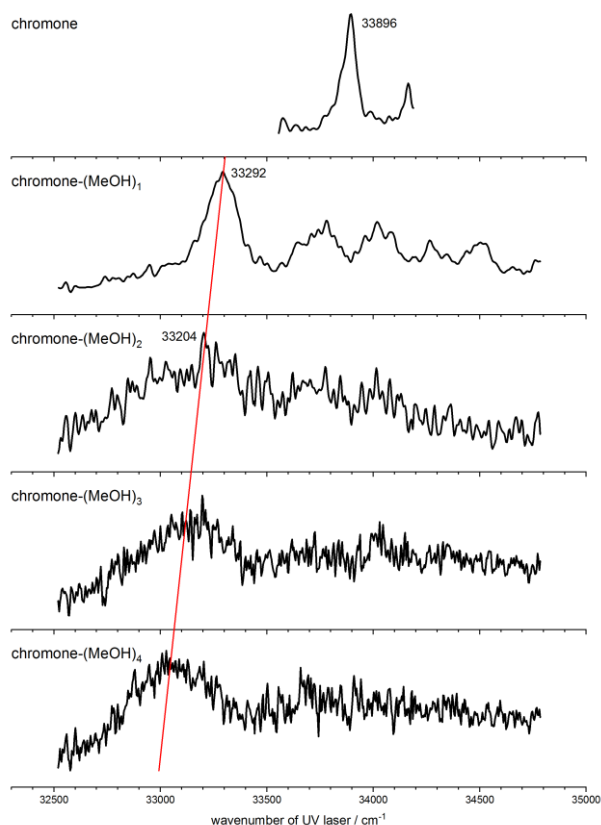


Figure S1: 2C-R2PI spectra for the mass traces of chromone and chromone-(MeOH)₁₋₄ (from top to bottom), with UV-ionization@46838 cm⁻¹. The redshift of the 0-0 transition upon addition of methanol is indicated with a red line as a guide to the eye.

Within the context of the expected intersystem crossing with the suspected subsequent “evaporative cooling” mentioned in the main manuscript, mass spectra with different time delays between the excitation and ionization laser pulses were recorded to analyze the cluster distribution over time. For the chromone monomer and the chromone-(MeOH)_n clusters up to n=6, the integrated signal intensities were determined and illustrated in figure S2.

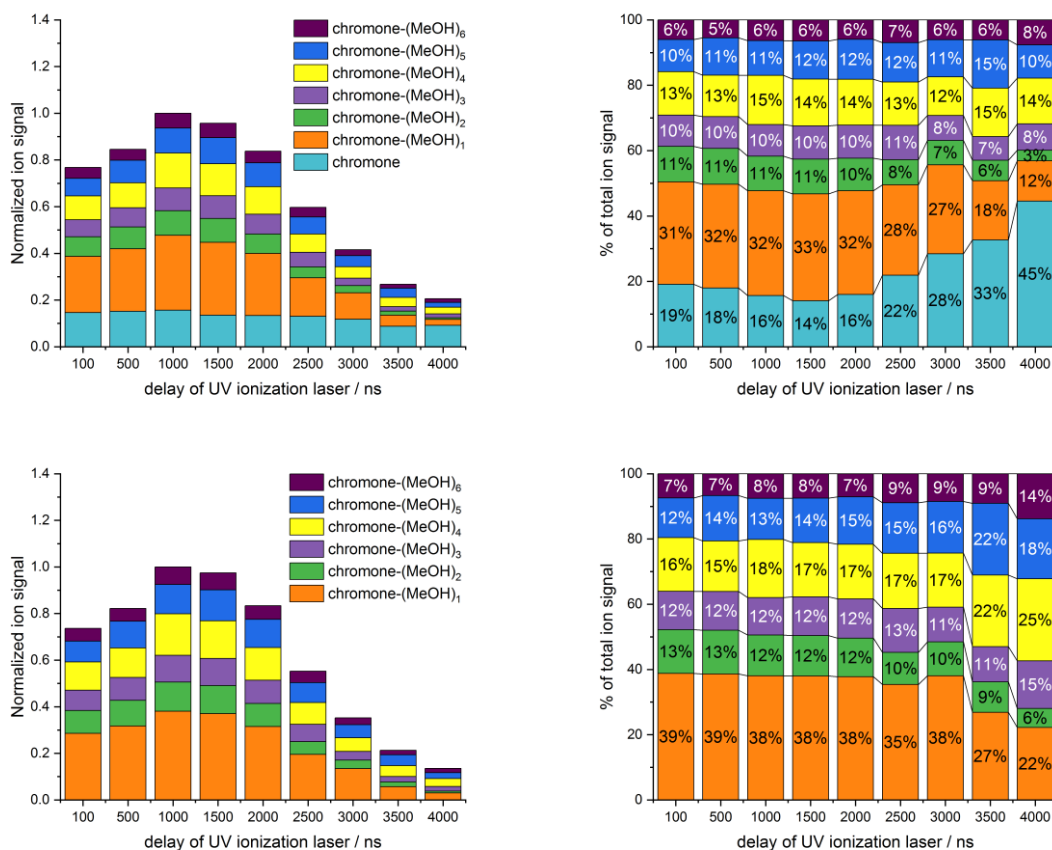


Figure S2: Normalized integrated ion signal intensities as a function of the time delay between the excitation and ionization laser pulses for chromone-(MeOH)_n clusters (n=1-6) and the chromone monomer (top left, bottom left) and the same as relative proportions of the sum over all signals (top right, bottom right). Despite the significant time-dependence of the total ion signal, the cluster distribution does not change significantly for delays between 100 and 3000 ns, which is especially visible when excluding the chromone monomer mass trace (bottom right).

Focussing on the top left diagram, it is noticeable that the sum of all considered ion signals shows an increase from 100 to 1000 ns and a successive more pronounced decrease towards the final data point at 4000 ns. To determine the cluster distribution, the relative proportion of each species was calculated for each time delay, resulting in the plot at the top right. It can be seen, that only at larger delay times (> 2000 ns), the relative chromone monomer ion signal intensity increases at the cost of the chromone-(MeOH)_{1,2} cluster signals, whereas the cluster distribution is constant for delays of 100 ns to 2000 ns. Thus, the “evaporative cooling” process seems to be finished after at most 100 ns, since no significant changes in the cluster distribution can be observed afterwards until a delay of 2000 ns. This is also supported by the nearly constant absolute ion signal of the chromone monomer which should increase if fragmentation of chromone-(MeOH)_n clusters occurs. It seems challenging to extract any further information from figure S2, as different effects could be responsible for the decrease of the chromone-(MeOH)_n cluster signals at delays > 2000 ns. For instance, the excited state lifetime of the (potentially hot) clusters (partially originating from fragmentation of larger clusters) is unknown, but can be decisive for ionization *via* R2PI. Furthermore, the excitation and ionization laser beams have to be spatially separated with increasing time delay between excitation and ionization, so that the detection within the Time-of-flight mass spectrometer might also influence this behavior. Nevertheless, omitting the constant chromone monomer signal intensity from the calculation (bottom left, bottom right) reveals that the cluster

distribution of the chromone-(MeOH)_n clusters can even be considered “stable” until 3000 ns. This indicates that, most importantly, the cluster distribution does not show significant changes for a time frame of 100 ns to 3000 ns and supports our claim that the “evaporative cooling” proposed in the manuscript is already completed at a shorter time scale.

IR/UV experiments on chromone-methanol

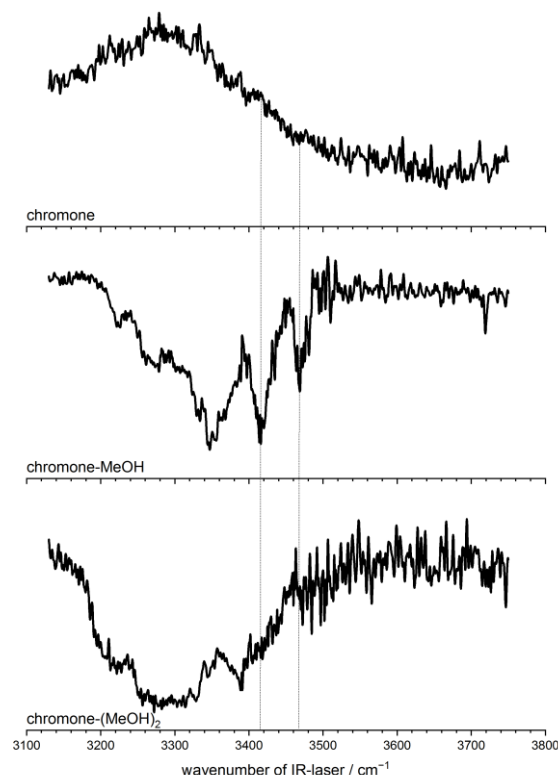


Figure S3: IR/R2PI spectra for the mass traces of chromone and chromone-(MeOH)₁₋₂, UV-excitation@33900 cm⁻¹, UV-ionization@46838 cm⁻¹; emphasizing that the features observed below 3400 cm⁻¹ on the chromone-MeOH mass trace are due to laser-induced fragmentation from larger clusters.

Analyzing the IR/R2PI spectrum displayed in figure S3, the increase of the signal intensity on the chromone monomer trace can be attributed to IR fragmentation of chromone-solvent clusters. The features below 3400 cm⁻¹ on the chromone-methanol mass trace are due to fragmentation effects of larger chromone-methanol clusters. Hereby, UV fragmentation effects should dominate, while the influence of (possibly weaker) IR fragmentation effects cannot be excluded. However, the two intense bands standing out at 3419 cm⁻¹ and at 3470 cm⁻¹ (highlighted with dashed lines) on the chromone-MeOH trace are unambiguously assigned to the chromone-MeOH species, as the other mass traces show no significant features in that spectral region (above 3400 cm⁻¹). The small peak at about 3720 cm⁻¹ is a sign of fragmentation effects of larger chromone-(MeOH)_n-H₂O aggregates. The broad unstructured feature on the chromone-(MeOH)₂ trace is again very likely affected by UV (and possibly IR) fragmentation of larger and less stable clusters.

The UV/IR/UV spectrum (figure S4) shows a broad structured band on the chromone-MeOH mass trace (dashed line), which is definitely blue-shifted relative to the broad dip on the chromone-(MeOH)₂ trace. Thus, the major features on the chromone-MeOH trace can definitely be assigned to the chromone-MeOH species and are not due to fragmentation. The small peak at about 3720 cm⁻¹ on the chromone-MeOH trace is explained by UV fragmentation of larger chromone-(MeOH)_n-H₂O

aggregates. The increase of the signal intensity on the chromone monomer trace is due to IR fragmentation of the chromone-MeOH species (and larger chromone-solvent clusters).

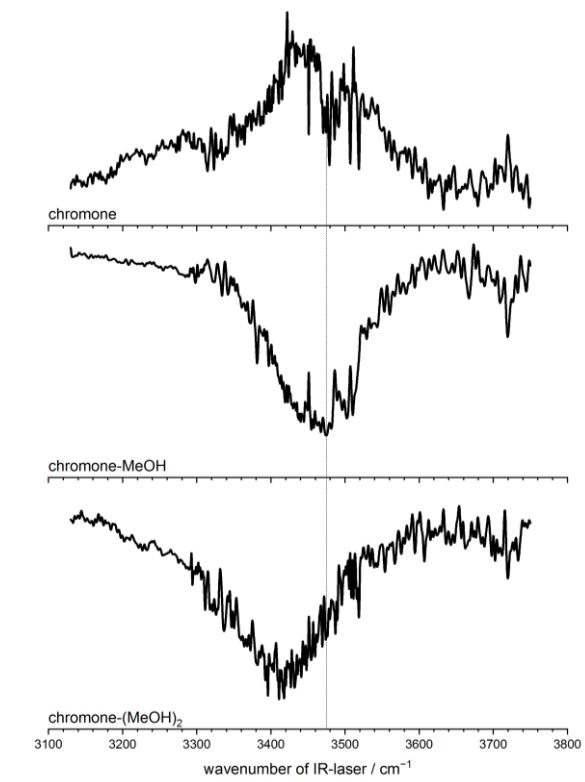


Figure S4: UV/IR/UV spectra for the mass traces of chromone and chromone-(MeOH)₁₋₂, UV-excitation@33900 cm⁻¹, UV-ionization@46838 cm⁻¹.

The sharp spikes which appear in the UV/IR/UV spectrum of chromone-methanol, in the spectral between 3450 and 3510 cm⁻¹, are caused by dips in the available IR laser power. For demonstration, the IR laser power curve for that spectral region is depicted in figure S5, together with the UV/IR/UV spectrum measured for chromone-methanol.

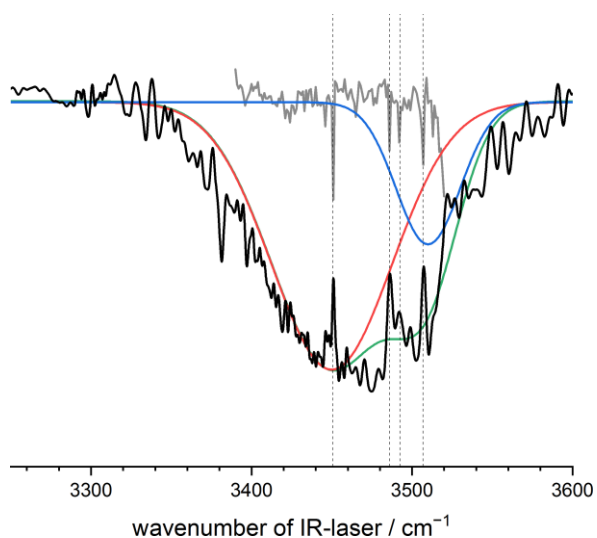


Figure S5: Laser power curve (grey trace) in comparison with the UV/IR/UV spectrum measured on the chromone-methanol trace. The correlation between the dips in the IR laser power curve and the discussed spikes observed in the IR experiment is illustrated by dashed grey lines.

Regarding the IR/R2PI and UV/IR/UV spectra of chromone-methanol a deconvolution with gaussians was performed (figure S6) to obtain a rough estimate for the relative population of the two competing isomers in the S_0 and T_1 state. For the S_0 state the ratio of both peak integrals amounts to 72:28 in favor of the outside isomer. Correcting for the different IR intensity of the bands results in a ratio of 66:34. Similarly, for the T_1 state, a ratio of 78:22 (uncorrected) and 72:28 (corrected) is obtained. Importantly, these values should only be understood as a rough estimate since other relevant factors as R2PI cross-sections, cooling efficiency and depletion efficiency cannot be addressed. Nevertheless, we can expect the increase in outside population to roughly match the increase in ΔE for the triplet state, which can be calculated by applying the Boltzmann formula, under the daring assumption that the temperatures in the S_0 and T_1 state are comparable. The preference for the outside isomer is clearly visible in the presented data, as well as the further increased population of the outside isomer in the excited state (see below). Interpretation of this value is difficult due to the inherent experimental errors. Nevertheless, the experimental prediction is close to the DLPNO-CCSD(T) value of 0.636, but differing significantly from the DFT value of 0.382 (DFT).

$$\frac{N(out)}{N(in)} = \exp(-\Delta E/RT)$$

$$\ln\left(\frac{N(out)}{N(in)}\right) = -\Delta E/RT$$

$$\frac{\ln\left(\frac{N(out, S_0)}{N(in, S_0)}\right)}{\ln\left(\frac{N(out, T_1)}{N(in, T_1)}\right)} = \frac{-\Delta E(S_0)/RT}{-\Delta E(T_1)/RT} = \frac{\Delta E(S_0)}{\Delta E(T_1)} = 0.702$$

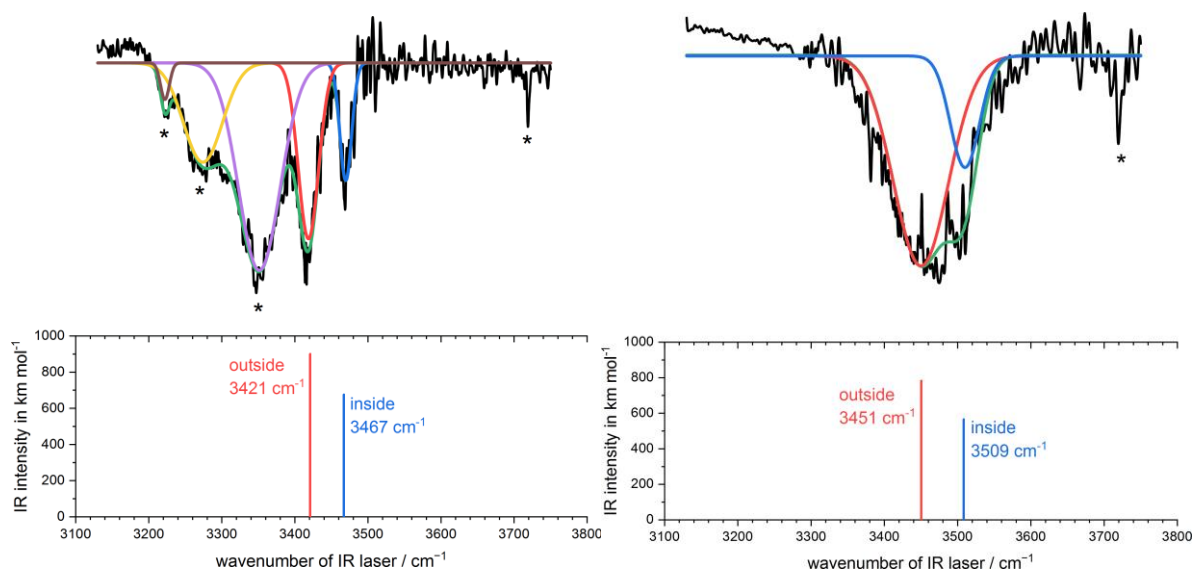


Figure S6: Theoretical and experimental IR spectra for the S_0 (left) and T_1 (right) state including gaussian fit functions to evaluate relative isomer populations. The convolution of all peaks (green) is composed of the inside (blue) and outside (red) peak with additional fragmentation peaks (purple, yellow, brown). Calculated OH stretching frequencies are obtained at CAM-B3LYP-D3(BJ)/def2-TZVP level, scaled by 0.95.

In the main manuscript, the experimental IR/R2PI were compared with the three energetically lowest structures since already the ether-bound cluster is energetically strongly disfavored compared to the carbonyl-bound clusters. Here, a full comparison of the experimental spectrum with all nine calculated isomers is shown (figure S7). All energetically less favored structures ($\Delta E > 15 \text{ kJ mol}^{-1}$) show a strongly blue-shifted OH stretching vibration relative to the experiment. Furthermore, the IR intensity of the considered vibration is significantly lowered because no coordination with the highly polar carbonyl group takes place. Thus, only the first two isomers are taken into consideration.

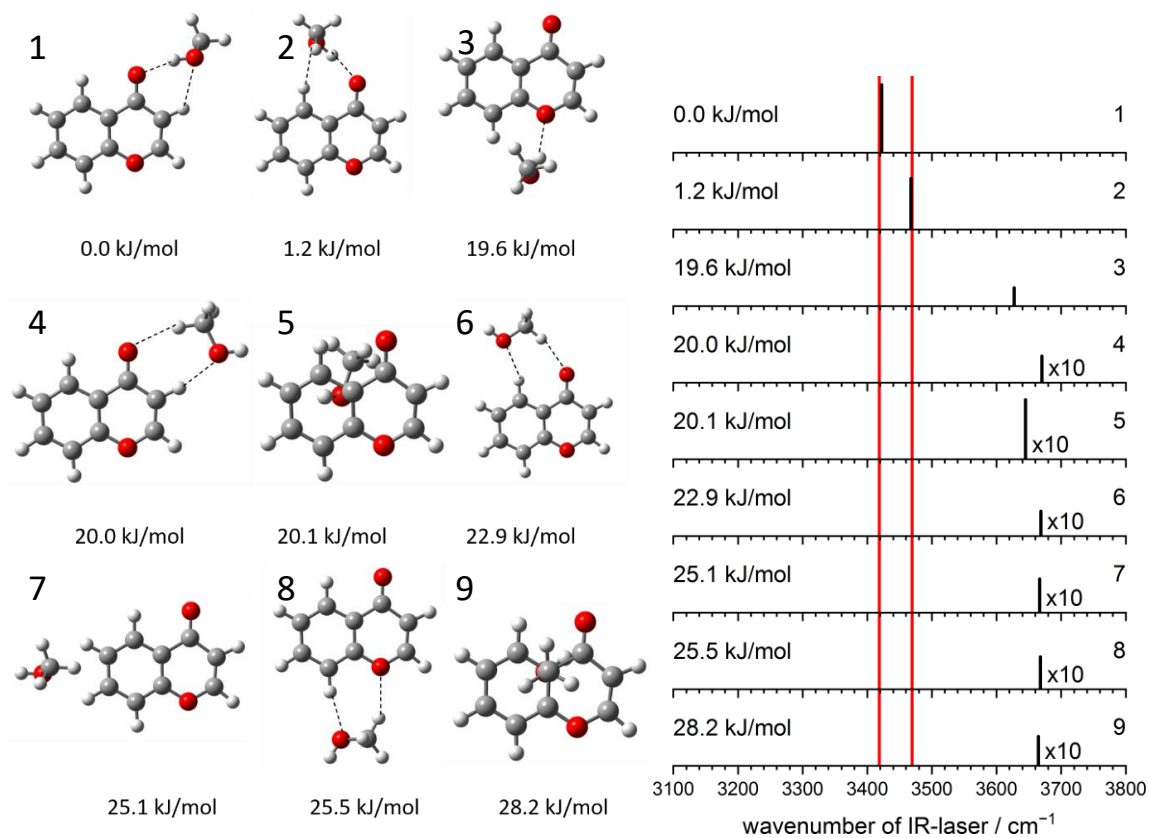


Figure S7: Calculated structures of chromone-MeOH with their respective electronic energies (left) and their respective IR spectra (right), compared with the experiment (red lines), showing that the carbonyl-bound structures exhibit the observed red-shift of the OH stretching band. Geometry optimizations and harmonic frequency calculations were performed at CAM-B3LYP-D3(BJ)/def2-TZVP level. Vibrational frequencies are scaled by 0.95.

IR/R2PI experiments on higher clusters

We also investigated the chromone-(MeOH)₂ complex in the electronic ground state, with the quantum chemical calculations identifying multiple structure types. For all energetically relevant isomers, a first methanol molecule is linked to the carbonyl group of the chromone unit. The additional methanol molecule is either hydrogen-bonded to the first solvent molecule (isomers 1-10 in figure S9) or can occupy another free binding site of chromone, such as the second free electron pair at the carbonyl oxygen atom (isomers 11-12 in figure S9). Hereby, the calculations clearly show that the first option is energetically advantaged, with a strong preference for the outside binding motif in comparison to the inside type. However, the measured spectrum (in figure S8) is not well resolved, so that we are not able to assign one specific structure to the experiment. Nevertheless, the outside-bound isomers 1 and 2, which are further stabilized *via* C–H···O contacts between chromone and the additional methanol molecule, exhibit the right pattern to be correlated to the spectrum, while (minor) contributions of other isomers, especially isomers 3-5 with occupation of the inside pocket, cannot be excluded. Finally, we cannot assign a specific outside-bound cluster, but may state that this motif contributes strongly to the experimental spectrum. This is further supported by the relative energy, which assigns the global minimum to these structures.

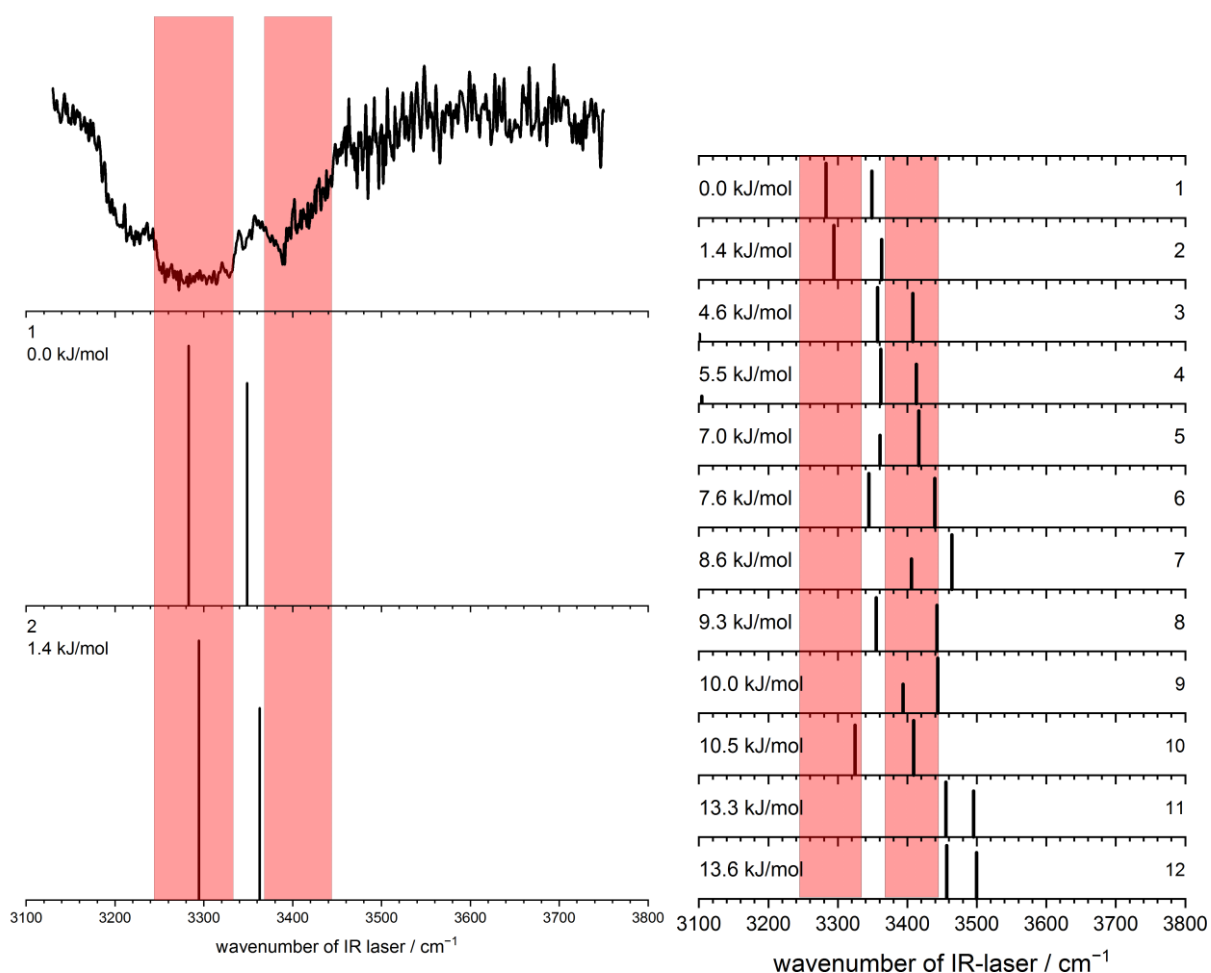


Figure S8: IR/R2PI spectrum of chromone-(MeOH)₂ compared with two calculated spectra of outside-bound clusters (left). A comparison with the IR spectra of all calculated structures is shown on the right, the red areas representing the broad features between 3244/3332 cm⁻¹ and 3368/3445 cm⁻¹. The given energies refer to electronic energies. The two outside-bound structures may correlate with the observed experimental pattern, especially the most red-shifted band, although contributions of

other isomers cannot be excluded. Geometry optimizations and harmonic frequency calculations were performed at CAM-B3LYP-D3(BJ)/def2-TZVP level. Vibrational frequencies are scaled by 0.95.

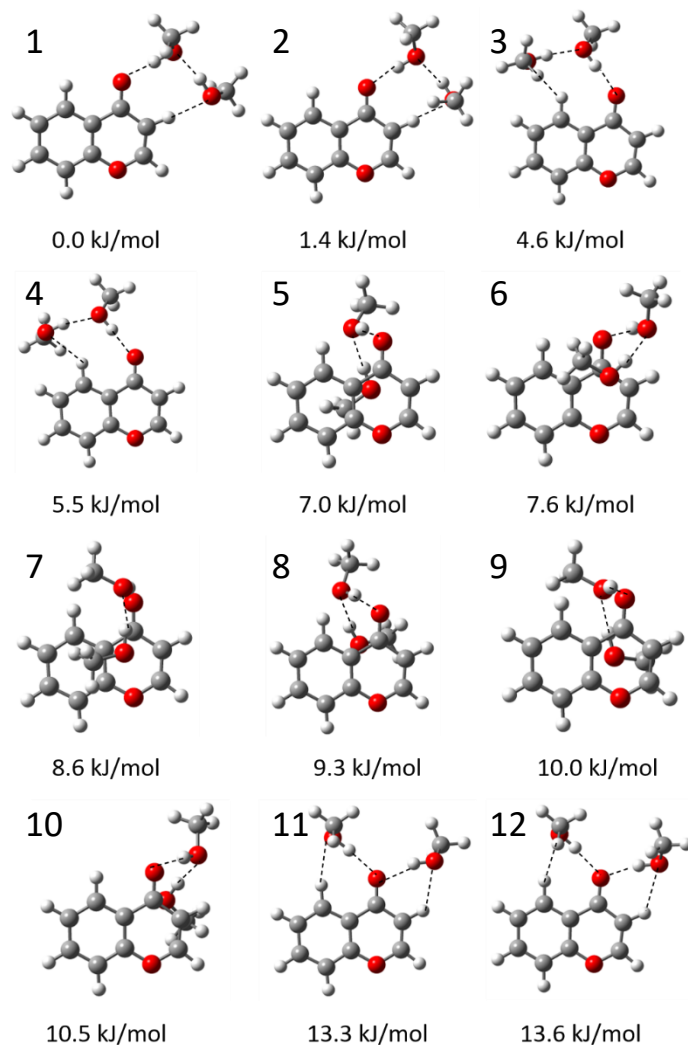


Figure S9: Optimized structures for the chromone-(MeOH)₂ cluster in the S₀ state with their respective electronic energies, as obtained at the CAM-B3LYP-D3(BJ)/def2-TZVP level.

Theoretical results

Further analysis of the excited states for chromone-methanol

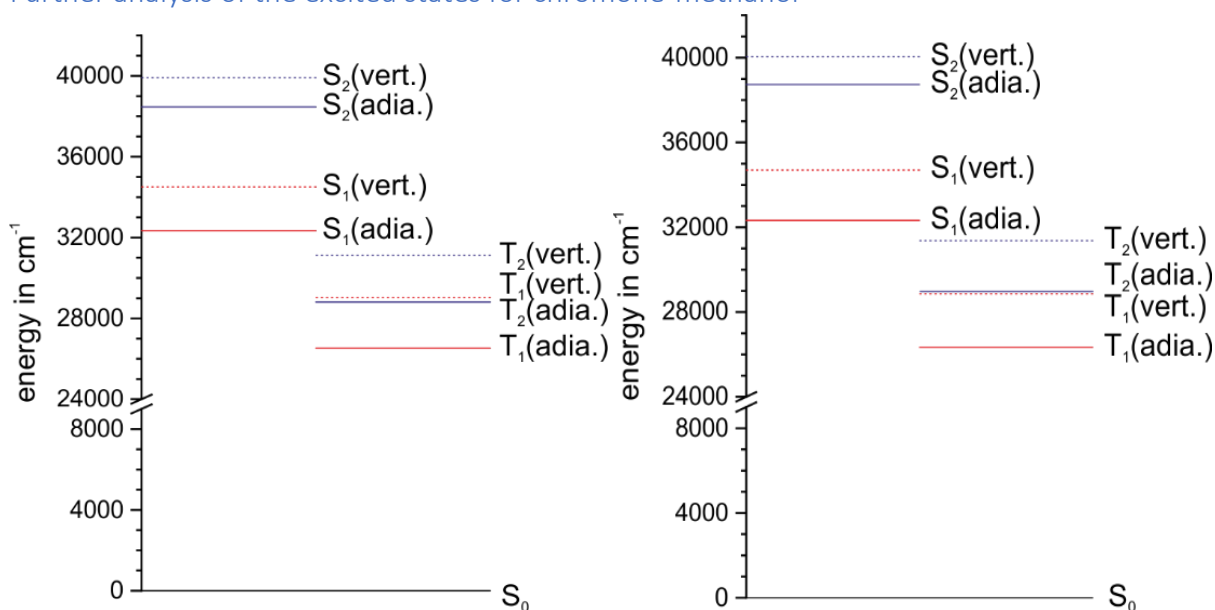


Figure S10: Jablonski diagram showing the first two singlet and triplet states, calculated at the TDDFT/CAM-B3LYP-D3(BJ)/def2-TZVP level; inside binding motif (left) and outside binding motif (right).

To analyze the electronic excitation and subsequent intersystem crossing, we calculated the excitation energies (figure S10) and natural transition orbitals (figures S11-S14) for the inside and outside isomers, for the first two excited singlet and triplet states using TDA-TDDFT/CAM-B3LYP/def2-TZVP. The usage of the Tamm-Dancoff approximation instead of the Random-Phase approximation was necessary to converge the calculations for the triplet states, while CAM-B3LYP was required to converge the excited singlet states. We observe a significant deviation from the experimental values since the band at 33292 cm^{-1} is assigned to the S_2 state, which is calculated at 39916 cm^{-1} (inside) and 40043 cm^{-1} (outside), respectively. Considering the character of the vertical excitations within the singlet manifold, we can state that the $S_0 \rightarrow S_1$ transition is of n, π^* type, while the $S_0 \rightarrow S_2$ transition is of π, π^* type. The calculations confirm the weakness of the $S_0 \rightarrow S_1$ transition, with a oscillator strength, which is weaker by a factor of around 8000 in comparison to the $S_0 \rightarrow S_2$ transition. The $S_0 \rightarrow S_2$ transition is of similar strength for the inside and outside motif. This should result in a negligible influence on the R2PI cross section, as mentioned in the main manuscript. Natural transition orbitals (NTO)³ were calculated and are shown below (figures S11-S14). For the triplet manifold the $S_0 \rightarrow T_1$ transition is of π, π^* type while the $S_0 \rightarrow T_2$ transition is of n, π^* type. Interestingly, the T_2 and S_2 state are of different character, which could serve as an explanation for the observed strong intersystem crossing according to the rule of El-Sayed⁴, leading to the assignment of an $S_2(\pi, \pi^*) \rightarrow T_2(n, \pi^*)$ intersystem crossing with subsequent internal conversion into the T_1 state, contradicting the assignment of the ${}^3(n, \pi^*)$ state as the lowest triplet state.¹ The energetic difference between the unrelaxed S_2 state and relaxed T_1 state amounts to 13387 cm^{-1} or 160 kJ mol^{-1} (inside) and 13709 cm^{-1} or 164 kJ mol^{-1} (outside), respectively. At this point it should also be noted that the T_1 state is definitely reached in the performed experiment, since the vibrational frequencies predicted for the chromone-methanol cluster in its T_2 state [3625 cm^{-1} (inside), 3651 cm^{-1} (outside), 3612 cm^{-1} (ether)] do not correlate with the measured UV/IR/UV spectrum.

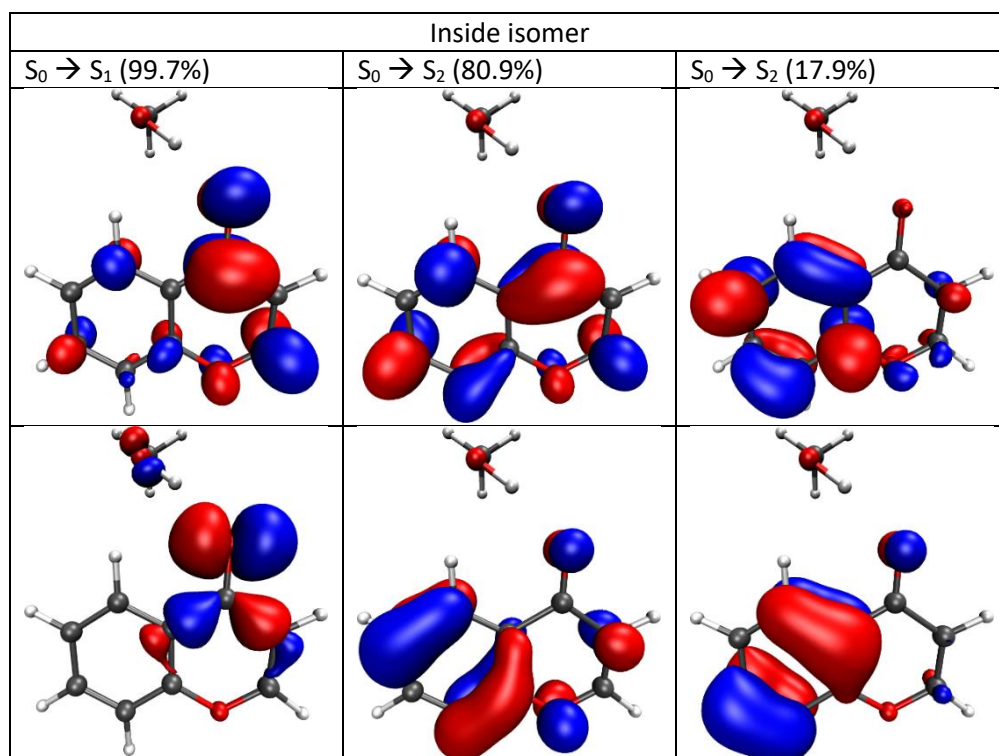


Figure S11: Natural transition orbitals, with occupied (bottom) and virtual (top) orbitals.

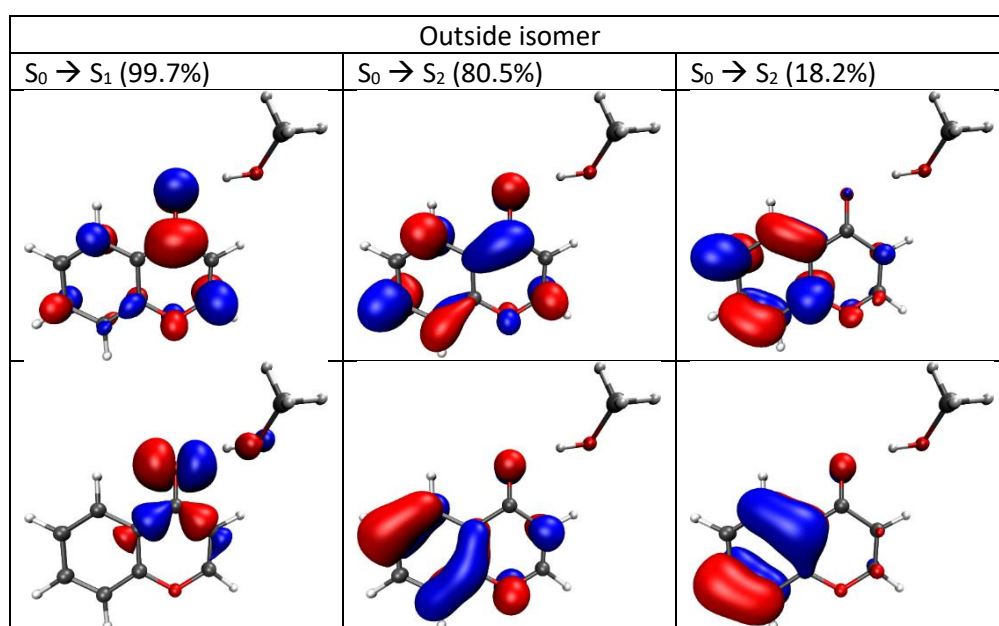


Figure S12: Natural transition orbitals, with occupied (bottom) and virtual (top) orbitals.

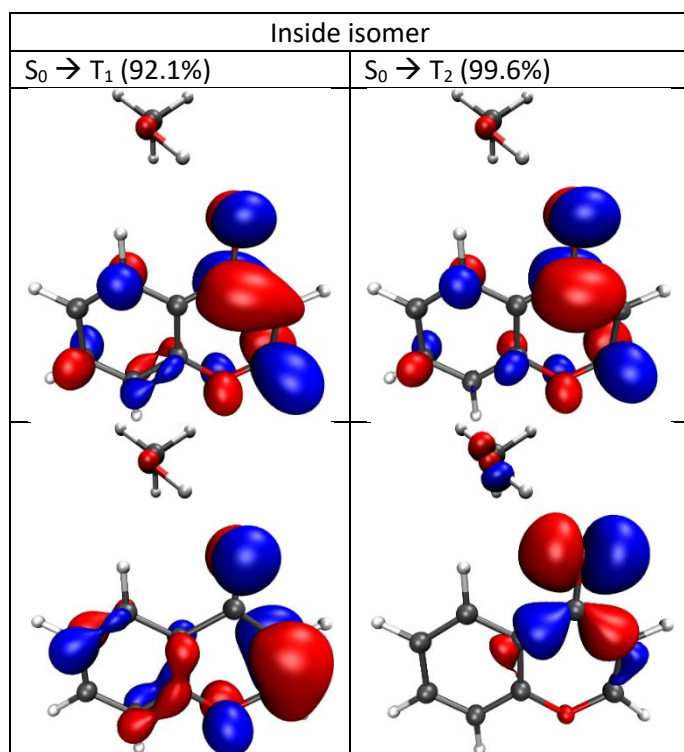


Figure S13: Natural transition orbitals, occupied (bottom) and virtual (top) orbitals.

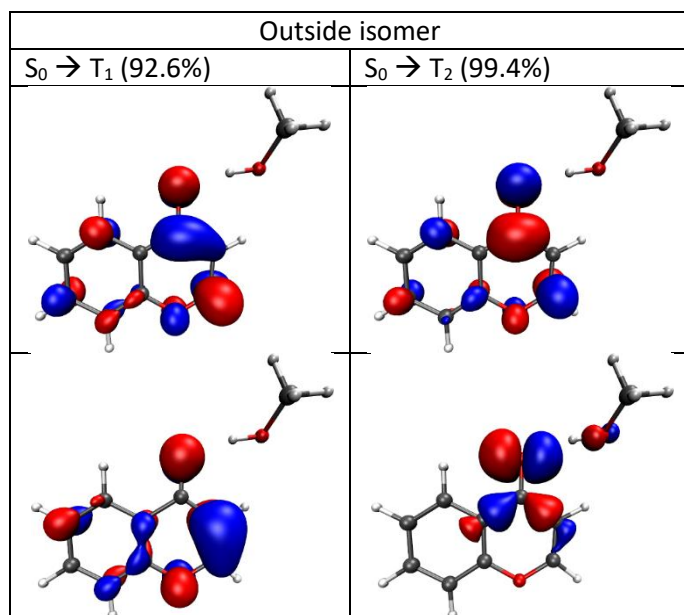


Figure S14: Natural transition orbitals, with occupied (bottom) and virtual (top) orbitals.

In the main manuscript, we refer to the triplet geometries calculated *via* UDFT not TDA-TDDFT, thus we performed TD-DFT calculations utilizing UDFT geometries to confirm that the order of the two triplet states is the same, which is indeed the case. The UDFT calculations allow us to handily extract the spin densities, which are plotted below (figure S15). The spin density is strongly localized on the distorted 4-pyrone ring of the chromone moiety, especially on the carbon atom next to the ether oxygen.

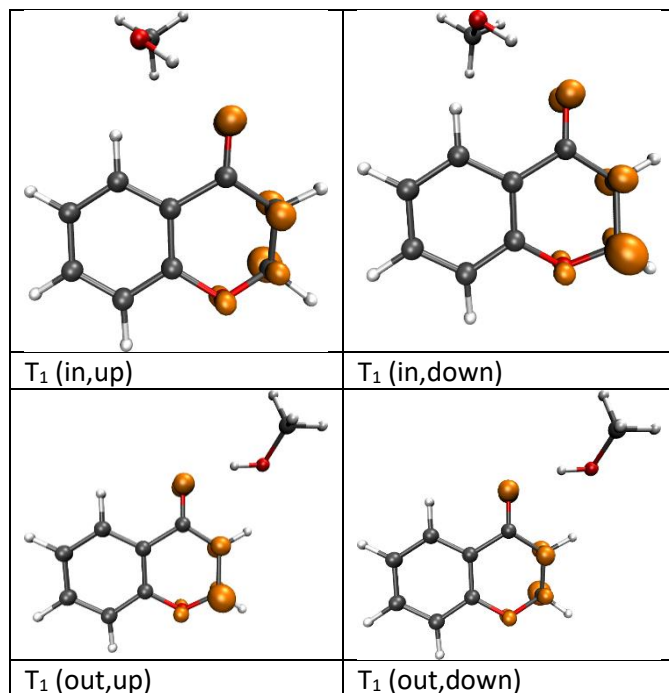


Figure S15: Spin densities of chromone-MeOH in the T₁ state, which are localized onto the 4-pyrone ring of the chromone molecule.

Further analysis of the T₁ state

The description of the lowest triplet state (T₁) is possible by either TD-DFT, using the S₀ as reference or UDFT, using the triplet state as reference. Both methods result in the loss of planarity of the 4-pyrone ring (see figure S16), resulting in “up” and “down” isomers for the triplet state. “Up” is referring to the geometry where the puckered carbon atom is on the same side of the 4-pyrone plane as the solvent molecule, “down” for the inverse configuration. Comparing the geometries calculated by TD-DFT (in red) and UDFT (in blue), the geometric distortion is much more pronounced for the latter (see figure S17). Both methods have in common that the geometric distortion is completely localized onto the 4-pyrone ring, which is demonstrated in figure S17, where all eight possible structures are displayed (UDFT/TD-DFT, in/out, up/down).

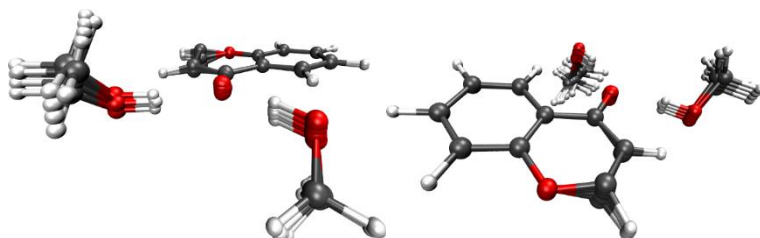


Figure S16: Overlay of all triplet structures, showing the conservation of the benzene ring planarity in chromone

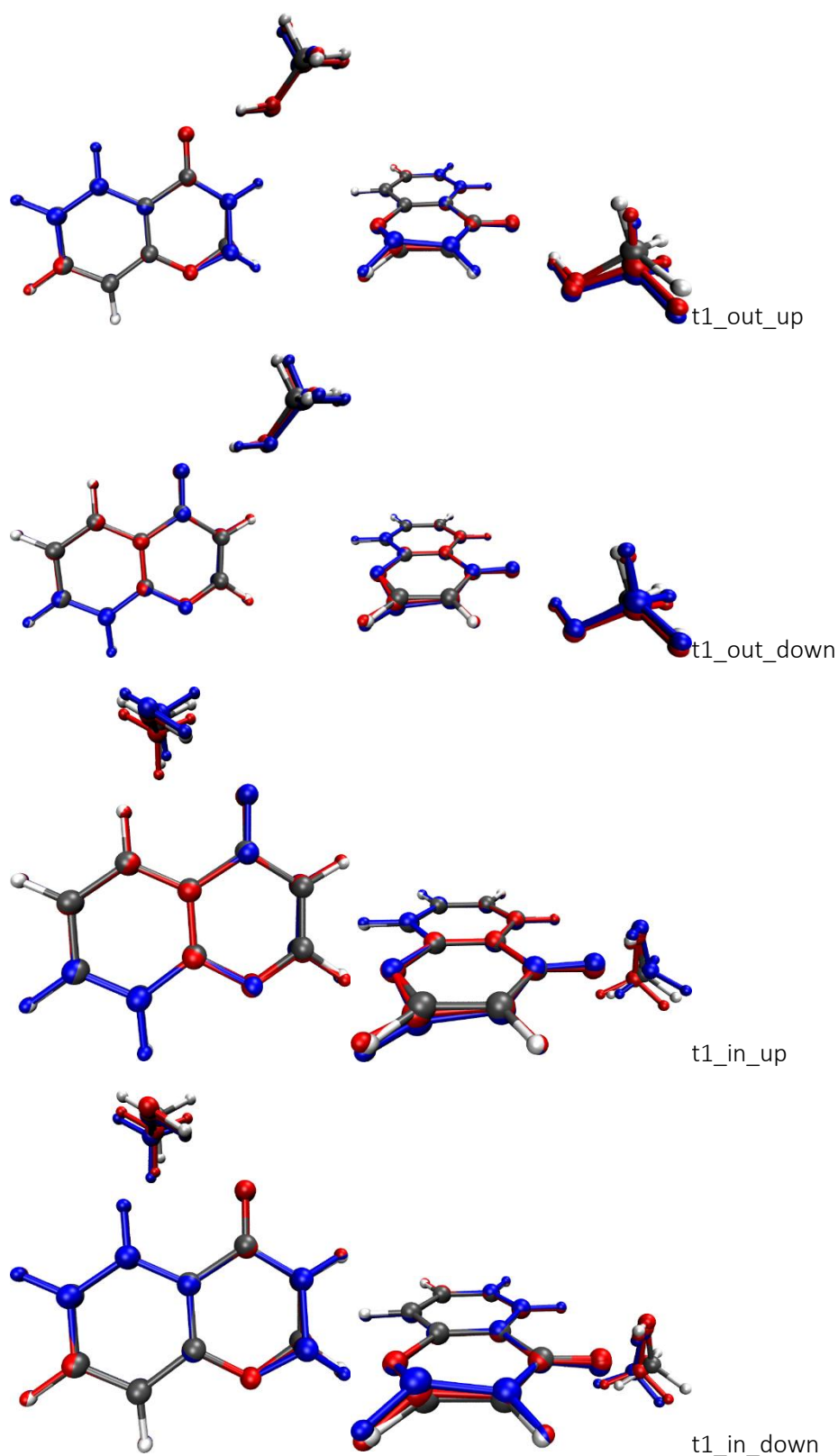


Figure S17: Overlay of multiple structures of chromone-MeOH, ground state (standard colors), TDDFT (red) and UDFT (blue), indicating that ring puckering is stronger in the UDFT case. From top to bottom: outside, up / outside,down / inside,up / inside,down. The stronger distortion of the 4-pyrone ring for the UDFT geometries is clearly visible as well as the conservation of the still planar aromatic ring.

To compare the quality of both approaches, SAPTO/jun-cc-pVTZ and DLPNO-CCSD(T)/def2-TZVP calculations were performed on the relaxed geometries, with the results shown in table S1.

Table S1: Comparison of electronic energies calculated with SAPTO/def2-TZVP and DLPNO-CCSD(T)/def2-TZVP for UDFT and TD-DFT inside/outside geometries in their respective up/down configuration, indicating that UDFT provides a better description of the system since TD-DFT geometries provide worse results (higher energy or failing) in most cases. The relative energies are in reference to the lowest energy of the outside,down structure obtained by UDFT.

Geometry	in	in	out	out	in	in	out	out
Puckering	up	down	up	down	up	down	up	down
Method	UDFT	UDFT	UDFT	UDFT	TD-DFT	TD-DFT	TD-DFT	TD-DFT
E(SAPTO) in kJ/mol	-21.84	-21.82	-24.15	-24.25	n. a.	117.97	-27.86	-27.85
ΔE (DLPNO-CCSD(T)) in kJ/mol	2.69	2.39	0.07	0.00	7.73	7.30	5.53	5.63

The data show that the UDFT geometries are able to describe both up and down isomers for the inside and outside structures in a satisfactory manner. The relative energies for the outside structure are around 3 kJ/mol higher using the UDFT geometry, but the TD-DFT geometries fail to provide meaningful SAPTO values for inside structures. The DLPNO-CCSD(T) results support this conclusion: The description with TDDFT leads to around 5 kJ/mol higher energies for both isomers, indicating that UDFT provides a better description of the global minimum. Thus, for further analysis in the main manuscript as well as in the supporting information, the UDFT geometries are used.

Still, the question whether the up and down isomer differ significantly remains to be answered. Comparisons of the relative energies and frequencies obtained by UDFT as well as the relative energies obtained *via* SAPTO and LED-DLPNO-CCSD(T) are shown in table S2. No method estimates a ΔE greater than 0.3 kJ/mol between the up and down conformation so that the in and out motifs can be interpreted as doubly-degenerated states with respect to the ring puckering. Both configurations exhibit nearly equal OH stretching frequencies, thus differentiating between both structures in the experimental spectrum is not possible.

Table S2: Comparison of energies and frequencies obtained by UDFT, SAPTO and DLPNO-CCSD(T) for the up/down configurations of both inside and outside motif. The corresponding spin expectation value of the UDFT calculation does not show significant spin contamination.

Geo	Puckering	$\langle S^2 \rangle$	ΔE (UDFT)	$\tilde{\nu}$ (OH) in cm^{-1}	ΔE (SAPTO) in kJ/mol	ΔE (DLPNO-CCSD(T)) in kJ/mol
in	up	2.025	0.15	3690	0	0.30
in	down	2.025	0	3693	0.02	0
out	up	2.024	0.02	3635	0.10	0.07
out	down	2.024	0	3632	0	0

A detailed discussion of the energy decomposition analysis obtained *via* SAPTO can be found in the main manuscript, while a complete decomposition of the SAPTO energy is given in table S3. To simplify discussion, only the slightly more stable down configuration is considered when analyzing the triplet states. The results of the LED-DLPNO-CCSD(T) method are discussed in the following.

Table S3: Results of energy decomposition analysis by SAPT0/jun-cc-pVDZ. The raw values for each interaction for the respective electronic state and isomer (col. 2-5), the energy difference between the *inside* and *outside* isomer for each interaction (col. 6,7) and the change in ΔE going from the S_0 to T_1 state (col. 8). A detailed explanation and derivation of all contributions can be found in literature.⁵ The electrostatic and exchange contribution only consist of one term, the induction interaction consists of three terms $E_{ind,resp}^{(20)}$, $E_{exch-ind,resp}^{(20)}$, $\delta_{HF}^{(2)}$. The dispersion interaction is split into $E_{disp}^{(20)}$ and $E_{exch-disp}^{(20)}$, which can be separated further into same-spin and opposite-spin parts. All values in kJ/mol.

	Inside (S0)	Outside (S0)	Inside (T1)	Outside (T1)	$\Delta E(S0)$	$\Delta E(T1)$	$\Delta\Delta E(S0,T1)$
E_{elst}	-57.9	-60.4	-43.5	-50.8	2.5	7.3	4.8
$E_{elst}^{(10)}$	-57.9	-60.4	-43.5	-50.8	2.5	7.3	4.8
E_{exch}	57.5	58.7	50.4	56.5	-1.2	-6.1	-4.8
$E_{exch}^{(10)}$	57.5	58.7	50.4	56.5	-1.2	-6.1	-4.8
E_{ind}	-18.2	-18.9	-13.5	-16.0	0.6	2.4	1.8
$E_{ind,resp}^{(20)}$	-24.1	-27.0	-19.3	-24.0	2.9	4.7	1.8
$E_{exch-ind,resp}^{(20)}$	13.4	15.8	11.6	14.7	-2.4	-3.1	-0.6
$\delta_{HF}^{(2)}$	-7.5	-7.7	-5.9	-6.7	0.2	0.8	0.6
E_{disp}	-16.4	-15.2	-15.2	-14.0	-1.3	-1.2	0.0
$E_{disp}^{(20)}$	-20.0	-18.9	-18.2	-17.3	-1.1	-0.9	0.2
$E_{exch-disp}^{(20)}$	3.5	3.7	2.9	3.3	-0.2	-0.4	0.5
$E_{disp,SS}^{(20)}$	-10.0	-9.4			-0.5		
$E_{disp,OS}^{(20)}$	-10.0	-9.4			-0.5		
$E_{exch-disp,SS}^{(20)}$	2.0	2.1			-0.1		
$E_{exch-disp,OS}^{(20)}$	1.5	1.6			-0.1		
E_{tot}	-35.1	-35.7	-21.8	-24.2	0.6	2.4	1.8

Table S4: Energy decomposition analysis with LED-DLPNO-CCSD(T)/def2-TZVP, $\Delta E_{geo-prep}$ is the energetic penalty for distorting the monomers into the dimer geometry, $\Delta E_{el-prep}^{ref.}$ is the electronic preparation in the reference (Hartree-Fock), $E_{elstat}^{ref.}$ and $E_{exch}^{ref.}$ describe the electrostatic and exchange inter-fragment contributions in the reference (HF), while E_{disp}^{C-CCSD} describe the dispersive contribution from the correlation energy. $\Delta E_{non-disp}^{C-CCSD}$ contains some electronic preparation from the correlation energy, but also any non-dispersive correlation energy (charge transfer, intrafragment double excitations and singles contributions). $\Delta E_{int}^{C-(T)}$ describes the change for the triples correction. $\Delta(S_0)$ and $\Delta(T_1)$ describe the difference between inside and outside isomer for each contribution, with positive values indicating a preference for the outside isomer. All values in kJ/mol.

	Inside (S ₀)	Outside (S ₀)	Inside (T ₁)	Outside (T ₁)	$\Delta(S_0)$	$\Delta(T_1)$
$\Delta E_{geo-prep}$ (Chromon)	0.6	0.3	0.2	-0.2	0.3	0.5
$\Delta E_{geo-prep}$ (MeOH)	0.1	0.2	0.2	0.5	-0.2	-0.3
$\Delta E_{el-prep}^{ref.}$ (Chromon)	92.5	95.9	72.5	81.9	-3.4	-9.3
$\Delta E_{el-prep}^{ref.}$ (MeOH)	82.0	81.8	70.8	77.4	0.3	-6.6
$E_{elstat}^{ref.}$	-166.1	-171.3	-135.1	-154.8	5.1	19.7
$E_{exch}^{ref.}$	-29.1	-29.1	-26.3	-28.1	0.0	1.9
$\Delta E_{non-disp}^{C-CCSD}$	3.9	3.3	5.8	6.9	0.5	-1.1
E_{disp}^{C-CCSD}	-13.7	-12.7	-14.0	-12.5	-1.1	-1.5
$\Delta E_{int}^{C-(T)}$	-2.0	-2.0	-1.5	-0.7	-0.1	-0.8
ΔE (total)	-31.9	-33.4	-27.4	-29.7	1.5	2.4

As discussed above and in the main manuscript, LED-DLPNO-CCSD(T) predicts the outside isomer as the more stable isomer both in the S₀ and T₁ state. Although SAPT0 and LED-DLPNO-CCSD(T) are difficult to compare directly due to their different approach (SAPT: perturbative, DLPNO: supramolecular), careful analysis is still possible. This shows *e.g.* that, similar to the SAPT0 values, the electrostatic interaction is the strongest attractive interaction with dispersion being significantly weaker. Comparing the contributions for the inside and outside isomer, nearly all contributions are equal in value except the attractive electrostatic interaction as well as the related electronic preparation of the chromone. This can be interpreted as better orbital overlap between the carbonyl group and the OH group of the methanol for the outside motif, resulting in a stronger hydrogen bond and overall higher binding energy in the S₀ state. Analyzing the T₁ state confirms the main theses in the main manuscript. The ΔE is mostly influenced by the electronic preparation of both MeOH and chromone as well as the electrostatic interaction. Although the electronic preparation penalty is higher for the outside isomer by 9.3 and 6.6 kJ/mol (15.9 kJ/mol total), this is more than compensated by the increased electrostatic contribution of 19.7 kJ/mol resp. to the inside isomer. We observe again a side dependence in the triplet state, resulting in significantly increased electronic

preparation for the methanol, adapting to the flexible outside pocket. Furthermore, the binding energy is lowered upon electronic excitation, again coinciding with SAPTO results. Finally, the negative geo-prep energy for the chromone molecule is of course unphysical. Since the deformation energy seems to be quite small (< 0.5 kJ/mol), this numeric error occurs due to the accuracy of the DLPNO-CCSD(T) method. Deformation energies calculated by DFT are discussed in the following, and confirm this hypothesis.

Binding and deformation energies

The OH stretching frequency of an H-donor is closely related to the strength of the hydrogen-bond established with the H-acceptor. Thus, the observed blue-shift of the OH stretching frequency switching from the S_0 to the T_1 state should be visible in binding energy calculations. The binding energy is calculated in following manner:

$$E_{BDE} = E'_{Chromon} + E'_{MeOH} - E_{Dimer}$$

with: $E'_{Chromon}, E'_{MeOH} =$ Energy of resp. molecule in the dimer geometry

For the discussion of the BDE, we deliberately chose not to apply a BSSE correction. A comparing simulation for the S_0 geometries reveals that the difference between “inside” and “outside” is insignificant (both: 3.9 kJ/mol). Furthermore, it is known that the usual counter-poise correction⁶ scheme can lead to deviations from the true BDE⁷. Finally, the deformation energy is calculated in a similar manner by taking the energy difference of the relaxed monomer and the monomer in the dimer geometry.

Table S5: Binding and deformation energies for the chromone-MeOH cluster for the S_0 and T_1 state for both geometries (inside/outside). For the triplet state, the puckering of the 4-pyrone ring is also considered. All values are given in kJ/mol.

State	Geo	Puckering	Method	BDE	$E_{Def}(Chromon)$	$E_{Def}(MeOH)$
S_0	in	-	DFT	40.2	0.8	0.5
S_0	out	-	DFT	41.2	0.5	0.6
T_1	in	up	UDFT	35.5	0.6	0.3
T_1	in	down	UDFT	35.6	0.6	0.4
T_1	out	up	UDFT	38.6	0.2	0.4
T_1	out	down	UDFT	38.6	0.2	0.4

Starting with the deformation energies, it is remarkable how all values are below 1 kJ/mol, indicating low barriers for reorganization. The binding energy is strongest for the outside isomer in general, which is reasonable, since it is the global minimum. The observed blue-shift of the OH stretching frequency can be explained by the reduced binding energy in the triplet state, while the larger splitting of the frequencies of the two relevant isomers is caused by the increased difference in binding energy from 1 kJ/mol to 3 kJ/mol.

Barriers for isomer interconversion

As explained in the main manuscript, the interconversion barriers between different isomers were calculated by relaxed scans along an appropriate coordinate with the results shown below (fig. S18-22).

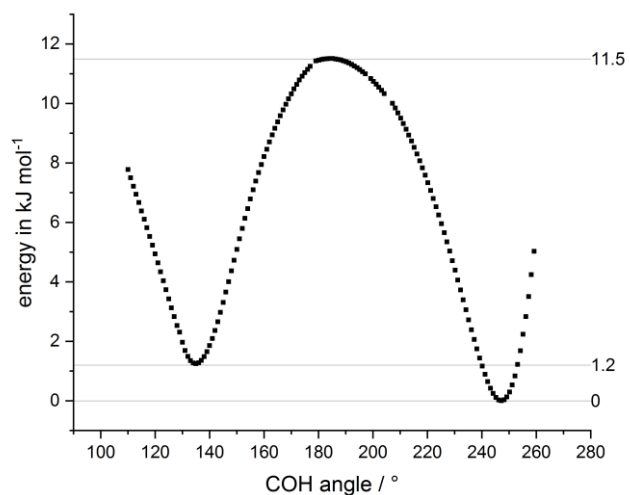


Figure S18: Interconversion barrier between inside and outside isomer in the S0 state

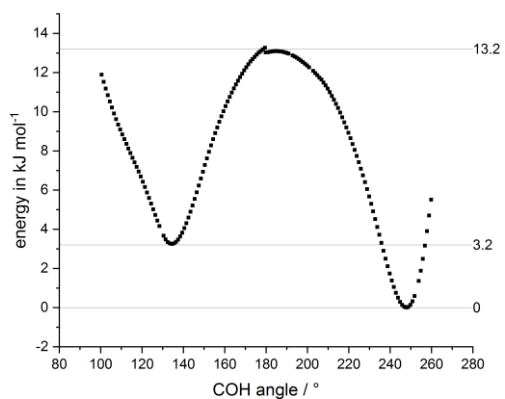


Figure S19: Interconversion barrier between inside and outside isomer in the T1 state (down configuration)

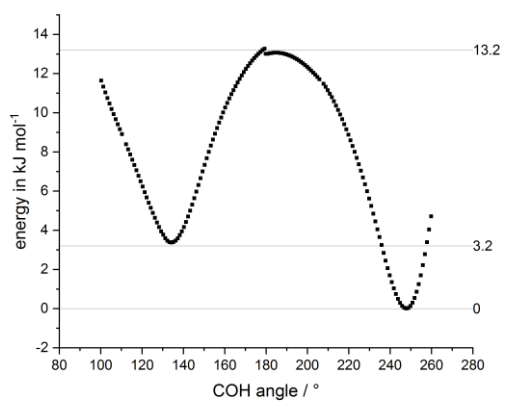


Figure S20: Interconversion barrier between inside and outside isomer in the T1 state (up configuration).

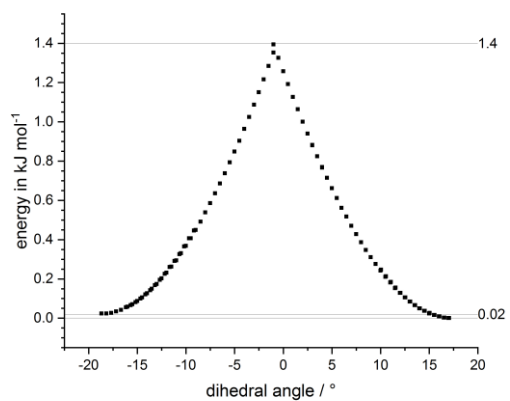


Figure S21: Interconversion barrier between up and down isomer in the T1 state (outside motif), the lowest line denotes the zero (omitted for clarity).

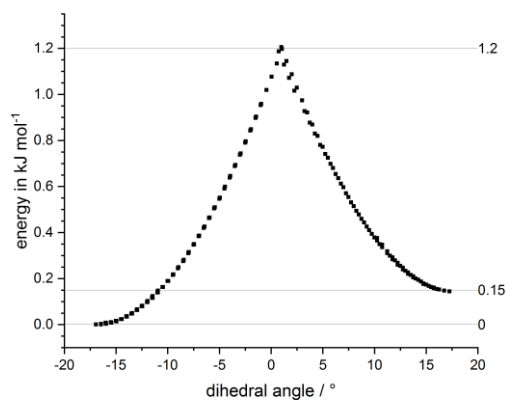


Figure S22: Interconversion barrier between up and down isomer in the T1 state (inside motif)

References

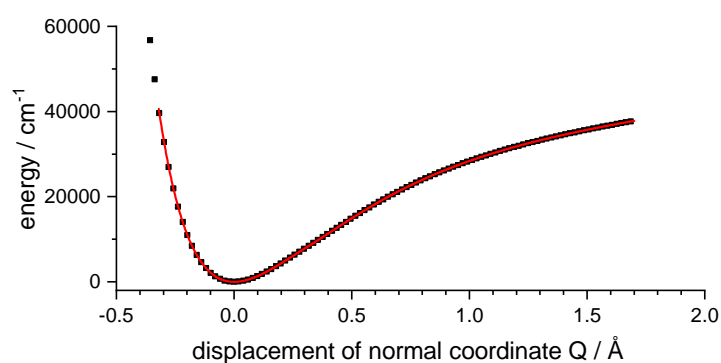
- 1 T. Itoh, *J. Photochem. Photobiol. A: Chem.*, 2010, **214**, 10–15.
- 2 K. Bartl, A. Funk and M. Gerhards, *ChemPhysChem*, 2009, **10**, 1882–1886.
- 3 R. L. Martin, *J. Chem. Phys.*, 2003, **118**, 4775–4777.
- 4 M. Baba, *J. Phys. Chem. A*, 2011, **115**, 9514–9519.
- 5 B. Jeziorski, R. Moszynski and K. Szalewicz, *Chem. Rev.*, 1994, **94**, 1887–1930.
- 6 S. F. Boys and F. Bernardi, *Mol. Phys.*, 2006, **19**, 553–566.
- 7 a) J. R. Alvarez-Idaboy and A. Galano, *Theor. Chem. Acc.*, 2010, **126**, 75–85; b) A. Galano and J. R. Alvarez-Idaboy, *J. Comput. Chem.*, 2006, **27**, 1203–1210; c) J. C. López, J. L. Alonso, F. J. Lorenzo, V. M. Rayón and J. A. Sordo, *J. Chem. Phys.*, 1999, **111**, 6363–6374; d) H. Valdés and J. A. Sordo, *J. Comput. Chem.*, 2002, **23**, 444–455; e) H. Valdés and J. A. Sordo, *J. Phys. Chem. A*, 2002, **106**, 3690–3701;

Appendix B

Dispersion in ground state and benchmark of anharmonic frequencies

In the following, the calculated one-dimensional potential curves used for the variational calculations are given. The used cubic spline is shown in red. Additionally, the corresponding normal mode is shown for non-trivial cases. The used program code for the variational calculation is also given.

B.1 ¹PrTPM



(A) monomer, CH stretching mode

FIGURE B.1: Potential energy curves for the ¹PrTPM monomer.

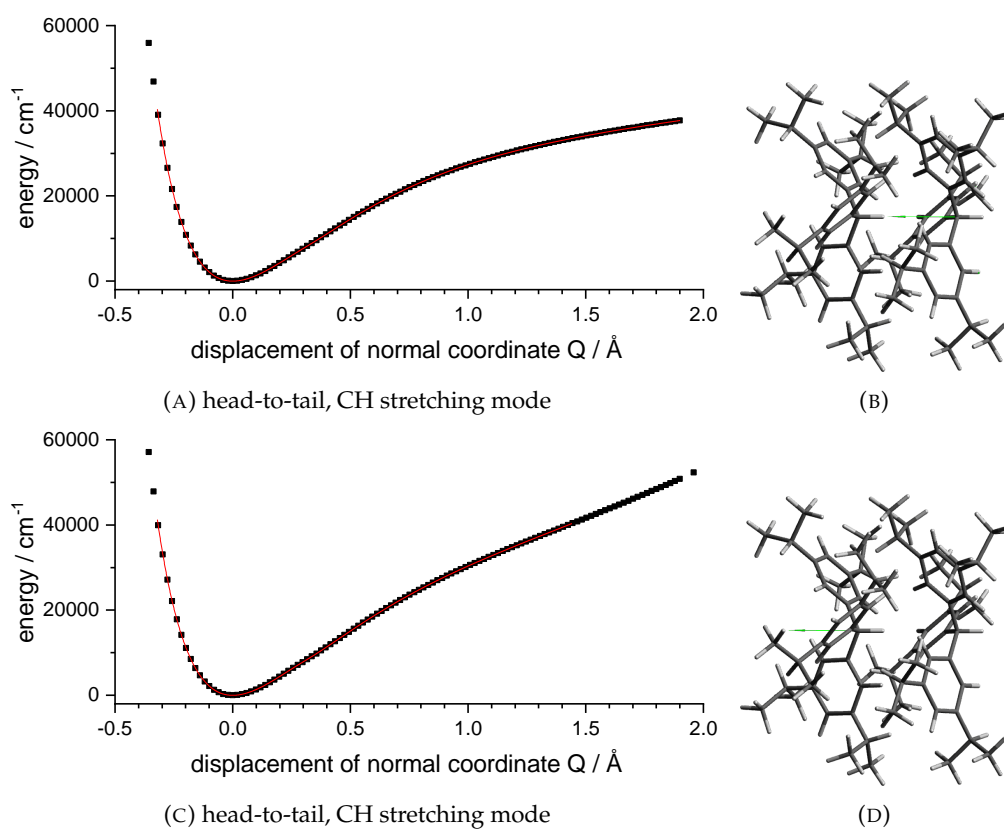


FIGURE B.2: Potential energy curves for the head-to-tail motif of the $^1\text{PrTPM}$ dimer with the corresponding normal modes.

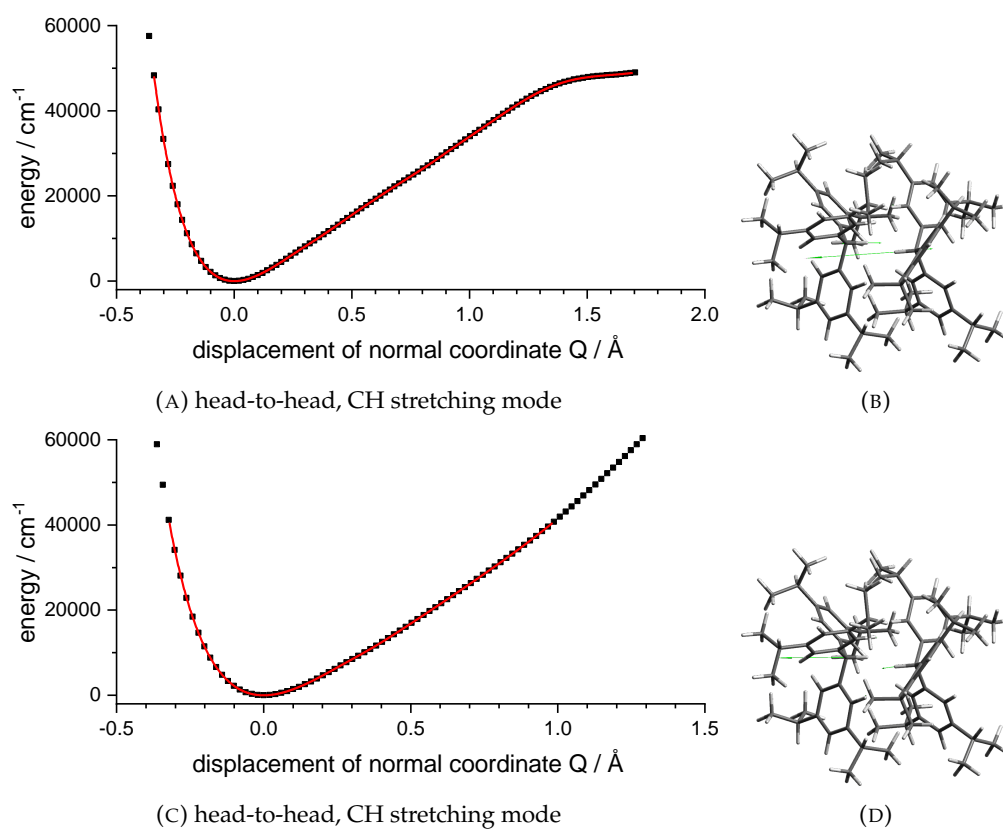


FIGURE B.3: Potential energy curves for the head-to-head motif of the *i*PrTPM dimer with the corresponding normal modes.

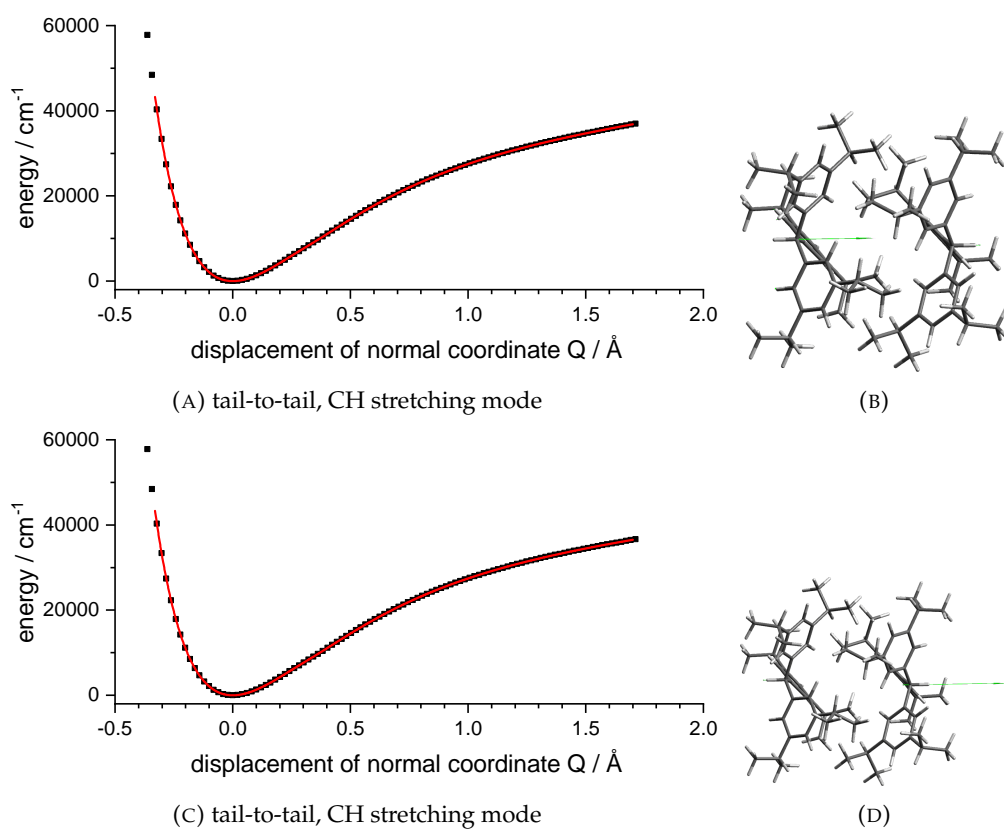


FIGURE B.4: Potential energy curves for the tail-to-tail motif of the ${}^1\text{PrTPM}$ dimer with the corresponding normal modes.

B.2 Benchmarking tests

Potential energy curves for B3LYP-D3(BJ)

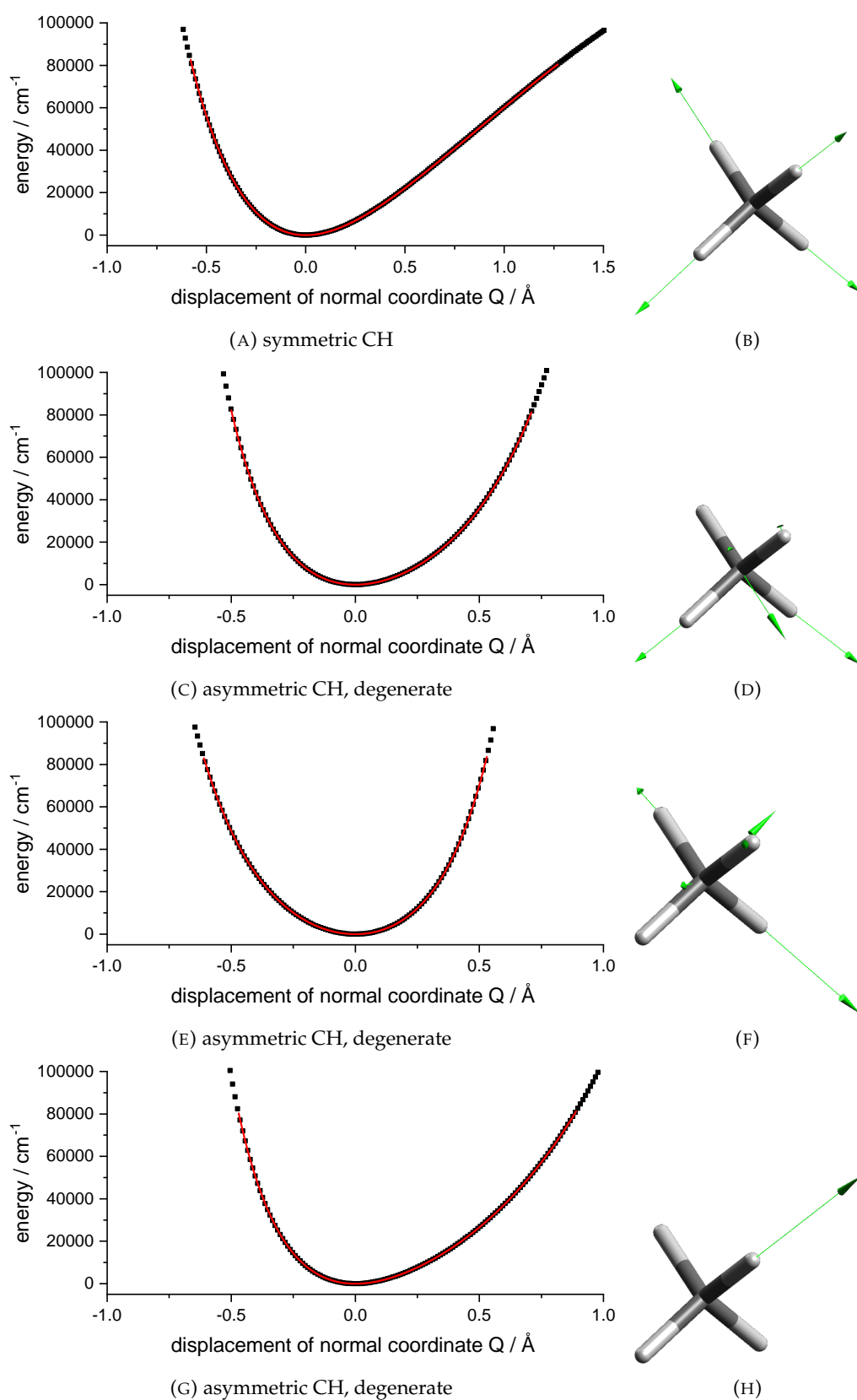
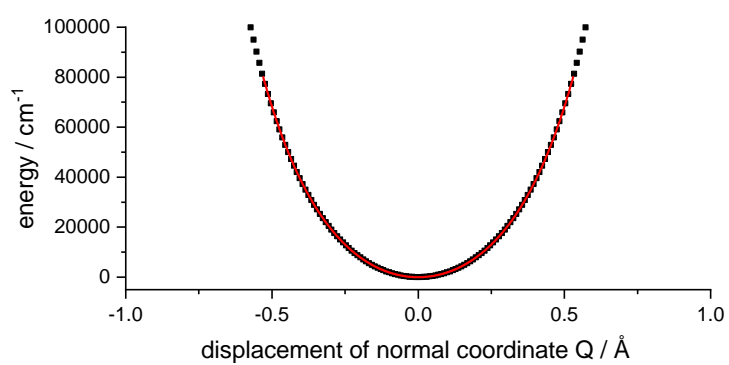
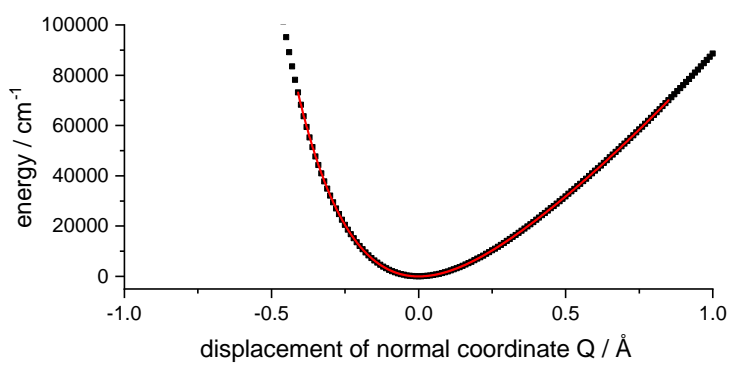


FIGURE B.5: Potential energy curves and corresponding normal mode for methane.



(A) asymmetric CH



(B) symmetric CH

FIGURE B.6: Potential energy curves for acetylene.

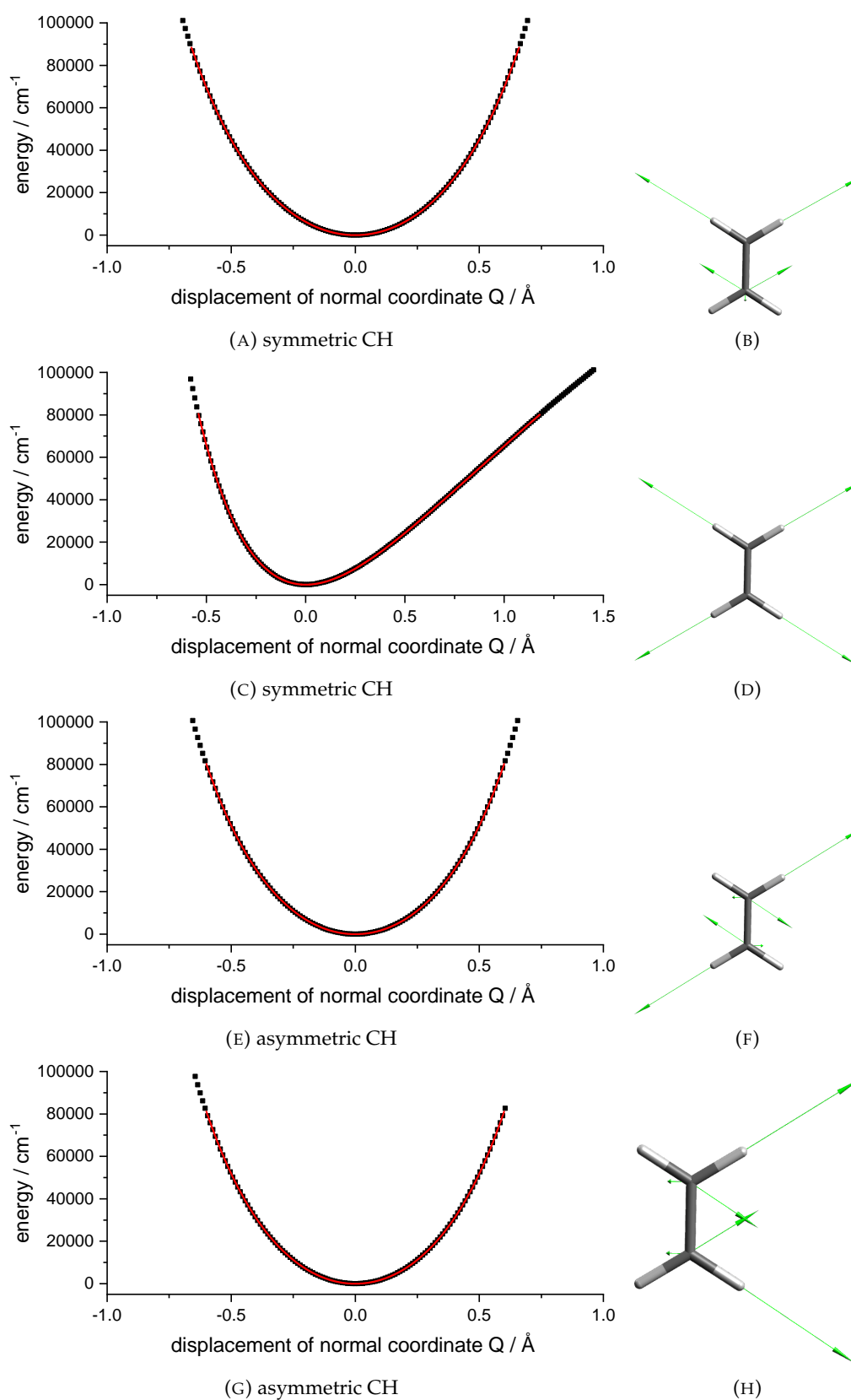


FIGURE B.7: Potential energy curves and corresponding normal mode for ethylene.

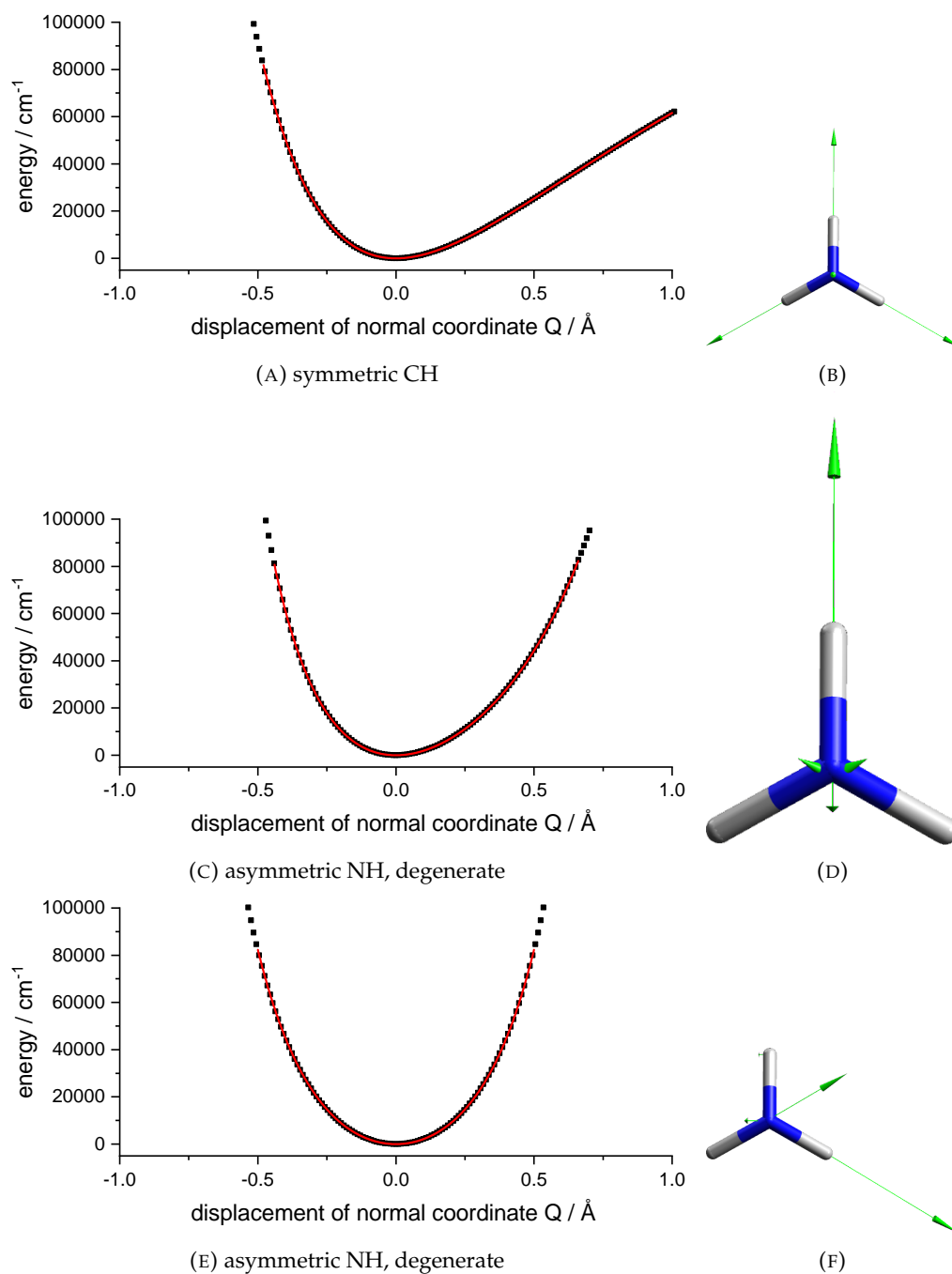


FIGURE B.8: Potential energy curves and corresponding normal mode for ammonia.

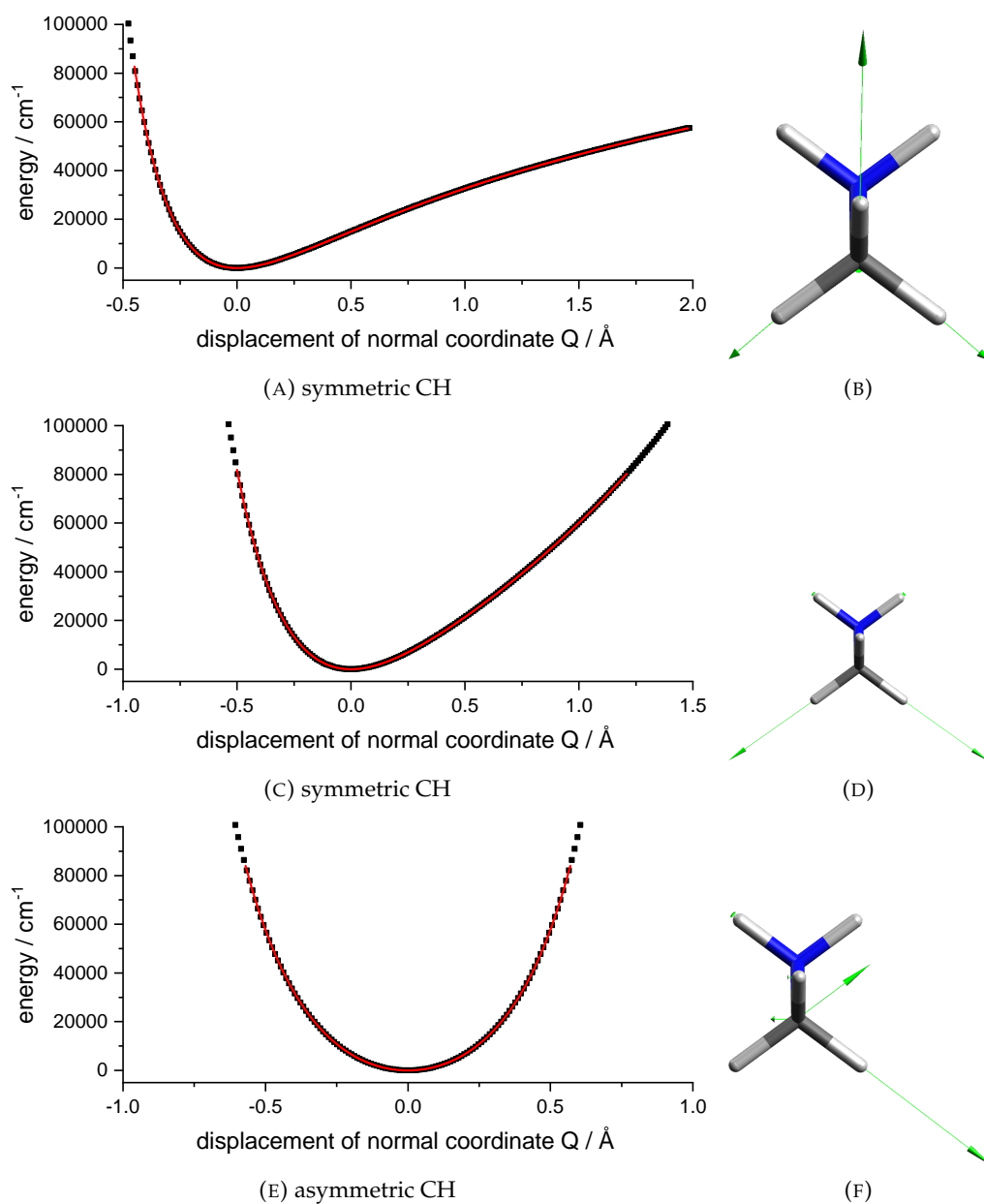


FIGURE B.9: Potential energy curves and corresponding normal mode for methylamine.

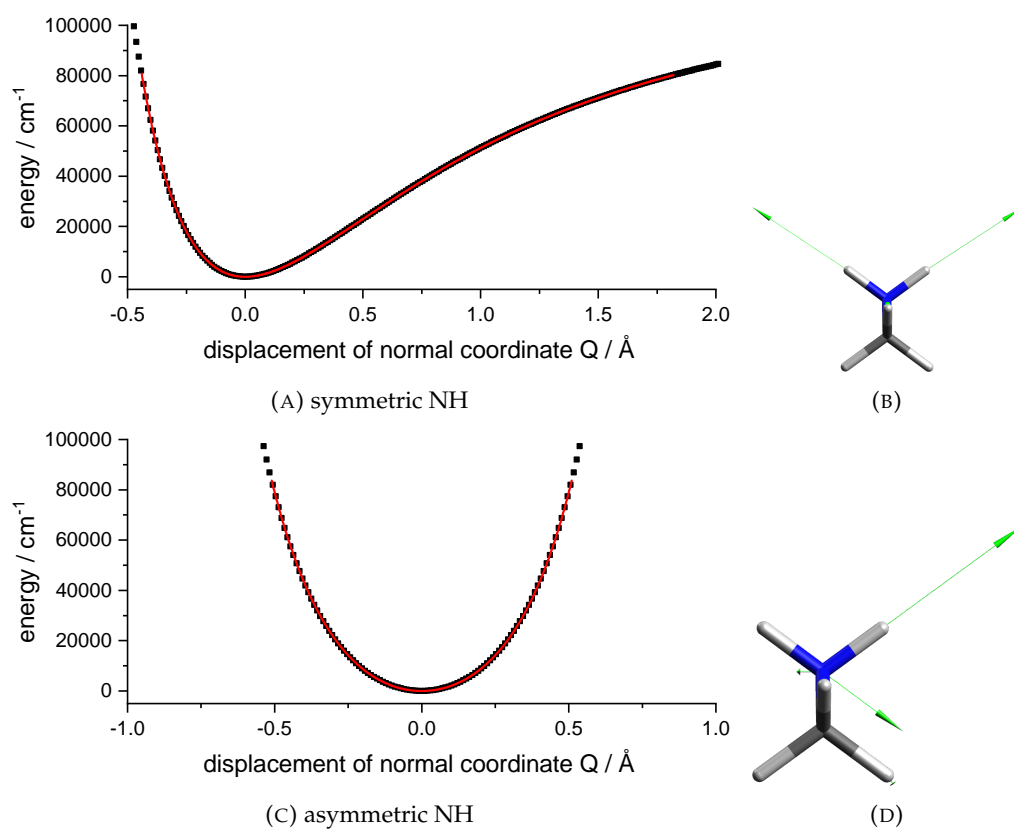


FIGURE B.10: Potential energy curves and corresponding normal mode for methylamine.

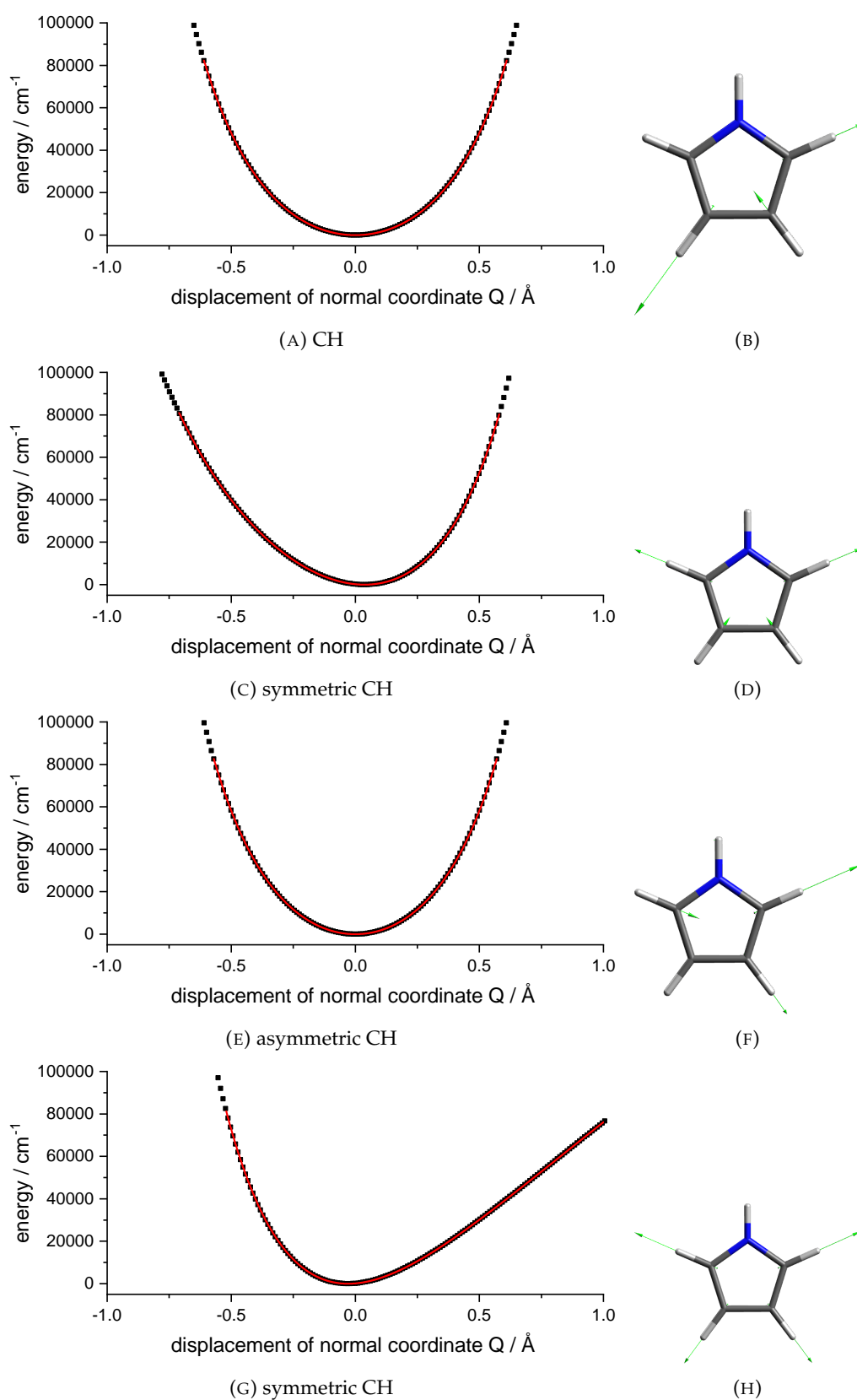


FIGURE B.11: Potential energy curves and corresponding normal mode for pyrrole.

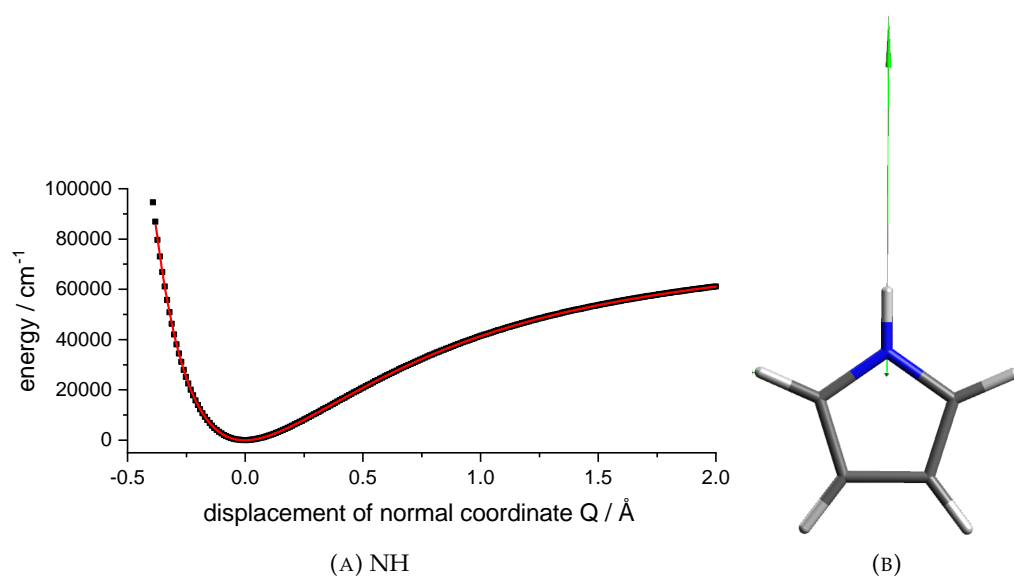
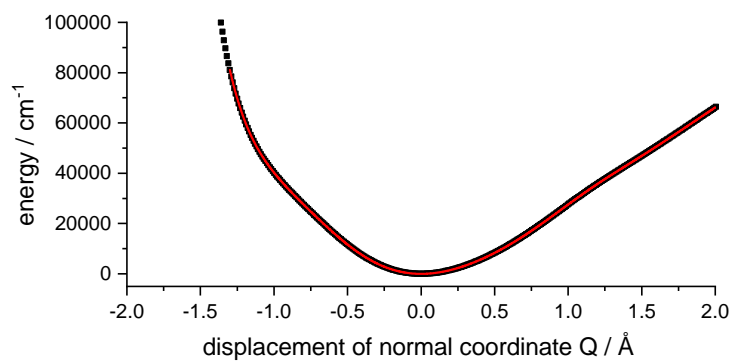
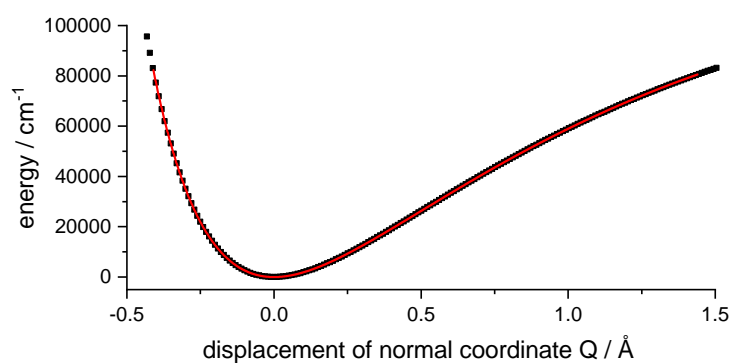


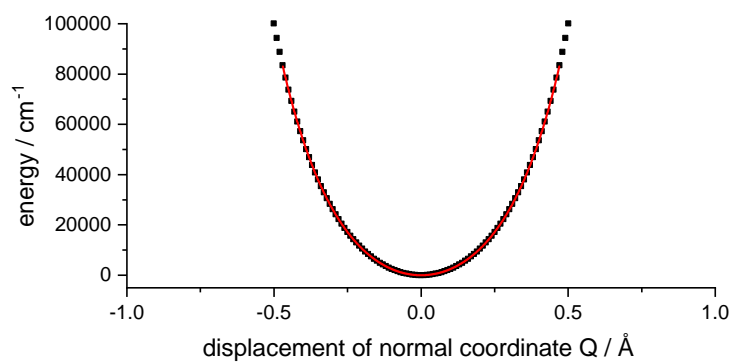
FIGURE B.12: Potential energy curve and corresponding normal mode for pyrrol.



(A) OH bend



(B) symmetric OH



(C) asymmetric OH

FIGURE B.13: Potential energy curves for water.

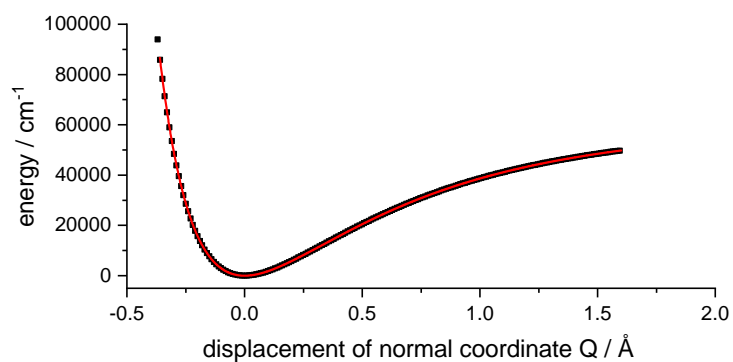


FIGURE B.14: Potential energy curves for the OH stretching vibration of methanol.

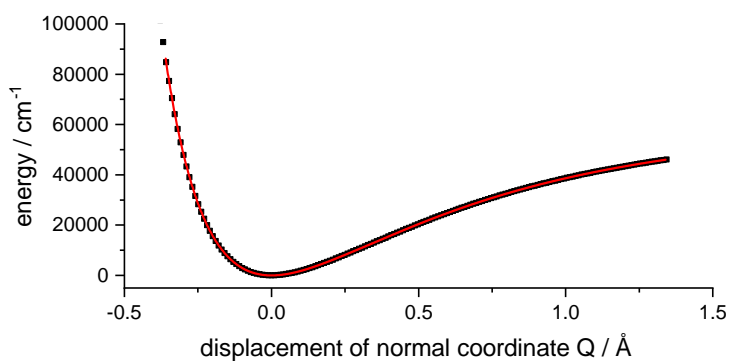


FIGURE B.15: Potential energy curves for the OH stretching vibration of phenol.

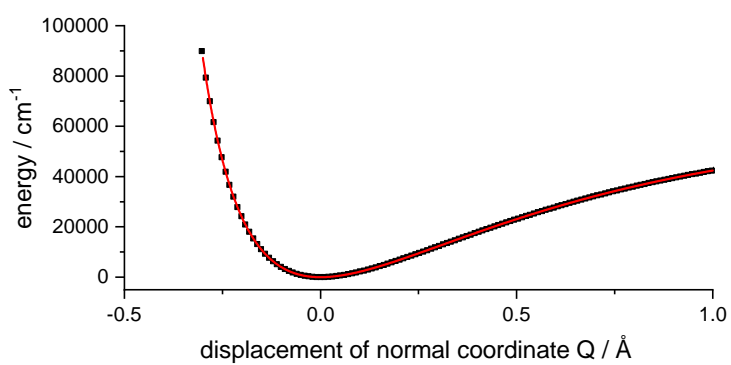


FIGURE B.16: Potential energy curves for dihydrogen.

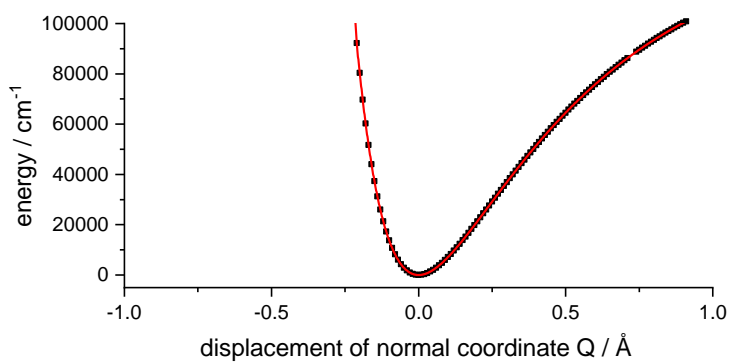


FIGURE B.17: Potential energy curves for carbon monoxide.

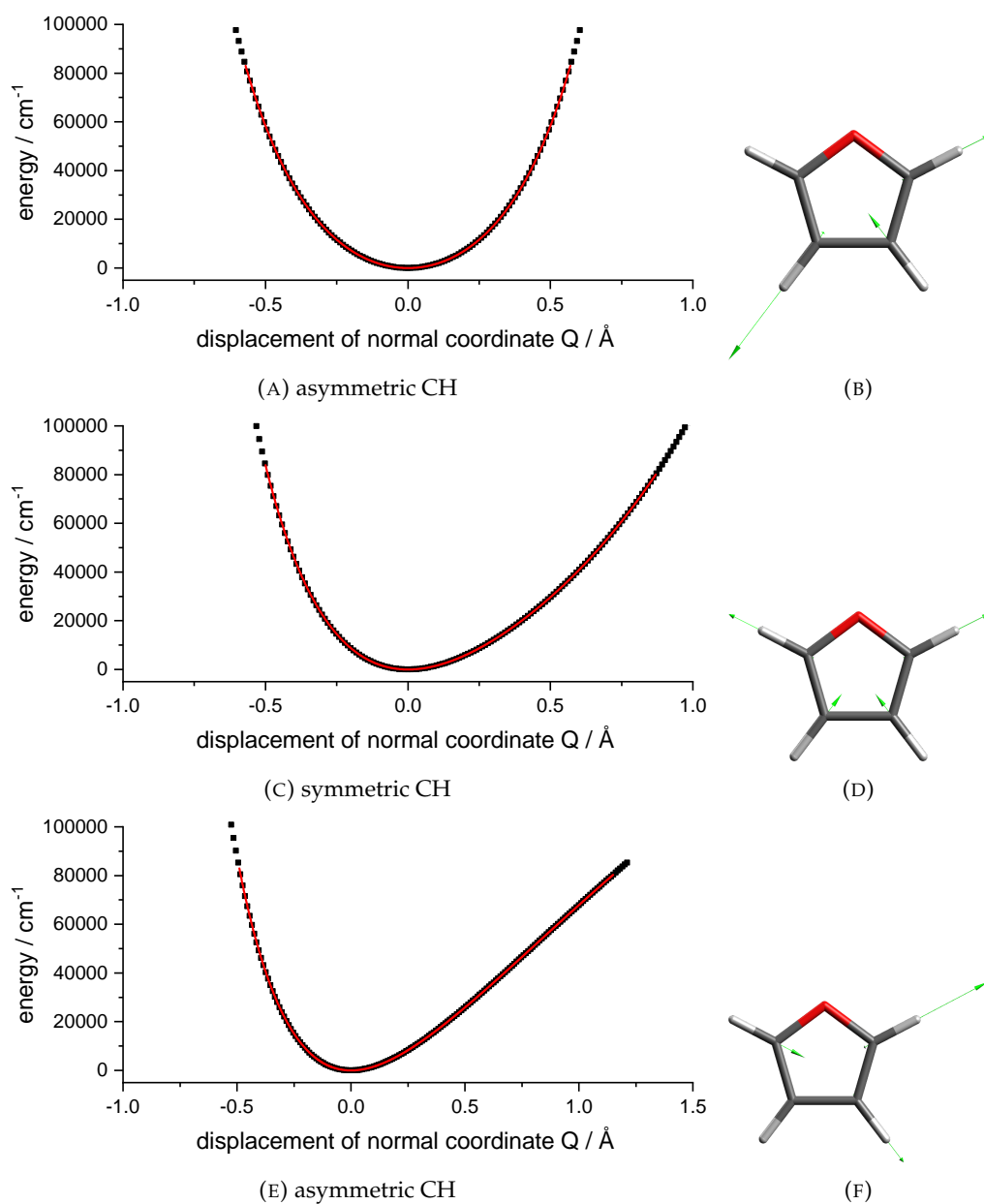


FIGURE B.18: Potential energy curves and corresponding normal mode for furan.

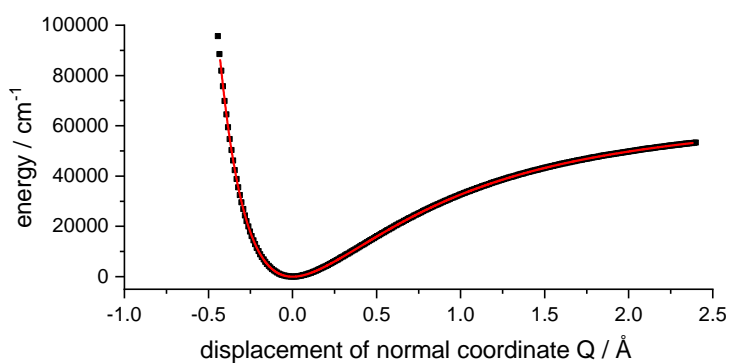


FIGURE B.19: Potential energy curves for the CH stretching vibration of methyl fluoride.

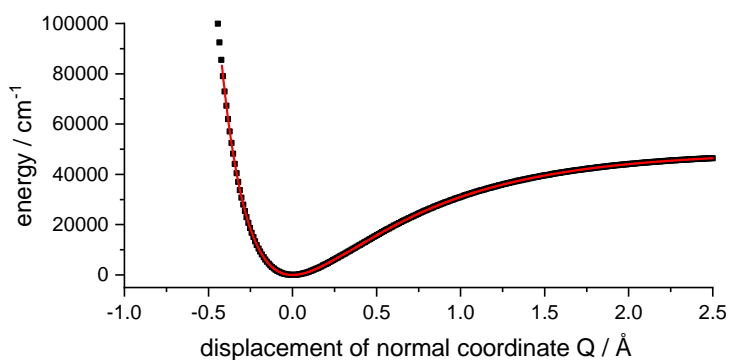


FIGURE B.20: Potential energy curves for the CH stretching vibration of methyl chloride.

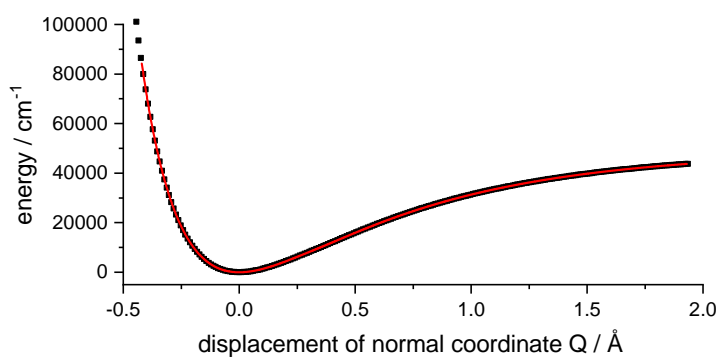


FIGURE B.21: Potential energy curves for the CH stretching vibration of methyl bromide.

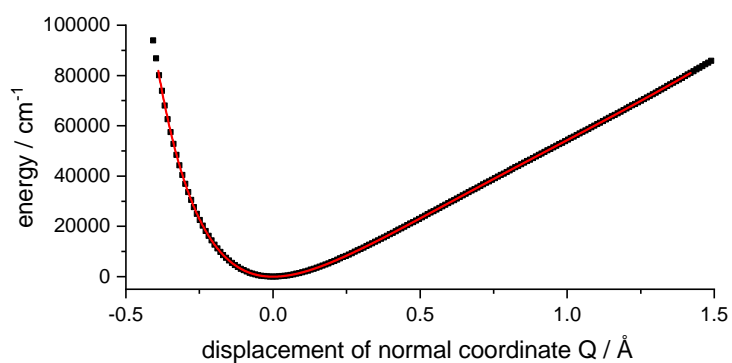


FIGURE B.22: Potential energy curves for the CH stretching vibration of fluoroethyne.

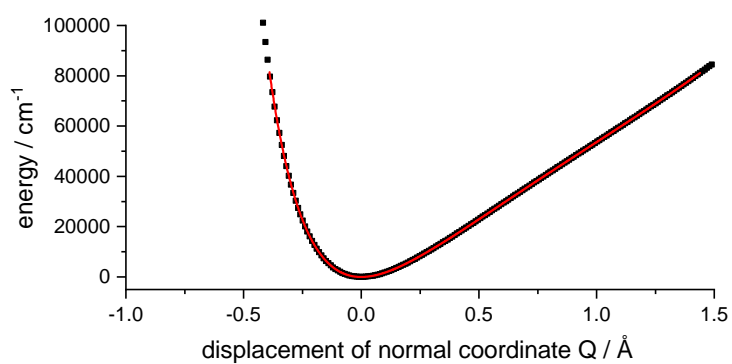


FIGURE B.23: Potential energy curves for the CH stretching vibration of chloroethyne.

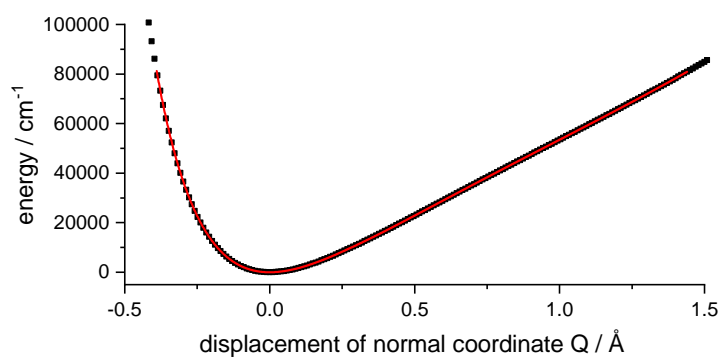


FIGURE B.24: Potential energy curves for the CH stretching vibration of bromoethyne.

Potential energy curves for M06-2X(D3)

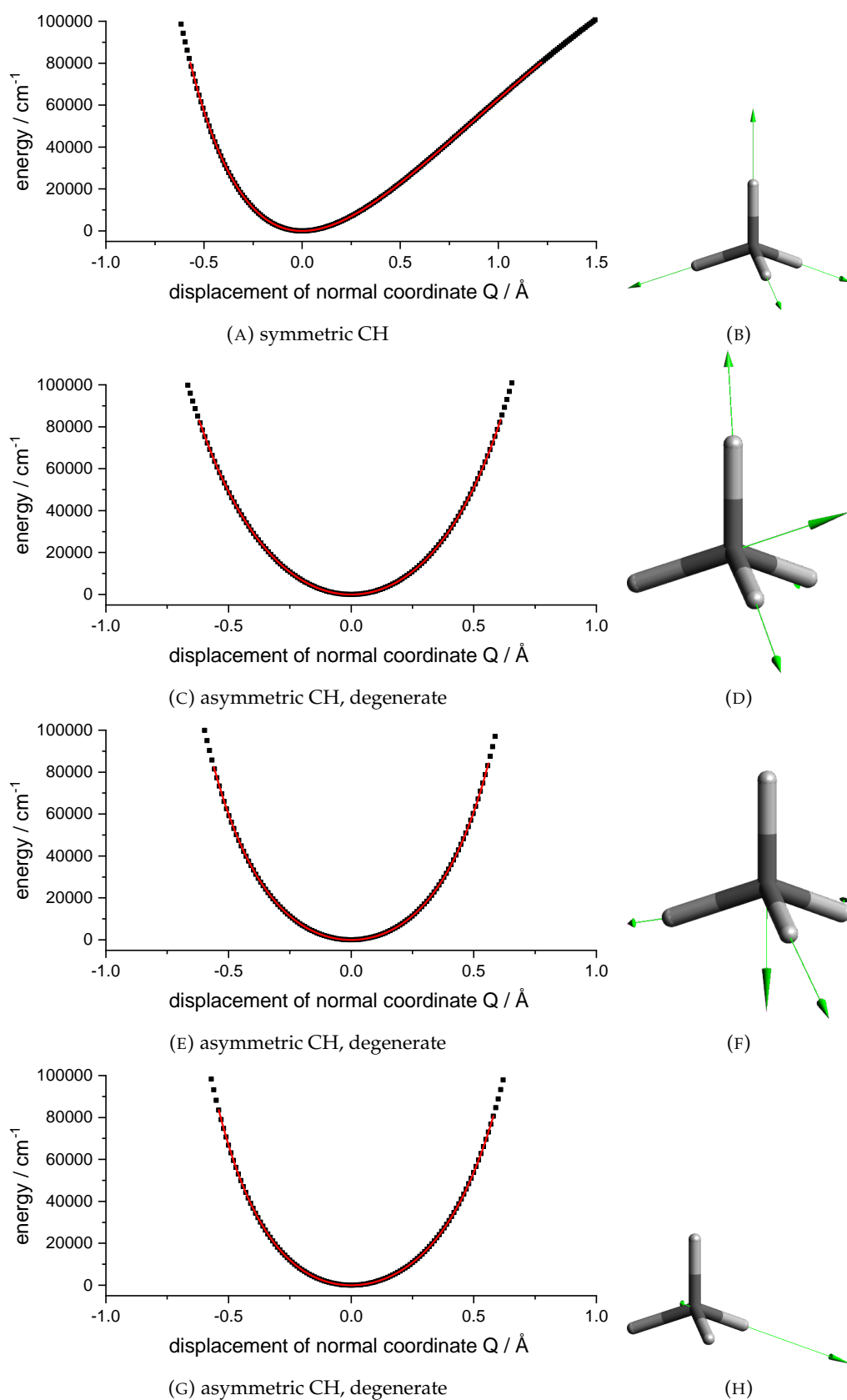
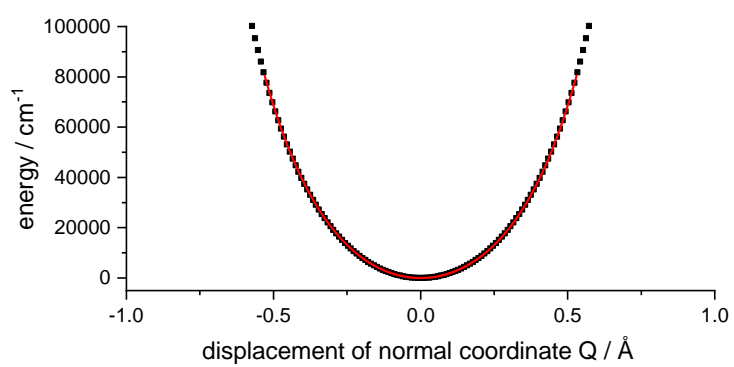
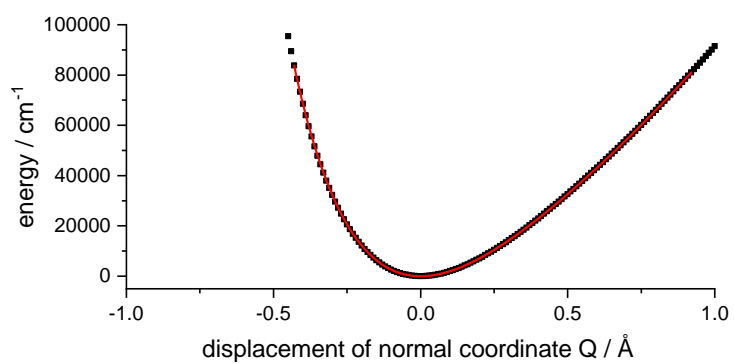


FIGURE B.25: Potential energy curves and corresponding normal mode for methane.



(A) asymmetric CH



(B) symmetric CH

FIGURE B.26: Potential energy curves for acetylene.

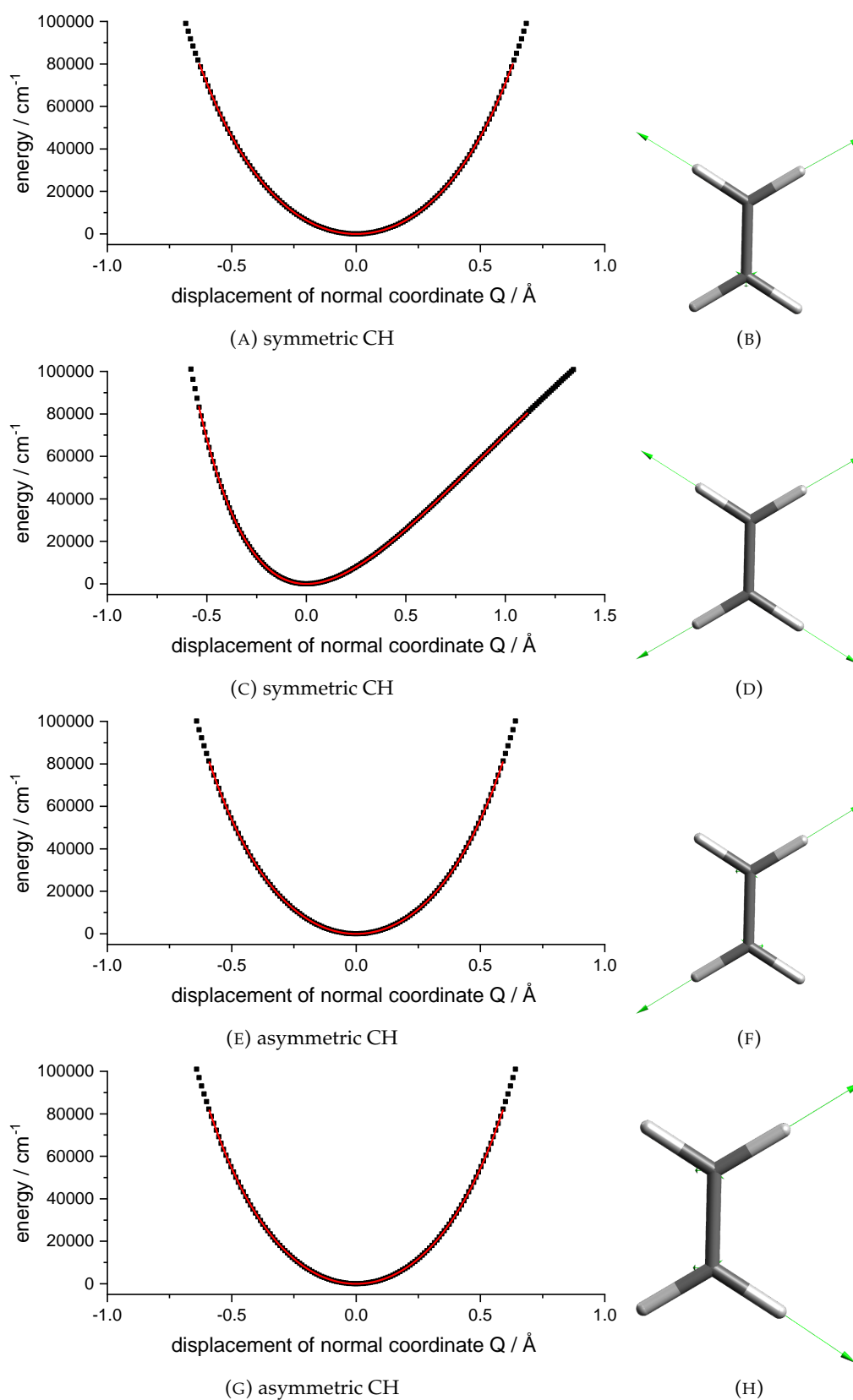


FIGURE B.27: Potential energy curves and corresponding normal mode for ethylene.

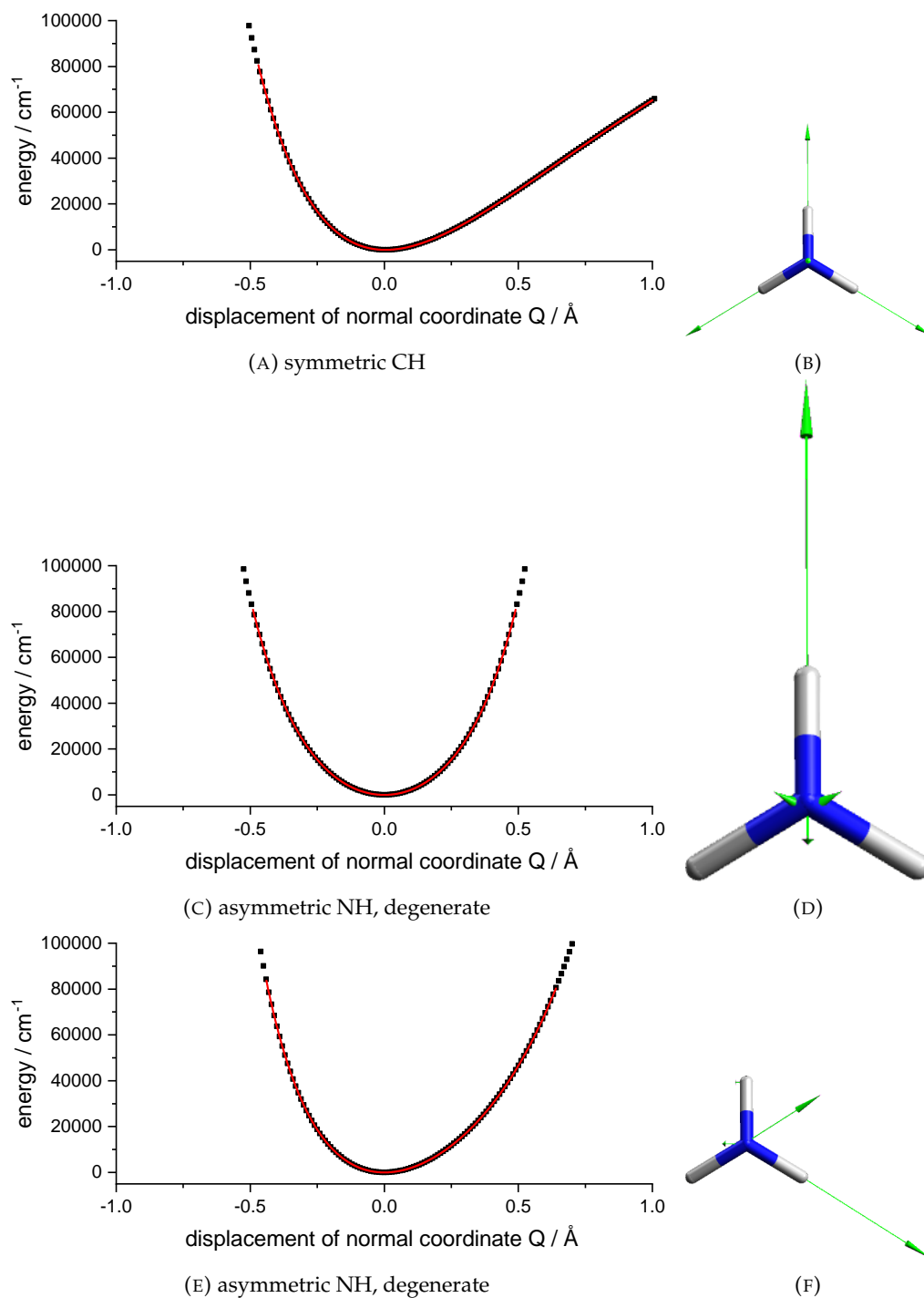


FIGURE B.28: Potential energy curves and corresponding normal mode for ammonia.

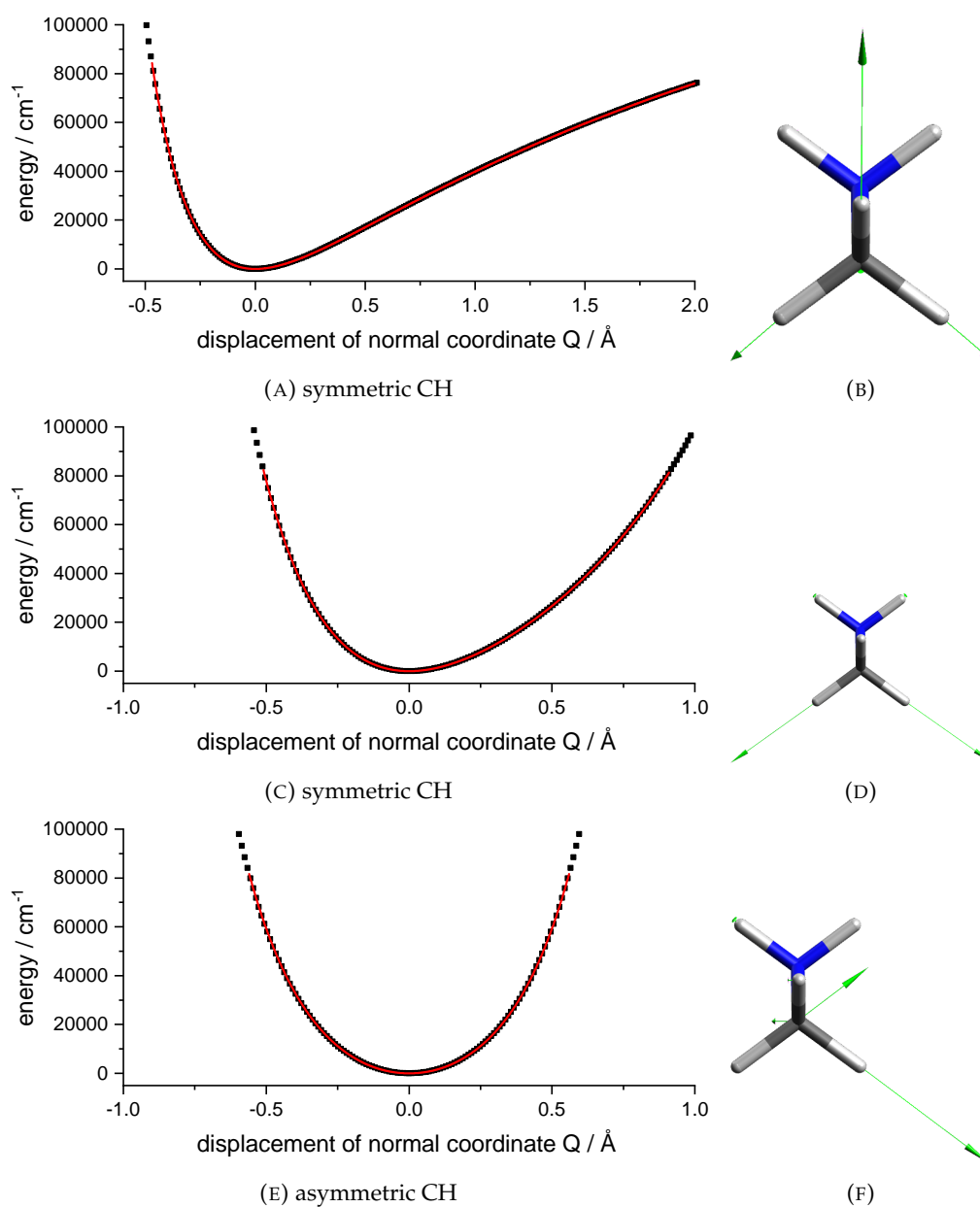


FIGURE B.29: Potential energy curves and corresponding normal mode for methylamine.

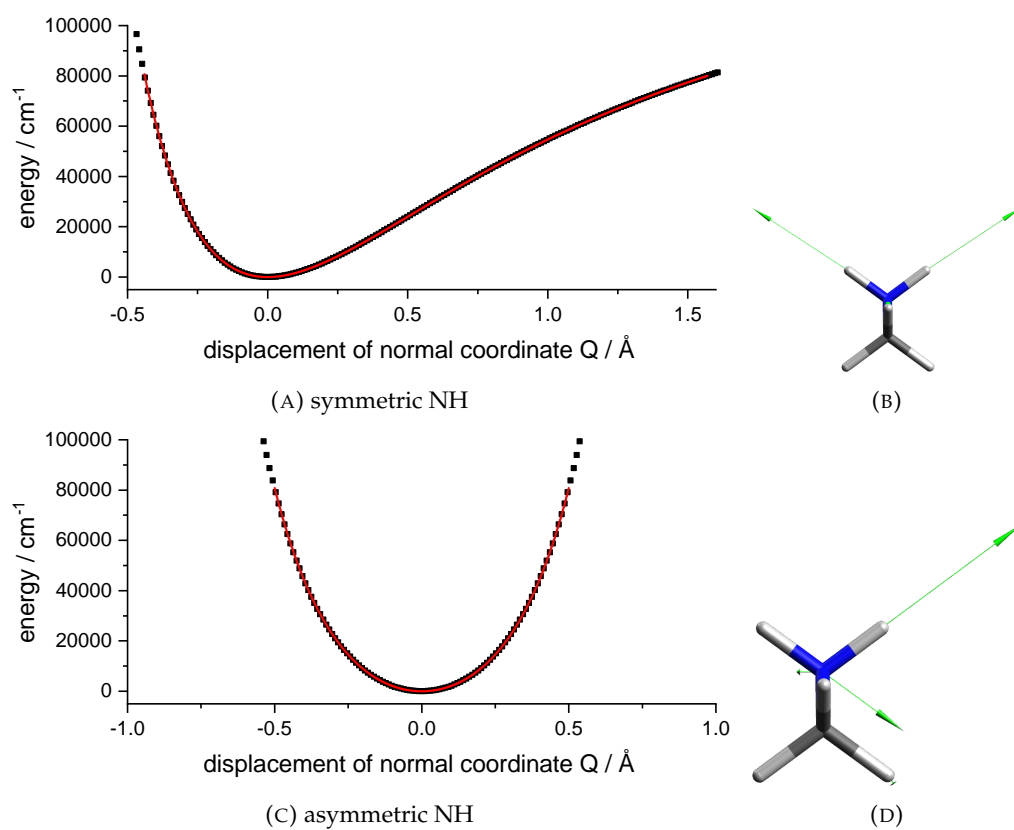


FIGURE B.30: Potential energy curves and corresponding normal mode for methylamine.

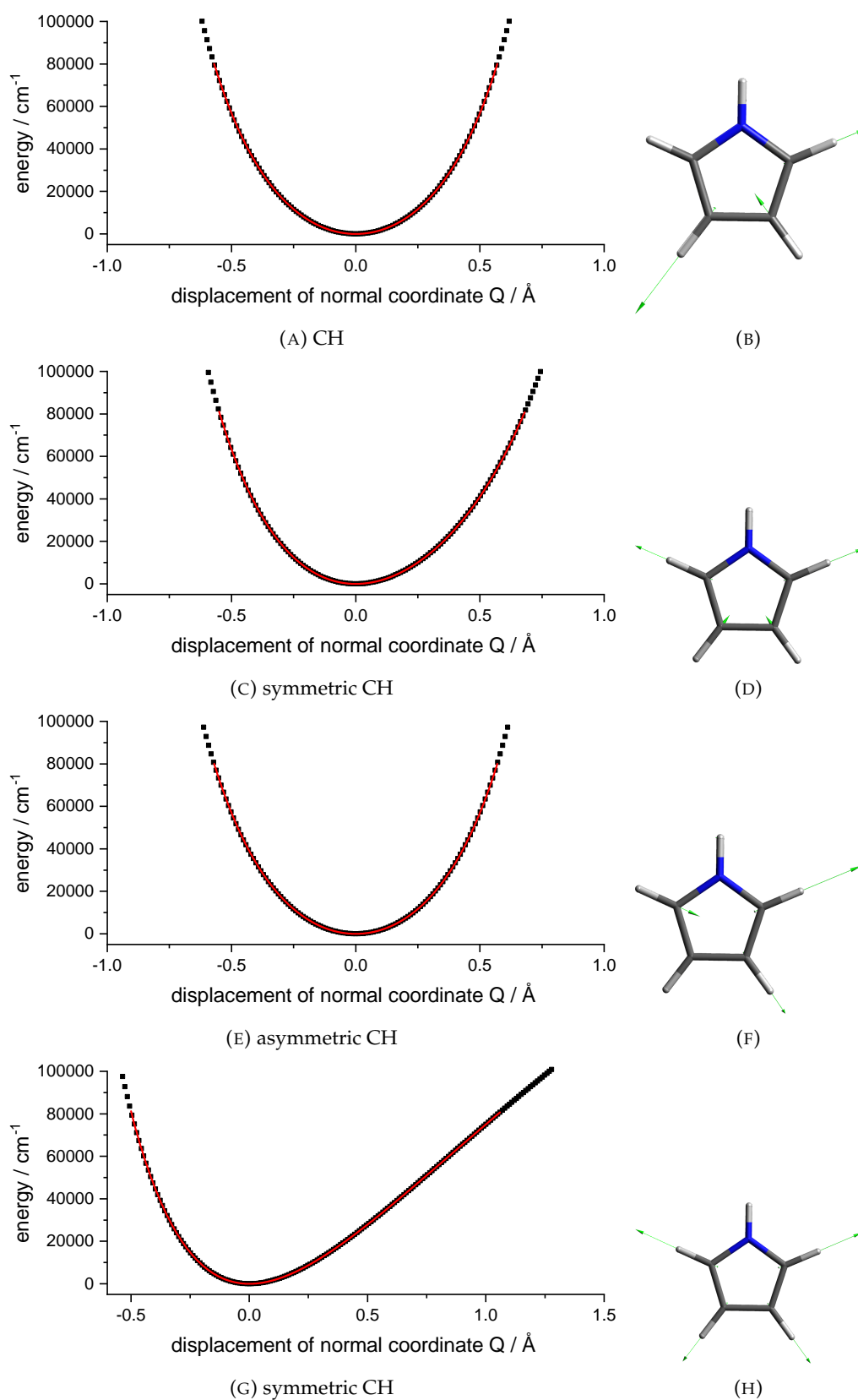


FIGURE B.31: Potential energy curves and corresponding normal mode for pyrrole.

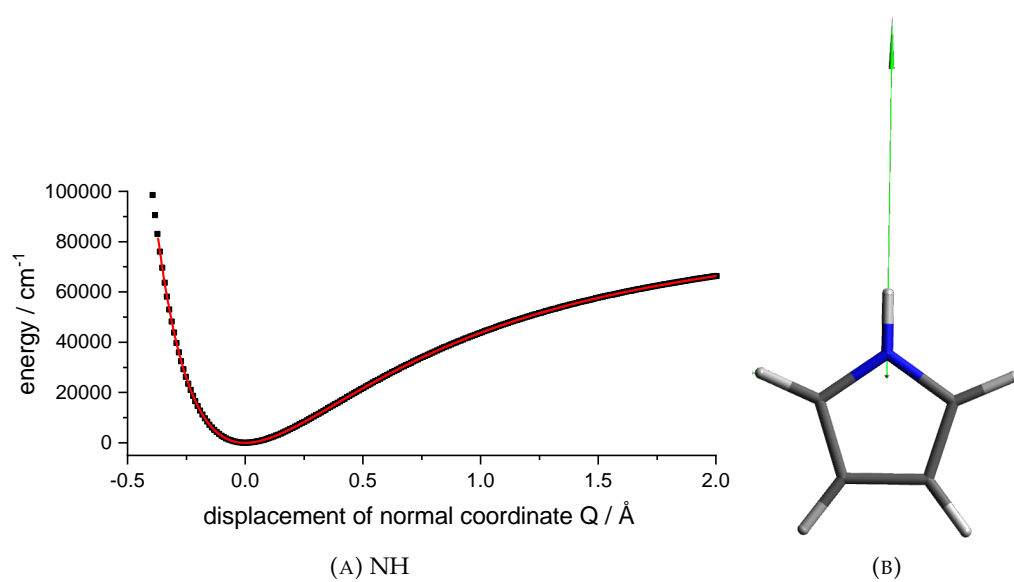
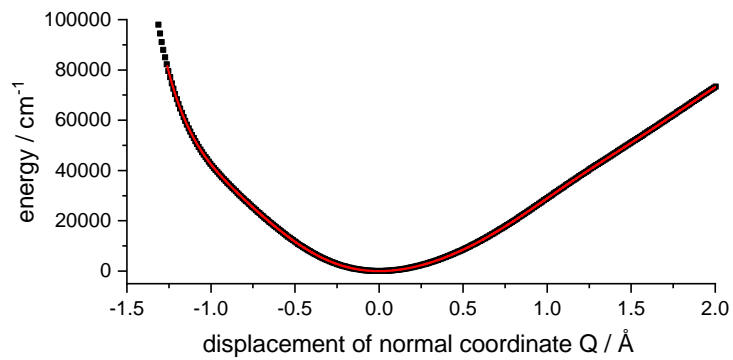
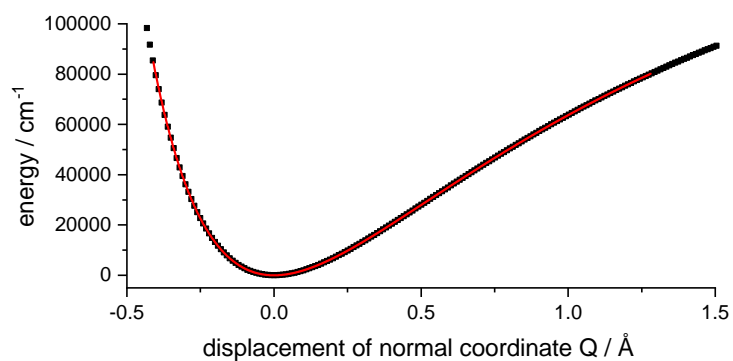


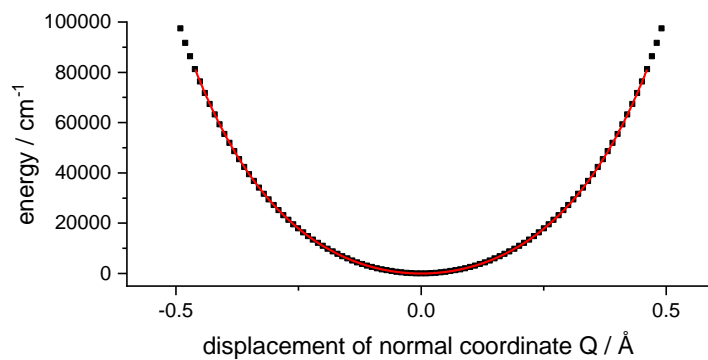
FIGURE B.32: Potential energy curve and corresponding normal mode for pyrrol.



(A) OH bend



(B) symmetric OH



(C) asymmetric OH

FIGURE B.33: Potential energy curves for water.

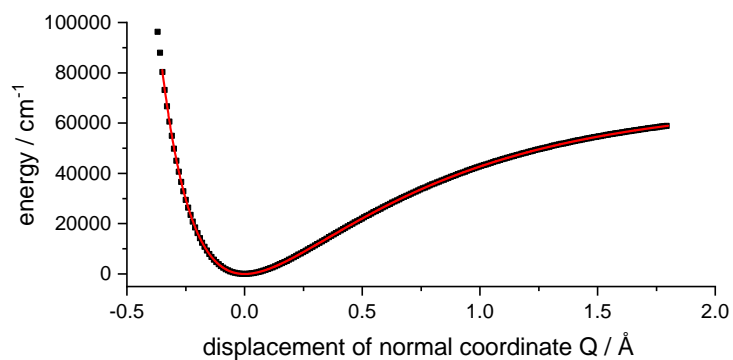


FIGURE B.34: Potential energy curves for the OH stretching vibration of methanol.

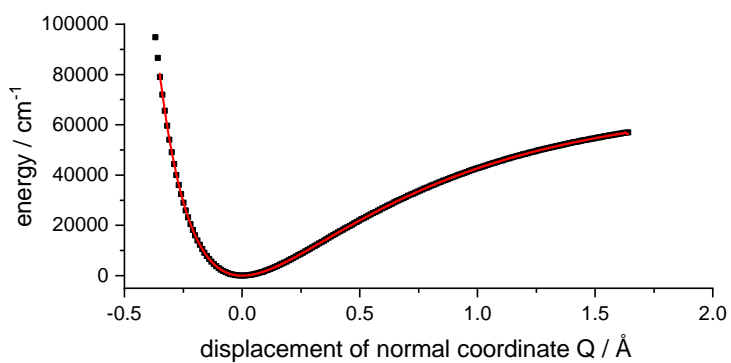


FIGURE B.35: Potential energy curves for the OH stretching vibration of phenol.

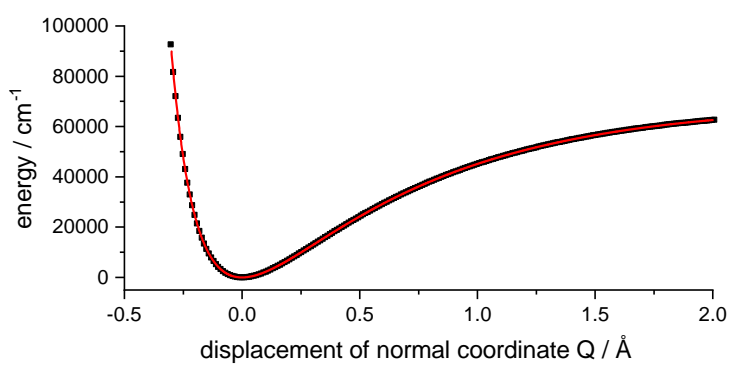


FIGURE B.36: Potential energy curves for dihydrogen.

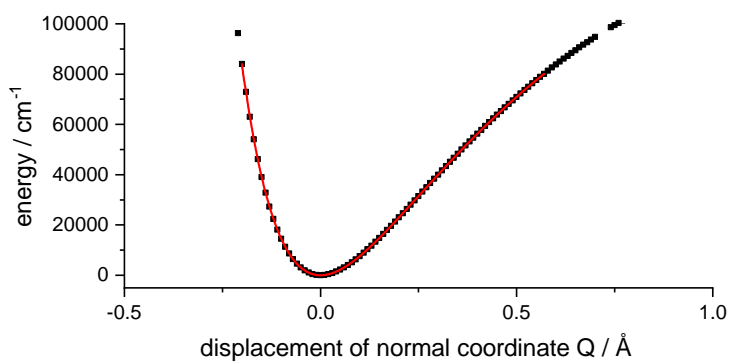


FIGURE B.37: Potential energy curves for carbon monoxide.

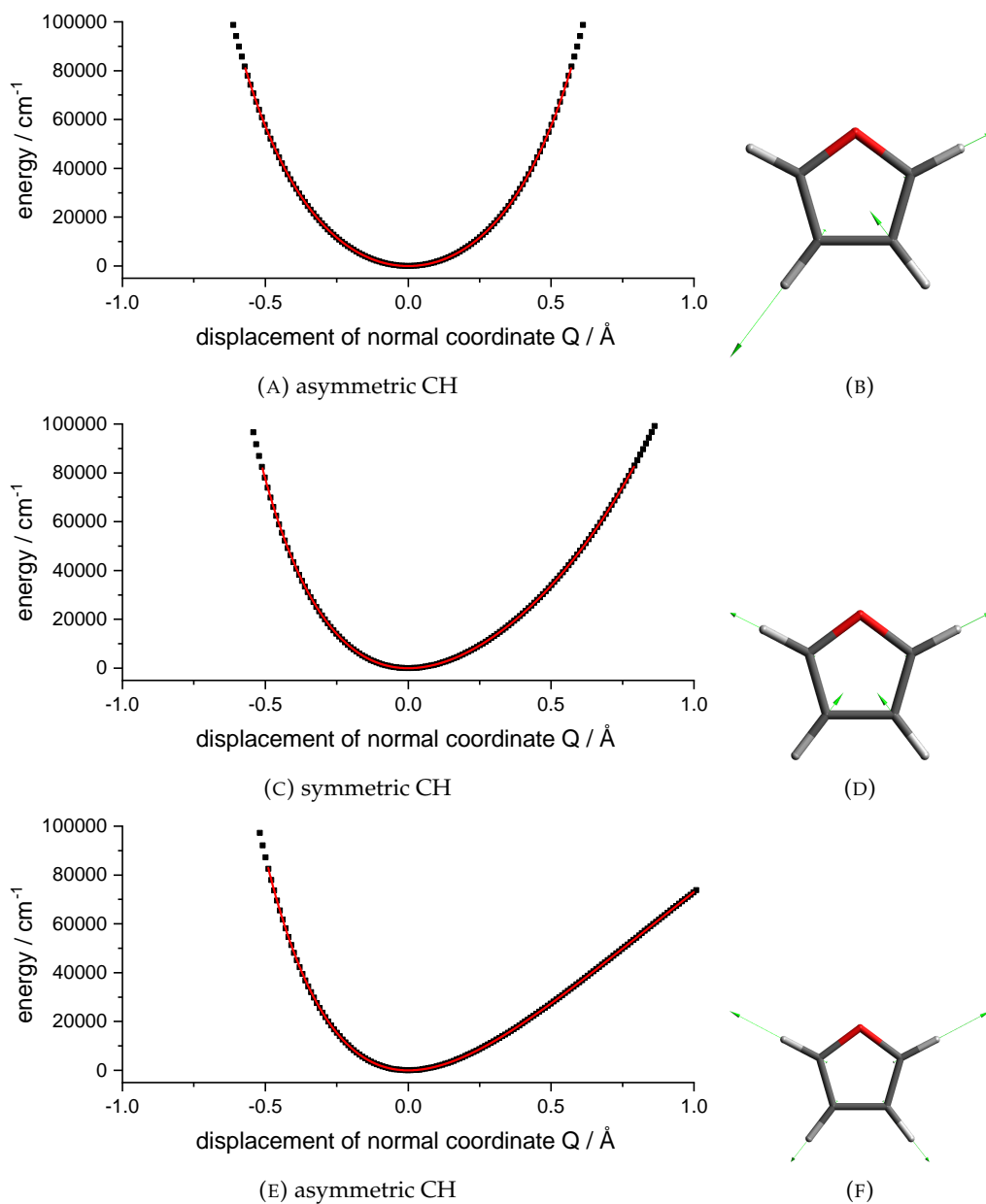


FIGURE B.38: Potential energy curves and corresponding normal mode for furan.

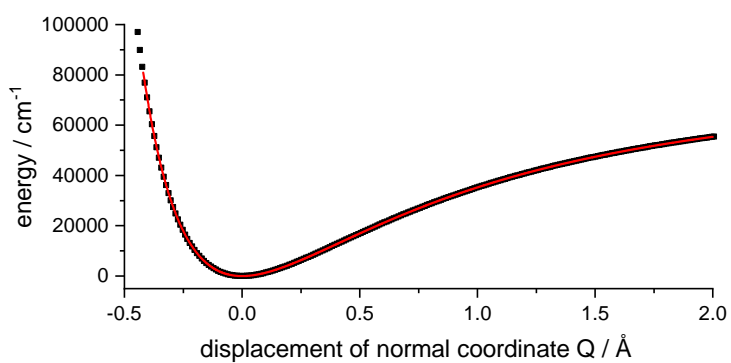


FIGURE B.39: Potential energy curves for the CH stretching vibration of methyl fluoride.

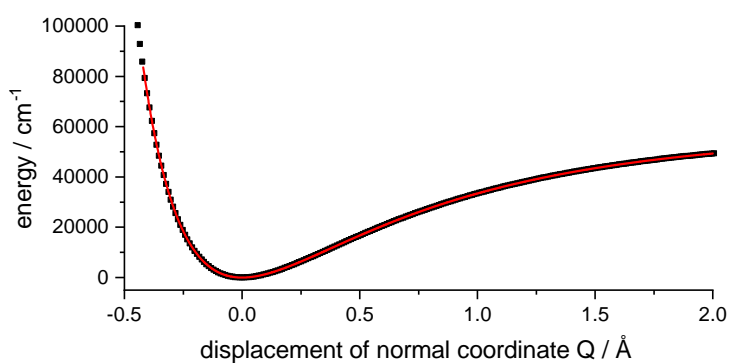


FIGURE B.40: Potential energy curves for the CH stretching vibration of methyl chloride.

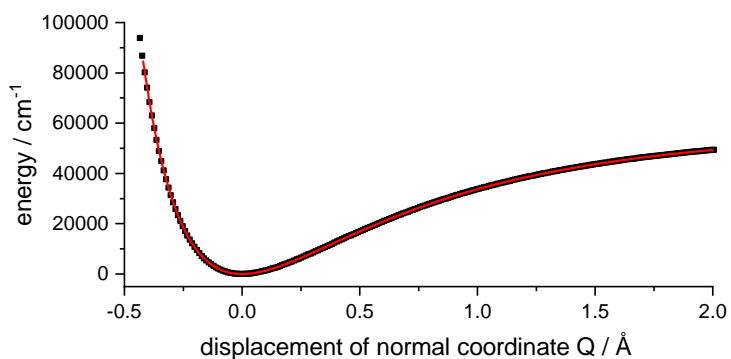


FIGURE B.41: Potential energy curves for the CH stretching vibration of methyl bromide.

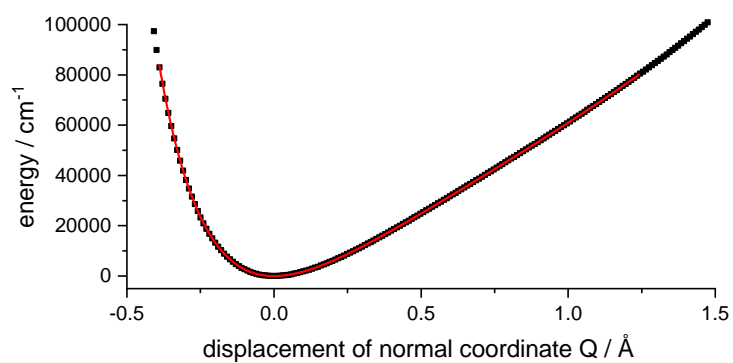


FIGURE B.42: Potential energy curves for the CH stretching vibration of fluoroethyne.

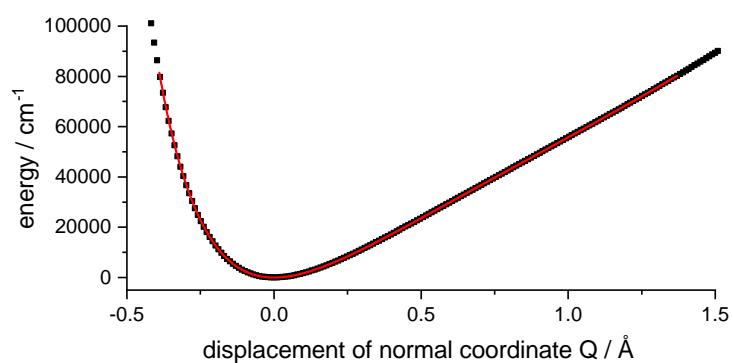


FIGURE B.43: Potential energy curves for the CH stretching vibration of chloroethyne.

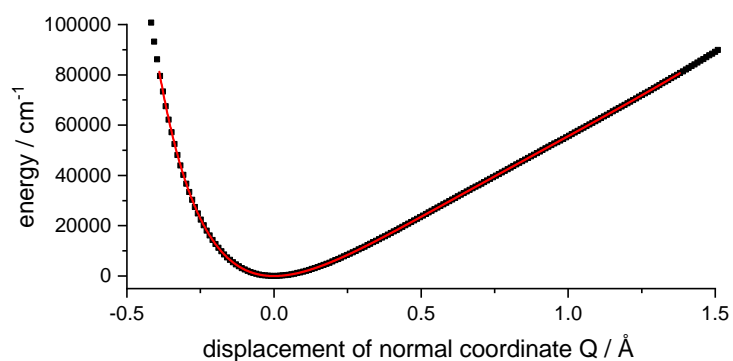


FIGURE B.44: Potential energy curves for the CH stretching vibration of bromoethyne.

B.3 Source code

In this section the source code of the variational program is given. First, the fortran code of the ritz program is given which is used to calculate the Hamilton matrix. This program requires multiple inputs which are given in the "eingaben.dat" file. The "eingaben.dat" file consists of 15 lines although not all are relevant for the one-dimensional calculation carried out in this work. m_{ueX} describes the reduced mass in a.u. and k_{raftX} the force constant in N/m. u_X and o_X stand for the upper and lower limit in Å while $s_{chritteX}$ represents the number of supporting points of the used spline. X stands for the dimension X the value is referring to. Due to the one-dimensional nature of the calculations in this work, the values for the first and second dimensions are set to default values and only the m_{ue3} , k_{raft3} , u_3 , o_3 and $s_{chritte3}$ variables are changed. The ritz program needs the spline to calculate the Hamilton matrix, which has to be supplied in a "start3d.dat" file in the fortran number format. To make the generation of the input files easier, the "ritz.py" program can be used which requires the starting x-value as parameter. The spline has to be supplied in a "spline.dat" file containing the y-values of the spline. The "ritz.py" program then generates the required "eingaben.dat" and "start3d.dat" files for the ritz program.

Upon completion of the ritz program, the "pruef2HMAT.py" program is used to extract the calculated matrix elements from the "pruefung.dat" file generated by the ritz program. It requires the amount of basis functions as parameter. The generated HMAT file contains the final Hamilton matrix which is diagonalized with the "diagritz" program. Unfortunately, only a compiled version of unreadable machine code is available. The resulting eigenvalues can be checked in the "Results.vib" file. Since the choice of force constant for basis function must not necessarily be good, the calculation should be redone if the $c(0)^2$ value is too low (should be near 0.99). To make this easier, the "autoritz.py" program was written to automate this process. Of all mentioned programs, "ritz.py" and "autoritz.py" were programmed by myself while all other programs are the work of Andreas Funk and Markus Gerhards.

eingaben.dat

```

10 - mue1
1 - kraft1
-1 - u1
1 - o1
10 - mue2
1 - kraft2
-1 - u2
1 - o2
2.3178 - mue3
638 - kraft3
-0.32 - u3
1.7 - o3
100 - schritte1
100 - schritte2
2021 - schritte3

```

RITZ_10.f

```

C---- Dieses Programm berechnet die Energieeigenwerte
C---- einer Potentialhyperflaeche , gebildet durch
C---- drei harmonische Oszillatoren

```

```

program ritz

```

```

IMPLICIT NONE

```

```

C--- max2: Anzahl Basisfunktionen
C--- max22: Quadrat der Anzahl Basisfunktionen
C--- max3: Ausgangspunkte fuer Grid - entfaellt beim Einlesen
C--- max4: Punkte fuer die numerische Integration
C--- max5: Matricelemente 3D

```

```

INTEGER max2,max22,max3,max4,max5,min

```

```

PARAMETER(max2=9)

```

```

PARAMETER(max22=15)

```

```

PARAMETER(max3=20)

```

```

PARAMETER(max4=100001)

```

```

PARAMETER(max5=63)

```

```

PARAMETER(min=0)

```

```

INTEGER i , j , k , i1 , i2 , j1 , j2 , m , l , n

```

```

INTEGER schritte1 , schritte2 , schritte3

```

```

INTEGER dat1 , dat2 , dat3 , lauf , laufa , zaehlen

```

```

INTEGER zahl1 , zahl2 , z1 , z2

```

```

DOUBLE PRECISION wert , wert2

```

```

DOUBLE PRECISION Pi , taustart

```

```

DOUBLE PRECISION o1 , o2 , o3 , u1 , u2 , u3 , hilf , tau

```

```

DOUBLE PRECISION ukin1 , ukin2 , ukin3 , okin1 , okin2 , okin3

```

```

C      DOUBLE PRECISION bereich1 , bereich2
      DOUBLE PRECISION kraft1 , kraft2 , kraft3 , mue1 , mue2 , mue3
          DOUBLE PRECISION beta1 , beta2 , beta3
      DOUBLE PRECISION tauwert (min : max2) , olap (min : max2 , min : max2)
      DOUBLE PRECISION kmat1 (min : max2 , min : max2)
      DOUBLE PRECISION kmat2 (min : max2 , min : max2) , kmat3 (min : max2 , min : max2)
      DOUBLE PRECISION hmat2 (min : max22 , min : max22)
      DOUBLE PRECISION kmat (min : max5 , min : max5)
      DOUBLE PRECISION hmat3 (min : max5 , min : max5)
      DOUBLE PRECISION hmat (min : max2 , min : max2)
      DOUBLE PRECISION z2d (max4 , max4)
C---- DOUBLE PRECISION data (max3 , max3 , max3) , data2 (max4 , max3 , max3)

      DOUBLE PRECISION norm1 (min : max2) , norm2 (min : max2) , norm3 (min : max2)

      DOUBLE PRECISION diff1 , diff2 , diff3 , FAK , xwert (max4)
      DOUBLE PRECISION xi (max4) , yi (max4) , zi (max4) , zwert (max4)
C--  DOUBLE PRECISION xxwert (max4) , yywert (max4)

      EXTERNAL FAK

      Pi=3.141592653589793285D0

C---- zaehlen der Anzahl 2-D Fits
      zaehlen = 0

      OPEN(22 , FILE='eingaben.dat')

C---- Eingabe der red. Masse in amu, Kraftkonstante in N/m,
C---- untere und obere Grenze in Angstroem (erste Bewegung)
      READ(22 , *) mue1
      READ(22 , *) kraft1
      READ(22 , *) u1
      READ(22 , *) o1

C---- Eingabe der red. Masse in amu, Kraftkonstante in N/m,
C---- untere und obere Grenze in Angstroem (zweite Bewegung)

      READ(22 , *) mue2
      READ(22 , *) kraft2
      READ(22 , *) u2
      READ(22 , *) o2

C---- Eingabe der red. Masse in amu, Kraftkonstante in N/m,
C---- untere und obere Grenze in Angstroem (dritte Bewegung)

      READ(22 , *) mue3
      READ(22 , *) kraft3
      READ(22 , *) u3
      READ(22 , *) o3

```

```

C---- Zahl der Stuetzpunkte fuer die numerische Integration 1
      READ(22,*) schritte1

C---- Zahl der Stuetzpunkte fuer die numerische Integration 2
      READ(22,*) schritte2

C---- Zahl der Stuetzpunkte fuer die numerische Integration 2
      READ(22,*) schritte3

      CLOSE(22)

      OPEN(23,FILE='pruefung.dat')

C---  Bennung der dat-Werte, falls Spline reaktiviert wird
      dat1 = 1
      dat2 = 1
      dat3 = 1

      beta1 = sqrt(mue1 * kraft1)
      beta1 = (beta1/1.05459D-34) * sqrt(1.66056D-27)
      beta1 = sqrt(beta1)

      o1 = o1 * beta1 * 1.0D-10
      u1 = u1 * beta1 * 1.0D-10

      beta2 = sqrt(mue2 * kraft2)
      beta2 = (beta2/1.05459D-34) * sqrt(1.66056D-27)
      beta2 = sqrt(beta2)

      o2 = o2 * beta2 * 1.0D-10
      u2 = u2 * beta2 * 1.0D-10

      beta3 = sqrt(mue3 * kraft3)
      beta3 = (beta3/1.05459D-34) * sqrt(1.66056D-27)
      beta3 = sqrt(beta3)

      o3 = o3 * beta3 * 1.0D-10
      u3 = u3 * beta3 * 1.0D-10

      okin1 = 6.0D0 * beta1 * 1.0D-10
      okin2 = 6.0D0 * beta2 * 1.0D-10
      okin3 = 6.0D0 * beta3 * 1.0D-10

      ukin1 = - okin1
      ukin2 = - okin2
      ukin3 = - okin3

      write(23,*)
      write(23,*) u1,o1,ukin1,okin1
      write(23,*) u2,o2,ukin2,okin2
      write(23,*) u3,o3,ukin3,okin3

```

```

    write(23,*)
    write(23,*) schritte1 ,schritte2 ,schritte3
    write(23,*) beta3

C----- Integrationsintervalle fuer die numerische Achse

    diff1 = ( o1 - u1 ) / ( schritte1 - 1 )
    diff2 = ( o2 - u2 ) / ( schritte2 - 1 )
    diff3 = ( o3 - u3 ) / ( schritte3 - 1 )

C----- *****

C----- Berechnung der Normierungsfaktoren fuer die harmonischen Funktionen
C      Achtung: hier haben alle Richtungen die gleiche Zahl von Basisfkt.
C      - beta ist in der Integrationsvariable und entfaellt daher -

    DO i = 0,max2
      norm1(i) = (1.0D0) / ( FAK(i) * (2.0D0)**i * sqrt(Pi) )
      norm1(i) = sqrt(norm1(i))
      norm2(i) = norm1(i)
      norm3(i) = norm1(i)
    ENDDO

C----- *****

C----- Im folgenden werden die Matrixelemente der potentiellen Energie
C----- berechnet. Die tau-Integrale werden numerisch berechnet.

C----- Initialisierung von hmat3

    DO i = 0,max5
      DO j = 0,max5
        hmat3(i,j) = 0.0D0
        kmat(i,j) = 0.0D0
      ENDDO
    ENDDO

C----- Einfuegen 1D Check

    OPEN(19,FILE='start3d.dat')

    DO m = 1,schritte3
      write(23,*) m
      READ(19,*) xi(1),yi(1),zi(m),zwert(m)
      write(23,*) zi(m),zwert(m)
    ENDDO

    write(23,*) schritte3

    DO j = 1,schritte3
      write(23,*) j

```

```

        zi(j) = zi(j) * beta3 * 1.0D-10
        write(23,*) zi(j),zwert(j)
    ENDDO

    CLOSE(19)
    write(23,*)
    GOTO 999

C--- *****
C--- aeussere numerische Achse ist die x-Achse

    taustart = u1
    lauf = 0
    laufa = 0
    WRITE(23,*)
    WRITE(23,*) ' _Durchfuehren_ der _numerischen_ Integrationen_ ... _'

    DO 800 k = 1,(schritte1 -2)
        tau = taustart + k * diff1
        lauf = lauf + 1

C---- Ausschneiden der 2D-Flaechen entlang der x-Achse

    OPEN(19,FILE='start3d.dat')

    DO i = 1,k
        DO j = 1,schritte2
            DO m = 1,schritte3
                READ(19,*) xi(i),yi(j),zi(m),z2d(j,m)
            ENDDO
        ENDDO
    ENDDO

    DO j = 1,schritte2
        yi(j) = yi(j) * beta2 * 1.0D-10
    ENDDO

    DO m = 1,schritte3
        zi(m) = zi(m) * beta3 * 1.0D-10
    ENDDO

    CLOSE(19)

C    write(23,*)
    IF (k .EQ. 10) THEN
        DO i = 1,schritte3
            Write(23,*) xi(k),yi(1),zi(i),z2d(1,i)
        ENDDO
    ENDIF
C    write(23,*)

```

```

      CALL RI2D(hmat2,dat2,dat3,schritte2,schritte3,yi,zi,z2d,
$          norm2,norm3,diff2,u2,zaehlen)

C----- trigonometrische Funktionen
      CALL taufunk2(tauwert,max2,tau,norm1)

      zahl1 = -1

      DO 820 i1 = 0,max2
        DO 830 j1 = 0,max22
          zahl1 = zahl1 + 1
          zahl2 = -1
          DO 840 i2 = 0,max2
            DO 850 j2 = 0,max22
              zahl2 = zahl2 + 1
              hilf = tauwert(i1) * hmat2(j1,j2) * tauwert(i2) * diff1
              hmat3(zahl1,zahl2) = hilf + hmat3(zahl1,zahl2)
850          ENDDO
840        ENDDO
830      ENDDO
820    ENDDO

      IF (lauf.eq.10) THEN
        laufa = laufa + lauf
        lauf = 0
        WRITE(23,*)
        WRITE(23,*) laufa, '_Integrationen_durchgefuehrt'
        CALL FLUSH(23)
      ENDIF
800  ENDDO

C----- Im folgenden werden die Randwerte 1 und Schritte zur korrekten Be-
C----- rechnung von Ober- und Untersumme hinzuaddiert
C----- Zum letzten Summanden wird die kinetische Energie hinzuaddiert

      DO 950 k = 0,1
        tau = taustart + k * (schritte1-1) * diff1

      OPEN(19,FILE='start3d.dat')

      IF (k .EQ. 0) THEN
        DO j = 1,schritte2
          DO m = 1,schritte3
            READ(19,*) xi(1),yi(j),zi(m),z2d(j,m)
          ENDDO
        ENDDO
      ELSE
        DO i = 1,schritte1
          DO j = 1,schritte2
            DO m = 1,schritte3
              READ(19,*) xi(i),yi(j),zi(m),z2d(j,m)
            ENDDO
          ENDDO
        ENDDO
      ENDIF
    ENDDO
  ENDDO

```

```

        ENDDO
    ENDDO
ENDDO
        ENDIF

DO j = 1,schritte2
    yi(j) = yi(j) * beta2 * 1.0D-10
ENDDO

DO m = 1,schritte3
    zi(m) = zi(m) * beta3 * 1.0D-10
ENDDO

CLOSE(19)

CALL RI2D(hmat2,dat2,dat3,schritte2,schritte3,yi,zi,z2d,
$         norm2,norm3,diff2,u2,zaehlen)

C---- trigonometrische Funktionen
CALL taufunk2(tauwert,max2,tau,norm1)

zahl1 = -1

DO 978 i1 = 0,max2
DO 979 j1 = 0,max22
    zahl1 = zahl1 + 1
    zahl2 = -1

DO 980 i2 = 0,max2
DO 981 j2 = 0,max22

    zahl2 = zahl2 + 1
    hilf = tauwert(i1) * hmat2(j1,j2) * tauwert(i2) * diff1

    IF (k .eq. 0) THEN
        hmat3(zahl1,zahl2) = hilf + 2.0D0 * hmat3(zahl1,zahl2)
    ELSE
        hmat3(zahl1,zahl2) = (hmat3(zahl1,zahl2) + hilf)/2.0D0
    ENDIF

981     ENDDO
980     ENDDO
979     ENDDO
978     ENDDO
950 ENDDO

C---- *****

999 CALL HIROT(zi,zwert,schritte3,norm3,hmat)

```



```

C----- *****
C      Berechnung der Matrixelemente der kinetischen Energie

      DO i = 0,max2
        DO j = 0,max2
          kmat1(i,j) = 0.0D0
          kmat2(i,j) = 0.0D0
          kmat3(i,j) = 0.0D0
        ENDDO
      ENDDO

      CALL kmatrix(kmat1,max2,ukin1,okin1,kraft1,mue1)
      CALL kmatrix(kmat2,max2,ukin2,okin2,kraft2,mue2)
      CALL kmatrix(kmat3,max2,ukin3,okin3,kraft3,mue3)

      DO i=0,max2
        DO j=0,max2
          olap(i,j) = 0.0D0
        ENDDO
      ENDDO

      DO i=0,max2
        olap(i,i) = 1.0D0
      ENDDO

C----- Addieren der kinetischen Energie zur potentiellen Energie
C      1 D Check

      write(23,*) '_reine_kmatrix_'
      DO i = 0,max2
        DO j=0,max2
          write(23,*) i,j,kmat3(i,j)*219475.0D0, kmat3(j,i)*219475.0D0
        ENDDO
      write(23,*)
      ENDDO
      write(23,*)

      write(23,*) '_reine_Hmatrix_'
      DO i=0,max2
        DO j=0,max2
          write(23,*) i,j,hmat(i,j)*219475.0D0, hmat(j,i)*219475.0D0
        ENDDO
      ENDDO
      write(23,*)

      DO i=0,max2
        DO j=0,max2
C      write(23,*) i,j,hmat(i,j)*219475.0D0, hmat(j,i)*219475.0D0
          hmat(i,j) = hmat(i,j) + kmat3(i,j)
          hmat(i,j) = hmat(i,j) * 219475.0D0
        ENDDO
      ENDDO

```

```

ENDDO

DO i=0,max2
  write(23,*) hmat(i,i)
ENDDO

DO i=1,max2
  xwert(i) = hmat(i,i) - hmat(i-1,i-1)
  write(23,*) xwert(i)
ENDDO
write(23,*)

DO i=0,max2
  DO j=0,max2
    write(23,*) hmat(i,j)
  ENDDO
  write(23,*)
ENDDO

GOTO 998

```

C---- *Addieren der kinetischen Energie zur potentiellen Energie*

```

zahl1 = -1
zahl2 = -1
z1 = zahl1
z2 = zahl2

DO i=0,max2
  DO j=0,max2
    DO k=0,max2

      z1 = z1 + 1
      z2 = -1

      DO l=0,max2
        DO m=0,max2
          DO n=0,max2

            z2 = z2 + 1
            hmat3(z1,z2) = hmat3(z1,z2)+olap(i,l)*olap(j,m)*kmat3(k,n)
            hmat3(z1,z2) = hmat3(z1,z2)+olap(i,l)*kmat2(j,m)*olap(k,n)
            hmat3(z1,z2) = hmat3(z1,z2)+kmat1(i,l)*olap(j,m)*olap(k,n)

            kmat(z1,z2) = kmat(z1,z2) + olap(i,l)*olap(j,m)*kmat3(k,n)
            kmat(z1,z2) = kmat(z1,z2) + olap(i,l)*kmat2(j,m)*olap(k,n)
            kmat(z1,z2) = kmat(z1,z2) + kmat1(i,l)*olap(j,m)*olap(k,n)

          ENDDO
        ENDDO
      ENDDO
    ENDDO
  ENDDO
ENDDO

```

```

        ENDDO
        ENDDO
    ENDDO
C----- *****

        write (23,*)
        DO i = 0,max5
            DO j = 0,max5
                Write (23,*) kmat(i,j)
            ENDDO
        ENDDO

        WRITE(23,*)  ' _Alle_Integrationen_durchgefuehrt '
        WRITE(23,*)
        WRITE(23,*)  ' _Schreiben_der_H-Matrix..._ '
        CALL FLUSH(23)

C----- Berechnung der H-Matrixelemente der potentiellen Energie in Wellenzahlen

        DO i = 0,max5
            DO j = 0,max5
                hmat3(i,j) = hmat3(i,j) * 219475.0D0
            ENDDO
        ENDDO

C----- *****

C----- Schreiben der Matrixelemente fuer die Diagonalisierung

        OPEN(20,FILE='HMAT.dat')
        wert = 1.0D0
        wert2 = 0.0D0

C----- ***** erste Zeile *****

        WRITE(20,*) wert
        DO 500 i = 1,max5
            WRITE(20,*) wert2
500    ENDDO

C----- *****

C----- ***** zweite bis vorletzte Zeile *****

        DO 600 i = 1,(max5-1)
            DO 620 j = 0,(i-1)
                WRITE(20,*) hmat3(i,j)
620    ENDDO

        WRITE(20,*) wert

        DO 640 j = (i+1),max5

```

```

        WRITE(20,*) wert2
640    ENDDO
600    ENDDO

C----- *****
C----- *** letzte Zeile *****

        DO 700 i = 0,(max5-1)
        WRITE(20,*) hmat3(i,max5)
700    ENDDO

        WRITE(20,*) wert

C----- *****
C----- *** Diagonalelemente der H-Matrix

        DO 750 i = 0,max5
        WRITE(20,*) hmat3(i,i)
750    ENDDO

C----- *****

        CLOSE(20)

C----- Berechnung der H-Matrixelemente der potentiellen Energie in Wellenzahl

C      DO i = 0,max5
C      DO j = 0,max5
C      hmat3(i,j) = hmat3(i,j) * 219475.0D0
C      ENDDO
C      ENDDO

C----- *****

998    CONTINUE

        WRITE(23,*) 'Programm beendet!_!_!'
        CLOSE(23)

        STOP
        END

C----- Die folgende Subroutine berechnet die Integrale entlang der zwei-
C----- dimensionalen Schnitte.

        SUBROUTINE RI2D(hmat2,dat2,dat3,schritte2,schritte3,yi,zi,z2d,
$                    norm1,norm2,diff2,u2,zaehlen)

        IMPLICIT NONE

        INTEGER max2,max22,max3,max4,min

```

```

PARAMETER(max2=9)
PARAMETER(max22=15)
PARAMETER(max3=20)
PARAMETER(max4=100001)
PARAMETER(min=0)

INTEGER  dat2 , dat3
INTEGER  schritte2 , schritte3 , zaehlen
INTEGER  i , j , i1 , i2 , i3 , i4 , j1 , j2 , lauf2 , laufa2
INTEGER  zahl1 , zahl2
DOUBLE PRECISION  u2 , diff2 , taustart , tau
DOUBLE PRECISION  z2d(max4,max4) , yi(max4) , zi(max4)
DOUBLE PRECISION  hmat2(min:max22,min:max22)
DOUBLE PRECISION  hmat(min:max2,min:max2) , tauwert(0:max2)
DOUBLE PRECISION  norm1(min:max2) , norm2(min:max2) , hilf
C      DOUBLE PRECISION  yywert(max4) , zzwert(max4)
C      DOUBLE PRECISION  daten(max4,max4) , HX(max3,max4)
DOUBLE PRECISION  zwert(max4)

C      xdim  = max3
C      ydim  = max3
C      xxdim = max4

C      imode = 1

zaehlen = zaehlen + 1

C      CALL GRID(xdim , dat2 , yi , ydim , dat3 , zi , z2d ,
C      $          xxdim , schritte2 , yywert , schritte3 , zzwert ,
C      $          daten , HX , imode , nerr )

C      WRITE(23 ,*)
C      WRITE(23 ,*) zaehlen , '. 2D-Spline wurde durchgefuehrt :
C      ,
C      WRITE(23 ,*) ' IMODE : ' , IMODE
C      WRITE(23 ,*) ' NERR  : ' , NERR
C      Write(23 ,*)
C      CALL FLUSH(23)
C---- *****

C---- Initialisierung von hmat2
DO  i = 0,max22
  DO  j = 0,max22
    hmat2(i , j) = 0.0D0
  ENDDO
ENDDO
C---- *****

taustart = u2
lauf2 = 0

```

```

    laufa2 = 0

DO 888  i3 = 1,(schritte2 - 2)
    tau = taustart + i3 * diff2
    lauf2 = lauf2 + 1

    DO  i = 1,schritte3
        i4 = i3 + 1
        zwert(i) = z2d(i4 , i)
    ENDDO

C---- Berechnung der H-Matrixelemente fuer die erste Dimension

    CALL HIROT(zi , zwert , schritte3 , norm2 , hmat)

C---- *****

C----  trigonometrische Funktionen
    CALL taufunk2(tauwert , max2 , tau , norm1)

    zahl1 = -1

DO 821  i1 = 0,max2
    DO 831  j1 = 0,max2
        zahl1 = zahl1 + 1
        zahl2 = -1

        DO 841  i2 = 0,max2
            DO 851  j2 = 0,max2

                zahl2 = zahl2 + 1
                hilf = tauwert(i1) * hmat(j1 , j2) * tauwert(i2) * diff2
                hmat2(zahl1 , zahl2) = hilf + hmat2(zahl1 , zahl2)

851         ENDDO
841         ENDDO
831         ENDDO
821         ENDDO

C        IF (lauf2 .eq. 500) THEN
C            laufa2 = laufa2 + lauf2
C            lauf2 = 0
C            WRITE(23 , *)
C            WRITE(23 , *) laufa2 , ' Integrationen durchgefuehrt '
C            CALL FLUSH(23)
C        ENDIF
888  ENDDO

C---- Im folgenden werden die Randwerte 1 und Schritte zur korrekten Be-
C---- rechnung von Ober- und Untersumme hinzuaddiert

```

```

DO 951 i3 = 0,1
  tau = taustart + i3 * (schritte2 - 1) * diff2
  DO i = 1,schritte3
    IF (i3.eq.0) THEN
      zwert(i) = z2d(i,1)
    ELSE
      zwert(i) = z2d(i,schritte3)
    ENDIF
  ENDDO

C---- Berechnung der H-Matrixelemente fuer die erste Dimension

CALL HIROT(zi,zwert,schritte3,norm2,hmat)

C---- *****

C---- trigonometrische Funktionen
CALL taufunk2(tauwert,max2,tau,norm1)

zahl1 = -1

DO 941 i1 = 0,max2
  DO 942 j1 = 0,max2
    zahl1 = zahl1 + 1
    zahl2 = -1

    DO 943 i2 = 0,max2
      DO 944 j2 = 0,max2

        zahl2 = zahl2 + 1
        hilf = tauwert(i1) * hmat(j1,j2) * tauwert(i2) * diff2

        IF (i3 .eq. 0) THEN
          hmat2(zahl1,zahl2) = hilf + 2.0D0 * hmat2(zahl1,zahl2)
        ELSE
          hmat2(zahl1,zahl2) = (hmat2(zahl1,zahl2) + hilf)/2.0D0
        ENDIF

944      ENDDO
943    ENDDO
942  ENDDO
941 ENDDO
951 ENDDO

RETURN
END

C---- *****

C---- *****
C---- Die folgende Subroutine fuehrt eine numerische Berechnung der

```

C----- *Matrixelemente in der ersten Dimension durch*

```

SUBROUTINE hirot(xwert,V,schritte ,norm,hmat)
IMPLICIT NONE

INTEGER max2,max4,min
PARAMETER(max2=9)
PARAMETER(max4=100001)
PARAMETER(min=0)
INTEGER i,j,k,g1,g2,schritte
DOUBLE PRECISION delta,x,delta1,erst,letzt,xend
DOUBLE PRECISION xstart,Pi
DOUBLE PRECISION xwert(max4),V(max4)
DOUBLE PRECISION norm(min:max2)
DOUBLE PRECISION hmat(min:max2,min:max2)
DOUBLE PRECISION FAK,FWERT
EXTERNAL FAK

```

```
Pi=3.141592653589793285D0
```

C----- *****

```

DO i = 0,max2
  DO j = 0,max2
    hmat(i,j) = 0.0D0
  ENDDO
ENDDO

```

```

xstart = xwert(1)
delta = xwert(2) - xwert(1)

```

C----- *****

```
DO 200 k = 1,(schritte-2)
```

```

x = xstart + k * delta
delta1 = V(k+1) * delta
  DO 300 i = 0,max2
    DO 400 j = 0,i
      hmat(i,j) = hmat(i,j) + fwert(i,x,max2)*fwert(j,x,max2)*delta1
    ENDDO
  ENDDO
ENDDO

```

400
300
200

```
xend = xwert(schritte)
```

```

DO 402 i = 0,max2
  DO 404 j = 0,i
    erst=fwert(i,xstart,max2) * fwert(j,xstart,max2) * V(1) * delta
    letzt=fwert(i,xend,max2) * fwert(j,xend,max2)*V(schritte)*delta
    hmat(i,j) = hmat(i,j) + (letzt + erst)/2.D0
  ENDDO
ENDDO

```



```

404   ENDDO
402   ENDDO

C---- Normierung und Umrechnung auf Hartree

      DO 420 i = 0,max2
        DO 430 j = 0,i
          hmat(i,j) = ( hmat(i,j) * norm(i) * norm(j) ) / 219475.D0
          hmat(j,i) = hmat(i,j)
430     ENDDO
420   ENDDO

      RETURN
      END

      SUBROUTINE          kmatrix(kmat,max2,u,o,kraft,mue)

      IMPLICIT NONE

      INTEGER max1,max2,min
      PARAMETER(max1=3)
C     PARAMETER(max2=9)
      PARAMETER(min=0)

      INTEGER i,j,k
      DOUBLE PRECISION mue,kraft,o,u,eo,eu
      DOUBLE PRECISION faktor,faktor2,faktor3,Pi
      DOUBLE PRECISION norm(min:max2),OG(min:max2),UG(min:max2)
      DOUBLE PRECISION kmat(min:max2,min:max2)
      DOUBLE PRECISION matrix(min:max1,min:max2,min:max2)
      DOUBLE PRECISION FAK
      EXTERNAL FAK

      Pi=3.141592653589793285D0

C---- Berechnung der Normierungsfaktoren fuer die harmonischen Funktionen

      DO 210 i = 0,max2
        norm(i) = (1.0D0) / ( FAK(i) * (2.0D0)**i * sqrt(Pi) )
        norm(i) = sqrt(norm(i))
210   CONTINUE

C----- *****

      eo = o * o
      eo = exp(-eo)
      eu = u * u
      eu = exp(-eu)

C---- Berechnung der Funktionswerte der Hermite-Polynome

```

```

OG(0) = 1.0D0
UG(0) = 1.0D0
OG(1) = 2.0D0 * o
UG(1) = 2.0D0 * u

DO 220 i = 2,max2
OG(i) = (2.0D0)*(o * OG(i-1) - (i-1)* OG(i-2))
UG(i) = (2.0D0)*(u * UG(i-1) - (i-1)* UG(i-2))

220 ENDDO

C----- *****

C---- Berechnung der Integrale des Typs x**k exp(-x**2)

matrix(0,0,0) = sqrt(Pi)
matrix(1,0,0) = 0.0D0
matrix(2,0,0) = 0.5D0 * sqrt(Pi)
matrix(3,0,0) = 0.0D0

C----- *****

C---- Berechnung der Integrale des Typs H * exp(-x**2)
DO 240 i= 1,max2
matrix(0,i,0) = - OG(i-1) * eo + UG(i-1) * eu ;
matrix(0,0,i) = matrix(0,i,0);
240 ENDDO

C----- *****

C---- Berechnung der Integrale des Typs x**k H exp(-x**2)
DO 250 k = 1,3
DO 260 i=1,max2
matrix(k,i,0) = -eo * OG(i-1) * o**k + eu * UG(i-1) * u**k
matrix(k,i,0) = matrix(k,i,0) + k * matrix(k-1,i-1,0)
matrix(k,0,i) = matrix(k,i,0)
260 ENDDO
250 ENDDO

C----- *****

C---- Berechnung der Integrale des Typs H * H * exp(-x**2)
DO 270 i=1,max2
DO 280 j=1,i
matrix(0,i,j) = -OG(i-1) * OG(j) * eo + UG(i-1) * UG(j) * eu
matrix(0,i,j) = matrix(0,i,j) + 2.0D0*j*matrix(0,j-1,i-1)
matrix(0,j,i) = matrix(0,i,j)
280 ENDDO
270 ENDDO

```

```

C----- *****
C----- Berechnung der Integrale des allg. Typs  $x^{**k} H H \exp(-x^{**2})$ 
      DO 290 k=1,3
        DO 300 i=1,max2
          DO 310 j = 1,i
            matrix(k,i,j) = -eo*OG(j)*OG(i-1)* o**k + eu*UG(j)*UG(i-1)* u**k
            matrix(k,i,j) = matrix(k,i,j) + k*matrix(k-1,i-1,j)
            matrix(k,i,j) = matrix(k,i,j) + 2.D0*j*matrix(k,i-1,j-1)
            matrix(k,j,i) = matrix(k,i,j)
310      ENDDO
300      ENDDO
290      ENDDO

C----- *****
C----- Berechnung der H-Matrixelemente der kinetischen Energie

      faktor = sqrt(kraft / mue) * 1.05459D-34
      faktor = -faktor/(2.D0 * sqrt(1.66056D-27) * 4.3598D-18)

      faktor2 = norm(0) * faktor
      faktor3 = norm(1) * faktor

      DO 320 i = 0,max2
        kmat(i,0) = (matrix(2,i,0) - matrix(0,i,0)) * faktor2 * norm(i)
        kmat(i,1)=(-6.D0*matrix(1,i,0)+2.D0*matrix(3,i,0))* faktor3*norm(i)
320      ENDDO

      DO 330 i = 0,max2
        DO 340 j = 2,max2
          kmat(i,j)=4.D0*j*(j-1) * matrix(0,i,j-2) - 4.D0*j*matrix(1,i,j-1)
          kmat(i,j) = kmat(i,j) - matrix(0,i,j) + matrix(2,i,j) ;
          kmat(i,j) = kmat(i,j) * norm(i) * norm(j) * faktor;
340      ENDDO
330      ENDDO

C----- *****

      RETURN
      END

C----- Funktionswerte der Basisfunktionen bestimmen

      DOUBLE PRECISION FUNCTION FWERT(n,x,max2)
      IMPLICIT NONE
      INTEGER          n,i,jj,max2
      DOUBLE PRECISION x,G(0:max2)

      IF (n .EQ. 0 )   FWERT = 1.0D0 * exp(- (x*x)/2 )

```

```

IF (n .EQ. 1 )   FWERT = 2.0D0 * x * exp(- (x*x)/2 )
IF (n .GT. 1 )  THEN
                G(0) = 1.0D0
                G(1) = 2.0D0 * x
                DO i=2,n
G(i)=(2.0D0) * (x * G(i-1)-(i-1)*G(i-2))
                ENDDO
                FWERT = G(n) * exp(- (x*x)/2 )
                ENDIF

RETURN
END

C----- *****
C----- *****

C----- Harmonische Oszillator-Funktionen als Basis

SUBROUTINE taufunk2 (tauwert ,max2, tau ,norm2)

IMPLICIT NONE
INTEGER max2, i
DOUBLE PRECISION tauwert (0:max2) ,norm2 (0:max2)
DOUBLE PRECISION tau , FWERT
EXTERNAL FWERT

DO i = 0 ,max2
    tauwert(i) = FWERT(i ,tau ,max2) * norm2(i)
ENDDO

RETURN
END

C----- *****

C----- Fakultaetsberechnung *****

DOUBLE PRECISION FUNCTION FAK(n)

IMPLICIT NONE
INTEGER i ,n
DOUBLE PRECISION hilf

IF (n .eq. 0 ) THEN
    FAK=1.0D0
ELSE
    hilf=1.0D0
DO 100 i=1,n
    hilf = i * hilf
100 CONTINUE
FAK = hilf

```

```
ENDIF
```

```
RETURN
```

```
END
```

ritz.py

```
#!/usr/bin/python
```

```
import sys, subprocess
```

```
data2 = []
```

```
spline = []
```

```
string = ""
```

```
spline_y = ""
```

```
i = 0
```

```
def bash_command(cmd):
```

```
    subprocess.Popen(cmd, shell=True, executable='/bin/bash')
```

```
f = open("spline.dat", "r")
```

```
input = f.readlines()
```

```
f.close()
```

```
for line in input:
```

```
    spline_y = line.strip()
```

```
    spline_x = float(sys.argv[1]) + float(i)*0.001
```

```
    spline_x = "%.6E" % float(spline_x)
```

```
    spline_y = "%.6E" % float(spline_y)
```

```
    string = "0.000000D+00_0.000000D+00"+"_" + str(spline_x) + "_" + str(spline_y)
```

```
    spline.append(string)
```

```
    i = i + 1
```

```
f = open("start3d.dat", "w")
```

```
for line in spline:
```

```
    line = str(line)
```

```
    line.replace("E", "D")
```

```
    f.write(line)
```

```
f.close()
```

```
f = open("eingaben.dat", "w")
```

```
start = str(sys.argv[1])
```

```
end = str(float(start)+i*0.001-0.001)
```

```
points = str(i)
```

```
f.write("10\n")
```

```
f.write("1\n")
```

```
f.write("-1\n")
```

```
f.write("1\n")
```

```
f.write("10\n")
```

```

f.write("1\n")
f.write("-1\n")
f.write("1\n")
f.write("red_mass\n")
f.write("coeff\n")
f.write(start+"\n")
f.write(end+"\n")
f.write("100\n")
f.write("100\n")
f.write(points+"\n")
f.write("10\n")

```

```
bash_command("sed -i 's/E/D/g' start3d.dat")
```

pruef2HMAT.py

```

from sys import argv
import itertools

```

```

pruef = open('pruefung.dat', 'r').readlines()
pruef = pruef[-1*(int(argv[1]) + int(argv[1])**2 + 1) : -1]
hmat = []
for line in pruef:
    if line.strip() != '':
        hmat.append(line)

```

```

for i, j in enumerate(itertools.product(range(1, int(argv[1])+1), range(1, int(argv[1])+1))):
    hmat[i] = ('%d_%d' % (j[0], j[1])) + hmat[i]

```

```
open('HMAT', 'w').writelines([argv[1] + '\n' + hmat])
```

autoritz.py

```
#!/usr/bin/python
```

```
import os
```

```
def ritz_calc(number):
```

```
    command="sed -i \"s/coeff/\"+str(number)+\"/\>_eingaben.dat"
```

```
    os.system("cp_eingaben.dat_eingaben_save.dat")
```

```
    os.system(command)
```

```
    os.system("/home2/strebert/bin/ritz/RITZ_10.x")
```

```
    os.system("python_/home2/strebert/bin/ritz/pruef2HMAT.py_10")
```

```
    os.system("/home2/strebert/bin/ritz/diag_ritz_>_/dev/null")
```

```
    os.system("mv_eingaben_save.dat_eingaben.dat")
```

```
    f = open("Results.vib", "r")
```

```
    for line in f:
```

```
        if "1_<--_0" in line:
```

```
            freq=line.split("0")[1].strip()
```

```
        if "eigenfunction" in line:
```

```
            norm=line.split(":")[1].strip()
```

```
        return norm

#####

low=10
high=2000
diff=high-low

while diff > 1:
    print(str(low)+"_"+str(high))
    low_result=ritz_calc(low)
    high_result=ritz_calc(high)
    mid = (low+high)//2
    if ritz_calc(mid+1) > ritz_calc(mid):
        low=mid
    else:
        high=mid
    diff=high-low
os.system("mv_Results.vib_"+str(mid))
```


Appendix C

Chromone derivatives

C.1 Ground state

In the following, additional information concerning the clusters of methanol with the chromone derivatives is given. First, a table with selected geometric parameters for both inside and outside motif is introduced. Secondly, minimum geometries calculated at CAM-B3LYP-D3(BJ)/def2-TZVP level are displayed.

TABLE C.1: Selected distances d for clusters of methanol and chromone derivatives calculated at CAM-B3LYP-D3(BJ)/def2-TZVP level. All distances are given in Å, ΔE is given in kJ/mol.

Nr	Derivat	ΔE	$d(\text{CO})$ In/Out		$d(\text{OH-O})$ In/Out		$d(\text{OH})$ In/Out	
0	Chromon	1.2	1.22	1.22	1.84	1.84	0.97	0.97
1	6-SiMe ₃ ,2-Nitro	-6.6	1.22	1.22	1.91	1.88	0.97	0.97
2	6- ^t Bu,2-Nitro	-6.3	1.22	1.22	1.87	1.87	0.97	0.97
3	6-SiMe ₃	-5.2	1.22	1.23	1.86	1.83	0.97	0.97
4	6-Methoxy	-5.0	1.23	1.23	1.84	1.84	0.97	0.97
5	6- ^t Bu	-4.6	1.22	1.23	1.84	1.83	0.97	0.97
6	6-Ethyl,2-Nitro	-4.0	1.22	1.22	1.87	1.88	0.97	0.97
7	6-Methyl,2-Nitro	-1.6	1.22	1.22	1.88	1.88	0.97	0.97
8	6,7,8-Methyl 2-Nitro	-1.4	1.22	1.22	1.88	1.87	0.97	0.97
9	6-SiH ₃ ,2-Nitro	-0.9	1.22	1.22	1.90	1.89	0.97	0.97
10	6-Ethyl	-0.8	1.22	1.23	1.85	1.83	0.97	0.97
11	6-Methyl, 2-CF ₃	-0.4	1.22	1.22	1.87	1.86	0.97	0.97
12	2-Nitro	-0.2	1.22	1.22	1.87	1.89	0.97	0.97
13	6-Methyl	-0.1	1.22	1.23	1.85	1.83	0.97	0.97
14	6,7,8-Methyl	0.0	1.22	1.23	1.84	1.82	0.97	0.98
15	6-SiH ₃	0.5	1.22	1.22	1.86	1.84	0.97	0.97
16	2-Chlor	0.9	1.22	1.22	1.85	1.85	0.97	0.97
17	7-Methyl	1.0	1.22	1.23	1.84	1.84	0.97	0.97
18	2-Fluor	1.0	1.22	1.22	1.84	1.85	0.97	0.97
19	2-CF ₃	1.0	1.22	1.22	1.87	1.87	0.97	0.97
20	7-Methoxy	1.1	1.22	1.23	1.83	1.83	0.97	0.97
21	2-Isocyanid	1.4	1.22	1.22	1.86	1.86	0.97	0.97
22	2-Cyanid	1.5	1.22	1.22	1.87	1.88	0.97	0.97
23	8-Methoxy	1.6	1.22	1.23	1.84	1.83	0.97	0.97
24	8-Methyl	1.7	1.22	1.23	1.84	1.83	0.97	0.97
25	2-Cyanat	1.9	1.22	1.22	1.86	1.86	0.97	0.97
26	2-Isocyanat	2.8	1.22	1.23	1.84	1.84	0.97	0.97

TABLE C.2: Selected distances d and angles a for clusters of methanol and chromone derivatives calculated at CAM-B3LYP-D3(BJ)/def2-TZVP level. All distances are given in Å, ΔE is given in kJ/mol.

Nr	Derivat	ΔE	$a(\text{COH})$	In/Out	$a(\text{OH-O})$	In/Out	$d(\text{CH-O})$	In/Out	$a(\text{CH-O})$	In/Out
0	Chromon	1.2	135.0	112.8	167.2	164.6	2.29	2.43	162.4	129.1
1	6-SiMe ₃ -2-Nitro	-6.6	133.9	112.9	163.6	159.1	2.22	2.34	167.2	129.9
2	6- ^t Bu-2-Nitro	-6.3	132.9	112.9	166.0	159.5	2.19	2.34	165.9	129.8
3	6-SiMe ₃	-5.2	134.3	113.0	165.8	164.9	2.24	2.44	165.8	128.9
4	6-Methoxy	-5.0	134.5	113.1	167.0	164.9	2.23	2.46	165.5	128.7
5	6- ^t Bu	-4.6	133.9	113.1	167.5	164.9	2.23	2.45	166.2	128.8
6	6-Ethyl-2-Nitro	-4.0	131.4	112.9	167.1	159.3	2.22	2.34	157.9	129.9
7	6-Methyl-2-Nitro	-1.6	134.2	112.8	165.8	159.0	2.25	2.33	164.5	129.9
8	6,7,8-Methyl-2-Nitro	-1.4	134.5	113.1	165.0	160.4	2.27	2.36	163.0	129.4
9	6-SiH ₃ -2-Nitro	-0.9	134.3	112.7	162.6	157.6	2.22	2.31	165.9	130.3
10	6-Ethyl	-0.8	134.4	113.1	165.8	165.0	2.27	2.45	159.7	128.8
11	6-Methyl-2-CF ₃	-0.4	134.5	112.9	165.6	161.2	2.27	2.36	163.4	130.6
12	2-Nitro	-0.2	134.3	112.7	165.5	158.1	2.25	2.32	163.7	130.2
13	6-Methyl	-0.1	134.8	113.1	166.8	164.8	2.28	2.44	162.3	128.9
14	6,7,8-Methyl	0.0	134.9	113.2	167.2	165.6	2.30	2.45	161.8	128.4
15	6-SiH ₃	0.5	134.7	112.8	164.8	164.0	2.24	2.42	164.8	129.3
16	2-Chlor	0.9	134.8	112.9	167.2	162.7	2.28	2.39	162.8	129.8
17	7-Methyl	1.0	134.6	113.1	167.7	164.6	2.29	2.45	161.9	128.9
18	2-Fluor	1.0	135.0	112.3	167.5	162.7	2.27	2.39	163.1	128.4
19	2-CF ₃	1.0	134.6	112.8	165.9	160.7	2.27	2.35	163.2	130.7
20	7-Methoxy	1.1	134.3	113.1	167.5	165.2	2.29	2.44	161.3	128.9
21	2-Isocyanid	1.4	134.6	112.3	166.4	160.1	2.27	2.33	163.3	130.5
22	2-Cyanid	1.5	134.3	112.4	165.9	158.8	2.26	2.30	163.7	131.4
23	8-Methoxy	1.6	135.6	113.0	167.5	164.9	2.32	2.44	161.6	128.9
24	8-Methyl	1.7	135.4	113.0	167.2	164.8	2.30	2.43	162.1	129.0
25	2-Cyanat	1.9	135.0	111.8	166.1	160.3	2.26	2.32	163.6	129.5
26	2-Isocyanat	2.8	134.9	112.0	167.1	162.7	2.28	2.34	162.5	130.8

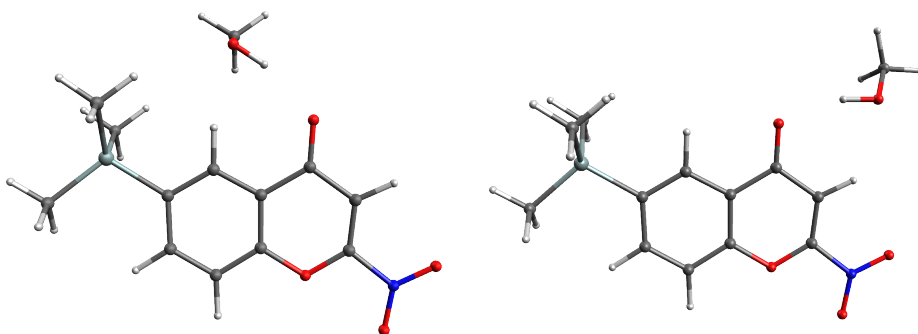


FIGURE C.1: Structures of 6-SiMe₃, 2-nitrochromone with methanol for both inside and outside motif

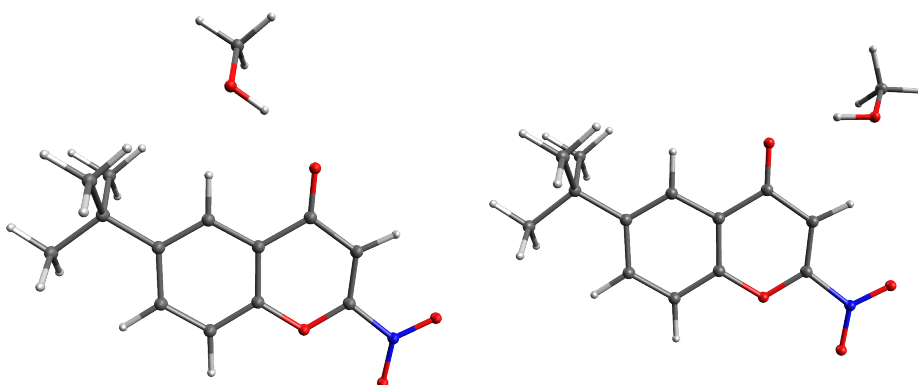


FIGURE C.2: Structures of 6-^tBu, 2-Nitrochromone with methanol for both inside and outside motif

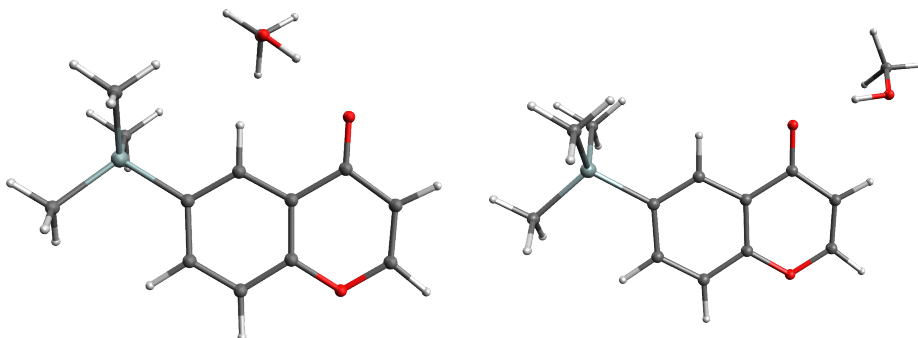


FIGURE C.3: Structures of 6-SiMe₃chromone with methanol for both inside and outside motif

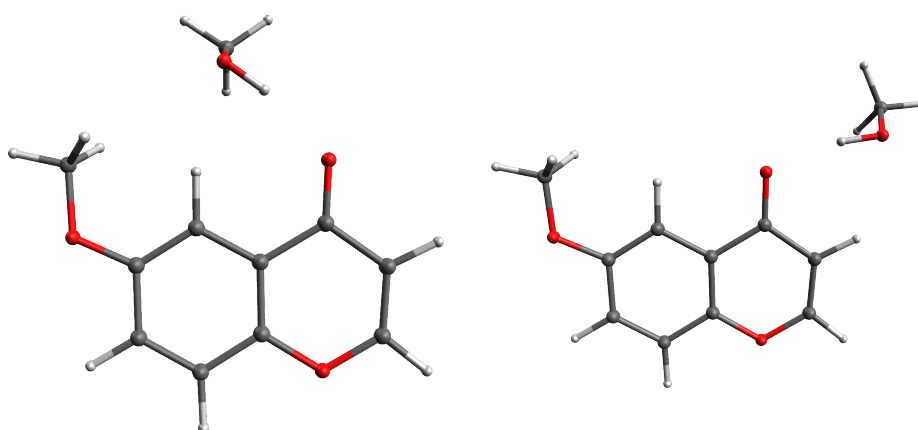


FIGURE C.4: Structures of 6-methoxychromone with methanol for both inside and outside motif

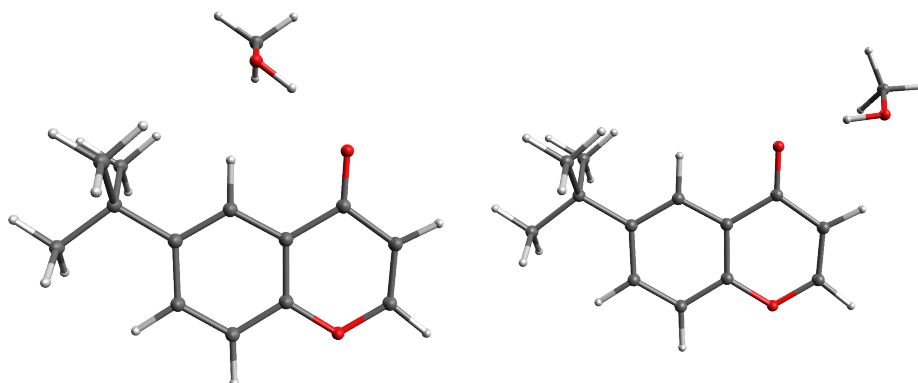


FIGURE C.5: Structures of 6-^tBu-chromone with methanol for both inside and outside motif

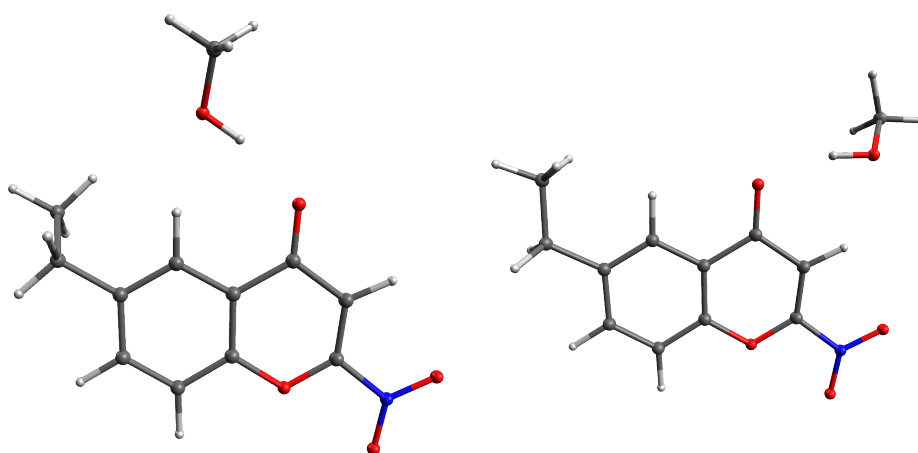


FIGURE C.6: Structures of 6-ethyl, 2-nitrochromone with methanol for both inside and outside motif

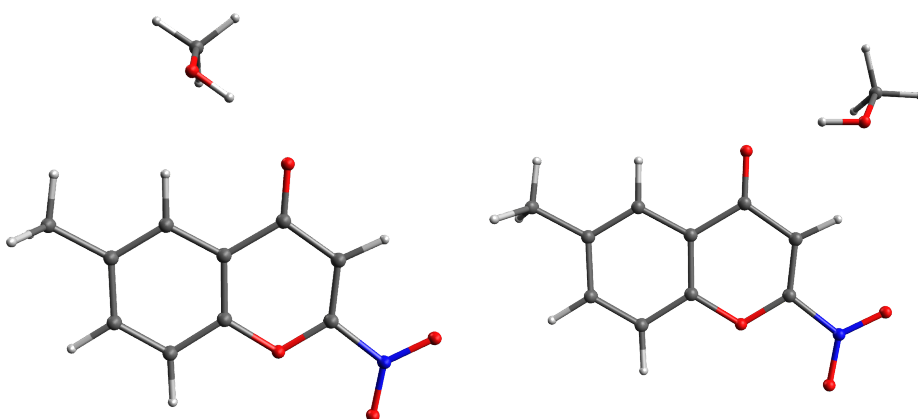


FIGURE C.7: Structures of 6-methyl, 2-nitrochromone with methanol for both inside and outside motif

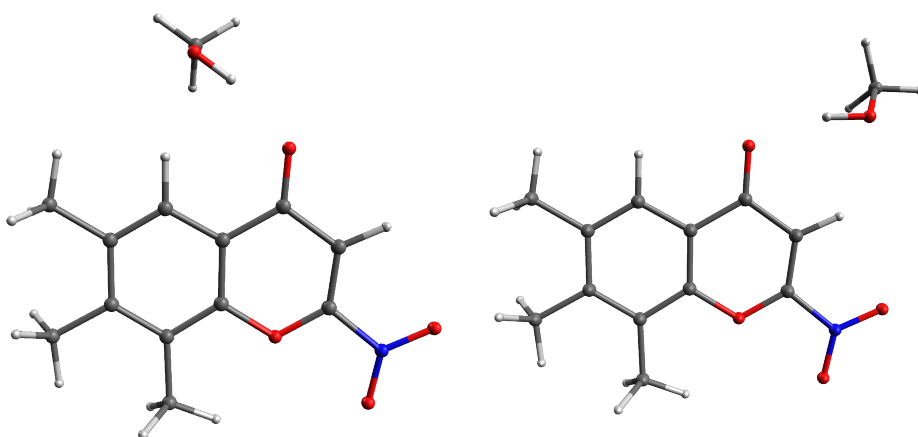


FIGURE C.8: Structures of 6,7,8-methyl, 2-nitrochromone with methanol for both inside and outside motif

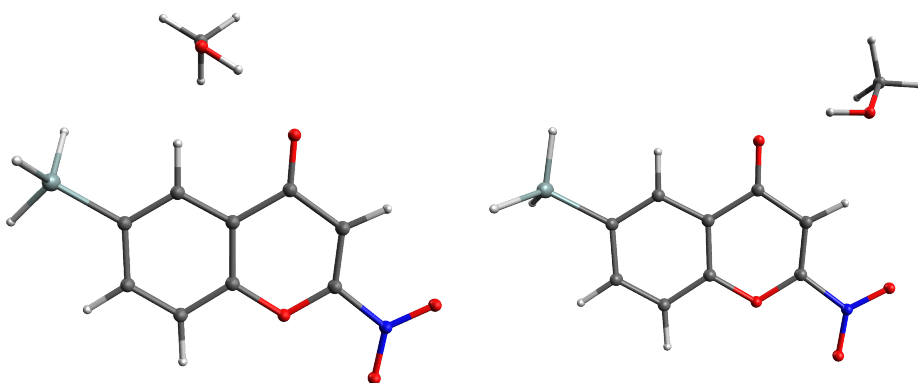


FIGURE C.9: Structures of 6-SiH₃chromone with methanol for both inside and outside motif

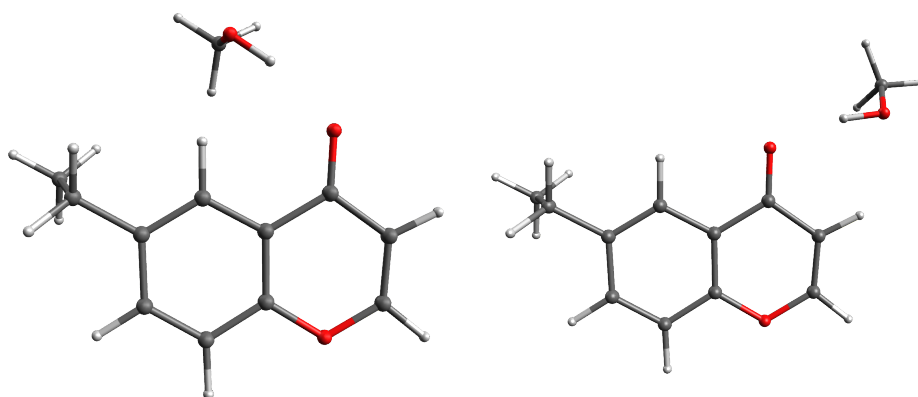


FIGURE C.10: Structures of 6-ethylchromone with methanol for both inside and outside motif

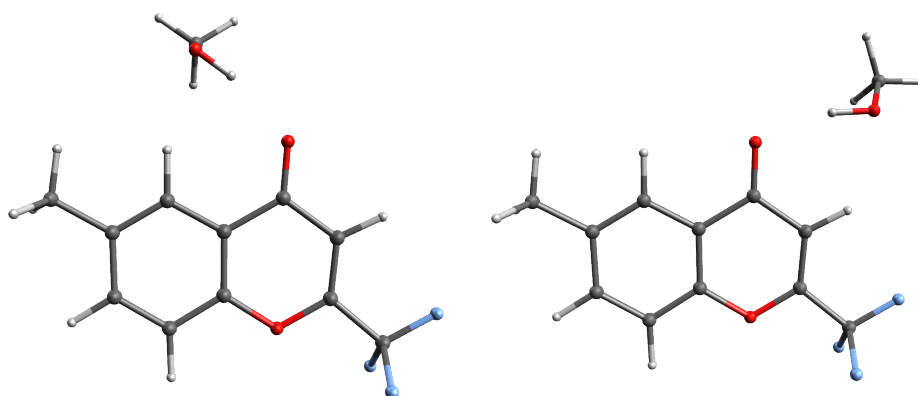


FIGURE C.11: Structures of 6-methyl, 2-CF₃chromone with methanol for both inside and outside motif

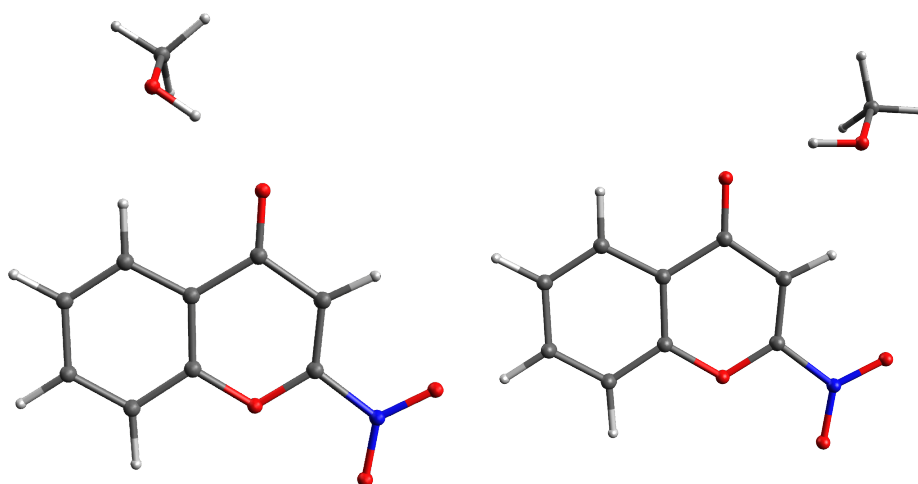


FIGURE C.12: Structures of 2-nitrochromone with methanol for both inside and outside motif

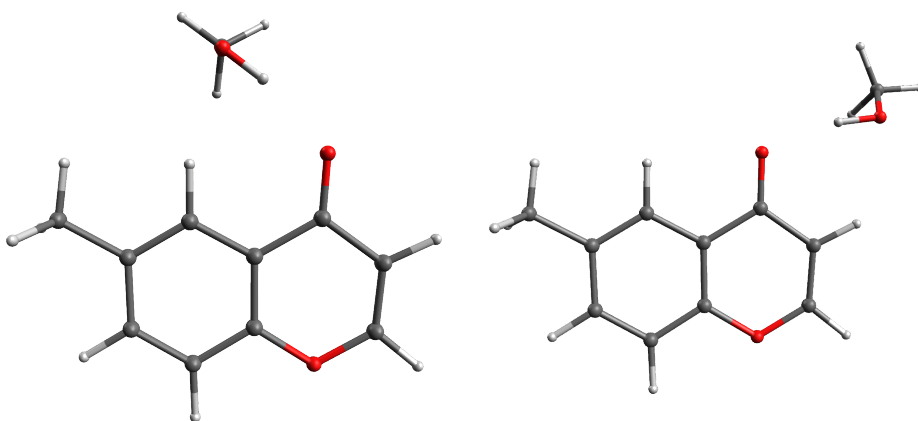


FIGURE C.13: Structures of 6-methylchromone with methanol for both inside and outside motif

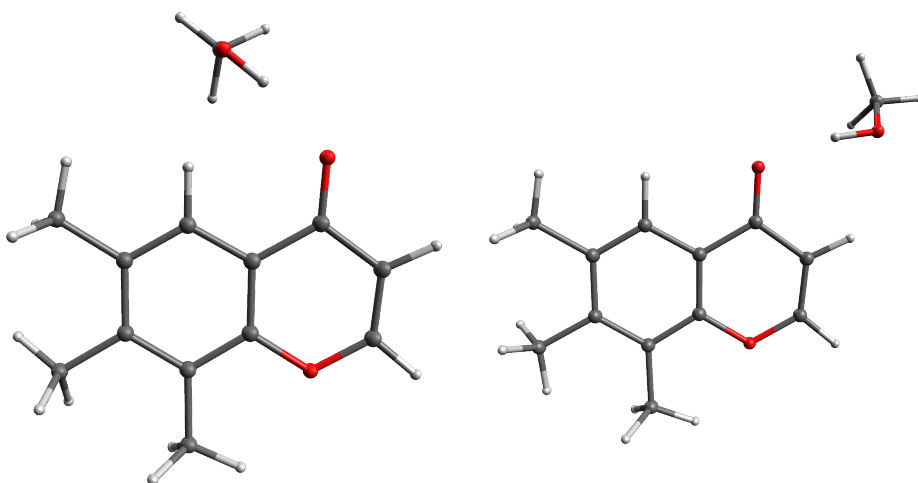


FIGURE C.14: Structures of 6,7,8-methylchromone with methanol for both inside and outside motif

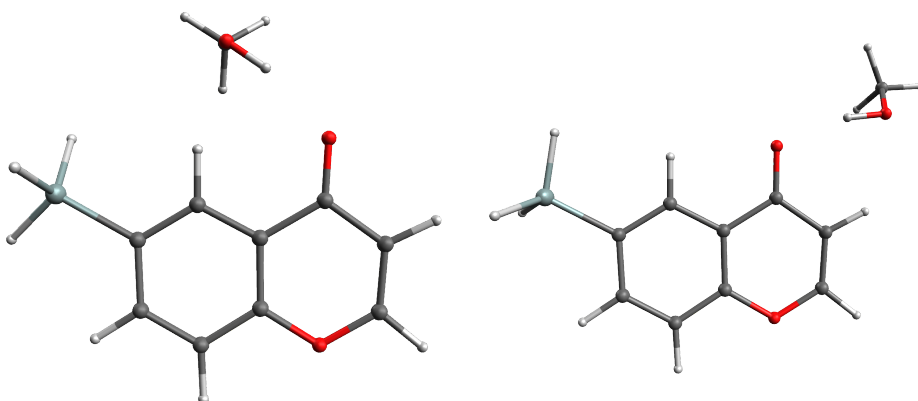


FIGURE C.15: Structures of 6-SiH₃-chromone with methanol for both inside and outside motif

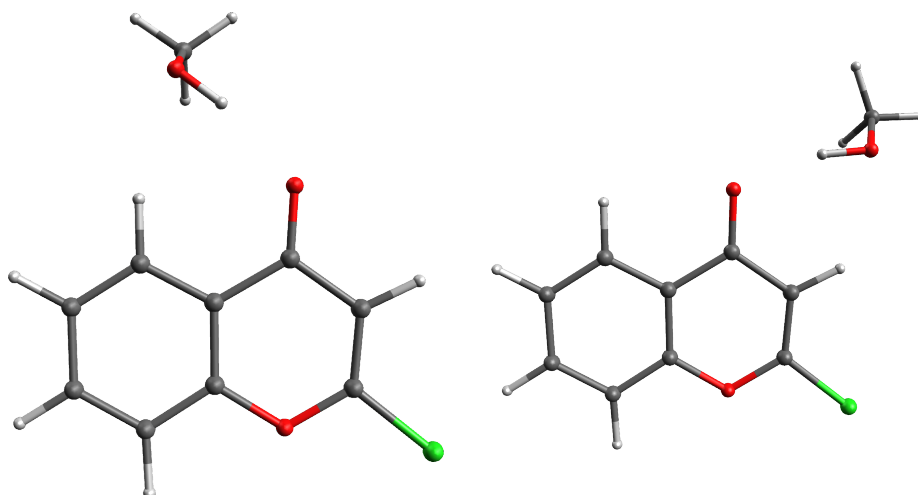


FIGURE C.16: Structures of 2-chlorochromone with methanol for both inside and outside motif

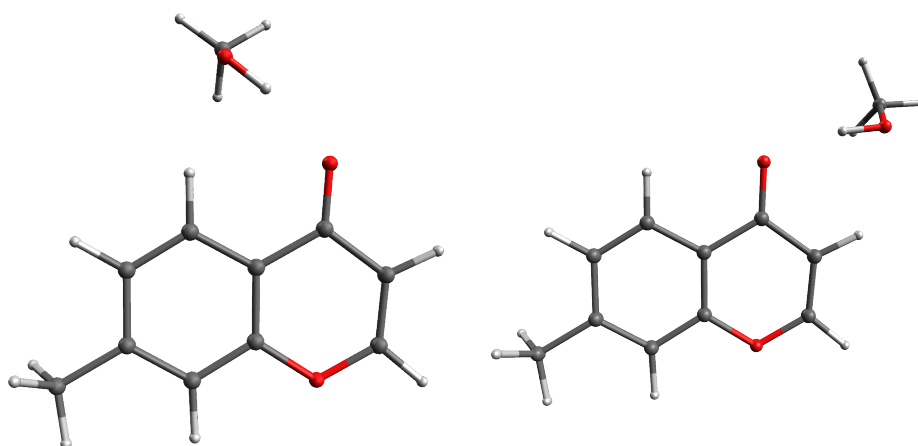


FIGURE C.17: Structures of 7-methylchromone with methanol for both inside and outside motif

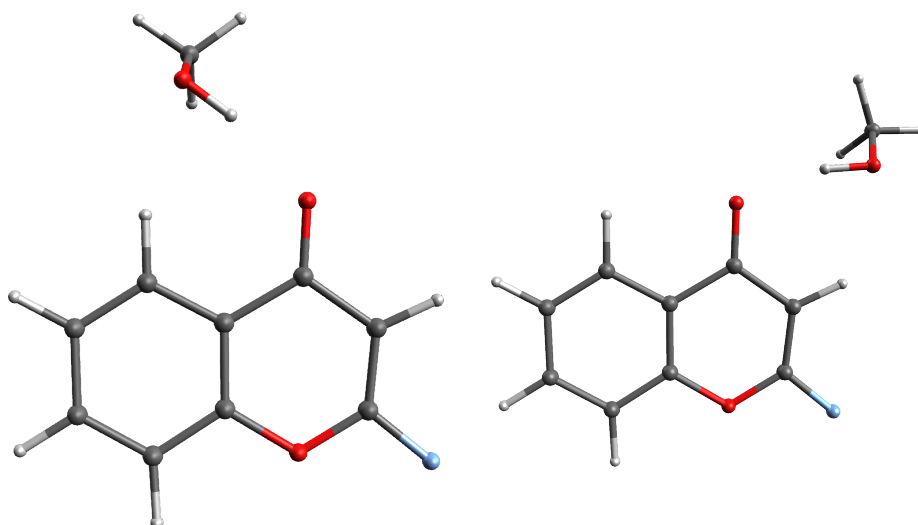


FIGURE C.18: Structures of 2-fluorochromone with methanol for both inside and outside motif

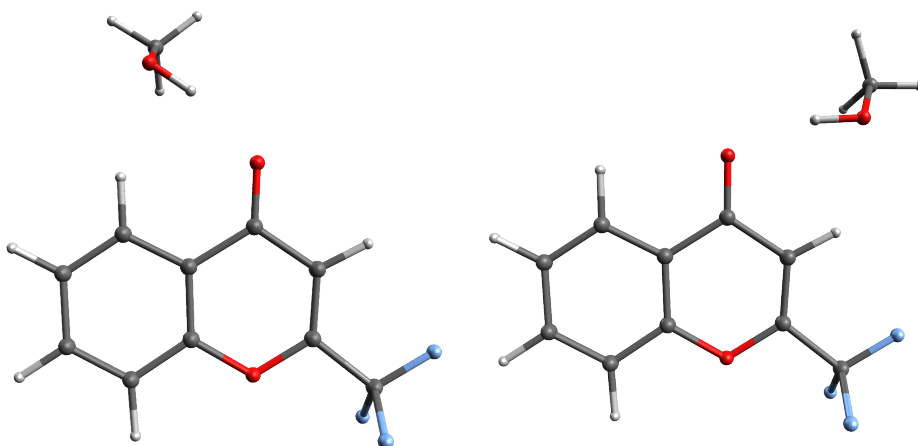


FIGURE C.19: Structures of 2-CF₃-chromone with methanol for both inside and outside motif

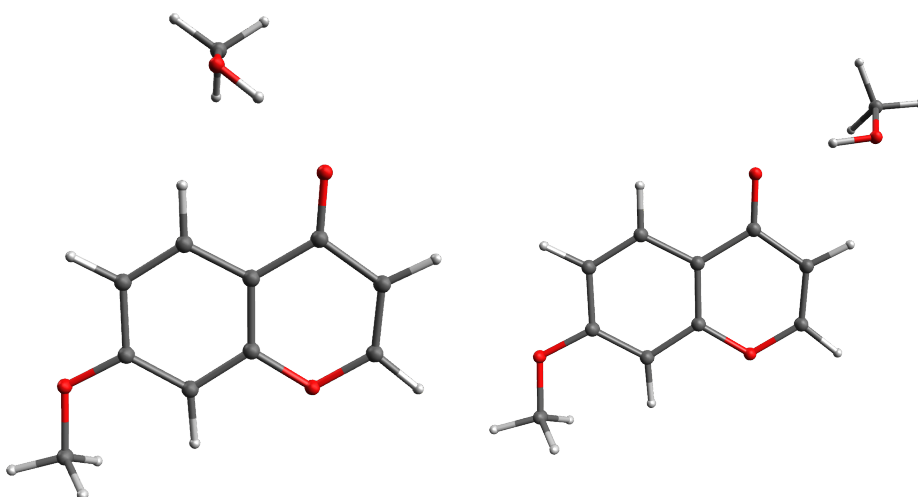


FIGURE C.20: Structures of 7-methoxychromone with methanol for both inside and outside motif

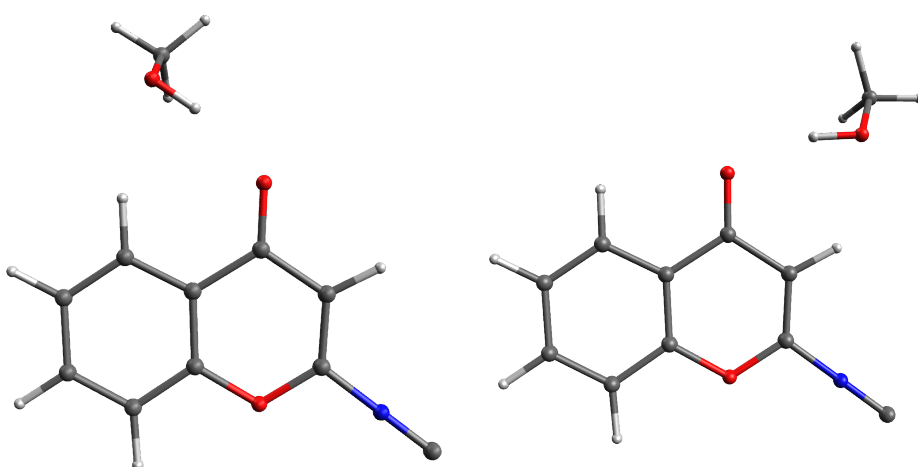


FIGURE C.21: Structures of 2-isocyanidochromone with methanol for both inside and outside motif

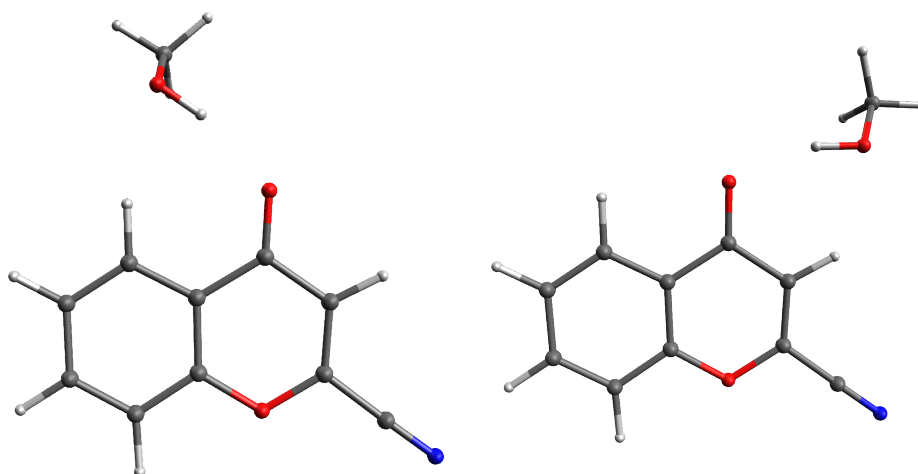


FIGURE C.22: Structures of 2-cyanidechromone with methanol for both inside and outside motif

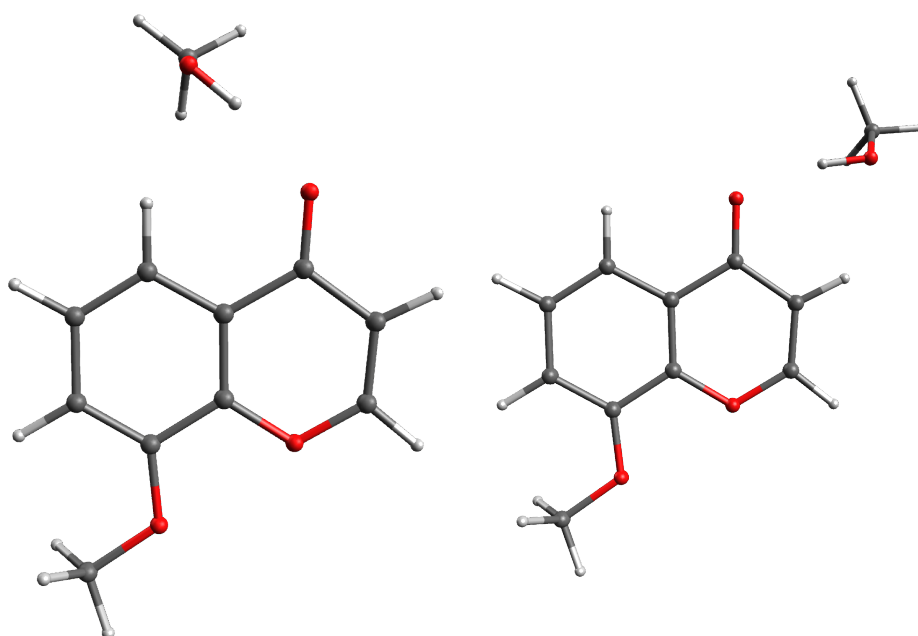


FIGURE C.23: Structures of 8-methoxychromone with methanol for both inside and outside motif

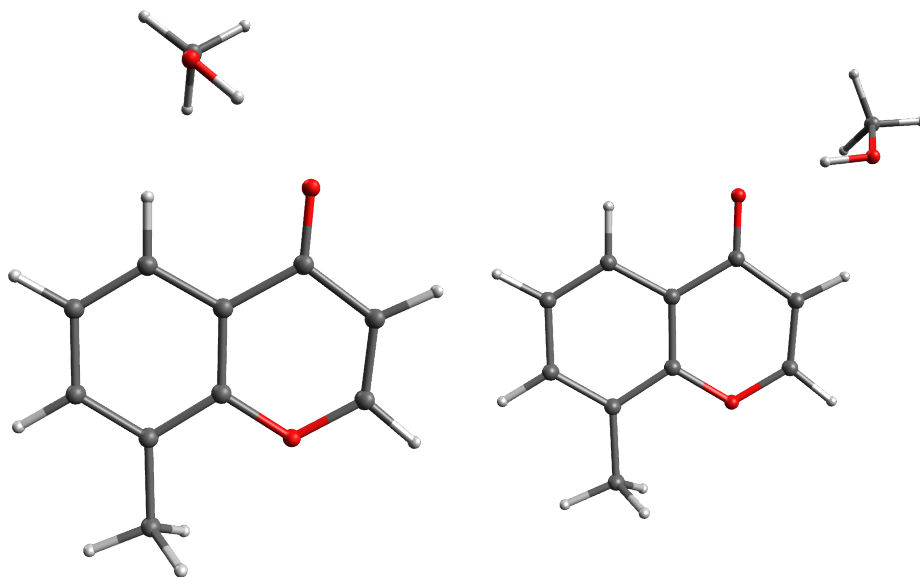


FIGURE C.24: Structures of 8-methylchromone with methanol for both inside and outside motif

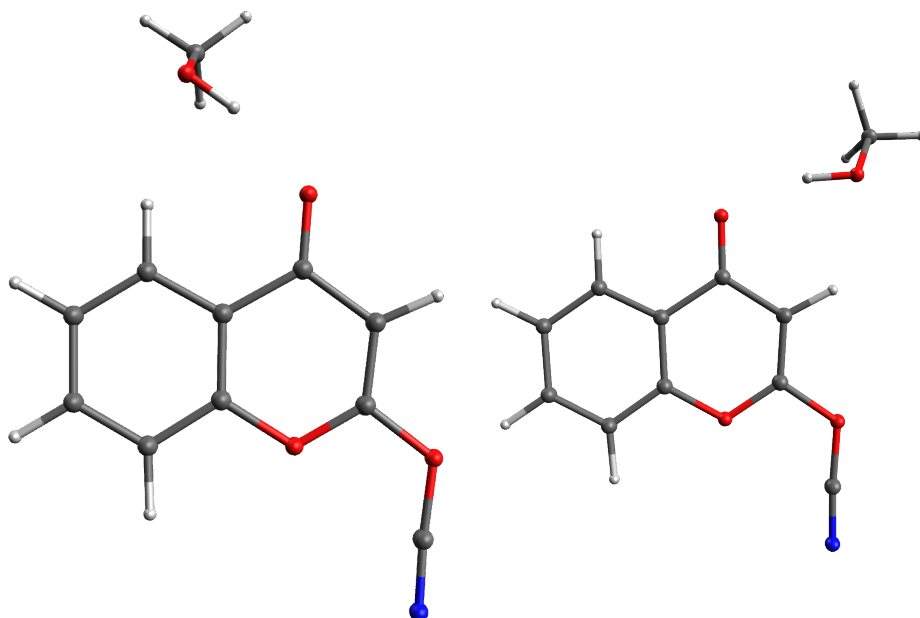


FIGURE C.25: Structures of 2-cyanatechromone with methanol for both inside and outside motif

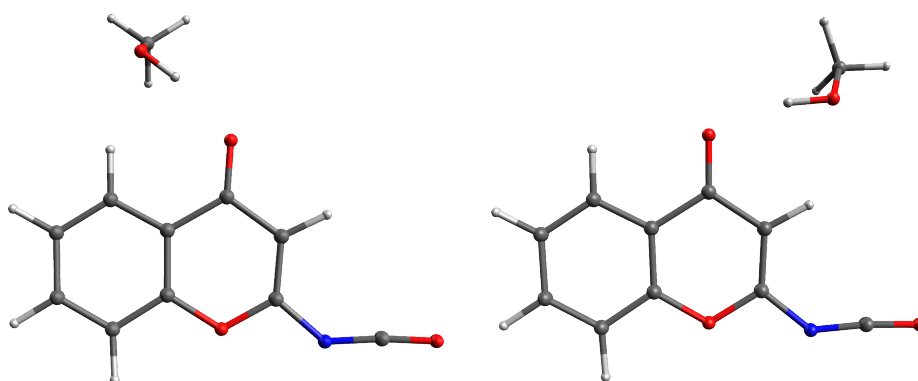


FIGURE C.26: Structures of 2-isocyanatechromone with methanol for both inside and outside motif

C.2 Excited state

Additional information concerning the excited state is given in the following. At first, the natural transition orbitals (NTOs), describing the vertical electronic excitations starting from the electronic ground state of each cluster are shown. Only the most dominant part of the decomposition is given, with the percentage given in the respective caption.

Natural transition orbitals

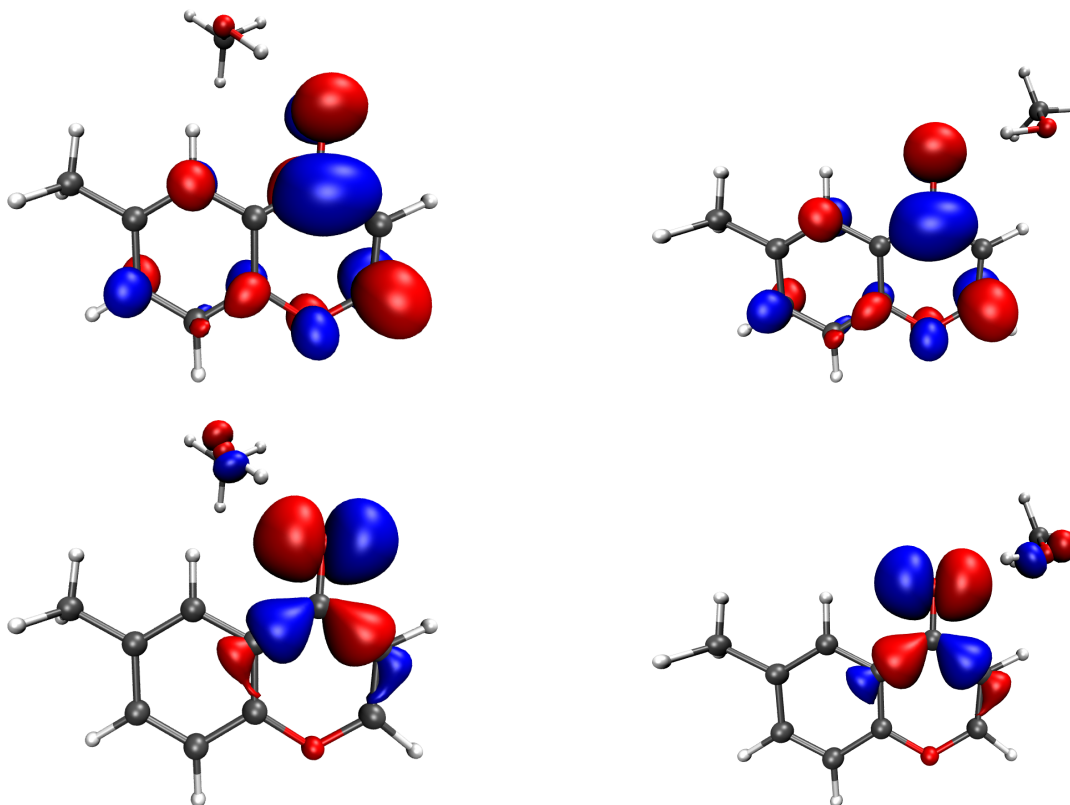


FIGURE C.27: NTOs of 6-methylchromone-methanol cluster for both inside and outside motif, $S_0 \rightarrow S_1$ with the occupied NTO at the bottom. The NTO pair accounts for 99% (out) and 99% (in) of the calculated transition.

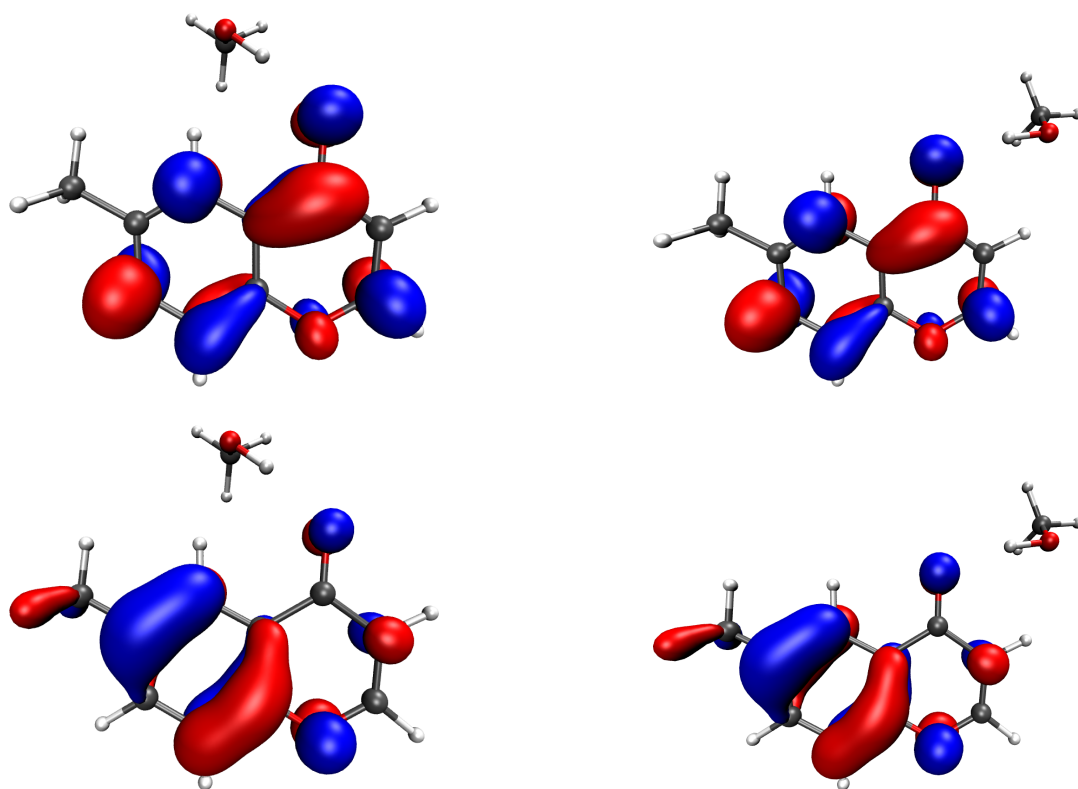


FIGURE C.28: NTOs of 6-methylchromone-methanol cluster for both inside and outside motif, $S_0 \rightarrow S_2$ with the occupied NTO at the bottom. The NTO pair accounts for 83% (out) and 84% (in) of the calculated transition.

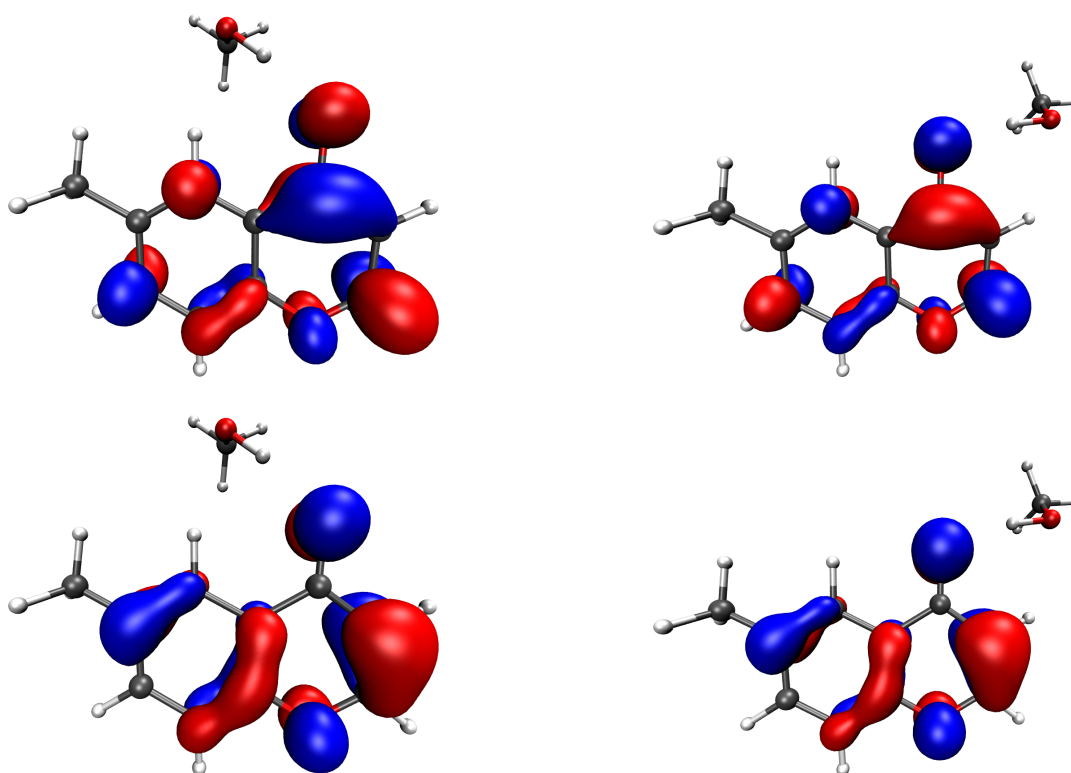


FIGURE C.29: NTOs of 6-methylchromone-methanol cluster for both inside and outside motif, $S_0 \rightarrow T_1$ with the occupied NTO at the bottom. The NTO pair accounts for 91% (out) and 91% (in) of the calculated transition.

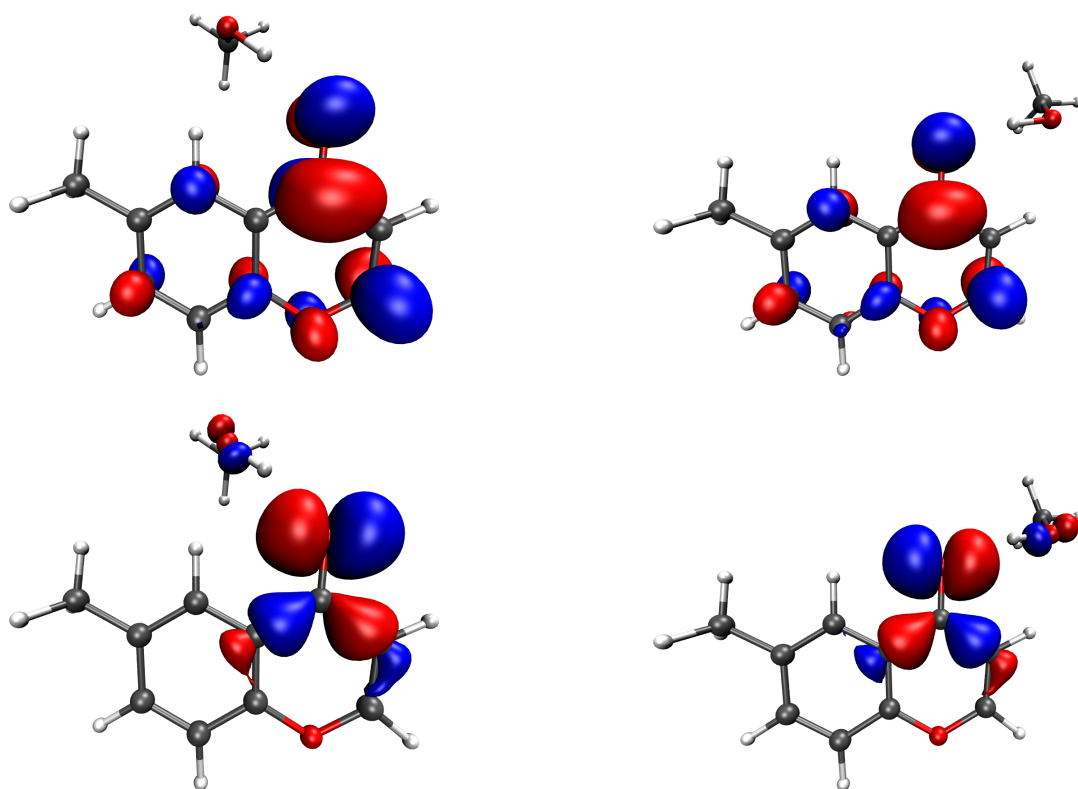


FIGURE C.30: NTOs of 6-methylchromone-methanol cluster for both inside and outside motif, $S_0 \rightarrow T_2$ with the occupied NTO at the bottom. The NTO pair accounts for 98% (out) and 99% (in) of the calculated transition.

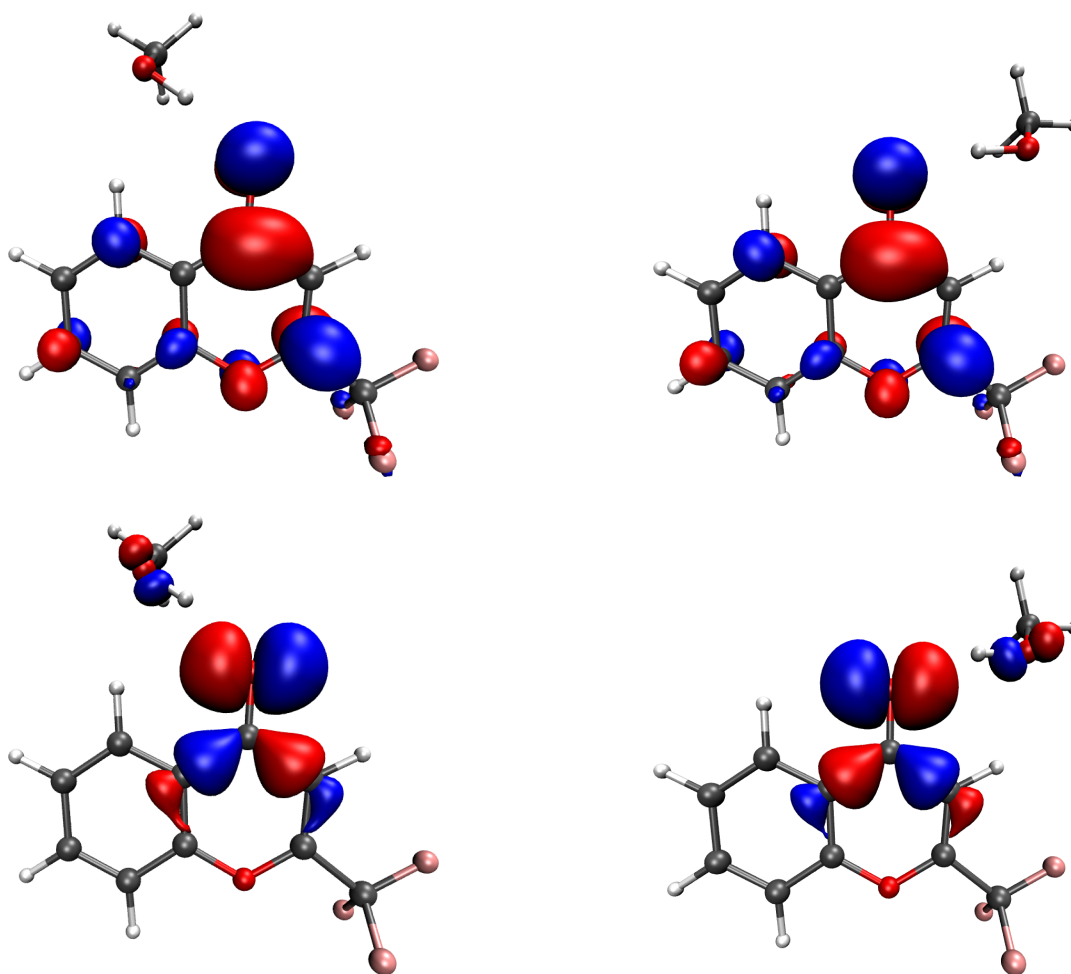


FIGURE C.31: NTOs of 2-CF₃chromone-methanol cluster for both inside and outside motif, $S_0 \rightarrow S_1$ with the occupied NTO at the bottom. The NTO pair accounts for 99% (out) and 99% (in) of the calculated transition.

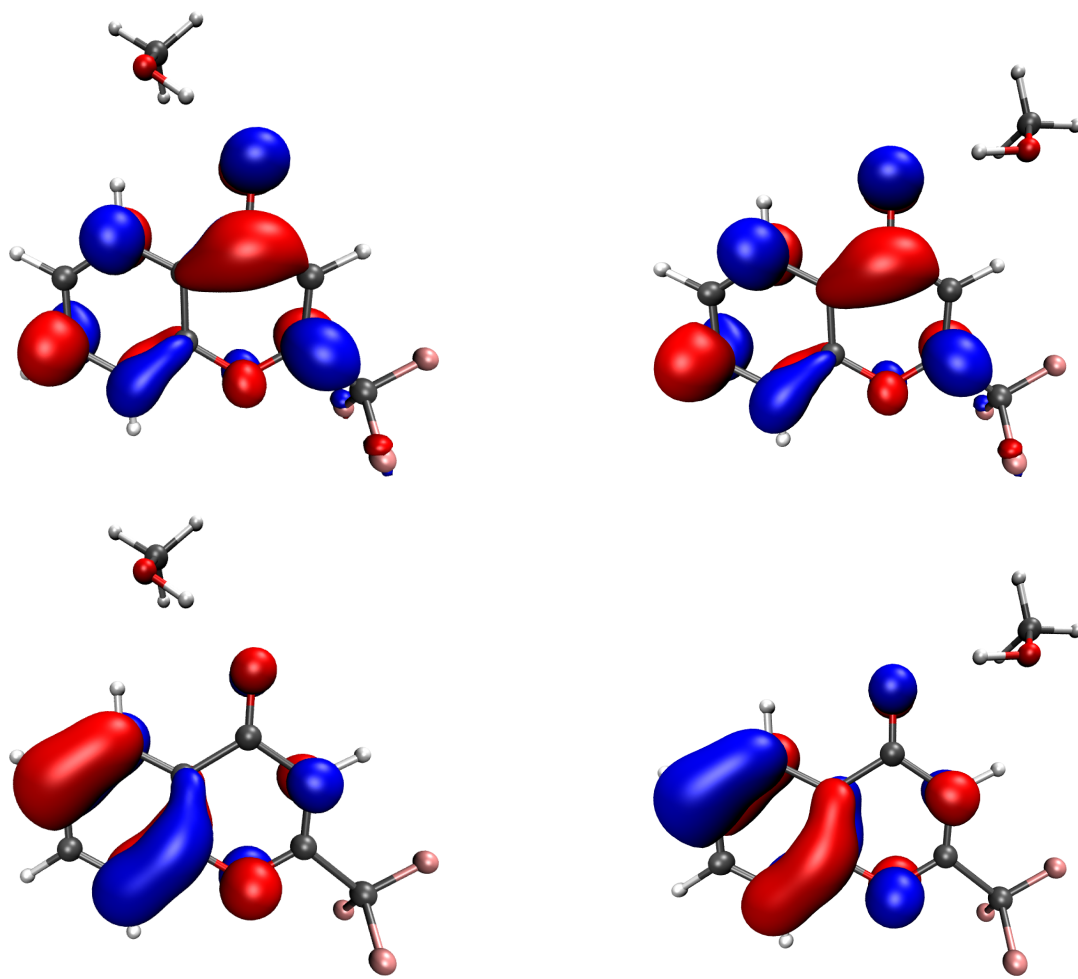


FIGURE C.32: NTOs of 2-CF₃chromone-methanol cluster for both inside and outside motif, $S_0 \rightarrow S_2$ with the occupied NTO at the bottom. The NTO pair accounts for 82% (out) and 83% (in) of the calculated transition.

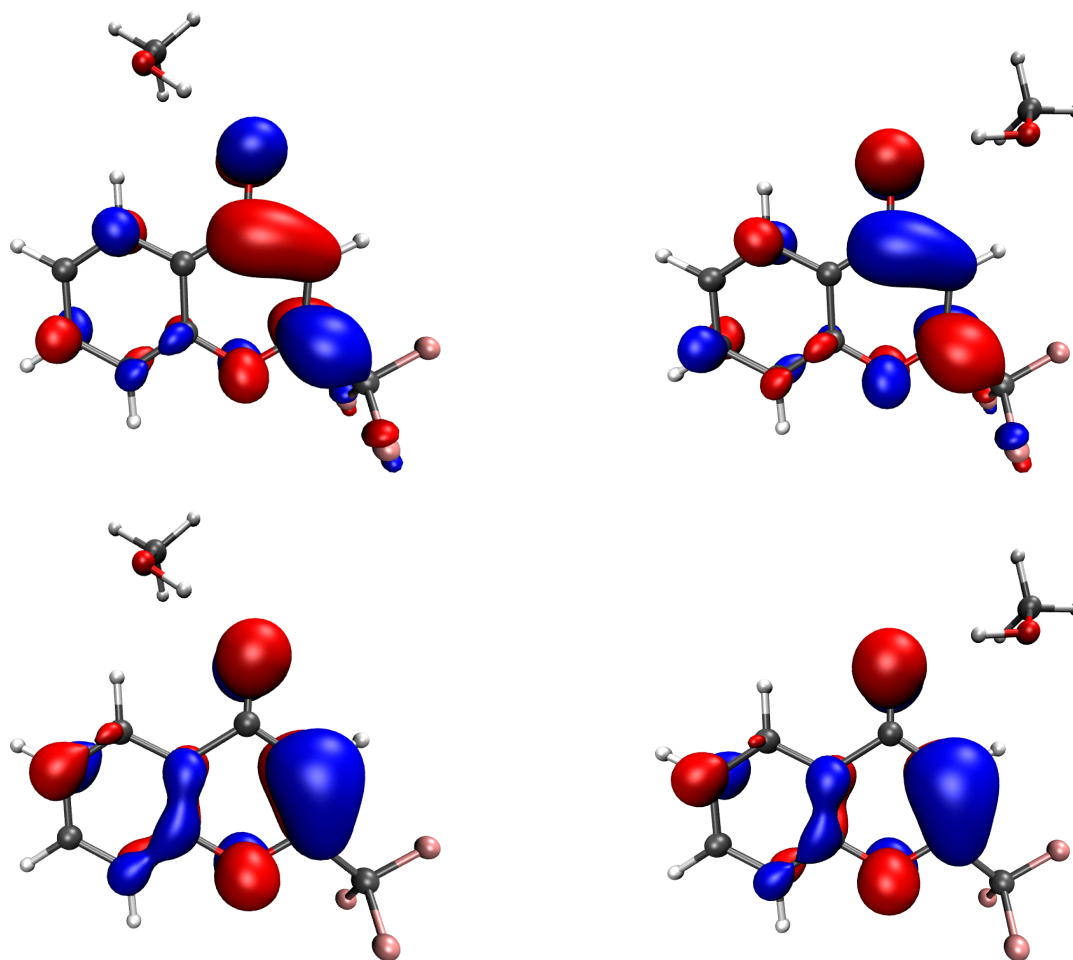


FIGURE C.33: NTOs of 2-CF₃chromone-methanol cluster for both inside and outside motif, $S_0 \rightarrow T_1$ with the occupied NTO at the bottom. The NTO pair accounts for 93% (out) and 93% (in) of the calculated transition.

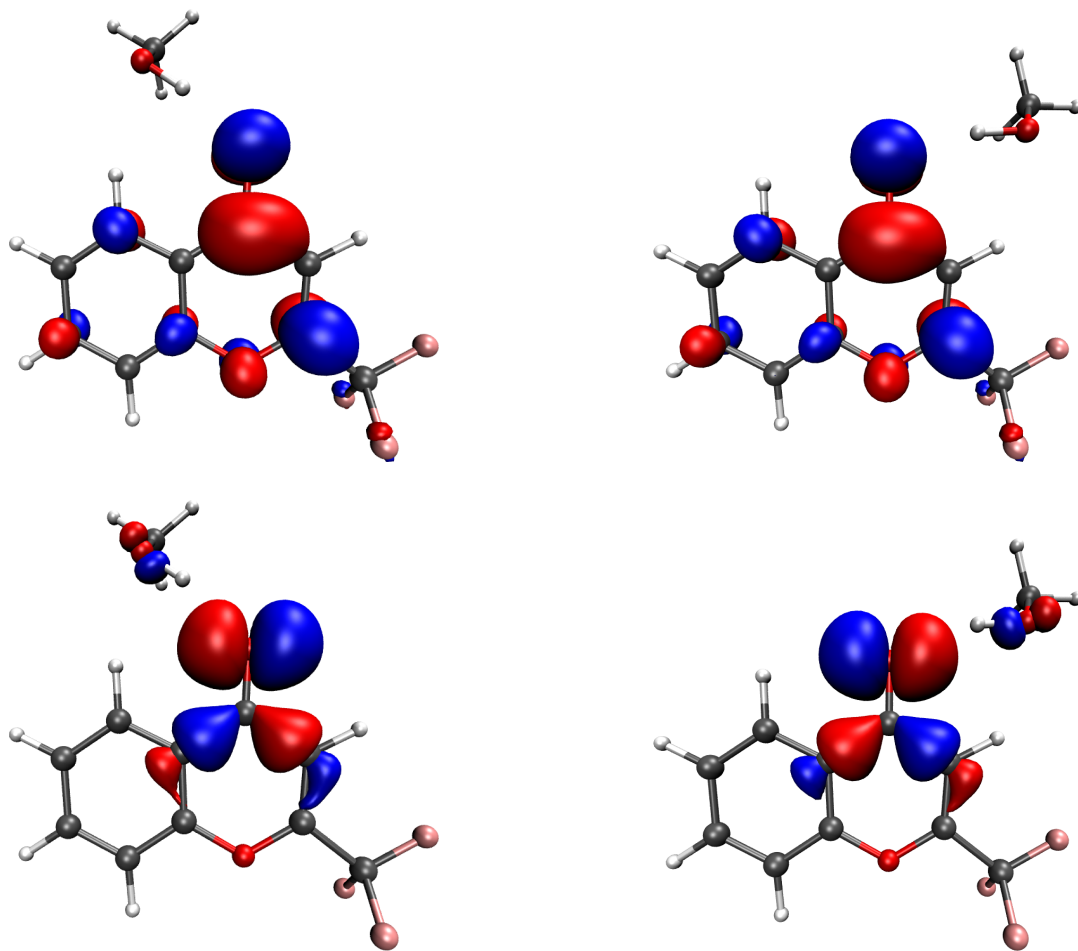


FIGURE C.34: NTOs of 2-CF₃chromone-methanol cluster for both inside and outside motif, $S_0 \rightarrow T_2$ with the occupied NTO at the bottom. The NTO pair accounts for 99% (out) and 99% (in) of the calculated transition.

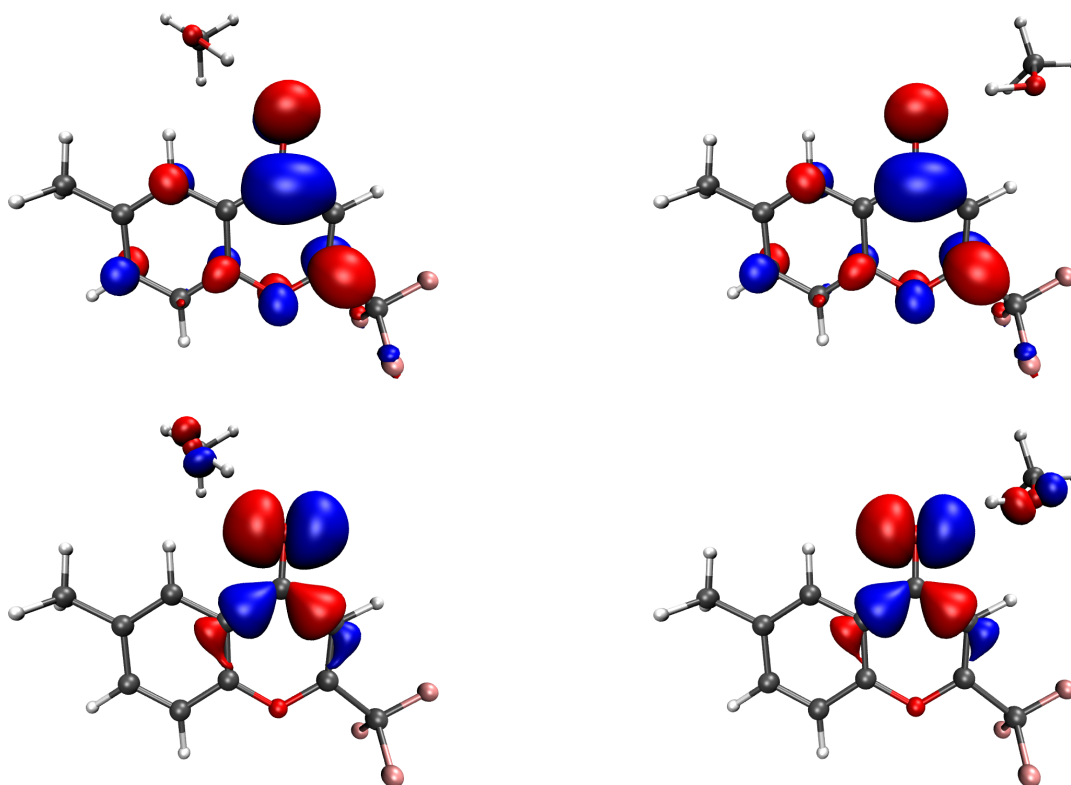


FIGURE C.35: NTOs of 2-CF₃,6-methylchromone-methanol cluster for both inside and outside motif, $S_0 \rightarrow S_1$ with the occupied NTO at the bottom. The NTO pair accounts for 99% (out) and 99% (in) of the calculated transition.

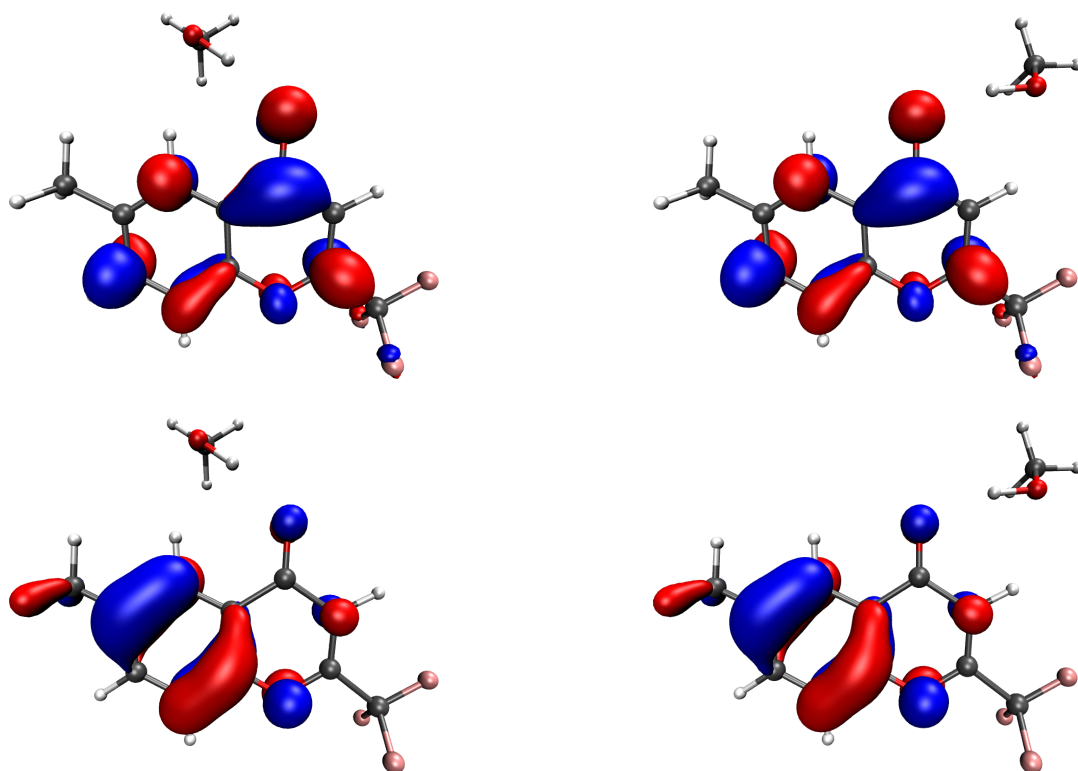


FIGURE C.36: NTOs of 2-CF₃,6-methylchromone-methanol cluster for both inside and outside motif, $S_0 \rightarrow S_2$ with the occupied NTO at the bottom. The NTO pair accounts for 85% (out) and 86% (in) of the calculated transition.

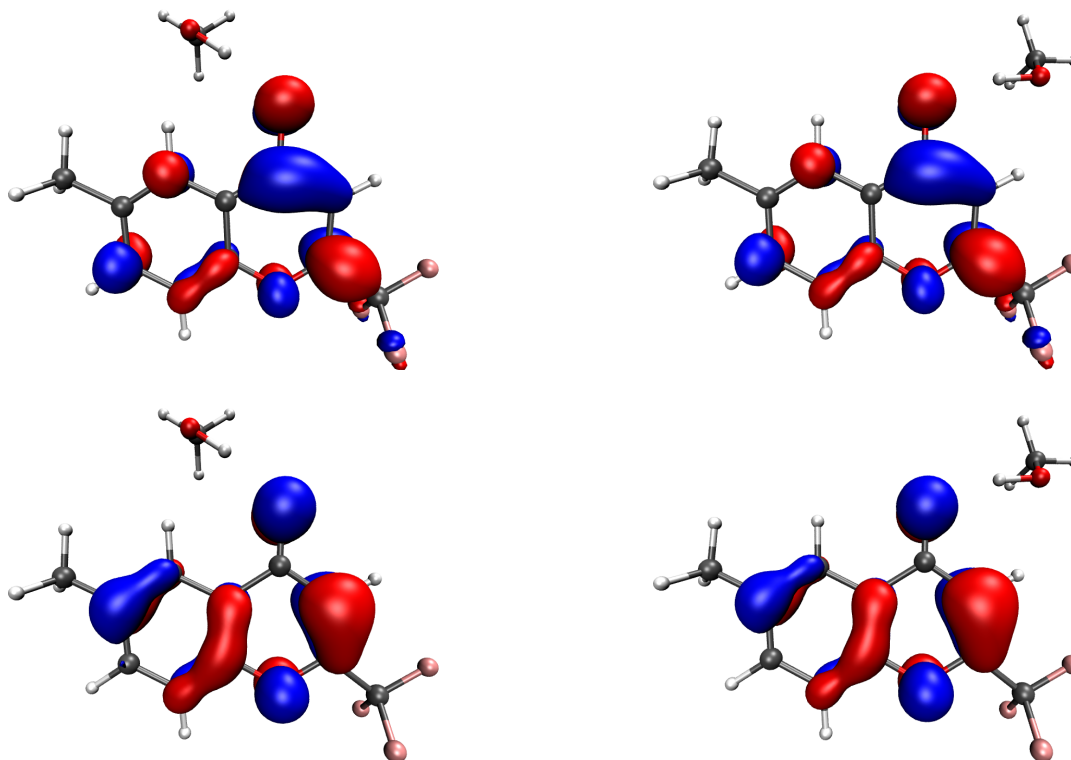


FIGURE C.37: NTOs of 2-CF₃,6-methylchromone-methanol cluster for both inside and outside motif, $S_0 \rightarrow T_1$ with the occupied NTO at the bottom. The NTO pair accounts for 92% (out) and 92% (in) of the calculated transition.

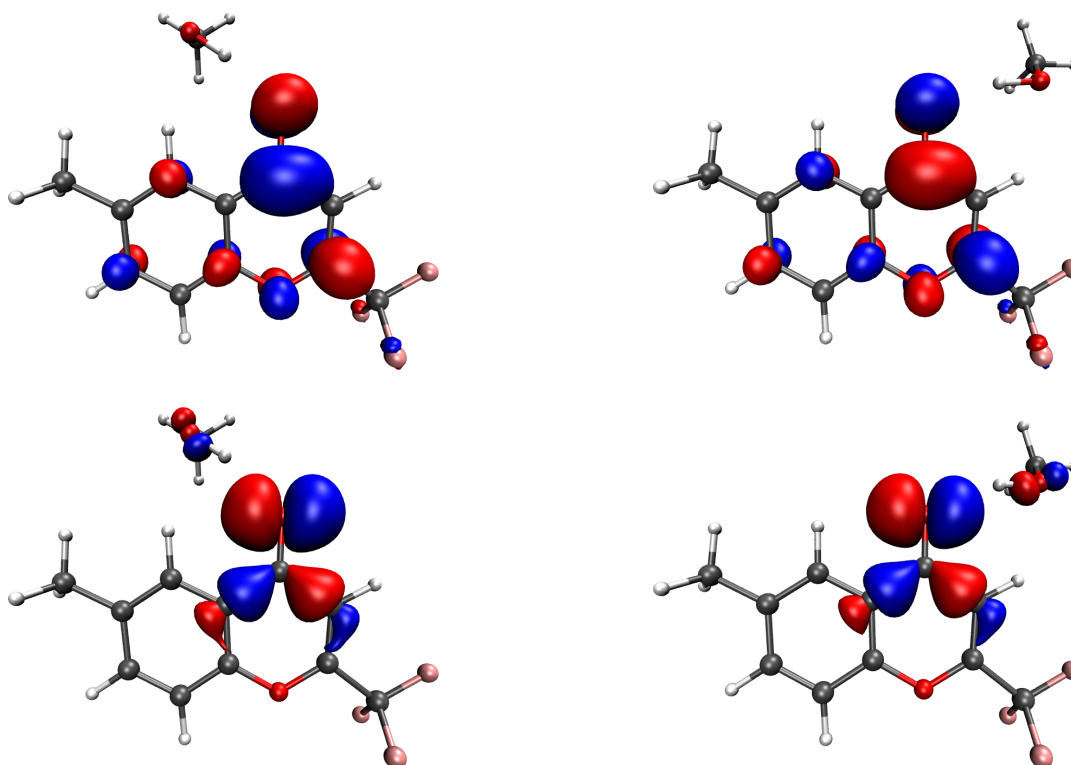


FIGURE C.38: NTOs of 2-CF₃,6-methylchromone-methanol cluster for both inside and outside motif, $S_0 \rightarrow T_2$ with the occupied NTO at the bottom. The NTO pair accounts for 99% (out) and 99% (in) of the calculated transition.

Appendix D

Reprint Permissions

For the publications and certain images, a reprint permission had to be obtained, which are displayed here.

Image "Gecko" on page 3 from website www.pixabay.com.^[15]

Pixabay license

Our license empowers creators and protects our community. We want to keep it as simple as possible. Here is an overview of what Pixabay content can and can't be used for. What is allowed? All content (e.g. images, videos, music) on Pixabay can be used for free for commercial and noncommercial use across print and digital, except in the cases mentioned in "What is not allowed". Attribution is not required. Giving credit to the artist or Pixabay is not necessary but is always appreciated by our community. You can make modifications to content from Pixabay.

What is not allowed? This section only applies to media users and not to the appropriate artists. Don't redistribute or sell Pixabay content on other stock or wallpaper platforms. Don't sell unaltered copies of content, e.g. don't sell an exact copy of a stock photo as a poster, print or on a physical product. Don't portray identifiable people in a bad light or in a way that is offensive. Don't use content with identifiable persons or brands to create a misleading association with a product or service.

Illustration "Supersonic Beam" on page 16 from Laserspektroskopie 2, W. Demtröder, 149.

The license agreement is printed in the following.

**SPRINGER NATURE LICENSE
TERMS AND CONDITIONS**

Aug 09, 2022

This Agreement between Patrick Strebert ("You") and Springer Nature ("Springer Nature") consists of your license details and the terms and conditions provided by Springer Nature and Copyright Clearance Center.

License Number	5364750585849
License date	Aug 09, 2022
Licensed Content Publisher	Springer Nature
Licensed Content Publication	Springer eBook
Licensed Content Title	Laserspektroskopie in Molekularstrahlen
Licensed Content Author	Wolfgang Demtröder
Licensed Content Date	Jan 1, 2013
Type of Use	Thesis/Dissertation
Requestor type	academic/university or research institute
Format	print and electronic
Portion	figures/tables/illustrations
Number of figures/tables /illustrations	1
Will you be translating?	no

Circulation/distribution	100 - 199
Author of this Springer Nature content	no
Title	Investigations on dispersion-bound complexes in multiple electronic states
Institution name	Technische Universität Kaiserslautern
Expected presentation date	Oct 2022
Portions	Figure 4.6 on page 149
Requestor Location	Patrick Strebert Erwin-Schrödinger-Straße 52 Kaiserslautern, 67663 Germany Attn: Patrick Strebert
Total	0.00 EUR

Terms and Conditions

Springer Nature Customer Service Centre GmbH Terms and Conditions

This agreement sets out the terms and conditions of the licence (the **Licence**) between you and **Springer Nature Customer Service Centre GmbH** (the **Licensor**). By clicking 'accept' and completing the transaction for the material (**Licensed Material**), you also confirm your acceptance of these terms and conditions.

1. Grant of License

1. 1. The Licensor grants you a personal, non-exclusive, non-transferable, world-wide licence to reproduce the Licensed Material for the purpose specified in your order only. Licences are granted for the specific use requested in the order and for no other use, subject to the conditions below.

1. 2. The Licensor warrants that it has, to the best of its knowledge, the rights to license reuse of the Licensed Material. However, you should ensure that the material you are requesting is original to the Licensor and does not carry the copyright of another entity (as credited in the published version).

1. 3. If the credit line on any part of the material you have requested indicates that it was reprinted or adapted with permission from another source, then you should also seek permission from that source to reuse the material.

2. Scope of Licence

2. 1. You may only use the Licensed Content in the manner and to the extent permitted by these Ts&Cs and any applicable laws.

2. 2. A separate licence may be required for any additional use of the Licensed Material, e.g. where a licence has been purchased for print only use, separate permission must be obtained for electronic re-use. Similarly, a licence is only valid in the language selected and does not apply for editions in other languages unless additional translation rights have been granted separately in the licence. Any content owned by third parties are expressly excluded from the licence.

2. 3. Similarly, rights for additional components such as custom editions and derivatives require additional permission and may be subject to an additional fee.

Please apply to

Journalpermissions@springernature.com/bookpermissions@springernature.com for these rights.

2. 4. Where permission has been granted **free of charge** for material in print, permission may also be granted for any electronic version of that work, provided that the material is incidental to your work as a whole and that the electronic version is essentially equivalent to, or substitutes for, the print version.

2. 5. An alternative scope of licence may apply to signatories of the [STM Permissions Guidelines](#), as amended from time to time.

3. Duration of Licence

3. 1. A licence for is valid from the date of purchase ('Licence Date') at the end of the relevant period in the below table:

Scope of Licence	Duration of Licence
Post on a website	12 months
Presentations	12 months
Books and journals	Lifetime of the edition in the language purchased

4. Acknowledgement

4. 1. The Licensor's permission must be acknowledged next to the Licenced Material in print. In electronic form, this acknowledgement must be visible at the same time as the figures/tables/illustrations or abstract, and must be hyperlinked to the journal/book's homepage. Our required acknowledgement format is in the Appendix below.

5. Restrictions on use

5. 1. Use of the Licensed Material may be permitted for incidental promotional use and minor editing privileges e.g. minor adaptations of single figures, changes of format, colour and/or style where the adaptation is credited as set out in Appendix 1 below. Any other changes including but not limited to, cropping, adapting, omitting material that affect the meaning, intention or moral rights of the author are strictly prohibited.

5. 2. You must not use any Licensed Material as part of any design or trademark.

5. 3. Licensed Material may be used in Open Access Publications (OAP) before publication by Springer Nature, but any Licensed Material must be removed from OAP sites prior to final publication.

6. Ownership of Rights

6. 1. Licensed Material remains the property of either Licensor or the relevant third party and any rights not explicitly granted herein are expressly reserved.

7. Warranty

IN NO EVENT SHALL LICENSOR BE LIABLE TO YOU OR ANY OTHER PARTY OR ANY OTHER PERSON OR FOR ANY SPECIAL, CONSEQUENTIAL, INCIDENTAL OR INDIRECT DAMAGES, HOWEVER CAUSED, ARISING OUT OF OR IN CONNECTION WITH THE DOWNLOADING, VIEWING OR USE OF THE MATERIALS REGARDLESS OF THE FORM OF ACTION, WHETHER FOR BREACH OF CONTRACT, BREACH OF WARRANTY, TORT, NEGLIGENCE, INFRINGEMENT OR OTHERWISE (INCLUDING, WITHOUT LIMITATION, DAMAGES BASED ON LOSS OF PROFITS, DATA, FILES, USE, BUSINESS OPPORTUNITY OR CLAIMS OF THIRD PARTIES), AND WHETHER OR NOT THE PARTY HAS BEEN ADVISED OF THE POSSIBILITY OF SUCH DAMAGES. THIS LIMITATION SHALL APPLY NOTWITHSTANDING ANY FAILURE OF ESSENTIAL PURPOSE OF ANY LIMITED REMEDY PROVIDED HEREIN.

8. Limitations

8. 1. BOOKS ONLY: Where 'reuse in a dissertation/thesis' has been selected the following terms apply: Print rights of the final author's accepted manuscript (for clarity, NOT the published version) for up to 100 copies, electronic rights for use only on a personal website or institutional repository as defined by the Sherpa guideline (www.sherpa.ac.uk/romeo/).

8. 2. For content reuse requests that qualify for permission under the [STM Permissions Guidelines](#), which may be updated from time to time, the STM Permissions Guidelines supersede the terms and conditions contained in this licence.

9. Termination and Cancellation

9. 1. Licences will expire after the period shown in Clause 3 (above).

9. 2. Licensee reserves the right to terminate the Licence in the event that payment is not received in full or if there has been a breach of this agreement by you.

Appendix 1 — Acknowledgements:

For Journal Content:

Reprinted by permission from [the Licensor]: [Journal Publisher (e.g. Nature/Springer/Palgrave)] [JOURNAL NAME] [REFERENCE CITATION (Article name, Author(s) Name), [COPYRIGHT] (year of publication)

For Advance Online Publication papers:

Reprinted by permission from [the Licensor]: [Journal Publisher (e.g. Nature/Springer/Palgrave)] [JOURNAL NAME] [REFERENCE CITATION (Article name, Author(s) Name), [COPYRIGHT] (year of publication), advance online publication, day month year (doi: 10.1038/sj.[JOURNAL ACRONYM].)

For Adaptations/Translations:

Adapted/Translated by permission from [the Licensor]: [Journal Publisher (e.g. Nature/Springer/Palgrave)] [JOURNAL NAME] [REFERENCE CITATION (Article name, Author(s) Name), [COPYRIGHT] (year of publication)

Note: For any republication from the British Journal of Cancer, the following credit line style applies:

Reprinted/adapted/translated by permission from [the Licensor]: on behalf of Cancer Research UK: : [Journal Publisher (e.g. Nature/Springer/Palgrave)] [JOURNAL NAME] [REFERENCE CITATION (Article name, Author(s) Name), [COPYRIGHT] (year of publication)

For Advance Online Publication papers:

Reprinted by permission from The [the Licensor]: on behalf of Cancer Research UK: [Journal Publisher (e.g. Nature/Springer/Palgrave)] [JOURNAL NAME] [REFERENCE CITATION (Article name, Author(s) Name), [COPYRIGHT] (year of publication), advance online publication, day month year (doi: 10.1038/sj.[JOURNAL ACRONYM].)

For Book content:

Reprinted/adapted by permission from [the Licensor]: [Book Publisher (e.g. Palgrave Macmillan, Springer etc)] [Book Title] by [Book author(s)] [COPYRIGHT] (year of publication)

Other Conditions:

Version 1.3

Questions? customercare@copyright.com or +1-855-239-3415 (toll free in the US) or +1-978-646-2777.

Publication I

"Dispersion-Bound Isolated Dimers in the Gas Phase: Observation of the Shortest Intermolecular C-H...H-C Distance via Stimulated Raman Spectroscopy", D. Maué, P. H. Strebert, D. Bernhard, S. Rösel, P. R. Schreiner, M. Gerhards, *Angew. Chem. Int. Ed.*, **2021**, *60*, 11305–11309. DOI: 10.1002/anie.202016020

This is an open access article under the terms of the Creative Commons Attribution-NonCommercial-NoDerivs License, which permits use and distribution in any medium, provided the original work is properly cited, the use is non-commercial and no modifications or adaptations are made.

Do I need to request permission to use my own work as my dissertation? If you are the author of a published Wiley article, you have the right to reuse the full text of your published article as part of your thesis or dissertation. In this situation, you do not need to request permission from Wiley for this use. <https://www.wiley.com/network/researchers/latest-content/how-to-clear-permissions-for-a-thesis-or-dissertation>

Publication II

"Chromone–methanol clusters in the electronic ground and lowest triplet state: a delicate interplay of non-covalent interactions", P. Boden, P. H. Strebert, M. Meta, F. Dietrich, C. Riehn, M. Gerhards, *Phys. Chem. Chem. Phys.*, **2022**, *24*, 15208-15216. DOI: 10.1039/D2CP01341J

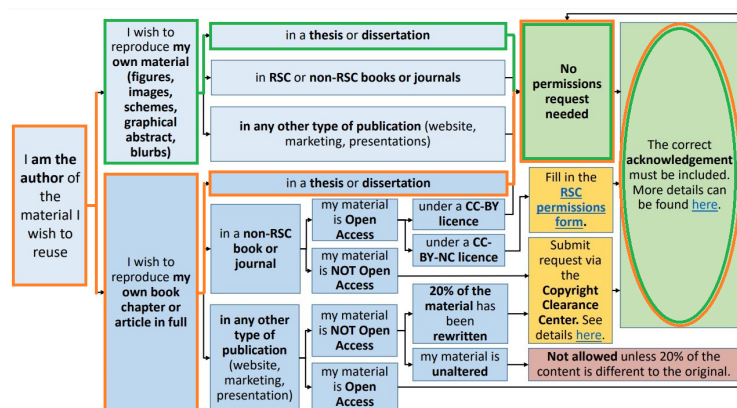


FIGURE D.1: Reuse permissions requests from <https://www.rsc.org/journals-books-databases/author-and-reviewer-hub/authors-information/licences-copyright-permissions/>

Appendix E

Contributions to conferences

E.1 Oral presentations

- 4th Summer School of the Priority Program SPP 1807, Paderborn, 16.07. - 19.07.2019
- 5th Summer School of the Priority Program SPP 1807, digital, 04.03. - 05.03.2021
- Frühjahrstagung der Deutschen Physikalischen Gesellschaft (DPG) 2021, Kaiserslautern (digital), 20.09. - 24.09.2021
- 6th Summer School of the Priority Program SPP 1807, digital, 15.03. - 16.03.2022

E.2 Poster presentations

- 54. Symposium on Theoretical Chemistry, Halle (Saale), 17.09. - 20.09.2018
- 9. Molecular Quantum Mechanics Conference, Heidelberg, 30.06. - 05.07.2019
- 55. Symposium on Theoretical Chemistry, Rostock, 22.09 - 26.09.2019
- 120. Bunsentagung, Regensburg (digital), 10.05. - 12.05.2021

Danksagung

Das Zustandekommen Dissertation wäre ohne die Kooperation und den Austausch mit zahlreichen Personen nicht in der Form möglich gewesen. Mein besonderer Dank gilt daher:

Prof. Dr. Markus Gerhards, der mich bereits im Studium für die physikalische Chemie begeisterte und nach der Masterarbeit in seine Arbeitsgruppe aufnahm. Ich werde die zahlreichen wissenschaftlichen, aber auch nicht-wissenschaftlichen Diskussionen in guter Erinnerung halten.

PD Dr. Christoph Riehn, der nach dem Verscheiden von Markus die Betreuung in einer schwierigen Situation übernahm. Er leistete einen großen Beitrag die zweite Hälfte meiner Doktorarbeit erfolgreich zu gestalten und sogar noch eine Publikation zu veröffentlichen.

Prof. Dr. Gereon Niedner-Schatteburg, in dessen Gruppe ich im Rahmen von Bachelorarbeit und Forschungspraktikum meine ersten wissenschaftliche Schritte tat. Natürlich möchte ich mich auch für die Übernahme des Zweitgutachtens, die administrative Übernahme des Arbeitskreises bedanken und es mir ermöglichte die Doktorarbeit geregelt abzuschließen.

Jun.-Prof. Sabine Becker für die Übernahme des Vorsitzes der Prüfungskommission.

dem gesamten Arbeitskreis Gerhards mit all seinen aktuellen und ehemaligen Mitgliedern für die tolle Arbeitsatmosphäre und Kooperationen bei allen Problemen im Laboralltag, insbesondere:

Dr. Pol Boden, der mit mir zusammen das Gasphasenlabor unsicher gemacht und mich als Laborkollege stets unterstützt hat.

Dr. Fabian Dietrich für die zahlreichen fachlichen Diskussionen. Seinen Beitrag zu der Publikation bzgl. der Chromon-Methanol-Clustern und beim Korrekturlesen der Arbeit möchte ich besonders hervorheben.

Dr. Kirsten Schwing, für die Koordination des Arbeitskreises und stete Hilfsbereitschaft und Unterstützung.

Dr. Dominique Maué und Dr. Dominic Bernhard, die mich in den Alltag im Gasphasenlabor, die laserspektroskopischen Experimente und quantenchemischen Rechnungen eingeführt und ausgebildet haben und zahlreiche Fragen beantworten mussten.

Prof. Dr. van Wüllen für die Durchführung einiger Rechnungen für das ^tBuTPM Dimer und die Bearbeitung jeglicher Anliegen bezüglich des Rechenclusters, die die zahlreichen quantenchemischen Rechnungen dieser Arbeit erst möglich gemacht hat.

den Studenten, die ich im Rahmen von Forschungspraktika und Abschlussarbeiten betreuen durfte und mich in meiner Arbeit zeitweise begleitet haben: Marcel Meta, Sarah Schröck, Marvin Theisen, Sophie Thommes und Nils Wolfgramm.

der Chemikalienausgabe mit Ludvik Napast, Jürgen Rahm und Frank Schröer für die zahlreichen Gasflaschen und Chemikalien, die auch abseits der regulären Öffnungszeiten den Besitzer gewechselt haben.

dem gesamten Flur im fünften Stock mit den Mitarbeitern der Arbeitsgruppen Niedner-Schatteburg, Meyer und Becker für die angenehme Atmosphäre und Hilfe bei den kleinen und großen Problemen.

dem Sekretariat der physikalischen Chemie mit Frau Heieck, Frau Harrison-Weber und Frau Stemler.

dem Dekanat der Chemie, insbesondere Frau Schramm und Frau Mounassib.

der deutschen Forschungsgemeinschaft (DFG) für die finanzielle Unterstützung im Rahmen des Schwerpunktprogrammes "Control of London Dispersion Interactions in Molecular Chemistry" (SPP1807).

allen Kooperationspartnern im Rahmen des SPP 1807 für den wissenschaftlichen Austausch im Rahmen von zahlreichen Treffen, insbesondere Sören Rösel und Prof. Dr. Schreiner für die Synthese des ^tBuTPM.

dem Deutschlandstipendium, welches mich im Rahmen meines Bachelor- und Masterstudium unterstützt hat. Hierbei möchte ich der BASF sowie den Stadtwerken Kaiserslautern für die Förderung danken.

zuletzt natürlich meiner Familie und engen Freunden, die mich zeitlebens unterstützt haben.

Lebenslauf

Persönliche Daten

Patrick Horst Strebert
Adresse: Erwin-Schrödinger-Straße 52
67663 Kaiserslautern
Rheinland-Pfalz, Deutschland
E-Mail: strebert@rhrk.uni-kl.de

Ausbildung

10/2013 – 11/2016 Technische Universität Kaiserslautern, Bachelor of Science, Chemie
10/2016 – 09/2018 Technische Universität Kaiserslautern, Master of Science, Chemie
11/2018 – heute Technische Universität Kaiserslautern, Promotion, Physikalische Chemie
Untersuchung von London-Dispersion mittels Gasphasenspektroskopie